Scuola Internazionale Superiore degli Studi Avanzati

ENTANGLEMENT AND CONSTRAINED DYNAMICS IN STRONGLY CORRELATED SYSTEMS

Ph.D. thesis
in
STATISTICAL PHYSICS

Candidate:
Giuliano Giudici

Supervisor:
Marcello Dalmonte

Academic Year 2019-2020

List of publications

Publications included in this thesis:

- G. Giudici, T. Mendes-Santos, P. Calabrese, M. Dalmonte
  Entanglement Hamiltonians of lattice models via the Bisognano-Wichmann theorem
  Physical Review B 98, 134403 (2018)
- T. Mendes-Santos, G. Giudici, R. Fazio, M. Dalmonte
  Measuring von Neumann entanglement entropies without wave functions
  New Journal of Physics 22, 013044 (2020)
- T. Mendes-Santos, G. Giudici, M. Dalmonte, M. A. Rajabpour
  Entanglement Hamiltonian of quantum critical chains and conformal field theories
  Physical Review B 100, 155122 (2019)
- X. Turkeshi, T. Mendes-Santos, G. Giudici, M. Dalmonte
  Entanglement-Guided Search for Parent Hamiltonians
  Physical Review Letters 122, 150606 (2019)
- G. Giudici, A. Angelone, G. Magnifico, Z. Zeng, G. Giudice, T. Mendes-Santos, M. Dalmonte
  Diagnosing Potts criticality and two-stage melting in one-dimensional hard-core boson models
  Physical Review B 99, 094434 (2019)
- F. M. Surace, P. P. Mazza, G. Giudici, A. Lerose, A. Gambassi, M. Dalmonte
  Lattice gauge theories and string dynamics in Rydberg atom quantum simulators
  Physical Review X 10, 021041 (2020)
- G. Giudici, F. M. Surace, J. E. Ebot, A. Scardicchio, M. Dalmonte
  Breakdown of ergodicity in disordered U(1) lattice gauge theories
  Physical Review Research 2, 032034(R) (2020)

Forthcoming publications discussed in this thesis:

- G. Giudici, N. Schuch
  Locality optimization of tensor network parent Hamiltonians
  In preparation

Other publications not included in this thesis:

- G. Mussardo, G. Giudici, J. Viti
  The coprime quantum chain
  Journal of Statistical Mechanics: Theory and Experiment, 033104 (2017)
- E. M. Inack, G. Giudici, T. Parolini, G. Santoro, S. Pilati
  Understanding quantum tunneling using diffusion Monte Carlo simulations
  Physical Review A 97, 032307 (2018)
- T. Parolini, E. M. Inack, G. Giudici, S. Pilati
  Tunneling in projective quantum Monte Carlo simulations with guiding wave functions
  Physical Review B 100, 214303 (2019)
- F. M. Surace, G. Giudici, M. Dalmonte
  Weak-ergodicity-breaking via lattice supersymmetry
  arXiv:2003.11073

Introduction

Many-body quantum systems exhibit a variety of fascinating phenomena that marked the last half-century research activity in condensed matter physics. At zero temperature, phase transitions are driven entirely by quantum fluctuations [1]. The latter can lead to completely novel phases of matter that go beyond the classical Landau spontaneous symmetry breaking paradigm [2] and stand out for their non-local order and sensitivity to the topology of the manifold on which the system is set [3]. When a temperature is switched on, quantum statistical mechanics is commonly used to describe the combined effect of thermal and quantum fluctuations. The eigenstates thermalization hypothesis (ETH) [4, 5] legitimizes our use of statistical ensembles, explaining how they arise from a unitary time evolution, with exceptions to such a generic scenario - manifested as lack of equilibration - attracting interest on their own [6, 7].

Over the last decades, concepts and tools originally conceived and developed within the context of quantum information have profoundly improved our understanding of strongly correlated quantum matter [8]. A pivotal role in this endeavor had been played by entanglement: given a bipartition A, B of a quantum state $|\psi\rangle$, all the information about its entanglement properties is carried by the reduced density matrix (RDM) $\rho_A = \mathrm{Tr}_B|\psi\rangle\langle\psi|$. Various measures have been defined to quantify the amount of entanglement contained in a pure quantum state. One of the most popular is the von Neumann entanglement entropy, which is the Shannon entropy of the eigenvalues of ρ_A, namely the entanglement spectrum (ES). Ground states of local Hamiltonians have very low entanglement entropy, generally scaling with the area of the boundary separating the two subsystems. Exceptions to this "area law" are tied to the nature of the fundamental excitations, a paradigmatic example being the logarithmic scaling in one-dimensional conformal field theories [9]. The entanglement entropy time dependence when the system is out-of-equilibrium can even be used to identify ETH violations [10]. Moreover, entanglement measures are crucial to quantify the complexity of quantum states and our capability of representing them efficiently [11]. The area law of entanglement is the ultimate reason for the success, in one-dimensional systems, of entanglement-based approximation schemes such as the density-matrix renormalization group algorithm [12], that led to the development of the theory of tensor networks [13]. Most importantly, entanglement properties are now experimentally accessible in systems with few qubits. For instance, full state tomography has been successfully applied to directly obtain all the matrix elements of the RDM [14] and quadratic functions of the RDM have been measured from interfering two identical copies of a many-body state [15] or by performing random measurements on a single copy of the state [16].

Until now, entanglement has been investigated based on a few entanglement measures extracted from the entanglement spectrum, such as the above-mentioned entanglement entropy. However, only the knowledge of the full ES distribution and the RDM eigenvectors can give complete information on the quantum correlations encoded in the state. It is the purpose of Chapter 1 to address a full characterization of the functional form of the RDM by shifting the focus from wavefunctions to entanglement Hamiltonians. The entanglement Hamiltonian (EH) of a subsystem A is defined from the RDM as $\rho_A = e^{-\tilde{H}_A}$ and captures all the entanglement properties of the quantum state.

The ground state EH of a many-body system is a well-known object in quantum field theory (QFT). The path integral representation of the RDM enables to prove that the EH admits a strikingly simple expression in terms of the Hamiltonian density [17], known as the Bisognano-Wichmann theorem [18, 19]:

$$\tilde{H}_A = \int_A r(x)h(x)dx, \tag{1}$$

where $r(x)$ is the distance of the point x from the boundary between the two subsystems, while $h(x)$ is the Hamiltonian density. As we will show, the reliability of this QFT prediction turns out to be extraordinarily far-reaching on microscopic lattice models when a proper discretization of the continuum EH is performed. Its locality, which follows from this QFT result, has two remarkable advantages. First, it provides a viable route to measure entanglement properties in experiments, by means of quantum simulation and spectroscopy of the EH. Second, it paves the way to the application of statistical mechanics tools to compute entanglement witnesses, via the use of numerical algorithms that are scalable in any dimension.

The knowledge of the EH remarkably provides direct access to the entanglement properties of the ground state without the need for the ground state wavefunction. Yet, in some situations, the wavefunction is the only thing at disposal, while its parent Hamiltonian, i.e. a Hamiltonian whose ground state is the wavefunction at hand, is unknown. Examples include topologically non-trivial states such as resonating valence bond [20] and Laughlin wavefunctions [21]. Given the relation between the EH and the Hamiltonian of the system in Eq. (1), the problem of finding a parent Hamiltonian for a target state represents a complementary approach to shed light on the entanglement structure of the state. In fact, although the correspondence between many-body quantum states and parent Hamiltonians is not one-to-one, the relationship between a wavefunction and its EH can be inverted utilizing Eq. (1) to yield a valid parent Hamiltonian. In Chapter 2 we will demonstrate this by devising an entanglement-guided search built on Eq. (1). We will prove its effectiveness on various wavefunctions carrying a large correlation length with respect to the lattice spacing, a condition that is necessary to justify the applicability of QFT. A somewhat opposite scenario comes out when the target wavefunction is an exact tensor network state. Tensor network states exhibit a very simple, yet non-trivial, entanglement pattern, which cannot be fully captured by Eq. (1). This fact is easy to understand in one dimension, where their entanglement spectrum is made of only a few non-vanishing eigenvalues. Although their simple entanglement structure guarantees the locality of their parent Hamiltonian, the latter can be a fairly complicated object in more than one dimension [22]. The second part of Chapter 2 will be devoted to the study and simplification of tensor network parent Hamiltonians, with particular attention to two-dimensional, topologically ordered states.

While in the first two chapters we will be mainly concerned with equilibrium features of idealized many-body systems bearing theoretical, more than experimental, relevance, in Chapter 3 we will turn to realistic experimental setups, where quantum dynamics serves as a probe for both equilibrium and out-of-equilibrium properties [23]. As a matter of fact, quantum simulators have already been proven capable of outperforming classical tensor network algorithms for computing the dynamics of one dimensional many-body systems at long times [24], and they represent one of the most promising routes towards the understanding of strong quantum correlations in more than one dimension. The main focus will be on a quantum simulator built out of Rydberg atom arrays [25]. By coherently coupling the ground state of neutral Rubidium atoms to a highly excited Rydberg state, it is possible to obtain an effective multi-qubit system whose dynamics is governed by a Hamiltonian with tunable couplings. The dipole-dipole interactions between Rydberg states naturally induce a constraint which forbids the simultaneous occupation of the excited state for atoms that are nearby on the lattice, realizing the so-called Rydberg blockade. The resulting quantum dynamics unveils novel out-of-equilibrium phenomena calling for a theo-

retical explanation: local observables do not thermalize when prepared in specific initial states. This evidence points at a new kind of ETH violation, dubbed "weak" since it only affects a small fraction of energy eigenstates, now called many-body quantum scars [26].

After fully characterizing the phase diagram of the constraint Rydberg atom chain, we will uncover a profound connection between this system and a $U(1)$ lattice gauge theory (LGT) [27]. Achieving experimental control on synthetic gauge fields is one of the pillars of quantum simulations, and a crucial step to deepen our understanding of fundamental interactions. However, there is presently no experimental evidence that atomic systems can be used to simulate lattice gauge theories at large scales. This limitation stems from the very characteristic aspect that distinguishes lattice gauge theories from other statistical mechanics models, i.e, the presence of local constraints on the possible configurations, in the form of a Gauss law, which cannot be easily implemented in actual experimental realizations. These local constraints turn out to be naturally mapped into the Rydberg blockade, and the experimental setup of Ref. [25] represents the first large-scale quantum simulation of a lattice gauge theory. Motivated by the connection between LGTs and weak ETH violations, in the last part of Chapter 3, we will move to study the interplay between the Gauss constraint and strong ETH violations in disordered systems. This will be done through an extensive analysis of the spectral properties of a disordered version of one-dimensional quantum electrodynamics [28].

Bibliography

[1] S. Sachdev, *Quantum Phase Transitions*, Cambridge University Press, 1999.

[2] L. Landau, "On the theory of phase transitions", *Journal of Experimental and Theoretical Physics* 7 (1937), pp. 19–32.

[3] X. G. Wen, "Topological order in rigid states", *International Journal of Modern Physics B* 04.02 (1990), pp. 239–271.

[4] J. M. Deutsch, "Quantum statistical mechanics in a closed system", *Phys. Rev. A* 43 (1991), pp. 2046–2049.

[5] M. Srednicki, "Chaos and quantum thermalization", *Phys. Rev. E* 50 (1994), pp. 888–901.

[6] R. Nandkishore and D. A. Huse, "Many-Body Localization and Thermalization in Quantum Statistical Mechanics", *Annual Review of Condensed Matter Physics* 6.1 (2015), pp. 15–38.

[7] M. Rigol, V. Dunjko, and M. Olshanii, "Thermalization and its mechanism for generic isolated quantum systems", *Nature* 452.7189 (2008), pp. 854–858.

[8] X.-G. Wen, *Quantum Field Theory of Many-Body Systems*, Oxford University Press, 2004.

[9] P. Calabrese and J. Cardy, "Entanglement entropy and conformal field theory", *J. Phys. A: Math. Theor.* 42.50 (2009), p. 504005.

[10] J. H. Bardarson, F. Pollmann, and J. E. Moore, "Unbounded Growth of Entanglement in Models of Many-Body Localization", *Phys. Rev. Lett.* 109 (2012), p. 017202.

[11] N. Schuch et al., "Entropy Scaling and Simulability by Matrix Product States", *Phys. Rev. Lett.* 100 (2008), p. 030504.

[12] S. R. White, "Density matrix formulation for quantum renormalization groups", *Phys. Rev. Lett.* 69.19 (1992), pp. 2863–2866.

[13] U. Schollwöck, "The density-matrix renormalization group in the age of matrix product states", *Ann. Phys.* 326.1 (2011), pp. 96–192.

[14] C. F. Roos et al., "Bell States of Atoms with Ultralong Lifetimes and Their Tomographic State Analysis", *Phys. Rev. Lett.* 92 (2004), p. 220402.

[15] R. Islam et al., "Measuring entanglement entropy in a quantum many-body system", *Nature* 528.7580 (2015), pp. 77–83.

[16] T. Brydges et al., "Probing entanglement entropy via randomized measurements", *Science* 364 (2019), p. 260.

[17] E. Witten, "APS Medal for Exceptional Achievement in Research: Invited article on entanglement properties of quantum field theory", *Rev. Mod. Phys.* 90 (2018), p. 045003.

[18] J. J. Bisognano and E. H. Wichmann, "On the duality condition for a Hermitian scalar field", *J. Math. Phys.* 16.4 (1975), pp. 985–1007.

[19] J. J. Bisognano and E. H. Wichmann, "On the duality condition for quantum fields", *J. Math. Phys.* 17.3 (1976), pp. 303–321.

[20] P. Anderson, "Resonating valence bonds: A new kind of insulator?", *Materials Research Bulletin* 8.2 (1973), pp. 153–160.

[21] R. B. Laughlin, "Anomalous Quantum Hall Effect: An Incompressible Quantum Fluid with Fractionally Charged Excitations", *Phys. Rev. Lett.* 50.18 (1983), pp. 1395–1398.

[22] N. Schuch, I. Cirac, and D. Pérez-García, "PEPS as ground states: Degeneracy and topology", *Ann. Phys.* 325.10 (2010), pp. 2153–2192.

[23] A. Keesling et al., "Quantum Kibble–Zurek mechanism and critical dynamics on a programmable Rydberg simulator", *Nature* 568.7751 (2019), pp. 207–211.

[24] S. Trotzky et al., "Probing the relaxation towards equilibrium in an isolated strongly correlated one-dimensional Bose gas", *Nat. Phys.* 8.4 (2012), pp. 325–330.

[25] H. Bernien et al., "Probing many-body dynamics on a 51-atom quantum simulator", *Nature* 551.7682 (2017), p. 579.

[26] C. Turner et al., "Weak ergodicity breaking from quantum many-body scars", *Nature Physics* 14 (2018), p. 745.

[27] K. G. Wilson, "Confinement of quarks", *Phys. Rev. D* 10 (1974), p. 2445.

[28] J. Schwinger, "Gauge Invariance and Mass. II", *Phys. Rev.* 128 (1962), p. 2425.

Contents

Chapter 1

Entanglement Hamiltonians: from Quantum Field Theory to the lattice

This chapter is based on the following publications:

[1] G. Giudici, T. Mendes-Santos, P. Calabrese, M. Dalmonte
Entanglement Hamiltonians of lattice models via the Bisognano-Wichmann theorem
Physical Review B 98, 134403 (2018)

[2] T. Mendes-Santos, G. Giudici, R. Fazio, M. Dalmonte
Measuring von Neumann entanglement entropies without wave functions
New Journal of Physics 22, 013044 (2020)

[3] T. Mendes-Santos, G. Giudici, M. Dalmonte, M. A. Rajabpour
Entanglement Hamiltonian of quantum critical chains and conformal field theories
Physical Review B 100, 155122 (2019)

Over the last two decades, entanglement has emerged as a key tool to characterize many-body quantum systems. From a low-energy perspective, entanglement measures serve as a powerful tool to extract universal information about the collective behavior of quantum phases of matter [4, 5, 6, 7, 8]. From a quantum information point of view, they are fundamental to quantify the complexity of quantum states and our capability of representing them efficiently [9, 10, 11]. In particular, bipartite entanglement is typically described by considering the reduced density matrix ρ_A correspondent to a region A, that is obtained by tracing a state Ψ over the complement of A (which is denoted as B in the following):

$$\rho_A = \mathrm{Tr}_B |\Psi\rangle\langle\Psi| = \frac{e^{-\tilde{H}_A}}{\mathcal{Z}}. \tag{1.1}$$

The r.h.s. of this equation defines the so called entanglement (or modular) Hamiltonian (EH) [12], $\tilde{H}_A$. The latter shares the eigenvectors $|\phi_\alpha\rangle$ with ρ_A, and its spectrum is bounded from below. More importantly, the spectral properties of the EH uniquely determine the entanglement properties of the partition A of Ψ: for instance, its spectrum - the entanglement spectrum - determines the von Neumann entanglement entropy (VNE).

A direct knowledge of the functional form of $\tilde{H}_A$ is of tremendous utility for two main reasons. From the experimental side, it allows to measure entanglement properties of a given state via

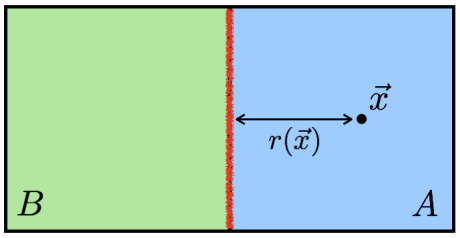

$$\tilde{H}_A = 2\pi \int_A d\vec{x}\, r(\vec{x})\, h(\vec{x})$$

Figure 1.1: Quantum field theory entanglement Hamiltonian for a half-bipartition of a (supposed to be) infinite system. In this case, the function $\Gamma(x)$ in Eq. 1.2 is 2π times the distance from the boundary between the two subsystems A and B.

direct engineering of the EH [13], in particular, in cases where direct access to the wave function is not scalable (such as in experiments requiring full state tomography) or not possible at all. Hence it provides a feasible route for the measurements of, e.g., entanglement spectra, which are experimentally challenging to access in a scalable manner [14]. From the theoretical side, it immediately opens up a new toolbox to investigate entanglement properties of lattice models using conventional statistical mechanics techniques, both numerical and analytical. However, in the context of many-body lattice models, it has proven very difficult to determine $\tilde{H}_A$ analytically even for free theories - the only results being the EH of the Ising [15, 16] and XYZ chain [17] away from criticality, of some one-dimensional free fermion systems [18, 19], and of few other less generic examples [15, 20].

In this chapter, we will argue, following Ref. [13] and basing on field theoretical results dating back to the 70's [21, 22], that the EH of the ground state of a wide variety of physical systems takes the following, remarkably simple, functional form

$$\tilde{H}_A = \int_A \Gamma(x) h(x) dx. \tag{1.2}$$

Here $h(x)$ is the Hamiltonian density, and the function $\Gamma(x)$ is a c-number that depends on the geometry of the bipartition. An example is depicted in Fig. 1.1, for a half-bipartition of an infinite system. Note that the EH of an interacting many-body ground state it is a priori a complicated, non-local object. Eq. 1.2 asserts that this is not the case: the EH can be expressed locally as an integral over the Hamiltonian density, modulated by a space-dependent factor.
We will show that the reliability of this continuum result is not spoiled by the introduction of a proper discretization, and that its discretized version allows to access with high accuracy ground-state entanglement properties in numerous lattice models. Eq. (1.2) holds under the assumption of Lorentz invariance of the quantum field theory, whose lattice implications will be discussed in great detail in what follows. After an extensive study of the validity of this equation, we will conclude that Eq. (1.2) provides an approximate identity that holds at the level of operators. Namely, its exponentiation produces an operator which is very close to the true ground state reduced density matrix in operator norm. For reasons that will become clear at the beginning of the next section, we will refer to the density matrix defined in Eq. (1.1) with the EH in Eq. 1.2, as ρ_{BW}.

In section 1.1, after recasting on the lattice Eq. (1.2), we provide a throughout investigation of the entanglement Hamiltonian correspondent to the ground state of lattice models. We verify their predictive power by systematically comparing several properties of the corresponding EHs to the original lattice model results. The main conclusion of our analysis is that this approach returns a closed-form expression for the lattice EH which accurately reproduces not only the

entanglement spectrum, but also properties directly tied to the eigenvectors of the reduced density matrix, such as correlation functions and order parameters. We concentrate our analysis on interacting one- (1D) and two-dimensional (2D) lattice models, spanning both quantum critical phases and points, and ordered, disordered, and symmetry-protected topological phases whose low-energy physics is captured by a quantum field theory with emergent Lorentz invariance (in the critical cases, this requires dynamical critical exponent $z = 1$). Overall, our results support the fact that the applicability of this approach solely relies on universal properties, in particular, on how accurately the low-energy properties of a lattice model are captured by a Lorentz-invariant quantum field theory.

In section 1.2 we will focus on the VNE. The latter remarkably provides a systematic way to connect wave function properties to all operational definitions of entanglement, and is of pivotal importance to both quantum information purposes and as a diagnostic tool in quantum many-body theory. Examples of its relevance include the existence of area laws bounding entanglement in ground state of local Hamiltonians [23], the sharp characterization of conformal field theories (CFTs) in one-dimension (1D) [24, 25, 26], topological order [27, 28] and spontaneous symmetry breaking [29]. We will exploit the knowledge of the ground state EH to compute the von Neumann entanglement entropy of ground states *without* relying on probing wave functions. As we will show, our approach enables accurate entanglement-based measurements of universal quantitites, such as the number of Nambu-Goldstone modes [29] and central charges [24, 25], at the percent level, even for modest system sizes. Most remarkably, it allows the calculation of the entanglement of many-body systems in a scalable manner, thanks to its thermodynamic analogy: this allows us to verify the onset of area law in two-dimensional quantum magnets, up to system sizes including $\mathcal{O}(10^3)$ spins. Such scalability is a key point when interested in universal quantities, as those that are captured by subleading corrections to the entropy in dimensions $D > 1$. In terms of techniques, our work complements the already successful QMC toolbox to lower-bound many-body entanglement via Renyi entropies [30, 31, 32, 33, 34, 8].

In section 1.3 we provide a systematic investigation of the accuracy of the Rényi entropy obtained from ρ_{BW} in the context of quantum critical chains. The low-energy degrees of freedom of these models are described by a CFT that is characterized by a central charge c. The main issues we address here are the following: we investigate whether the Rényi entropy obtained from ρ_{BW} is able to describe universal, leading contributions related to the central charge, non-universal terms of S_α, e.g., additive constants, and lattice-finite-size contributions of S_α that are related to universal properties [35, 36, 37]. The main conclusions drawn from our numerical analysis are the same for all the models studied: the Rényi entropies obtained from ρ_{BW}, which we call S_α^{BW}, converges to the exact ones in the thermodynamic limit; S_α^{BW} properly describes not just the logarithmically-divergent CFT term, but also corrections to the CFT scaling related to universal quantities (e.g., operator content of the theory). Overall, these results point to the fact that the predictive power of the BW-EH goes well beyond what is naively expected for typical field theory predictions, thus considerably extending its applicability window.

Throughout this chapter we will employ various numerical techniques, suchs as exact diagonalization, the Density Matrix Renormalization Group (DMRG) algorithm for ground states [9] and at finite temperature [38], and quantum Monte Carlo based on the Stochastic Series Expansion [39]. More details about the algorithms will be provided in the coming sections.

1.1 Entanglement Hamiltonians for many-body quantum systems on the lattice

Despite the first appearance of Eq. (1.2) dates back to 1975, in the context of axiomatic Quantum Field Theory, its relevance for condensed matter physics has been appreciated only recently. The specific form of the modular Hamiltonian, for a certain class of quantum field theories, is given for the first time in a series of papers by Bisognano and Wichmann, which can be recast in a single, general result that we refer to as Bisognano-Wichmann (BW) theorem [21, 22].
In Sec. 1.1.1, we review the BW theorem original formulation, its extensions in the context of conformal field theories, and present in detail its adaption to lattice problems. We present a qualitative discussion of the applicability regimes of this adaption, and then discuss the specific diagnostics we employ to compare the original EH result with the BW EH on the lattice, and our numerical approaches. In Sec. 1.1.5, we discuss our results in the context of 1D systems, starting with models endowed with discrete symmetries (Ising, Potts), and then moving to spin chains with continuous symmetries (XXZ and $J_1 - J_2$ models). In Sec. 1.1.6, we focus on 2D systems, discussing in detail the Heisenberg and XY models on both cylinder and torus geometries.

1.1.1 The Bisognano-Wichmann theorem and its conformal extensions

In an arbitrary relativistic quantum field theory [1], the general structure of the reduced density matrix of the ground state can be obtained for the special case of a bipartition between two half-spaces of an infinite system (i.e. $\vec{x} \equiv (x_1, x_2, \dots x_d) \in \mathbb{R}^d$ and $A = \{\vec{x} | x_1 > 0\}$). The BW theorem states that, for a given a Hamiltonian density $H(\vec{x})$ and for the half-bipartition above, the modular Hamiltonian of the ground state reads

$$\tilde{H}_A = 2\pi \int_{\vec{x}\in A} d\vec{x}\, (x_1 H(\vec{x})) + c', \tag{1.3}$$

where c' is a constant to guarantee unit trace of the density matrix, and the speed of sound has been set to unity. A first key feature of this result is that its applicability does not rely on any knowledge of the ground state, and thus can be applied in both gapped and gapless phases, and quantum critical points. Noteworthy is the fact that it is applicable in any dimensionality: this will turn particularly important below, as very little is known about entanglement Hamiltonians of lattice models beyond one-dimension. Moreover, Eq. (1.3) has a clear-cut physical interpretation in terms of entanglement temperature [40, 41, 42]: if we interpret ρ_A as thermal state, this corresponds to a state of the original Hamiltonian H with respect to a locally varying temperature, very large close to the boundary of A, and decreasing as $1/x_1$ far from it.

In the presence of conformal invariance, it is possible to further extend the BW result to other geometries [43, 44, 45, 46, 47]. In any dimension, it is possible to derive the modular Hamiltonian of a hyper-sphere of radius R [45]. Here, we will be interested in three specific cases in one spatial dimension, whose EHs were obtained in Ref. [46]. The first one concerns a finite partition of size ℓ embedded in the infinite line when $\tilde{H}_A$ read [45, 46]

$$\tilde{H}_A^{(\mathrm{CFT1})} = 2\pi \int_0^\ell dx \left[x \left(\frac{\ell - x}{\ell} \right) h(x) \right] + c'. \tag{1.4}$$

This formula can be generalized to the case of a finite partition of length ℓ in a ring of circum-

[1] We consider field theories whose Hilbert space is in tensor product form with respect to spatial partitions. The case of gauge theories with non-trivial centre will be studied elsewhere.

ference L [46]

$$\tilde{H}_A^{(\mathrm{CFT2})} = 2L \int_0^\ell dx \left[\frac{\sin\left(\frac{\pi(\ell-x)}{L}\right) \sin\left(\frac{\pi x}{L}\right)}{\sin(\pi\ell/L)} h(x) \right] + c'. \tag{1.5}$$

In addition, for a finite open system of length L and for a finite partition of length $L/2$ at its edge (i.e. $A = [0, L/2]$ and $B = [-L/2, 0]$) we have [46]

$$\tilde{H}_A^{(\mathrm{CFT3})} = 2L \int_0^{L/2} dx \sin\left(\frac{\pi x}{L}\right) h(x) + c'. \tag{1.6}$$

We mention that, in the vicinity of a conformal invariant critical point, an alternative description of the EH with respect to the original BW EH has been suggested [48].

Before turning to lattice models, it is worth to stress two properties of these results. The first is that, even if the modular operator is defined only from the ground state wave-function, it contains information about the entire operator spectrum of the theory. This suggests that universal properties of lattice models might be encoded in the deviations (including finite size ones) of the entanglement spectra evaluated from the Lattice Bisognano-Wichmann (LBW) entanglement Hamiltonian (which we describe in the next subsection) from the exact one. The second is that the BW result implies that the EH is local, and contains only few-body terms which are already present in the original model. This fact has some immediate consequences: *i)* it makes a direct experimental realization of the LBW EH feasible in synthetic quantum matter setups [13], and *ii)* it makes its direct study amenable to the same tools of statistical mechanics applicable to the original problem.

1.1.2 Discretization of the continuum entanglement Hamiltonian

Differently from the field theory case, much less is known about the entanglement Hamiltonian of ground states of lattice models. In some specific cases, direct insights can be gathered by the explicit structure of the ground state wave function. Examples include the determination of the ES and EH structure in strongly gapped phases [49, 50, 51, 52], where perturbative arguments are applicable, the EH obtained via variational wave-functions [53], or the Li and Haldane argument on the structure of the ES of topological phases [54, 55] - which can also be understood using the BW theorem [56]. Similar arguments can be applied to wave functions with very short correlation length ξ, as in those cases, the EH becomes essentially a projector for distances beyond ξ. Other fundamental insights could come from the related concepts of entanglement contour [57, 58, 59, 60, 61], probability distribution of the entanglement spectrum [62, 63, 64], and relative entropy [65, 66, 67, 68, 69].

Exact results without assuming any structure of the ground state wave-function have been derived only in few 1D free theories [15, 16, 18, 19](for recent results in the presence of pairing terms, see Ref. [70]) and for the massive regime of the XYZ model [17]. As we discuss below, these results are very suggestive about the correctness (and, at the same time, indicate potential limitations) of the LBW EH that we will discuss in the next subsections.

Our goal here is to provide a generic recipe to derive an approximate but very accurate (in particular, able to capture all universal features) EH of a lattice model without specific knowledge of the ground state wave-function. As the starting point, following Ref. [13], we recast the BW theorem and its conformal extension on the lattice, formulating simple candidate EHs. Explicitly, let us consider a lattice model in one or two dimensions with on-site and nearest-neighbour

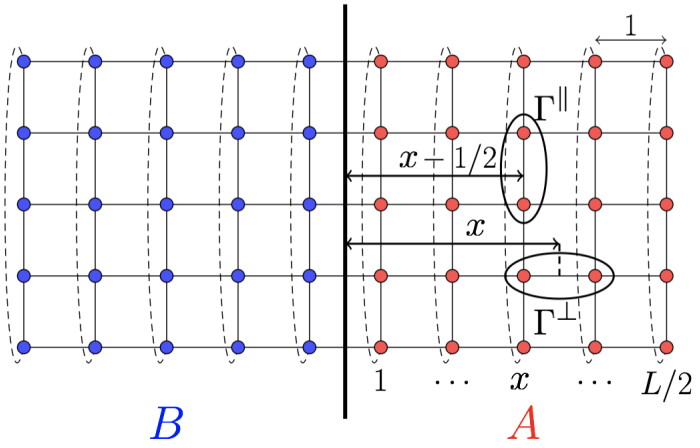

Figure 1.2: Sketch of the lattice configuration for two-dimensional systems: we consider systems with periodic boundary conditions along the y (vertical) direction, and either open or periodic boundary conditions along the x (horizontal) direction, of length L. The system bipartitions we consider are defined by $A = \{(x, y)|x \in [1, L/2]\}$. The distance from the boundary (Eq. (1.9)) corresponding to different Hamiltonian terms (indicated by encircled pairs) is portrayed schematically as the geometric distance of the center of the bond from the boundary.

couplings:

$$H = \Gamma \sum_{x,y,\delta=\pm 1} \left[h_{(x,y),(x+\delta,y)} + h_{(x,y),(x,y+\delta)} \right] + \Theta \sum_{x,y} l_{(x,y)}, \tag{1.7}$$

where Γ is a homogeneous coupling (e.g., exchange term) and Θ is an on-site term (e.g., transverse or longitudinal field). The spatial coordinates are defined as $x, y \in \{-L/2 + 1, \dots L/2\}$, where L is the linear size of the system, which we fix to be even. In one dimension (read just the x coordinate in the aforementioned expression) we study systems with both open (OBC) and periodic boundary conditions (PBC), while for in two dimensions we consider finite cylinder and torus geometries, see Fig. 1.2.

Let us now split the system into two equal halves; the corresponding lattice Bisognano-Wichmann EH (LBW-EH) is then given by

$$\tilde{H}_{A,BW} = \beta_{EH} \sum_{x,y,\delta=\pm 1} \left(\Gamma^{\perp}_{x}\, h_{(x,y),(x+\delta,y)} + \Gamma^{\parallel}_{x}\, h_{(x,y),(x,y+\delta)} \right) + \sum_{x,y} \Theta_x\, l_{(x,y)}, \tag{1.8}$$

where the inhomogeneous couplings and on-site terms depend on the distance from the boundary separating subsystem A and B (see Fig. 1.2) according to the geometry of the original system. In the case of a 1D chain with OBC or for the cylinder geometry in 2D, the BW theorem in Eq. (1.3) suggests

$$\Gamma^{\parallel}_{x} = x\Gamma, \qquad \Gamma^{\perp}_{x} = \left(x - \frac{1}{2} \right) \Gamma, \qquad \Theta_x = \left(x - \frac{1}{2} \right) \Theta. \tag{1.9}$$

This putative EH is expected to provide extremely accurate results being just the lattice discretization of Eq. (1.3), at least in the limit $L/2 \gg \xi$ when finite size effects are negligible. However, in the following, we will use this EH also for some critical cases in order to check how this copes with finite volume effects: this is a fundamental test in view of the application of our ideas to those systems that are not known a priori to be critical.

Contrary to plane and cylinder geometries, for the torus geometry we do not have any field

theoretical results to guide our ansatz. We just know that close to the two entangling surfaces, the EH must be a linear function of the separation. A possible smooth interpolation between the two linear regimes is suggested by Eq. (1.4) which has a suitable generalization for a sphere in arbitrary dimension [45]. Following this line of thoughts, we propose the ansatz

$$\Gamma_x = \frac{x\,(L/2-x)}{L/2}\Gamma, \quad \Gamma_y = \frac{\left(x-\frac{1}{2}\right)\left[\frac{L}{2}-\left(x-\frac{1}{2}\right)\right]}{L/2}\Gamma, \quad \Theta_x = \frac{\left(x-\frac{1}{2}\right)\left[\frac{L}{2}-\left(x-\frac{1}{2}\right)\right]}{L/2}\Theta. \quad (1.10)$$

For the 1D critical case, exact EH profiles can be obtained by discretizing Eqs. (1.5) and (1.6). For the half-bipartition of length $L/2$ of the ring one has

$$\begin{aligned} \Gamma_x &= \frac{L}{2\pi}\sin\left(\frac{2\pi x}{L}\right)\Gamma, \\ \Theta_x &= \frac{L}{2\pi}\sin\left(\frac{2\pi}{L}\left(x-\frac{1}{2}\right)\right)\Theta, \end{aligned} \quad (1.11)$$

while for the open chain

$$\begin{aligned} \Gamma_x &= \frac{L}{\pi}\sin\left(\frac{\pi x}{L}\right)\Gamma, \\ \Theta_x &= \frac{L}{\pi}\sin\left(\frac{\pi}{L}\left(x-\frac{1}{2}\right)\right)\Theta. \end{aligned} \quad (1.12)$$

Finally, the overall energy scale in (1.8), β_{EH}, is related to the "speed of sound", v, in the corresponding low-energy field theory

$$\beta_{EH} = \frac{2\pi}{v}. \quad (1.13)$$

The reason to use the name β_{EH} is that as for the thermodynamic inverse temperature $\beta = 1/T$, the BW overall energy scale plays the role of an effective temperature, as will be discussed in next section.

The velocity v may be fixed by matching the small momentum ($\hat{p}_k$) expansion of the lattice dispersion relation $E(k)$ with the relativistic one $E(p) = \sqrt{m^2v^4 + v^2p^2}$. Such a velocity is generically different from the quasiparticle one $V(k) \equiv dE(k)/dp_k$. The two coincide only for gapless theories where $E(k) = vk$

1.1.3 Regimes of applicability of the approach

A natural question to ask is, to which extend field theory results on the functional form of the EH are applicable to lattice models and in which sense. The LBW EH is not generically an exact form, even in the thermodynamic limit. This is, e.g., explicitly manifest in free fermion results [18, 19] showing that the exact EH of a Fermi sea not only has tiny deviations compared to the field theoretical BW EH, but also presents very small longer range terms completely absent in (1.3) (and the same happens also for the interacting XXZ spin chain [20]). Conversely, for the gapped regimes of the XYZ and Ising chains, the LBW EH is exact [17, 16] independently on the value of the correlation length - even when one would expect lattice effects to become dominant.

Before discussing in the next subsection a series of quantitative criteria to determine the applicability regimes of the LBW EH using numerical simulations (whose results are discussed in the next sections), we provide here a qualitative discussion.

When transposing the field theory predictions above on finite lattice models, three ingredients shall be considered: *i)* the loss of Lorentz invariance due to the lattice, even when it is recovered

as a low-energy symmetry; *ii)* for massive theories, the presence of a finite ξ/a ratio, leading to potentially harmful UV effects at the lattice spacing level; *iii)* finite volume effects (which can be partially taken into account in 1D CFTs).

In quantum field theory language and close to a quantum phase transition, the loss of Lorentz invariance is typically attributed to the fact that the lattice turns on several irrelevant operators which directly affect the Hamiltonian spectrum. At the level of the EH, to the best of our knowledge, this has not been discussed so far. Since there is abundant evidence that universal properties of lattice models (such as the entanglement entropy of models described at low energies by CFTs [26, 8]) are in excellent agreement with field theory expectations, it is natural to argue that the microscopic EH is governed by the LBW EH, plus terms that depend on irrelevant operators. We note that, in the specific case of spin models, a set of recent ansätze proposed in Ref. [51] falls into this category. Under this assumption, it is possible to argue that low-lying entanglement properties should be well captured by the lattice BW EH at least in the critical case. Similar arguments are at the basis of the use of the ES in topological models [56], in particular for quantum Hall wave-functions.

From a complementary viewpoint, it is possible to argue that, at least for the critical case, deviations are directly tied to curvature effects in the lattice dispersion relation. This sets an energy scale upon which excitations cease to be well described by a Lorentz invariant field theory. In the context of correlated fermions, we thus expect that the accuracy of the LBW EH degrades when the speed-of-sound-to-band-width ratio becomes small - down to the flat band case, which is not expected to be captured at all. This expectation is confirmed by free fermions exact calculations [18].

The effects of a finite ξ/a ratio have already been qualitatively discussed in Ref. [13]: in brief, as long as the correlation length is not of the same order of the lattice spacing (thus making a field theory description not immediately applicable), these deviations are negligible. We note that, for what concerns the ES, it has been observed that in the massive regime of the Ising model [16], in the close vicinity of the Affleck-Kennedy-Lieb-Tasaki point of bilinear-biquadratic spin-1 chains, and in gapped XXZ spin-chains the lattice BW EH is extremely accurate [13], so the validity of the approach even at $\xi \simeq a$ cannot be ruled out *a priori* (whilst has anyway to be justified *a posteriori*).

Finally, we discuss finite volume effects. Their estimate is non-trivial (except for those encoded in (1.11) and (1.12) for 1D CFTs): for this reason, we present below a finite-size scaling analysis of several quantities of interest. We anticipate that, at least for what concerns the low-lying entanglement spectrum, we observe universal scaling.

1.1.4 Numerical benchmark on microscopic lattice models

The reduced density matrix of subsystem A is written in terms of the BW-EH as

$$\rho_A \to \rho_{EH} = \frac{e^{-\tilde{H}_{A,BW}}}{Z}, \tag{1.14}$$

where the constant $Z = \mathrm{Tr}(e^{-\tilde{H}_{A,BW}})$, written in analogy to thermodynamics, ensures the normalization of ρ_{EH}. For now on, we call the exact reduced density matrix, ρ_A, and the one obtained with via the lattice BW, ρ_{EH}. The comparison of the thermal density matrix ρ_{EH} and the exact one is addressed at both the eigenvalues and eigenvectors level.

Entanglement spectrum. The first comparison between ρ_A and ρ_{EH} is at the level of the eigenvalues ϵ_α of the corresponding entanglement Hamiltonian. These eigenvalues are however affected by the values of both the non-universal constant c' in (1.3) and of the entanglement

temperature β_{EH} in (1.8). These non-universal constants must be fixed either by an exact calculation or by an independent numerical study. In some cases in the following we will perform this direct analysis. There is however an even better way to perform such a comparison which does not require an a priori knowledge of these non-universal constants. Indeed, let us consider the ratios

$$\kappa_{\alpha;\alpha_0} = \frac{\epsilon_\alpha - \epsilon_0}{\epsilon_{\alpha_0} - \epsilon_0}, \tag{1.15}$$

where ϵ_0 is the lowest entanglement energy on the system (corresponding to the largest eigenvalue of ρ_A), and ϵ_{α_0} is a reference state suitably chosen to accomodate degeneracies of the lowest eigenvalue in the EH spectrum. It is clear that the c' dependence of the eigenvalues cancels out in the differences taken in the numerator and in the denominator in (1.15). Taking the ratio in (1.15) cancels also the dependence on β_{EH}. For this reason we call the quantities (1.15) *universal ratios*.

We use the Density Matrix Renormalization Group (DMRG) to obtain these quantities for quantum spin chains of length up to 100 sites. The entanglement spectrum of the original system is computed keeping $100-150$ states and using the ground state as the target state in the proper symmetry sector. The lowest part of the BW-EH spectrum instead is obtained by targeting $5-10$ states in all the symmetry sectors. The magnitude of the discarded weight in the DMRG algorithm depends on the boundary conditions and on the system being homogeneous (exact ES computation) or not (BW-EH spectrum computation). When the homogeneous system has OBC/PBC we were able to keep the truncation error always below $10^{-12}/10^{-8}$ for the largest systems sizes considered. This is achieved in few DMRG sweeps, typically 2 or 3. All measurements were performed after a minimum of 5 sweeps to ensure convergence of the algorithm. Oppositely, in the inhomogeneous case, more sweeps were required for DMRG to converge, and a minimum of 6 sweeps was always performed before collecting the eigenvalues of the BW-EH. However, since the BW system is open, we were always able to keep the truncation error below 10^{-10} for all the chains considered in what follows[2].

Entanglement eigenvectors. In order to understand the accuracy of the BW EH at the eigenvector level, we consider the overlaps

$$|\langle \psi_\alpha^{EH} | \psi_{\alpha'}^A \rangle| = M_{\alpha,\alpha'}, \tag{1.16}$$

for different levels of the spectrum. These eigenvectors are computed via Exact Diagonalization (ED) of both ρ_A and the BW-EH.

Correlation functions. Operators (observables) defined exclusively on subsystem A are directly related to ρ_A (ρ_{EH})

$$\langle O_A \rangle = \mathrm{Tr}(O_A \rho_A) \to \frac{\mathrm{Tr}\left(e^{-\tilde{H}_A} O_A\right)}{Z}. \tag{1.17}$$

Similarly the ground state properties of the subsystem A are directly related to the *thermal* properties of the EH-BW. Hence, as another check of the BW construction we use the finite-temperature QMC method Stochastic Series Expansion (SSE) and finite-temperature DMRG to obtain local and two-body correlation functions of the BW-EH system. We then compare these quantities with the exact ground state expectation values computed via DMRG and QMC [39,

[2]This reflects the fact that entanglement eigenstates have always an entanglement content which is typically equal or smaller than that of the ground state wave function.

71].

The SSE method samples terms in a power series of $e^{-\tilde{H}}$ in the partition function using local and loop (directed loop) updates [71]. For the BW-EH system, as the local effective temperature decreases (Hamiltonian couplings increases) away from the boundary, the use of loop updates is important to prevent the slowing down of autocorrelation times. In fact, the asymptotic autocorrelation times of local observables obtained with the directed-loop SSE algorithm is much smaller then the typical number of QMC measurements that we use, $N_{meas} \approx 10^8$. Thus, at least for the systems sizes that we consider (L up to 100) the slowing down of autocorrelation times is not an issue for the SSE simulations of BW-EH.

Finite-temperature DMRG accuracy was checked by varying both the number of states kept during the imaginary time evolution and the Trotter step employed. Since the imaginary time evolution is applied on a state in which the system is maximally entangled with an ancilla, if the Hamiltonian conserves some quantum number one can exploit it by preparing the maximally entangled initial state within a given symmetry sector of the Hilbert space and restricting the evolution to that sector [72]. Using this technique we were able to reach convergence of the results by keeping a maximum of 150 states per block. We used first order Trotter decomposition, which means one Trotter step per half sweep, with a Trotter step of 10^{-3}.

In the next two subsections, we report our results on the three criteria above for a set of lattice models in one and two-dimensions. It is worth stressing how the three diagnostics employed are sensitive to different features of the reduced density matrix. Universal entanglement gap ratios are insensitive to possible errors in the prefactors of the entanglement Hamiltonian (i.e., to β_{EH}), and are not informative about eigenstates. Oppositely, overlaps between entanglement eigenvectors are not informative about the spectrum, but rather describe the accuracy in having the same eigenvectors. Finally, correlation functions are sensitive to all details of the EH - both spectra, correct speed of sound, and eigenvectors. However, they are also a somewhat less direct as a diagnostic - for instance, very close correspondence in correlation functions can be obtained by considering density matrices with very different eigenvectors.

1.1.5 One dimension

One-dimensional quantum systems represent an ideal framework to test the applicability of LBW EH predictions. The main advantage here is that wave-function based methods such as DMRG and ED can be pushed to considerably large system sizes. In addition, the CFT results of Ref. [46] allow us to employ formulas which do consider a finite size of the subsystem (Eq. (1.4)) and of the system (Eq. (1.5),(1.6)), which implies that finite size effects can be controlled in a more efficient manner.

Transverse Field Ising Model. The quantum Hamiltonian of this model reads [7]:

$$H = -\sum_i \sigma_i^z \sigma_{i+1}^z - g \sum_i \sigma_i^x, \tag{1.18}$$

where $g > 0$ and σ^j are the Pauli matrices. The model can be solved exactly and it is diagonalized in terms of spinless fermions (with mode operators $b_k^\dagger, b_k$) as

$$H = \sum_k E(k) \left(b_k^\dagger b_k - \frac{1}{2} \right), \tag{1.19}$$

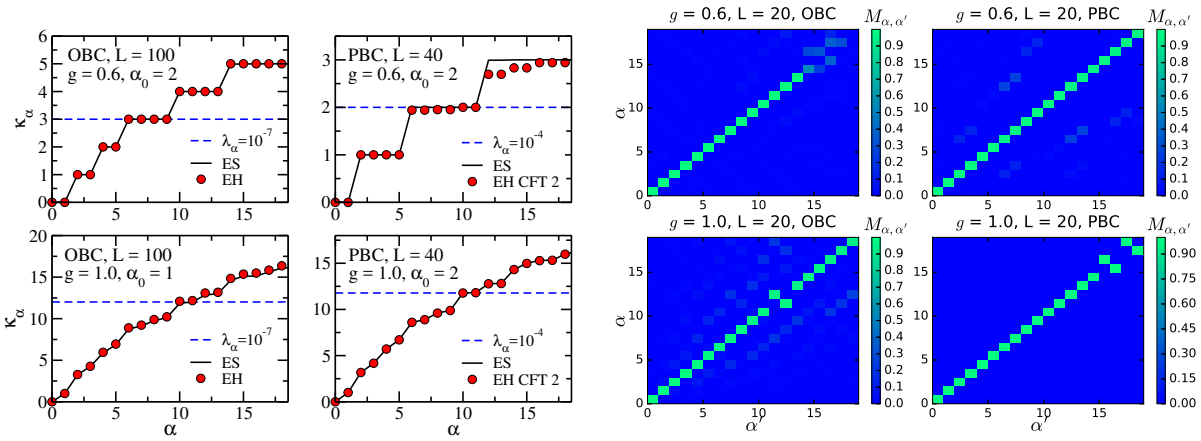

Figure 1.3: **Left**. Ratio κ_αs for the transverse field Ising chain. The black solid line and red circles stand for ratios computed from the exact ES and the EH spectrum respectively. The blue dashed line marks ρ_A eigenvalues with a magnitude indicated in the legend. PBC data slightly deviate from the field theory prediction in the ferromagnetic gapped phase $g = 0.6$, the maximum relative error being larger that 3% after the 13th eigenvalue. **Right**. Overlaps as defined in Eq. (1.16) for the transverse field Ising chain in the ferromagnetic phase $g = 0.6$ and at the critical point $g = 1.0$. Deviations from unity on the diagonal are of order 10^{-3} in all the cases considered up to the first 13 eigenstates. The few points close to the diagonal correspond to exact degeneracies in spectrum (not all degeneracies are off-set).

where $E(k) = \sqrt{(1-g)^2 + g(\hat{p}_k)^2}$, with $\hat{p}_k = 2\sin p/2$ being the lattice momentum [3]. By matching this dispersion relation with the relativistic one, we get the sound velocity $v = 2\sqrt{g}$ as a function of the lattice parameter g. The gap closes in the thermodynamic limit when $g = 1$. A quantum phase transition occurs at this point, separating a ferromagnetic phase for $g < 1$ from a paramagnetic phase for $g > 1$. In the former the $\mathbb{Z}_2$ symmetry of the model is broken by the ground state of the system, which is degenerate in the thermodynamic limit. The low energy physics of the quantum critical point is described by a $c = 1/2$ CFT.

For this model we expect the lattice discretization of Eq. (1.3) (i.e. Eq. (1.9)) to work well for a chain with OBC as long as the correlation length in the system is large w.r.t. the lattice spacing and small compared to the system size. In fact, the EH for a half-partition of an infinite chain can be computed exactly in the coordinate basis away from the critical point [16]. The result perfectly matches our lattice version of BW-theorem, although it does not predict the prefactor β_{EH}. In the PBC case instead we expect conformal BW-theorem Eq. (1.5) to fail as soon as a gap opens in the energy spectrum.

Fig. 1.3 (left) shows the universal ratios Eq. (1.15) computed from the ES both assuming OBC and PBC (black solid line). For the OBC case, we consider the EH in its original BW form, which allows to treat on the same footing gapped and gapless regimes.

These ratios are compared to the ones computed from the LBW-EH Eq. (1.9) in the former case and to the ones computed from Eq. (1.11) in the latter case (red circles). At the critical point the agreement is almost perfect in both cases: relative errors of the ratios are always smaller than 2%. Instead, in the ferromagnetic gapped phase, slight discrepancies are observed when the system is subjected to PBC: the ratios agree within 3% only as long as $\lambda_\alpha \lesssim 10^{-4}$.

Moving to the eigenvectors, the overlaps in Eq. (1.16), computed via ED, are plotted in Fig. 1.3 (right). Both in the OBC and PBC cases the magnitude of the overlaps is 1 with 10^{-3} accuracy, independently of the system being critical or gapped. Note however that overlaps of order 10^{-1} are observed also away from the diagonal at the critical point in the OBC case and

[3] For PBC $p = \frac{2\pi}{L}(n + 1/2)$ and $p = \frac{2\pi n}{L}$ in the sectors with even and odd number of fermions respectively, where $n = 0, 1, ..., L-1$. For OBC p is the solution of the equation $g \sin[(L+1)p]/\sin(Lp) = 1$

when the system is gapped in the PBC case. The latter fact is expected since Eq. (1.5) should provide the EH of a gapless system. We did also check the finite size scaling of the matrix norm of the difference between ρ_A and ρ_{EH} i.e. $||\rho_A - \rho_{EH}||$, where $||A|| = \sqrt{\mathrm{Tr}(AA^\dagger)}$. The magnitude of the matrix norm is of order 10^{-2} for the system sizes accessible with ED and it decreases with system size in all the cases considered.

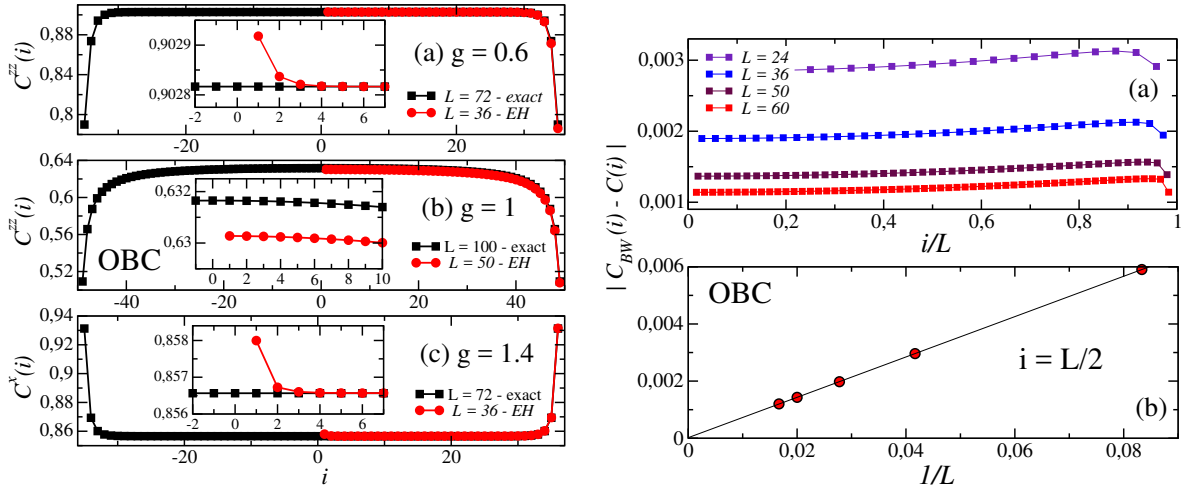

Figure 1.4: **Left.** (a-b): Local correlation function as defined in Eq. (1.20) for the transverse field Ising chain in the ferromagnetic phase $g = 0.6$ and at the critical point $g = 1.0$. The square (black) and circle (red) points are results for the original and the half-bipartion EH-BW systems, respectively. (c): local transverse magnetization in the paramagnetic phase. **Right**. Finite size scaling of the difference between BW thermal- and ground state- expectation values at the critical point of the Ising model, with OBCs. In (a), deviations are plotted for all the sites in the subsystem and they are largest close to the boundary away from the cut. In (b), deviations are plotted for a site in the middle of the subsystem and they clearly scale to zero as a power-law.

Expectation values of local observables are the only quantities considered here which are sensitive to the entanglement temperature. They thus probe more in depth this specific aspect of the BW theorem, which states that $\beta_{EH} = 2\pi/v$. Thanks to the exact solution of the model we know that $v = 2\sqrt{g}$. The local observable we consider for this model is

$$C^{zz}(i) = \left\langle \sigma_i^z \sigma_{i+1}^z \right\rangle . \tag{1.20}$$

Note that, since the two points are nearest-neighbours, this observable is expected to be the most sensitive to finite-lattice-spacing effects. The result of the comparison is depicted in Fig. 1.4 (left) (a-b) for the OBC case. The EH-BW results (red circles) are obtained as thermal averages computed via finite-temperature DMRG. Ground state averages (black square) are obtained using DMRG with the ground state of the system as a target state. The agreement is excellent (below percent level) in the gapped paramagnetic phase even close to the cut, where the choice of the proper β_{EH} almost completely cancels boundary effects. Relative errors in the bulk (including the open (right) boundary) are uniformly of order 10^{-6}, while they reach a magnitude of 10^{-3} close to the cut (see inset). At the critical point instead we observe uniform deviations of 0.5% over the whole half-chain. These are caused by finite size effects. Fig. 1.4 (right) shows the difference between the thermal LBW expectation value and the ground-state one for different system sizes. Discrepancies exhibit power-law scaling to zero.

In addition, we have also considered the expectation value of the transverse magnetization (i.e. along the x-axis)

$$C^x(i) = \langle \sigma_i^x \rangle . \tag{1.21}$$

In Fig. 1.4 (left) (c), we show the corresponding spatial profile under OBCs: the behavior is very similar to that of the C^{zz} correlator, with the maximum deviations of order 10^{-4} close to the boundary, which was expected if one considers the self-duality transformation of the model.

Three-states Potts Model. The quantum Hamiltonian of the three-state Potts Model is given by [73, 74]:

$$H = -\sum_i \left(\sigma_i \sigma_{i+1}^\dagger + \sigma_i^\dagger \sigma_{i+1}\right) - g \sum_i \left(\tau_i + \tau_i^\dagger\right), \tag{1.22}$$

where $g > 0$. The σ and τ matrices are defined as $\sigma|\gamma\rangle = \omega^{\gamma-1}|\gamma\rangle$, $\tau|\gamma\rangle = |\gamma+1\rangle$, $\omega = e^{i2\pi/3}$, and $\gamma = 0, 1, 2$. The phase diagram of this quantum chain is analogous to the Ising chain's one. The symmetry of the model is $\mathbb{Z}_3$ which is broken in the ferromagnetic phase with three degenerate ground states. In contrast to the Ising chain, the Hamiltonian Eq. (1.22) is non-integrable away from the critical point at $g = 1$. Here the spectrum can be computed [75] in terms of massless excitations whose dispersion relation reads

$$E(k) = \frac{3\sqrt{3}}{2}\, \hat{p}_k\,, \tag{1.23}$$

which matches the massless relativistic one with a sound velocity $v = 3\sqrt{3}/2$. This critical point is described by a CFT with central charge $c = 4/5$. [76, 77]

Lorentz invariance is expected for the continuum limit of the lattice theory also away from the gapless conformally invariant point and thus the discrete BW theorem Eq. (1.9) is expected to hold also when $g \neq 1$.

Fig. 1.5 (left) shows the comparison between the universal ratios Eq. (1.15) obtained from the ES and from the BW-EH for the system at the critical point ($g = 1$) and in the paramagnetic phase ($g = 1.4$). We see good agreement for both OBC and PBC also away from the critical point. In particular relative errors for the first 26 eigenvalues are smaller than 2% at the critical point, in both the OBC and PBC case. In the gapped paramagnetic phase instead their maximum magnitude is 0.5% and 4% in the OBC and PBC case respectively.

For this model we performed also a direct comparison of the spectra of ρ_A and ρ_{EH} at the critical point for which we need the sound velocity in Eq. (1.23). For OBC, Fig. 1.5 (right) shows the ES obtained by using both the infinite system EH (1.9) and the finite size CFT (1.12). The discrepancies between the ES of a finite system and the ES obtained from the infinite system EHs completely disappear when the CFT finite system EHs are used. For PBC instead the lattice discretization of the conformal EH BW in Eq. (1.11) is used which matches the direct results perfectly. For the sake of comparison, we have also computed the ES using with Eq. (1.10): the results, while approximately matching the density of states of the original model, are not able to reproduce the ES quantitatively. This comparison boosts the predictive power of the correct CFT EH, which, even on the lattice, almost completely suppressed finite size effects.

Overlaps, computed via ED, between ρ_A and LBW-EH eigenvectors are shown in Fig. 1.6 (left). Large ($\geq 1 - 10^{-3}$) overlaps involve all the first states in the two spectra both in the OBC and PBC cases. Non vanishing overlaps away from the diagonal are observed only in the gapped phase when the CFT EH Eq. (1.5) is employed, as expected. In Fig. 1.6 (right) we report also the finite size scaling of the lowest overlap $M_{0,0}$, which decreases/increases when the system is gapless/gapped. The apparent decreasing behaviour of the overlap at the critical point might be an artifact of the small system sizes accessible with ED for this model. A trustworthy extrapolation to the thermodynamic limit is not possible: however, it is very indicative that changes over a large window of L are at most of order 10^{-4}, strongly suggesting that the overlap will remain finite in the thermodynamic limit - a remarkable fact given that we are looking at

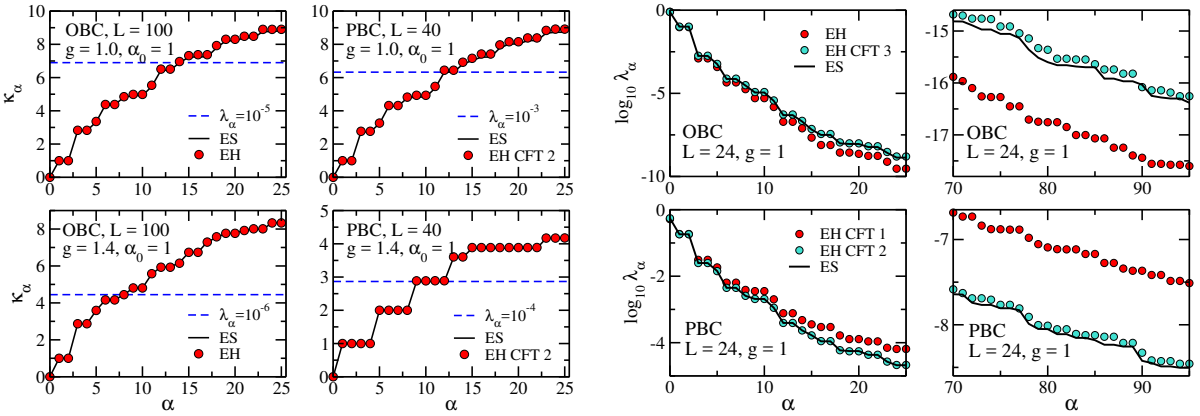

Figure 1.5: **Left.** Ratio κ_αs for the 3-state Potts chain. The black solid line and red circles stand for ratios computed from the exact ES and the EH spectrum respectively. The blue dashed line marks ρ_A eigenvalues with a magnitude indicated in the legend. **Right.** Spectra comparison for the 3-state Potts chain at the critical point. The black solid line is the exact ES. Red and turquoise circles are the ρ_{EH} eigenvalues computed via the infinite system EH (Eq.(1.3) for OBC and Eq. (1.4) for PBC) and via the CFT finite system EH (Eq.(1.6) for OBC and Eq. (1.5) for PBC) respectively. On the left λ_αs with $\alpha = 0, \dots 25$ and on the right with $\alpha = 70, \dots, 95$.

eigenvector properties. We have obtained similar results for all the 1D models discussed in this paper, but we did not report them because they are qualitatively equivalent to those in Fig. 1.6 (right).

We finally consider the two-point function of the order parameter at neighbour sites:

$$C(i) = \left\langle 2\,\mathrm{Re}\,\sigma_i \sigma_{i+1}^\dagger \right\rangle . \tag{1.24}$$

We compute this correlation function only for $g = 1$ in the OBC case because the sound velocity is known exactly only at the critical point. In order to use an unbiased approach here, which does not rely on the CFT know-how of finite volume effects embodied in Eq. (1.6), we have utilized the original BW formulation.

We used finite-temperature DMRG for the BW thermal average and ground state DMRG for the pure average over the ground state of the system. The result is reported in Fig. 1.7. As in the Ising case 0.5% discrepancies are observed uniformly on the whole subsystem length. As they reduce considerably when increasing system size, we attribute their origin to finite volume effects.

Spin-1/2 XXZ Model. The Hamiltonian of the XXZ spin-1/2 chain is [7]:

$$H = \sum_i \left(S_i^x S_{i+1}^x + S_i^y S_{i+1}^y + \Delta S_i^z S_{i+1}^z \right) . \tag{1.25}$$

This model is exactly soluble via Bethe ansatz, and its phase diagram supports three distinct phases. It is ferromagnetic for $\Delta < -1$, gapless critical (Luttinger liquid) for $-1 < \Delta \leq 1$ and antiferromagnetic for $\Delta > 1$. In the ferromagnetic phase, the $\mathbb{Z}_2$ spin reversal symmetry is spontaneously broken. The critical phase is described by a $c = 1$ CFT with varying Luttinger parameter $K = \pi/2 \arccos(-\Delta)$. The antiferromagnetic phase exhibits non-zero staggered magnetization, thus the spin reversal symmetry is broken by the 2-degenerate (quantum dressed) Néel states which live in the $S_z^{\mathrm{tot}} = 0$ sector.

For $\Delta < -1$ the low-lying excitations above the two magnetized ground states are transla-

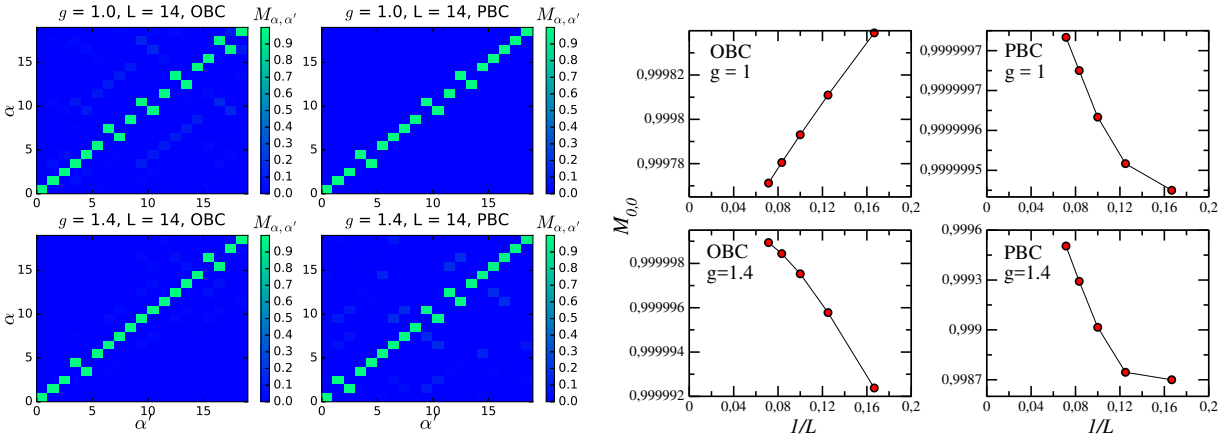

Figure 1.6: **Left.** Overlaps as defined in Eq. (1.16) for the three-state Potts chain at the critical point $g = 1.0$ and in the paramagnetic phase $g = 1.4$. Deviations from unity on the diagonal are smaller than 10^{-3}. The few points close to the diagonal correspond to exact degeneracies in spectrum. Largest non-vanishing overlaps away from the diagonal are observed in the PBC case when the gap spoils conformal invariance and thus the validity of Eq. (1.5). **Right.** Finite size scaling of the ground state overlaps $M_{0,0}$ as defined in Eq. (1.16) for the three-state Potts chain at the critical point $g = 1.0$ and in the paramagnetic phase $g = 1.4$.

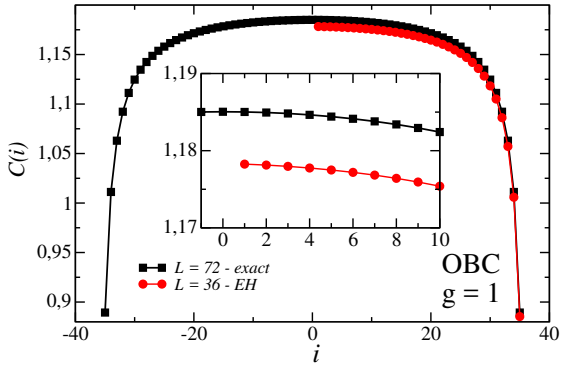

Figure 1.7: Nearest-neighbor correlation function Eq. (1.24) for the three-state Potts chain at the critical point $g = 1$. The square (black) and circle (red) points are results for the exact and the half-bipartition LBW EH systems, respectively. The inset magnifies the region close to the boundary.

tional invariant combinations of single-spin-flip states (magnons). Their exact dispersion relation reads

$$E(p_k) = 2\left(1 - \cos\left(\frac{2\pi k}{L}\right) - (\Delta + 1)\right), \tag{1.26}$$

which does not become relativistic in the continuum limit. At $\Delta = -1$ the gap closes but the magnon dispersion remains quadratic. Thus there is no underlying Lorentz invariance for $\Delta \leq -1$.

In the critical phase instead CFT predictions are in perfect agreement with lattice results for what concerns spectral [78] as well as correlation function properties [74, 79, 80]. Therefore, we expect the LBW theorem to be accurate in this phase. The point $\Delta = 1$ hosts a BKT phase transition which links the AFM phase to the critical line. Close to this point the fundamental excitations are usually called spinons and their dispersion relation is

$$E(k) = \frac{\pi}{2}\sin\left(\frac{2\pi k}{L}\right) = \frac{\pi}{2}\,\hat{p}_k\,, \tag{1.27}$$

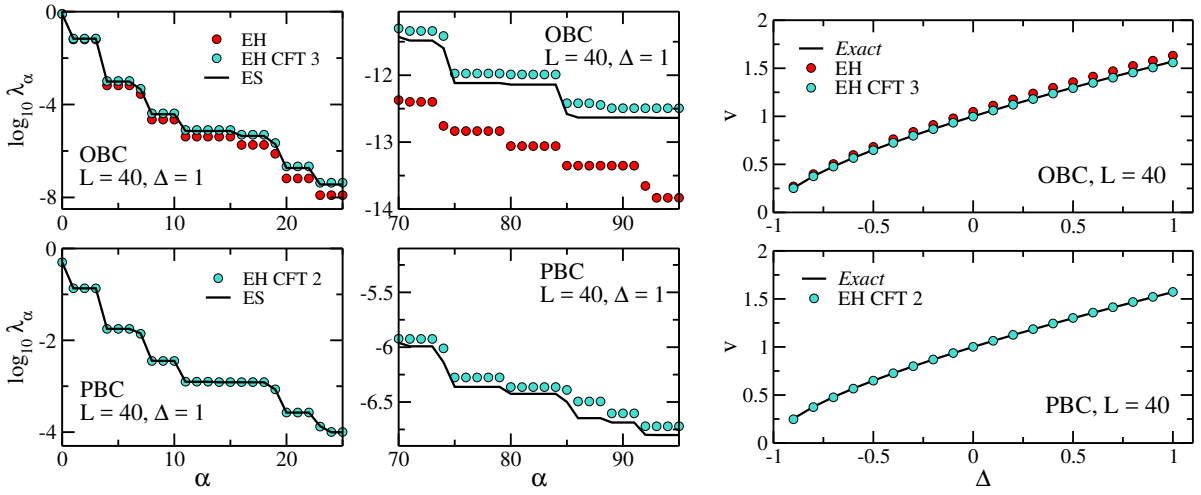

Figure 1.8: **Left.** Spectra comparison for the XXZ chain at the isotropic critical point. The black solid line is the exact ES. Red circles are the ρ_{EH} eigenvalues computed via the infinite system EH (Eq.(1.3) for OBC) and turquoise circles are computed via the CFT finite system EH (Eq.(1.6) for OBC and Eq. (1.5) for PBC, respectively). On the left λ_αs with $\alpha = 0, \dots 25$ and on the right with $\alpha = 70, \dots, 95$. **Right** Sound velocity exctracted via Eq. (1.29) from the first two eigevalues in the exact ES of a finite chain and in the EH spectrum, by using both the infinite system EHs (red circles) (Eq.(1.3) for OBC) and the finite system EHs (turquoise circles) (Eq.(1.6) for OBC and Eq. (1.5) for PBC). The result is plotted against the exact expression Eq. (1.28) for the sound velocity as a function of the anisotropy parameter Δ.

from which we read the sound velocity $v = \pi/2$ by comparison with the massless relativistic dispersion relation. Indeed, the sound velocity is exactly known in the entire critical line [79]:

$$v = \frac{\pi\sqrt{1-\Delta^2}}{2\arccos\Delta}. \tag{1.28}$$

In the Néel phase the quasi-particles acquire a mass, but in the scaling region close to $\Delta \to 1^+$ they do not to spoil relativistic invariance of the continuum theory. We point out that some of the results discussed here for OBC are connected with Refs. [50, 81, 82], which investigate the comparison between ES and the corner transfer matrix.

We report a direct comparison of the spectra of ρ_A and ρ_{EH} at the BKT point $\Delta = 1$, exploiting the knowledge of the sound velocity (1.28). Again for OBC we use both the infinite size formula (1.9) and the CFT finite size one (1.12). The latter perfectly reproduces the exact data. For PBC we only employ the lattice discretization of the CFT formula (1.11) finding a perfect match with the data from ρ_A.

As a by-product of BW theorem we can use the exact ES and the EH spectrum to compute the sound velocity of the model. Indeed the relation between the two sets of eigenvalues reads $\lambda_\alpha = \exp(-2\pi/v\ \varepsilon_\alpha)/Z$. We can take the ratio of two λs to eliminate the normalization constant and we can invert this relation to get

$$v_\alpha = \frac{2\pi(\epsilon_\alpha - \epsilon_0)}{\log\lambda_0/\lambda_\alpha}. \tag{1.29}$$

The result should be independent of α and this is indeed the case within negligible relative error. In Fig. 1.8 (right) we plot the sound velocity for $\alpha = 1$ as a function of Δ against the exact result (1.28). For OBC, we also use the infinite system EH (1.3) finding deviations only of few percent, as evident from the figure.

The two-point function we analyze for this model is the spin-spin correlation function

$$C_{spin}(i,r) = \left\langle S_i^z S_{i+r}^z \right\rangle, \tag{1.30}$$

that we compute using QMC. In this section we want to probe the thermodynamic values of this correlation. For this reason we do not exploit the finite size formulas for BW EH, but the infinite size ones (1.3) and (1.4) which we apply to OBC and PBC respectively. The results for $r = 1$ are reported in Fig. 1.9 (left) for the two OBC case. The two point of the phase diagram considered are the XX free fermions point $\Delta = 0$ and the BKT point $\Delta = 1$. The velocity in the entanglement temperature is provided by Eq. (1.28). In the OBC case the agreement is perfect also close to the boundary where the system has been cut. The BW EH reproduces very well also the amplitude and the frequency of the Friedel oscillations caused by the free ends of the chain, with a relative error always smaller than 1%.

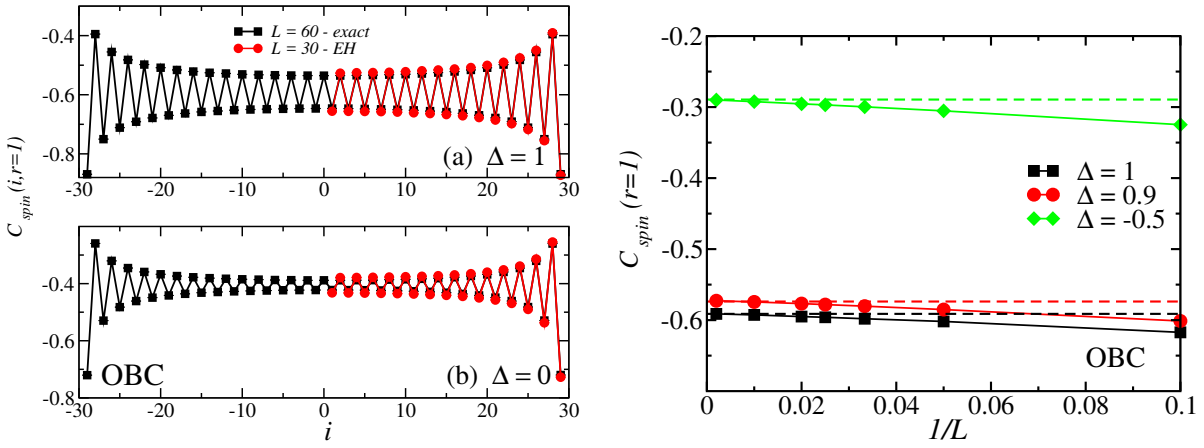

Figure 1.9: **Left.** Nearest-neighbour spin correlation function (1.30) as function of position i for chains with OBC for (a) $\Delta = 1$ and (b) $\Delta = 0$. The square (black) and circle (red) points are respectively the exact results and those from EH-BW. The Friedel oscillations are perfectly described by the EH approach. **Right.** $L \to \infty$ extrapolation of the average, $C_{spin}(r = 1) = 1/L \sum_i C(i, r = 1)$ for chains with OBC and different values of Δ. The horizontal lines represents the exact values of $C_{spin}(r = 1)$ for $L \to \infty$. In all the cases the EH-BW results converge to the exact ones in the thermodynamic limit.

In the PBC case the ground state average is homogeneous. In fact the parabolic inhomogeneous coupling in Eq. (1.4) suppresses the boundary effects which affect the non-translational invariant BW-EH. This is strongly reminiscent of sine-square deformation Hamiltonians, which are actually close in functional form to the LBW EH in the PBC case [83]. The result from the thermal average of LBW EH is indeed almost homogeneous and deviations from the expected ground state value are less than 0.1% (see Fig. 1.10 (left)).

Fig. 1.9 (right) shows the finite size scaling of the LBW-EH $C_{spin}(i, 1)$ with OBC, averaged over the whole chain, against the exact thermodynamic limit value (dashed line) for three values of the anisotropy parameter $\Delta = -0.5, 0.9, 1.0$. The result strongly indicates that the field theory prediction of BW theorem Eq. (1.3) is exact when $L \to \infty$. In Fig. 1.10 (right) we analyze the separation dependence of the 2-point function (1.30) at the isotropic point $\Delta = 1$. Small deviations (of order 1% on average with respect to r) are observed when r becomes of the order of the system size. These deviations, however, decrease as one increases L, see inset of Fig. 1.10.

Spin-1 Heisenberg Model. The isotropic spin-1 chain is the archetypical model of a symmetry protected topological phase (SPTP) [84, 55, 7]. This state of matter is characterized by a gap in the bulk, an even-degenerate ES, zero-modes living at the ends of an open chain and

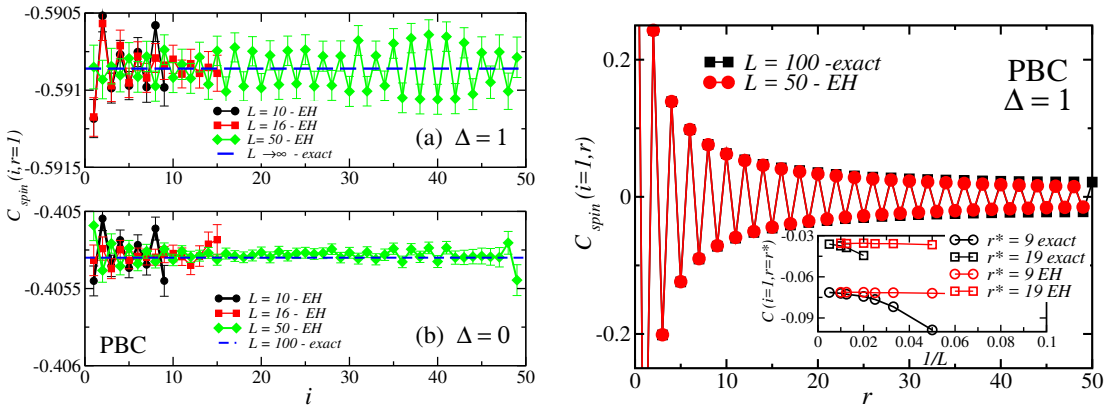

Figure 1.10: **Left.** Nearest-neighbour spin correlation function (1.30) as function of position i for chains with PBC for (a) $\Delta = 1$ and (b) $\Delta = 0$. The dashed line is the homogeneous exact result. The results obtained from the BW EH are approximately independent from the site i in the subsystem and they display small oscillation around the ground state value. **Right.** Decay of spin-spin correlations for the isotropic case, $\Delta = 1$. We compare the exact data (black squares) with the EH results (red circles). The *inset* shows the scaling with system size of correlations between different distances r^* for both BW and exact systems. The exact and BW results tend to the same value in the limit $L \to \infty$.

carrying fractionalized quantum numbers [54, 55]. The Hamiltonian of the model is the same as Eq. (1.25), but with the S^α matrices being the spin-1 representation of the rotation group. Long-range order associated with a hidden $\mathbb{Z}_2 \otimes \mathbb{Z}_2$ symmetry is captured by the non-local order parameters

$$C^\alpha_{str}(i,r) = -\langle S^\alpha_i \prod_{j=i+1}^{i+r-1} \exp\left(i\pi S^\alpha_j\right)\, S^\alpha_{i+r}\rangle, \tag{1.31}$$

which is non-vanishing for $r \to \infty$ for $\alpha = x, y, z$ (we focus in the following on the z component and drop the index α). The Haldane SPT phase extends in the parameter region $0 < \Delta \lesssim 1.17$ and it is separated from a gapless XY phase (on the left) by a BKT phase transition at $\Delta = 0$ and from a Néel phase (on the right) by a second order $c = 1/2$ phase transition at $\Delta \simeq 1.17$ [85]. In order to show the applicability of BW theorem for the computation of non-local operators, we compare the thermal expectation value obtained via finite-temperature DMRG using the BW EH Eq. (1.3) with the ground state average computed with DMRG. Although the system is gapped at the isotropic point, the correlation length of the system $\xi = v/m$ is quite large. In fact, the gap is known to be $m \simeq 0.40$ [9], while the sound velocity is estimated in the following to be $v \simeq 2.5$. Thus ξ is larger than 6 lattice spacings, making field theory prediction truthful on the lattice. The sound velocity necessary to compute the entanglement temperature is not known. We thus estimate it using the relation between ρ_A and EH eigenvalues, Eq. (1.29), as discussed previously. The result we get is independent of α within few percent relative error, both in the OBC and PBC cases and for all the lowest 30 eigenvalues computed. We then tuned β in order to remove completely boundary effects close to the cut. In this way we get a speed of sound $v = 2\pi/\beta = 2.475$. The results for the string order parameter are reported in Fig. 1.11. The data correspond to a string starting in the middle of the right half-subsystem ($i = L/4$) and ending in the middle of the left half ($i = -L/4$). Relative deviations of the ground state average from the thermal expectation value are uniformly of order 10^{-4} for $L > 50$.

$\mathbf{J_1 - J_2}$ Model. As a final test for the 1-dimensional case, we discuss the $J_1 - J_2$ quantum model, which includes next-to-nearest-neighbour interactions. The Hamiltonian of this spin-1/2

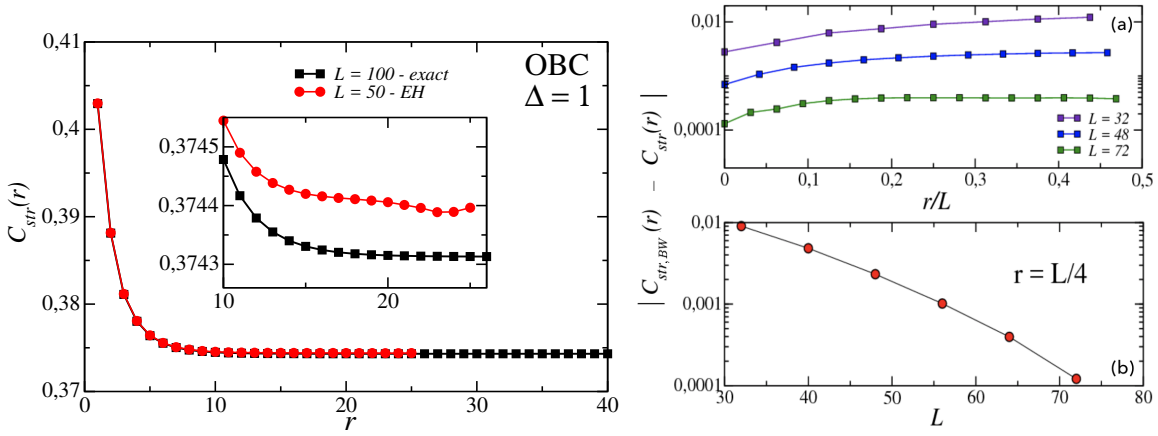

Figure 1.11: **Left.** Non-local order parameter as defined in Eq. (1.31) for the spin-1 XXZ chain at $\Delta = 1.0$. The square (black) and circle (red) points are results for the original and the half-bipartion EH-BW systems, respectively. **Right.** (a) Deviations between BW theorem thermal- and ground state-averages as a function of the r, for different system sizes. Relative errors are uniform and of order 10^{-4} for $L > 50$. (b) Finite size scaling of the deviations for $r = L/4$. Both plots indicate a discrepancy which is exponentially small in the system size.

quantum chain reads:

$$H = J_1 \sum_i \vec{S}_i \cdot \vec{S}_{i+1} + J_2 \sum_i \vec{S}_i \cdot \vec{S}_{i+2}, \tag{1.32}$$

where $J_1, J_2 > 0$ will be considered in what follows. When $J_2 = 0$ this model coincides with the XXZ chain at the BKT critical point. When J_2 is switched on, the model remains critical for a finite interval in J_2/J_1 and it is described by a $c = 1$ CFT with the same Luttinger parameter $K = 1/2$ throughout the whole interval [86]. When J_2/J_1 reaches the approximate value $J_2/J_1 \simeq 0.2411$ [87], a gap opens and the system enters a dimerized phase characterized by a non vanishing dimer-order parameter $d_i = \langle \vec{S}_{2i-1} \cdot \vec{S}_{2i} \rangle - \langle \vec{S}_{2i} \cdot \vec{S}_{2i+1} \rangle$. This phase contains an exactly solvable point for $J_2 = J_1/2$ [88], where the ground state factorizes into a product of spin-1 singlets on adjacent sites: $|\psi\rangle \propto (|\uparrow\downarrow\rangle - |\downarrow\uparrow\rangle)^{\otimes L/2}$. At this fine-tuned point the entanglement spectrum of the system is trivial, with either one or two equal non-vanishing eigenvalues (depending on the cut and with OBC). The same is not true for the BW-EH spectrum. Moreover the gap in the dimerized phase is maximum when $J_2 \simeq 0.6 J_1$ [89] and it slowly decreases with increasing J_2. We thus expect the worst results to be observed after the Majumdar-Ghosh factorization point with finite J_2. Note that the same behavior is expected close to any factorizable point, as discussed in the context of the Affleck-Kennedy-Lieb-Tasaki spin-1 chain in Ref. [13]. When $J_2 \to \infty$ the system reduces to two independent critical Heisenberg chains. Fig. 1.12 (left) shows the universal ratios Eq. (1.15) comparison between entanglement spectrum and LBW-EH spectrum for the OBC case where the system is in the middle of the critical phase ($J_2 = 0.1 J_1$), at the critical point ($J_2 = 0.2411 J_1$) and in the dimerized phase ($J_2 = 0.3 J_1$ and $J_2 = J_1$). In the first two cases the largest relative deviations are 2% and 8% respectively. When $J_2 = 0.3 J_1$ the gap is small and large discrepancies affect only eigenvalues in the ES smaller than 10^{-3}, where they reach 10% relative error. When $J_2 = J_1$ the gap is much larger and BW theorem does not reproduce the correct ratios for eigenvalues of the ρ_A of magnitude 10^{-2} and their degeneracies. Relative deviations are larger than 20% also for the first 10 ratios.

In Fig. 1.12 (right) we also show the finite size scaling of the overlaps Eq. (1.16) for the ground state. The overlap always increases for large system sizes in the PBC case, while it is decreasing in the OBC case for the lengths accessible via ED. We attribute the non-monotonic behaviour

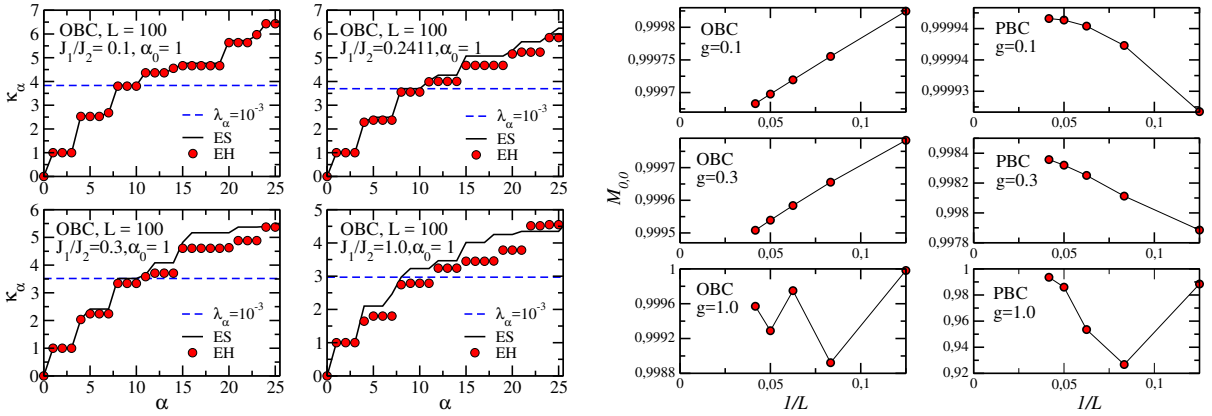

Figure 1.12: **Right.** Ratio κ_αs for the $J_1 - J_2$ chain with OBC. The black solid line and red circles stands for ratios computed from the exact ES and the EH spectrum respectively. The blue dashed line marks ρ_A eigenvalues with a magnitude indicated in the legend. Agreement with BW theorem is good in the middle of the critical phase and close to it (relative deviations smaller than 10%), while it gets worse as J_2/J_1 is increased away from the critical line (relative deviations larger than 20%). **Right.** Finite size scaling of the ground state overlap $M_{0,0}$ as defined in eq. Eq. (1.16) for the $J_1 - J_2$ chain for both OBC and PBC and for the three distinct values of the coupling constant $g = 0.1$ (gapless critical phase), $g = 0.3$ (gapped phase close to the critical point), $g = 1.0$ (gapped phase with large gap). In the OBC case the overlap decreases with the systems size, while it increases towards unity in the PBC case.

at $g = 1$ as a signal of the dimer order in the gapped phase.

1.1.6 Two dimensions

Differently from the one-dimensional case discussed so far, direct studies of entanglement Hamiltonians in interacting 2D and 3D models are lacking apart from few aforementioned cases discussed treated within perturbation theory. As such, the potential of applying the BW theorem reliably to lattice models can be of even stronger impact than in 1D systems. A closely related subject concerns topological matter, where Li and Haldane conjectured that the low-lying part of the ES is capturing the edge mode energetics [54].

In this section, we check the applicability of the LBW EH for the two-dimensional XXZ model on a square lattice, defined as:

$$H = J \sum_{\langle i,j \rangle} \left(S_i^x S_j^x + S_i^y S_j^y + \Delta S_i^z S_j^z \right), \tag{1.33}$$

for both the cylinder and the torus geometries, for which we employ Eq. (1.9) and (1.10) respectively. We focus on two cases: (i) the isotropic, $\Delta = 1$, and (ii) the XX, $\Delta = 0$ points. For these two values of Δ, the ground state of the system spontaneously breaks the continuous SU(2) and U(1) symmetries, respectively [90, 91]. In the first case, the low-lying field theory is a $\mathbb{CP}(1)$ model. In both cases, the low energy degrees of freedom of the system are characterized by a linear dispersion relation, and Lorentz-invariance emerges as an effective low-energy symmetry. Differently from the one-dimensional cases considered in the last section, exact diagonalization approaches are of little use here, as the LBW-EH approach cannot exploit lattice symmetries, as is limited to very small lattices where universality is most probably spoiled by finite volume effects. As such, we do not attempt comparisons based on entanglement spectrum and eigenvectors of BW-EH, but rather focus directly on the expectation values of first-neighbour correlation

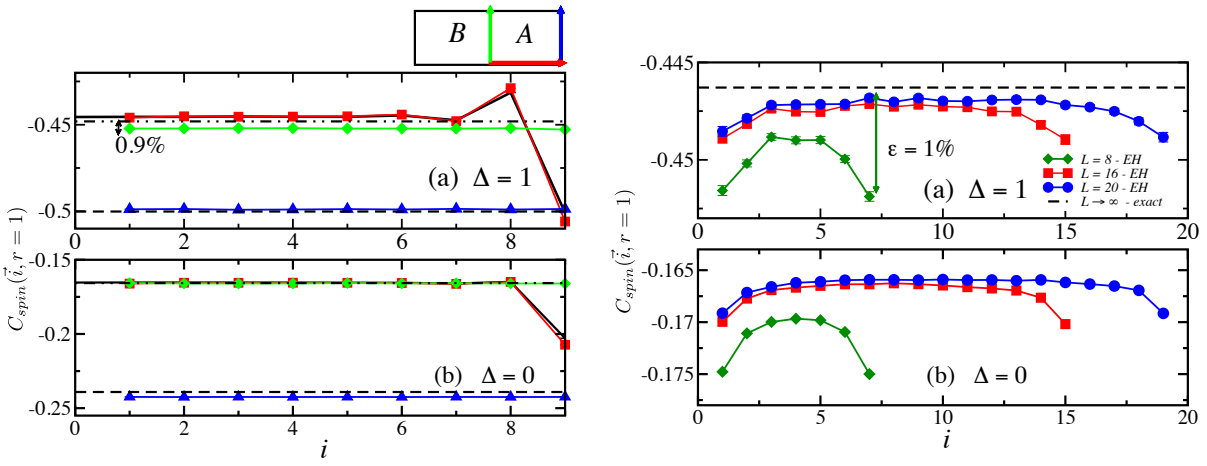

Figure 1.13: **Left.**Nearest-neighbor spin correlation function as function of bond index i for the 2D square lattice in the cylinder (BW) geometry for (a) $\Delta = 1$ and (b) $\Delta = 0$. The different points are the results of $C_{spin}(\vec{i}, r = 1)$ in different paths of the 2D system: red squares, blue triangles and green diamonds are along $(i_x = i, i_y = 1)$, $(i_x = L, i_y = i)$ and $(i_x = 1, i_y = i)$, respectively; see cartoon. In addition, the black curves are the exact ground state results for the system 20×10. **Right.**$C_{spin}(\vec{i}, r = 1)$ as function of bond index $\vec{i} = (i_x = i, i_y = 1)$ for different system sizes, L, in the 2D torus (CFT1) geometry. (a) $\Delta = 1$ and (b) $\Delta = 0$. The dashed horizontal line for $\Delta = 1$ is the exact result of $C_{spin}(\vec{i}, r = 1)$ extrapolated to the $L \to \infty$ limit [90].

functions

$$C_{spin}(\vec{i}, \vec{r}) = \left\langle S^z_{\vec{i}} S^z_{\vec{i}+\vec{r}} \right\rangle , \tag{1.34}$$

and the AFM order parameter. The sound velocities $v = 1.657J$ ($\Delta = 1$) and $v = 1.134J$ ($\Delta = 0$) obtained in Refs. [92] and [91], respectively, are used to calculate $\beta_{EH} = 2\pi/v$.

First, we discus the comparison of the BW-EH $C_{spin}(\vec{i}, r = 1)$ in the cylinder geometry with exact results, see Fig. 1.13 (left). Even for the relatively small system considered ($L = 10$), the agreement of $C_{spin}(\vec{i}, r = 1)$ with the exact results is very good. The LBW-EH qualitatively reproduces the behaviour of $C_{spin}(\vec{i}, r = 1)$, and the relative errors are $< 1\%$. Larger deviations are observed for correlations along the boundary between the two subsystems (green curve) and $\Delta = 1$ (these deviations are much milder in the anisotropic case). In the toroidal geometry, the exact formula of the modular Hamiltonian is not known even in the continuum. Here, we heuristically employ Eq. (1.10). In Fig. 1.13 (right), we plot the $C_{spin}(\vec{i}, r = 1)$ for different system sizes in the torus geometry. In this case, $C_{spin}(\vec{i}, r = 1)$ is almost homogeneous, with deviations smaller than $< 1\%$. Furthermore, as L increases the BW-EH results approaches the exact results obtained in the thermodynamic limit $L \to \infty$. This strongly suggests that the employed ansatz, whilst not necessarily exact, provides a very accurate description of 2D EH on tori. Finally, we discuss if the BW-EH describes the AFM long-range order in the $\Delta = 1$ case. The AFM phase is characterized by the order parameter

$$m^2 = \left\langle \frac{1}{N^2} \sum_{i,j} (-1)^{i+j} S_i S_j \right\rangle , \tag{1.35}$$

where i and j run on all the sites of the system and N is the total number of spins. If AFM long-range order is present, m^2 is finite in the thermodynamic limit, since AFM correlations remain nonzero at large distances. For a finite system, $2L \times L$, split in two equal halves of sizes $L \times L$, one can write $m^2 = m^2_A + m^2_B + m^2_{A,B} + m^2_{B,A}$, where m^2_A and m^2_B are the contributions

of subsystem A and B, respectively, and $m^2_{A,B}$ and $m^2_{B,A}$ are contributions of crossing terms. In the limit $N \to \infty$, all these four terms are equal, and $m^2 = 4m^2_A$. Fig. 1.14 shows the finite-size scaling of m^2 obtained with the BW-EH. As already observed for the first-neighbour correlation functions, m^2 is in good agreement with the exact result.

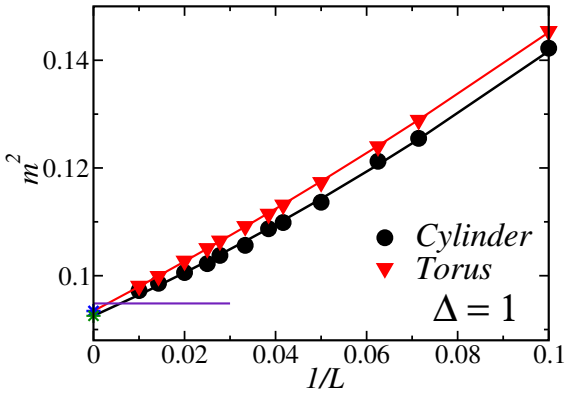

Figure 1.14: Finite-size scaling of m^2 for the EH-BW system ($L \times L$) in both the cylinder (black-square) and torus (red-circle) geometries. The horizontal line is the exact QMC value of m^2 obtained in Ref. [92].

We obtain $m^2(L \to \infty) = 0.0925(4)$ and $m^2(L \to \infty) = 0.0934(1)$ for the the cylinder and the torus geometries, respectively. The relative errors with QMC exact results, $m^2(L \to \infty) = 0.0948$ [92], are $\epsilon_{m^2} \approx 2.4\%$ and $\epsilon_{m^2} \approx 1.5\%$.

1.1.7 Conclusions

We have discussed an approach to systematically build approximate entanglement Hamiltonians of statistical mechanics models by applying the Bisognano-Wichmann theorem on the lattice. Starting from a recasting of the latter theorem on discrete space, we have presented a series of diagnostics based on the entanglement spectrum, the eigenvectors of the reduced density matrix, and expectation values of correlation functions. Based on these quantities, we have carried out numerical simulations for both 1D and 2D models whose low-energy physics is captured by a Lorentz invariant quantum field theory.

In critical cases, such as conformally invariant points and phases in 1D, and spontaneous-symmetry-breaking phases in 2D, our results strongly support that the lattice Bisognano-Wichmann entanglement Hamiltonian captures very accurately all properties of the original system. What is particularly striking is that even the eigenvectors of the reduced density matrix have very large overlaps, which seem not to vanish with increasing system size. This last fact is particularly surprising, as overlaps are quantities that typically vanish in the thermodynamic limit, suggesting that there might be deeper connections between the structure of the EH and the BW theorem directly at the lattice level. Let us also remark that our results show that the modified CFT formulas obtained by Cardy and Tonni [46] cope extremely well with finite-lattice spacing and, in fact, considerably reduce finite size effects when compared to the infinite-size BW EH.

In gapped systems, we typically find good agreement for both topologically trivial and non-trivial phases, with the exception of the $J_1 - J_2$ model: in this last case, the effects of strong dimerization considerably spoil the applicability of field theory results, as the phase itself does not support a description in terms of smoothly varying fields. Somehow surprisingly, degeneracies of the ES are well captured, and even the overlap of the entanglement ground state is anomalously large. In all cases investigated here, the CFT EH obtained with PBCs seems to apply equally well to both critical and off-critical cases. In analogy to the OBC case, we attribute this behavior to the fact that, sufficiently away from the boundary, the exact functional form of the EH is not

relevant as its ground state is locally the same as the original system.

At the methodological level, our study shows that well-established statistical mechanics tools such as DMRG and quantum Monte Carlo can be applied without major effort to the investigation of entanglement Hamiltonians. A first potential application along this route is the potential to carry systematic entanglement spectroscopy with QMC, not relying on reconstructing the ES from Rényi entropies [93], but rather on monitoring correlation functions in the entanglement ground state, and extract the corresponding entanglement gaps from the decay of correlation functions. A second application concerns the possibility of further severely reducing finite-size effects when measuring correlation functions by directly accessing a finite bipartition of an infinite system [4]. A third application is related to boosting procedures employed to extract the entanglement Hamiltonians given a ground state of interest, as discussed in two recent works [94, 95]. Our general analysis supports from the theoretical side the results obtained for the models considered in these works. Furthermore, from the experimental side, our results immediately extend the regime of applicability of the approach proposed in Ref. [13] to perform quantum simulation and spectroscopy of the EH, especially in two-dimensional interacting models, including connections to Unruh-type effects [96].

The discussion we have presented here only concerns statistical mechanics models whose Hilbert space can be written in tensor product form. An open question is to extend this approach to lattice gauge theories: in this context, a lattice version of BW can be constructed using established methods to properly build reduced density matrices that consider the effect of Gauss law at the boundary between two partitions [97, 98]. Another important feature of our approach is that, for critical systems, it is limited to quantum field theories with $z = 1$. While this encompasses a very broad class of quantum critical points, it would be interesting to extend the Bisognano-Wichmann theorem beyond its original applicability regime, thus providing a direct link between the dispersion relation of equilibrium systems and their ground state entanglement properties. Extending this correspondence could shed further light into the origin of area law (and violations thereof) of entanglement in the ground state of lattice models [6].

[4] This approach could also be employed in t-DMRG simulations.

1.2 Measuring entanglement entropy without wave-function

Despite its pivotal importance, the current understanding of entanglement measures in many-body systems is essentially limited to non-interacting theories or to lower bounds provided by Renyi entropies, due to the lack of methods to calculate the VNE in any dimension $D > 1$. This represents a key obstacle in determining both the capabilities of many-body systems in terms of quantum information processing (e.g., how much entanglement can be distilled by a given partition), and the generic relation between universal field theoretical descriptions and entanglement. In this section we overcome this obstacle by exploiting the knowledge of the functional form of the ground state EH to compute zero-temperature VNEs as thermal entropies of a system whose Hamiltonian is the Entanglement Hamiltonian Eq. (1.2). This simple observation allows to access entanglement entropies with any thermal algorithm. Most remarkably, QMC methods allow to push forward this idea to arbitrary dimension, providing a method which is scalable and applicable to a wide variety of lattice models.

In Sec. 1.2.1 we introduce our approach with particular attention to the QMC technique employed in $D > 1$, namely the Wang Landau (WL) algorithm [99]. In Sec. 1.2.2 we benchmark our method on 1D examples. In Sec. 1.2.3, we carry out QMC simulations on a series of 2D lattice models. For the 2D Heisenberg and XY models, we provide direct evidence that *(i)* the VNE is constrained by the area law (in agreement with lower bounds based on Renyi entropies), and *(ii)* the number of Goldstone modes can be determined with percent accuracy solely from entanglement properties. For the bilayer Heisenberg model, we study the geometric contribution to the entanglement entropy at its strongly coupled critical point, and verify a recent conjecture on $O(N)$ models [100]. Finally, in Sec. 1.2.4 we discuss the stability of the BW prescription for computing the VNE against imperfection in the EH.

1.2.1 Entanglement entropy as a thermal entropy

In what follows, we illustrate how to measure VNE in numerical simulations which do not have access to the system wave function. The strategy relies on any numerical method that is able to compute the thermodynamic entropy of the BW-EH at the entanglement temperature, β_{EH}. This can be achieved using QMC algorithms based on Wang Landau (WL) sampling [99].

Below, we illustrate this by applying the quantum version of the WL method performed in the stochastic series expansion (SSE) QMC framework [101, 102]. The key idea of the WL-SSE approach is to compute the density of states of the EH by considering a non-Markovian sampling based on the power expansion of the partition function [39, 71], Compared with the convetional quantum Monte Carlo (QMC) simulations, that is performed at a fixed temperature, the WL method features two main advantages for the study of the thermodynamic properties of the EH: (*i*) it allows to directly compute the thermal entropy at the "entanglement temperature" β_{EH}, and (*ii*) the thermodynamic properties of the EH are obtained for a broad range of temperature with a single run of the simulation.

The WL method was originally proposed for classical systems. For a quantum Hamiltonian, such as the BW-EH, one must map the system to a classical one. This is done, for instance, using the SSE framework, which considers the following form for the partition function

$$Z = \mathrm{Tr} e^{-\beta H} = \sum_{n=0}^{\infty} \frac{\beta^n}{n!} \mathrm{Tr}(-H)^n = \sum_{n=0}^{\infty} \beta^n g(n), \tag{1.36}$$

where the nth order series coefficient $g(n)$ plays the role of the density of states in the classical algorithm. We refer to Ref. [101, 102] for the general details of the computation of $g(n)$. Below we mention the technical aspects of the simulation that are relevant to reproduce our results.

The series expansion Eq.1.36 can be truncated at an order Λ, i.e., $n = 0, 1, ..., \Lambda$, without introducing systematic errors in the simulation. The choice of Λ is performed as in the conventional SSE simulations, see Refs. [39, 71], which gives as a result $\Lambda(\beta) \approx \beta|E(\beta)|$; where $E(\beta)$ is the expectation value of the total energy at inverse temperature β. The effect of the cutoff $\Lambda(\beta)$ is that the range of temperature that can be accessed is restricted to $\beta < \Lambda(\beta)/E(\beta)$. We simulate the BW-EH using $\Lambda(3\beta_{EH})$ as the cutoff. Instead, the computation of the BW VNE at β_{EH} are obtained utilizing a cutoff $\Lambda(\alpha\beta_{EH})$, with $\alpha = 1.3$. We checked that these results don't change upon increasing α.

In the WL-SSE algorithm, the sampling of the SSE configurations with different n is performed with a probability function that is proportional to the inverse of the density of states, $1/g(n)$. The WL sampling generates a histogram for the distribution of n that is flat, i.e., $H(n) \sim$ const; the histogram $H(n)$ is obtained counting the number of times a configuration with n is observed. The key point of the algorithm is that $g(n)$ can be computed by iteratively flattening $H(n)$. More specifically, one start with the guess $g(n) = 1$. Each time the configuration n is accepted $g(n)$ is multiplied by a factor f, i.e., $g(n) \to g_{\text{old}}(n)f$. This process is repeated until $H(n)$ is flat. In practice, we consider as a condition for the flatness of $H(n)$ a maximum deviation of 20% from the mean value. Once $H(n)$ is flat, it is reset to zero, and f is decreased by $\ln(f) \to \ln(f_{\text{old}})/2$ [103]. This process is repeated until convergence is achieved. Here we use the convergence condition proposed in Refs. [103, 104].

In addition to the aforementioned algorithm, we consider the optimized-broad-histogram algorithm proposed in Ref. [102] for the 2D Heisenberg model, see Fig. 1.16 (a). These results were obtained with the ALPS code [105, 106]. In this case, we confirm that the two methods give the same results (within error bars).

Finally, it is important to mention that the results for the BW entropy are obtained by doing an average of N_r independent WL simulations, i.e.,

$$S(\beta) = \frac{1}{N_r}\sum_{i=1}^{N_r} S_i(\beta). \tag{1.37}$$

The error bars are the standard deviation of the distribution $\{S_i\}$, and for all the results presented, we consider at least $N_r > 200$.

The use of local and loop updates in the WL-SSE sampling allows us to compute S_{BW} for systems with $\mathcal{O}(10^3)$ spins and $D \geq 1$. One point that is worth to emphasize is that the method is straightforward to implement on a working WL code, since it only requires to implement an inhomogeneous version of the system Hamiltonian, as in Eq. (1.2) [106].

1.2.2 One-dimensional critical systems

We now benchmark our strategy on one-dimensional critical systems, where the calculation of the VNE is amenable to both exact and tensor network simulations. In this case, the VNE of a subsystem of size L diverges logarithmically, $S(L) \propto c \ln L$, where c is the central charge of the underlying CFT.

In Fig. 1.15, we plot the BW VNE of the one-dimensional Heisenberg model (HM) and the quantum Ising model (QIM) at its quantum critical point, and under both PBCs and OBCs. Throughout this work, we employ dimensionless energy units for the sake of convenience. For the two models, the exact value of the entropy (empty circles) is evaluated using density-matrix-renormalization-group [9] (HM) and exact diagonalization methods (QIM) for a biparition of size L embedded in systems of size $2L$. The calculations of the BW-EH thermal entropy are carried out with QMC with both local and SSE directed-loop updates [39, 71] for the HM, and exact diagonalization for the QIM. In addition to the finite-size EH (red triangles), for the sake of

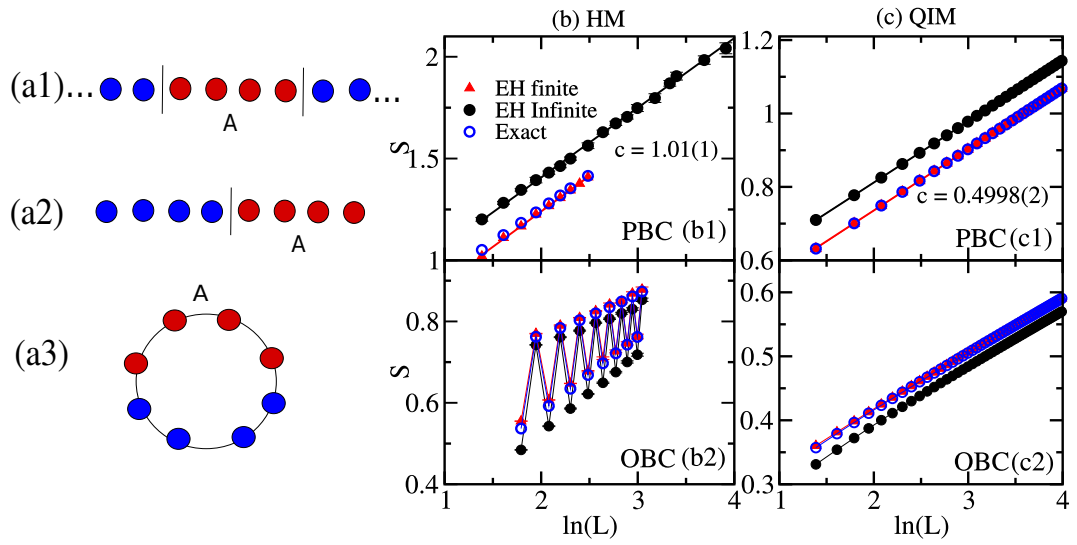

Figure 1.15: (a) Partitions of the one-dimensional systems: (a1) partition of length L embedded in an infinite system (infinite PBC); (a2) half-partition of a ring (finite PBC), (a3) half-partition of an open system (finite OBC). In panels (b) and (c) are shown results for the Heisenberg model and quantum Ising model, respectively, with PBC and OBC. The central charge obtained from the PBC VNE is in agreement with the exact results ($c = 1$ and $c = 0.5$). Error bars are smaller than the size of the symbols.

comparison, we also compute the entropy obtained utilizing the EH of a finite partition in an infinite system (black circles) [1]: the two are separated only by a constant shift that depends solely on the central charge.

For the PBC case the VNE increases logarithmically as expected: the corresponding central charge considering systems up to $L = 80$ (100) is in within 1% (0.05%) level with the exact results for the HM (QIM) - see Figs. 1.15 (b1) and (c1). For the OBC case, we observe an alternating term in the BW-EH entropy for the HM, but not for the QIM, see Figs. 1.15 (b2) and (c2). These result is in agreement with the exact VNE. As discussed in Ref. [107, 35], those oscillations are universal and due to the antiferromagnetic nature of the interactions, not appearing in the QIM [108] (in the latter, the effective Fermi momentum is either 0 or π). From the CFT perspective, the oscillations can be viewed as lattice corrections to the scaling dimension Δ_p: their decay as a function of the bipartition size is a power law whose exponent is related to Δ_p [35, 109].

The fact that the BW-EH faithfully reproduces not only the leading, but also the dominant subleading correction testifies its predictive power on generic universal quantities captured by the VNE. While, for instance, non-universal contributions such as additive constants in 1D shall not be immediately reproduced due to the field theoretical origin of the relation we employ, in all examples where a comparison to exact results is possible (essentially, 1D systems), we observe that even non-universal contributions are accurately captured: for instance, $\Delta S(L)$ goes to zero in the limit $L \to \infty$ both in the OBC and PBC cases. We attribute this to the fact that the BW-EH is actually able to reproduce a "partition function" whose corresponding Hamiltonian has the correct density of states, and whose generic correlation functions are correct [1]. In case only the first element was true, and, for instance, the overall scaling correction was wrong, one would have generically expected incorrect correlation functions. From a methodological viewpoint, this implies that our method may be used to check convergence of tensor network states in conformal phases, especially for large values of the central charge.

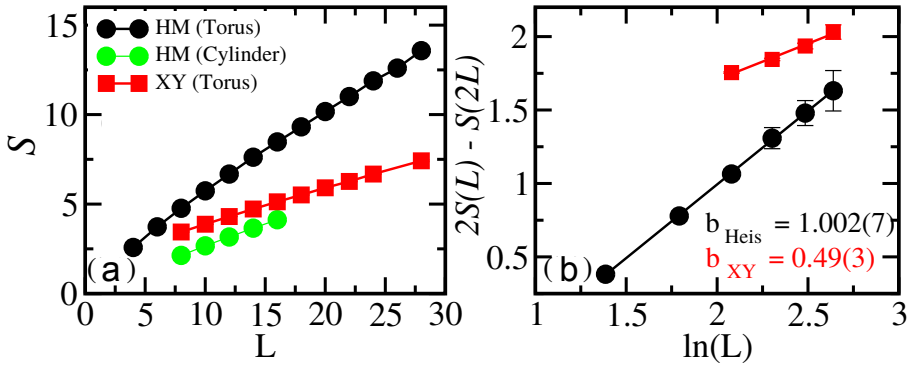

Figure 1.16: (a) Results for the HM and XY model. The x-axis of represents the linear size of the boundary, $L_y = L$, and the subsystem aspect ratio for the HM (torus) is $a.r. = L_y/L_x = 1$, while for the XY (torus) and the HM (cylinder), $a.r. = 2$. (b) Subleading term in S as function of $\ln L$. The number of Goldstone modes, $n_b = 2b$, is extracted with a linear fit, and agrees with the expected result.

1.2.3 Two dimensional systems

Quantum magnets. The VNE can describe universal properties of two-dimensional systems. For instance, the VNE of 2D ground states that break a continuous symmetry scales as $S(L) = AL + B\ln(L) + D$, where L is the linear size of the boundary. The A is the non-universal *area law* term [23], while, for a smooth boundary, the prefactor of the logarithmic term is a universal quantity related to the number of Nambu-Goldstone modes n_b, $B = n_b/2$, of the associated spontaneuosly-symmetry-broken (SSB) phase [30, 29, 110, 111]. As examples of SSB, we consider the 2D XY model and the Heisenberg model. In both cases, we perform QMC simulations of the EH and extract the corresponding VNE as a function of the subsystem linear size, L. The entropy is evaluated at $\beta_{EH} = 2\pi/v$, with $v_{Heis} = 1.658J$ [112] and $v_{XY} = 1.134J$ [91], using the WL-SSE algorithm.

In order to cast the BW-EH on two dimensional lattices we employ the same prescription adopted in Sec. 1.1. We also consider the CFT expression Eq. (1.4), which corresponds to the generalization of the BW to a subsytem that is embbeded in a infinite system; we call this subsystem-geometry of toroid.

We remind the reader that, as discussed in Ref. [1], for finite values of L_y, formula Eq. (1.4) is in principle only applicable to conformal field theories. Let us illustrate here a simple, non-rigorous argument that partly justifies the applicability of this approach to generic (i.e., non conformal) 2D models. Typically, the low energy theory will be made of gapless and gapped sectors. The description of the former will be scale invariant and relativistic invariant: while this does not guarantee emergent conformal invariance, exceptions are rare. The gapped part of the theory will (at most) contribute to the entanglement properties only in the very vicinity of the edge of the partition, where it would actually behave like a gapless theory. Far from the boundary, the reduced density matrix with respect to these degrees of freedom will be an identity operator (up to degeneracies). This indicates that the CFT formulas used above shall be applicable also to more general cases where some low-energy degrees of freedom are actually gapped. In the context of the 2D HM, the role of gapless degrees of freedom is played by the $\mathbb{C}P(1)$ model describing the emergent Nambu-Goldstone modes, and the gapped part of the theory is described by the massive Goldstone mode.

In Fig. 1.16 (b1), we show the scaling of the BW VNE for both cylinder and torus geometries. The scaling is clearly linear. In the case of the HM on a torus, we extracted the coefficient A by fitting these results to $S(L) = AL + B\ln(L) + D$, and obtain $A = 0.372(6)$, which is in agreement with a prediction based on spin-wave approximation [113] (discrepancy $< 3\%$).

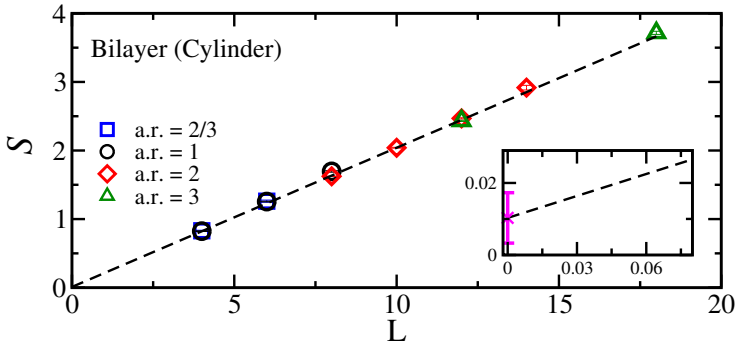

Figure 1.17: The plot shows the result for the bilayer HM entropy at the QCP, $g_c = 2.522$, and different $a.r. = L_y/L_x$, where $L_y = L$. The outcome is well described by a linear fit, and the y-intercept is $\gamma \approx 0$, see the *inset*.

In Fig. 1.16 (b2), we extract the subleading logarithmic correction by considering the entropy difference $2S(L) - S(2L) \simeq \frac{n_b \log(L)}{2}$ in toroidal geometries of circumference $2L$. The number of Nambu-Goldstone modes obtained from the prefactor of this term is in perfect agreement with field theoretical expectations [29, 113, 32, 114], with accuracy at the percent level or lower. The fact that the VNE returns a value which is considerably closer to the field theoretical prediction when compared to the one extracted from Renyi entropies [30, 32] may signal the fact that the latter are more affected by irrelevant operators, as observed in 1D [107, 35, 109], or may be due to the smoother continuity properties of the VNE.

Strongly coupled Quantum criticality. As a second example of a 2D system, we consider the bilayer Heisenberg model [115, 116]. This model describes a quantum phase transition induced by the inter-coupling g that belongs to the $O(3)$ universality class. We compute the BW-EH entropy at the QCP, $g_c = 2.522$, considering $\beta_{EH} = 2\pi/v$, with $v = 1.9001(2)$ [112]. For this universal class, it has been argued that there is a universal constant correction to the entanglement entropy that depends solely on the aspect ratio [100, 117]: for a cylinder geometry with PBC in the y direction, this constant has been conjectured to vanish, in sharp contrast to anti-PBC. Verifying this conjecture requires accurate values of the entropy at large system sizes of several hundred sites.

Our results up to partition of size $L = 18$ are depicted in Fig. 1.17. Within error bars, they show that $S(L)$ is independent of the aspect ratio of the subsystem, see Fig. 1.17, and have no detectable logarithmic subleading term (the $S(L) = AL + B\ln(L) + D$ fitting, gives $B = -0.05(8)$). The y-intercept of $S(L)$ is 0.010(7), which confirms the conjecture for the universal constant contribution for the $O(N)$ model [100].

1.2.4 Stability of the Bisognano-Wichmann entropy

We now discuss the stability of the approach to measure the BW-EH utilizing QMC simulations. The most critical step are uncertainty due to errors in determining β_{EH}. Since the density of states of the EH has qualitatively distinct properties from conventional density of states, it is of key importance to understand the sensitivity of the approach proposed here to such errors.

In Fig.1.18 (a1,b1), we show the value of the extracted entropy obtained via Wang-Landau sampling as a function of β, for both 1D and 2D HM. The insets magnify the region in the vicinity of the exact value of β_{EH}, signaled by a dashed vertical line: in this regime, the entropy is linearly sensitive to β. This implies that the accuracy in estimating S is ultimately limited by the accuracy on the sound velocity: this strengthen the applicability of our method to QMC simulations, where v can be measured very accurately via a variety of techniques [118, 112].

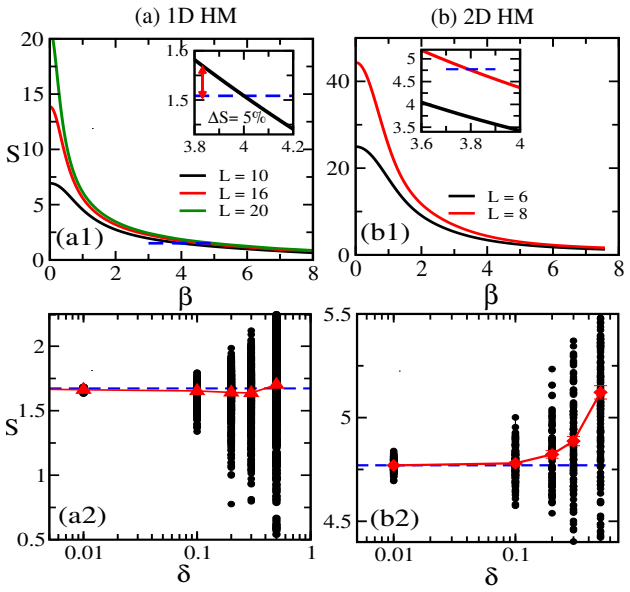

Figure 1.18: Panels (a1) and (b1) show the β-dependence of the BW-EH entropy for the 1D (infinitePBC) and 2D (torus) HM, respectively; the insets magnify the regions close to the numerical exact value of β_{EH} (dashed vertical line). Panels (a2) and (b2) show the BW-EH entropy as a function of the disorder magnitude δ for the (a2) 1D HM with $L = 16$ (infinite PBC) and (b2) 2D HM (torus) with $L = 8$ (see text). The circles (black points) are the value of S for a single realization of disorder, while the triangles (red points) are the averaged S (N_r = [100 - 200] realizations of disorder are used). The horizontal dashed line represents the value of S in the clean case.

Finally, we address the effects of random perturbations in the EH couplings Γ_x, which accounts for possible imperfect experimental realizations of the EH. We consider disordered couplings, $\Gamma_x \to \Gamma_x(1+\delta_x)$, where $\delta_x \in [-\delta, \delta]$, in the BW-EH of the HM (in 1D and 2D). Specifically, we are interested in understanding how the BW VNE is affected by a small amount of disorder.

In Fig. 1.18 (a2,b2) we show that the BW VNE is not appreciably affected by disorder up to strength of the order of 10%. For larger values of δ, we observe a considerable dependence on the disorder realization, as signalled by the visually large spreading of the values of S. Surprisingly, the mean value of the entropy is not dramatically affected. This remarkable stability is in contrast to what is typically found when studying the effects of disorder in the Hamiltonian couplings, which have a quantitatively larger effect on entropies. A possible element in support of this unexpected resilience is the fact that the VNE is endowed with particularly robust continuity properties with respect to changes in the entanglement spectrum (which is instead expected to be directly affected by the random couplings).

The generic approach described above can be extended to formulate protocols to measure the von Neumann entropy in experiments, complementing previous approaches based on Renyi entropies [119, 120, 121, 122, 123, 124, 125] and entanglement spectra [126, 13]. The key ingredient here is to obtain the density of states of the EH, whose microscopic implementation has been discussed in Ref. [13].

1.2.5 Conclusions

We have presented a method to measure the ground state von Neumann entropy of a broad class of lattice models via direct thermodynamic probe of the correspondent entanglement Hamiltonian. The method is straightforward to implement in quantum Monte Carlo simulations, and is of immediate applicability to experiments capable of measuring the density of states. It enables accurate predictions of universal quantities solely based on entanglement, thanks in particular to

its immediate scalability in numerical simulations. Future perspectives include the application of the method to other entanglement related quantities, such as the negativity, its extension to lattice gauge theories, and its integration with methods to determine the EH at finite temperature [94, 127].

1.3 Finite size corrections to the Bisognano-Wichmann theorem

In Secs. 1.1 and 1.2 we showed that the EH corresponding to the ground state of the lattice models whose low-energy physics is captured by a Lorentz invariant field theory can be approximated by a lattice adaptation of the Bisognano-Wichmann (BW) theorem, the corresponding reduced density matrix, ρ_{BW}, although not generically exact, accurately reproduces not just the low-lying entanglement spectrum, but also properties directly related to its eigenvectors, such as correlation functions and order parameters. Furthermore, the von Neumann entropy obtained from ρ_{BW}, i.e. S_1^{BW}, accurately describes universal properties, such as, the central charge of one-dimensional critical models. Since the BW-EH is based on a quantum field theory result, one expects that, while universal properties should be well captured, non-universal ones and contributions due to lattice and finite-size effects are not necessarily captured by ρ_{BW}. Here we focus on 1-dimensional critical systems, and we demonstrate that the capability of the EH in Eq. (1.2) to approximate ground state reduced density matrices on the lattice goes well beyond the universal low-energy regime. By analyzing the Rényi entropies obtained from the CFT generalizations of BW theorem, we prove that rho_{BW} encodes non-universal subleading corrections in the higher moments of the entanglement spectrum distribution.

In Sec. 1.3.1 we review the general behavior of the Rényi entropy in quantum critical chains and we describe the quantities analyzed in the subsequent sections. In Sec. 1.3.2 we present our comparison between the BW and the exact results of the Rényi entropy. Finally, in Sec. 1.3.3 we draw our main conclusions and connect them with other related works.

1.3.1 Rényi entropy via the Entanglement Hamiltonian

Over the last years, bipartite Rényi entropies (REs) have become a paradigmatic quantity in the characterization of quantum many-body lattice models [128, 23, 8]. In quantum critical chains, for instance, the scaling of the bipartite Rényi entropy of the ground state is associated with the underlying conformal field theory (CFT) describing its low energy properties [129, 130, 25]. When the subsystem consists of a single, simply connected interval, the leading and the subleading scaling of the Rényi entropy with the subsystem size give access to the corresponding central charge [129, 130, 25] and the operator content [131, 35, 36, 132, 37] of the theory, respectively. In more than one-dimension, REs also determine universal properties of the system, such as the number of Goldstone modes in spontaneously-symmetry-broken phases [29], and serve as a diagnostic tool to characterize topologically ordered phases [28, 27, 133].

From a quantum information perspective, REs characterize the entanglement between a subsystem A of a pure state (here we focus on the ground states and simply connected subsystems), $|\psi_{AB}\rangle$, and its complement B. In the following we consider the $\alpha-$Rényi entropies, defined as:

$$S_\alpha = \frac{1}{1-\alpha} \ln \mathrm{Tr} \rho_A^\alpha, \tag{1.38}$$

where $\rho_A = \mathrm{Tr}_B |\psi_{AB}\rangle\langle\psi_{AB}|$; with Tr_B being the trace over the complement of A. For the limiting case $\alpha = 1$, one obtains the von Neumann entropy, that is, the bipartite entanglement measure for pure states. REs with $\alpha > 1$ provide strict lower bounds on the entanglement between A and B.

In this work, we focus on partitions with the geometries shown in the Fig. 1.15 (a). As outlined in Sec. 1.1, the corresponding BW-EH can be obtained for CFT systems from the

following expression

$$\tilde{H}_{BW} = \beta_{BW} \left[\Gamma \sum_{n=1}^{L-1} \lambda(n)\, \hat{h}_{n,n+1} + \Theta \sum_{n=1}^{L} \lambda(n-1/2)\, \hat{l}_n \right], \tag{1.39}$$

with the appropriate choice of the couplings $\lambda(n)$. Here $\hat{h}_{n,n+1}$ and $\hat{l}_n$ are two-sites and single-site terms present in the Hamiltonian density. For a subsystem that is embedded in an infinite system (Fig. 1.15 (a1)), one has [45]

$$\lambda(n) = \frac{n(L-n)}{L}. \tag{1.40}$$

For finite systems with half-bipartition, i.e. $L = L_T/2$, in the case of open and periodic boundary conditions (Fig. 1.15 (a3) and (a2)) one has [46]

$$\lambda(n) = \frac{2L}{\pi} \sin\left(\frac{\pi n}{2L}\right), \tag{1.41}$$

and

$$\lambda(n) = \frac{L}{\pi} \sin\left(\frac{\pi n}{L}\right). \tag{1.42}$$

We call these partitions finite OBC and finite PBC, respectively.
Finally, we define the BW reduced density matrix as

$$\rho_{BW} = \frac{e^{-\beta_{BW} H_{BW}}}{Z_{BW}}, \tag{1.43}$$

where the constant $Z_{BW} = \mathrm{Tr} e^{-\beta_{BW} H_{BW}}$ guarantees the proper normalization of the BW reduced density matrix, $\mathrm{Tr}(\rho_{BW}) = 1$. For later convenience we define $H_{BW} = \tilde{H}_{BW}/\beta_{BW}$.

Let us now discuss how to obtain the Rényi entropy with the aid of the BW-EH. If we substitute the definition of the BW reduced matrix, Eq. (1.43), in Eq. (1.38), we obtain

$$S_\alpha^{BW} = \frac{\alpha \beta_{BW}}{1-\alpha} \left[F(\beta_{BW}) - F(\alpha \beta_{BW}) \right], \tag{1.44}$$

where $F(\beta_{BW}) = -\frac{1}{\beta_{BW}} \ln Z_{BW}$ is equal to the free energy of the BW-EH at the inverse entanglement temperature β_{BW}. In the limit $\alpha \to 1$, S_α reduces to the the von Neumann entropy, and S_1^{BW} reads

$$S_1^{BW} = \beta_{BW} \langle H_{BW} \rangle + \ln Z_{BW}, \tag{1.45}$$

which is nothing else but the definition of the thermodynamic entropy of the BW-EH system at β_{EH}. Both the BW Rényi entropy with $\alpha > 1$ and the von Neumann entropy can be obtained by computing the thermodynamic properties of the BW-EH. For instance, for a quadratic fermionic EH, we can write

$$H_q = \sum_k \epsilon(k) \hat{c}_k^\dagger \hat{c}_k, \tag{1.46}$$

where $\epsilon(k)$ is the single-particle spectrum of H_q. One then can simply employ the conventional definition of the free-energy for non-interacting fermions

$$F(\beta) = -\frac{1}{\beta}\sum_k \ln\left[e^{-\beta\epsilon(k)}+1\right], \tag{1.47}$$

and use Eq. (1.44) to compute S_α^{BW}. We use this expression to compute S_α^{BW} for both the XX and the transverse field Ising models, which are known to be mappable to free fermionic theories.

For models whose Hamiltonians cannot be cast in a quadratic form, one can use quantum Monte Carlo methods to compute S_α^{BW}. It is important to mention that the BW-EH of sign-problem-free models, as the ones considered here, is also sign-free. For models with the sign-problem, one can use tensor network methods to compute S_α^{BW}. We consider the quantum version of the Wang-Landau method [99] performed in the stochastic series expansion (SSE) framework [101, 102]. This method allows a direct calculation of the free-energy and the entropy of the BW-EH at $\beta = \beta_{EH}$. Here we use both local and SSE directed-loop updates to simulate the XXZ model [39, 71]. Using WL-QMC we can compute S_α^{BW} for system sizes comparable with the ones achievable with DMRG, $L \sim 10^2$. For interacting systems, we also employ exact diagonalization (ED) methods to compute S_α^{BW}. We compare S_α^{BW} with the Rényi entropy obtained with the exact reduced density matrix ρ_A. From now on we call the *exact* Rényi entropy S_α. For the non-interacting systems (XX and transverse field Ising models), we obtain S_α with the aid of the correlation matrix [134], and for interacting systems we use both ED and DMRG methods.

The Rényi entropy of the ground state of one-dimensional models whose low-energy physics is captured by a gapless relativistic field theory has been extensively studied by both analytical and numerical methods, see Refs. [128, 135, 23, 8] for reviews. There are numerous analytical and numerical results indicating that the leading asymptotic behavior of S_α for $\alpha \to 1^+$ coincides with the entropy of the vacuum in the CFTs [135], i.e. for $L/a \gg 1$ (a is the lattice spacing) $S_\alpha = S_\alpha^{CFT}$. For example, when the subsystem is a single interval of length L embedded in an infinite system (see Fig.1.15 (a1)), one has [129]

$$S_\alpha^{CFT}(L) = \frac{c}{6}\left(1+\frac{1}{\alpha}\right)\ln\frac{L}{a} + c'_\alpha, \tag{1.48}$$

where c is the central charge of the corresponding CFT and c'_α is a non-universal constant. The CFT formula is also generalized to a finite system with the length L_T where we have [129, 25]

$$S_\alpha^{CFT}(L, L_T) = \frac{c}{6\eta}\left(1+\frac{1}{\alpha}\right)\ln\left[\frac{\eta L_T}{\pi a}\sin\frac{\pi L}{L_T}\right] + c''_\alpha, \tag{1.49}$$

where $\eta = 1, 2$ for PBC/OBC, and c''_α is a non-universal constant.
Away from the asymptotic limit $L \gg a$ (from now on we set $a = 1$) it is known that S_α includes corrections to the CFT expressions, i.e.

$$C_\alpha(L) = S_\alpha(L) - S_\alpha^{CFT}(L) \neq 0. \tag{1.50}$$

As first noticed in the Ref. [107], for systems with OBC, the CFT formula cannot explain the oscillations observed in the von Neumann entropy. In Ref. [35], it was observed that parity oscillations in the S_α of the XXZ model can also occur in a system with PBC for $\alpha > 1$. There

it was proposed that the asymptotic leading term of $C_\alpha(L)$ is given by

$$d_\alpha(L) = f_\alpha \cos(2k_F L) \, |2L \sin(k_F)|^{-p_\alpha} \, , \tag{1.51}$$

where f_α is a nonuniversal constant, p_α is a universal critical exponent equal to $p_\alpha = 2K/\alpha$ and K is the Luttinger liquid parameter. For the XXZ model $k_F^{XXZ} = \pi/2$ and $d_\alpha(L)$ oscillates with L. In this case the presence of $d_\alpha(L)$ is confirmed by both exact numerical calculations based on DMRG [107] and the exact analytical expression for the Rényi entropy of the XX model [136]. The oscillatory behavior of these corrections is attributed to the tendency to antiferromagnetic order in the ground state of the XXZ model. Oppositely, for the transverse field Ising model, as $k_F^{Ising} = 2k_F^{XXZ}$, the leading term of $C_\alpha(L)$ is given by a nonoscillatory $d_\alpha(L)$ [35].

The fact that the asymptotic leading term of $C_\alpha(L)$ is equivalent to $d_\alpha(L)$ has been confirmed with DMRG calculations for models belonging to different universality classes in finite systems with both PBC and OBC [107, 36, 132, 37, 137]. These results support the following scenario for the models considered here: while the XXZ model exhibits oscillatory corrections to the CFT formula, the discrete-symmetric Z_2 transverse field Ising and Z_3 three-state Potts models exhibit no oscillations. Furthermore, the power law decay exponent of the leading term of $C_\alpha(L)$ is given by

$$p_\alpha = \frac{\tilde{\eta} X_e}{\alpha}, \tag{1.52}$$

where $\tilde{\eta} = 1, 2$ for OBC/PBC, and X_e is the scaling dimension of the energy operator. An exception is the von Neumann entropy of systems with PBC. In this case, the leading term of C_α does not oscillates with L, and the power law decay is given by $1/L^\nu$, where $\nu = 2$, as shown by numerical results based on DMRG [37].

The accuracy of ρ_{BW} relies on the underlying field theory being Lorentz invariant[5]. This is always the case for the quantum critical chains considered here, where conformal symmetry emerges as a feature of the low-energy degrees of freedom of the system. Even in this case, however, one shall expect that lattice effects are not completely suppressed, and the exact EH is not exactly given by Eq. (1.39). As an example, we mention the exact results for the EH of a free fermionic chain at half-filling, that are very close to the BW-EH, but presents tiny longer range terms that survives even in the $L \to \infty$ limit [16, 138]. These terms, completely absent in the BW-EH, are caused by the curvature arising in the dispersion relation of hopping fermions on the lattice away from Fermi points and they can be systematically computed [139]. In the context of lattice models the exact EH for a half chain is known for the transverse field Ising chain away from the criticality and the XXZ model in the massive phase [17, 140].

Since even when $L \to \infty$ the BW-EH is not exact in general (e.g., as for the free-fermion chain), one may wonder that the BW Rényi entropy: *i)* does not reproduce the non-universal contributions such as the additive constants c'_α (or c''_α), despite the fact that the low energy part of the spectrum of the BW-EH is in almost perfect agreement with the exact ones, as discussed in Ref. [1]; *ii)* does not capture the corrections to the CFT scaling associated to relevant (or irrelevant) operators, as discussed in the last section.

In order to investigate these issues, we consider the size scaling of the Rényi entropy obtained from ρ_{BW}. More specifically, we discuss the behavior of the leading terms of S_α^{BW} and the BW corrections to the CFT formula

$$C_\alpha^{BW}(L) = S_\alpha^{BW}(L) - S_\alpha^{CFT}(L) + c'_\alpha, \tag{1.53}$$

[5]For the BW-EH obtained from Eq.(1.40),(1.41),(1.42), the accuracy of ρ_{BW} relies on the underlying field theory being conformal invariant

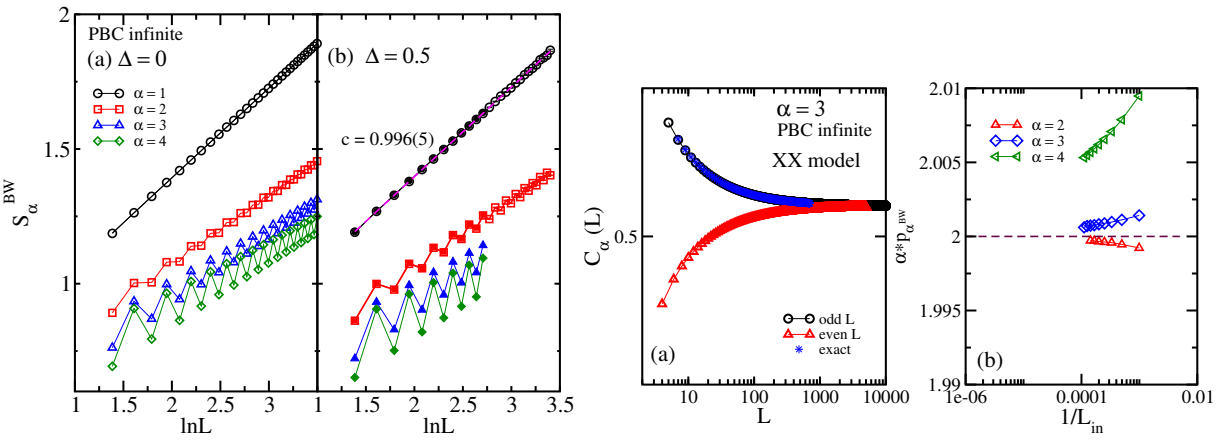

Figure 1.19: **Left.** BW Rényi entropy for the XXZ model with (a) $\Delta = 0$ and (b) $\Delta = 0.5$. Results for both even and odd values of L are shown. In panel (a) we obtain S_α^{BW} by diagonalizing the corresponding free-fermion BW-EH of the XX model, while in panel (b) we use both QMC (empty points) and ED (filled points). QMC error bars are smaller than the marker sizes. The values of the central charge extracted from S_1^{BW} is presented in panel (b). **Right.** C_α is presented in panel (a) for even and odd values of L; the blue points (stars) correspond to the exact results obtained with the correlation matrix technique [134]. In panel (b) we show p_α^{BW} calculated using the fitting procedure described in the main text; the dashed line represents the exact value of αp_α.

Note that for convenience, we add the constant c'_α (c''_α for a finite system). The asymptotic leading term of $C_\alpha^{BW}(L)$ is investigated by fitting it with the following function

$$F_\alpha(L) = A_\alpha + f_\alpha^{BW}/L^{p_\alpha^{BW}}, \tag{1.54}$$

where A_α, f_α^{BW} and p_α^{BW} are free parameters. As can be noted, apart from the constant A_α, the function $F_\alpha(L)$, neglecting the oscillating factor, has the same form of $d_\alpha(L)$ (Eq. (1.51)). We also consider the discrepancy between the BW and the exact Rényi entropy

$$dS_\alpha = |S_\alpha^{BW} - S_\alpha|. \tag{1.55}$$

We stress that, unlike previous studies that were mostly concerned with the low-lying part of the entanglement spectrum (ES), eigenvectors, and correlators [141, 138, 70, 1], we focus here on properties of the full reduced density matrix, such as momenta of the ES distribution (i.e. the REs). The analysis of the finite-size scaling of the REs allows us to check if ρ_{BW} captures universal properties of the system.

1.3.2 Rényi entropies on the lattice from the Bisognano-Wichmann theorem

In this section, we analyze the accuracy of S_α^{BW} and C_α^{BW} by directly comparing it with the results obtained from the exact ρ_A, and the general theoretical behavior of S_α known from CFT. We consider the partitions shown in Fig. 1.15 (a) (i.e. for finite systems we always consider half-partition). In particular, we discuss results for the XXZ chain, transverse field Ising (TFIM), three-state Potts (3SPM) and bilinear-biquadratic spin-1 (BBM) models. The exact Rényi entropy exhibits an oscillatory behavior with respect to L for the XXZ chain, whilst these oscillations are absent for both TFIM and 3SPM. We conclude this section by showing S_α^{BW} for the critical non-integrable BBM.

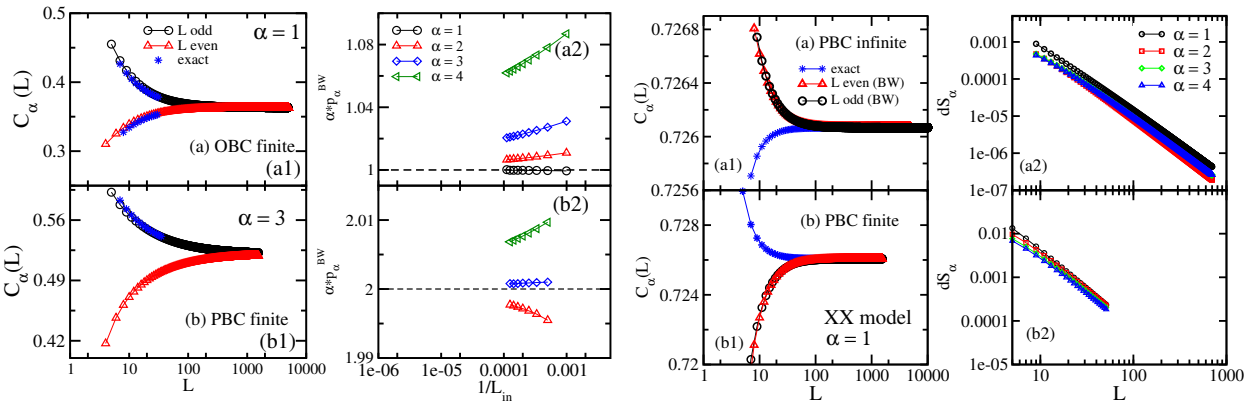

Figure 1.20: **Left.** Panels (a1) and (b1) present C_α for OBC and PBC, respectively, in the XX model; the blue points (stars) correspond to exact results obtained with the correlation matrix technique [134]. In panels (a2) and (b2) we show the results of the calculated p_α^{BW} for OBC and PBC, respectively, using the fitting procedure described in the main text; the dashed line represents the exact value of αp_α. **Right.** Panels (a1) and (b1) present the corrections to the scaling of the BW Rényi entropy, S_1^{BW}, for the infinite and finite PBC partitions, respectively, in the XX model. The blue points correspond to exact results. In panels (a2) and (b2) we show the discrepancy between the BW and the exact REs for the infinite and the finite PBC partitions, respectively, with different values of α

XXZ model. The XXZ model has been introduced in Sec. 1.1. The Hamiltonian is defined in Eq . (1.25). Here we focus on the parameter region $-1 < \Delta \leq 1$, where the ground state of the XXZ is gapless and can be described by a CFT with $c = 1$. We remind that, in this regime, the exact sound velocity is given by $v = \pi\sqrt{1-\Delta^2}/2 \arccos\Delta$. It is worth mentioning that the exact EH in the massive phase (i.e., $\Delta < -1$ or $\Delta > 1$) is equal to the BW-EH (with coupling $\lambda(n) = n$) for $L \to \infty$ [17, 140]. However, the corner transfer matrix method used to obtain this result is not applicable to the gapless regime discussed here.

The resulting BW-EH for $\Delta = 0$, that corresponds to the XX model, can be mapped to a free-fermion Hamiltonian with the aid of the Jordan-Wigner transformation. The S_α^{BW} (Eq. (1.44)) is then obtained by diagonalizing the $L \times L$ matrix. This method allows us to achieve very large subsystem sizes ($L \sim 10^4$), which is fundamental to determine the corrections to the leading term in S_α^{BW}. For $\Delta \neq 0$, the calculation of S_α^{BW} is limited to $L \leq 100$, and is performed using QMC and ED methods (see below).

For the PBC case, the size-scaling of the BW von Neumann entropy follows the expected behavior predicted by CFT, as discussed in Refs. [16, 138, 2], and illustrated in Fig. 1.19 (left) a for the $\Delta = 0$ case. We confirm this result for the XXZ model with $\Delta = 0.5$ using the Wang-Landau SSE method [101, 102]. We consider the following cutoff for the SSE series expansion: $\Lambda = 2.5\beta_{EH}|E(\beta_{EH})|$, where $E(\beta_{EH})$ is the expectation value of the total energy at inverse temperature β_{EH}. This choice of Λ allows us to obtain S_α^{BW} for $\alpha \leq 2$; for comparison, we also compute S_α^{BW} with ED. As shown in Fig. 1.19 (left) (b), we obtain $c = 0.996(5)$ by fitting the QMC data, $S_1^{BW}(L)$, for $L \leq 30$ with the CFT formula (Eq. (1.48)). More interestingly, we note that while S_1^{BW} is a smooth function, S_α^{BW} (for $\alpha > 1$) exhibits oscillations with L, as expected from the exact results when $\alpha > 1$. Furthermore, the decrease of these oscillations with L suggests that S_α^{BW} gives back the CFT formula in the asymptotic regime. Similar corrections to the CFT formula are observed in the OBC case [2]. We now investigate in more detail these corrections by presenting the results for $C_\alpha^{BW}(L)$ for different partitions.

We first consider $C_\alpha^{BW}(L)$ for the XX model in the infinite PBC case. The oscillatory behavior of S_α^{BW} is manifest when we plot $C_\alpha^{BW}(L)$ for even and odd values of L. As an example we show the $\alpha = 3$ case in Fig. 1.19 (right) (a). The asymptotic behavior of $C_\alpha^{BW}(L)$ is analyzed by fitting our results with Eq. (1.54) (in the fit, we just consider the values of $C_\alpha^{BW}(L)$ for odd L).

	$\alpha = 2$	$\alpha = 3$	$\alpha = 4$
BW	0.11422(5)	0.1614(5)	0.1743(5)
exact	0.11423...	0.1609...	0.1726...

Table 1.1: The table shows the comparison between the calculated f_α^{BW} (using the infinite PBC BW-EH) for the XX model and the exact coefficients f_α (Eq.(1.51)) taken from Ref. [136].

Although not shown here, we also considered other values of α, with similar conclusions. The fits are performed with respect to L in the interval $[L_{in}, L_{max}]$; where the maximum value considered for L_{in} is $L_{in} = L_{max} - 10^3$. As we improve the quality of the fit (i.e., increasing the value of L_{in}), the parameter p_α^{BW} converges to the expected scaling exponent, $p_\alpha = 2/\alpha$, see Fig. 1.19 (right) (b).

It is worth mentioning that the coefficient f_α^{BW} obtained from the fit is also in a quantitative agreement with the exact result for f_α obtained in Refs. [35, 136], see Table 1.1. In the Table we considered $\alpha = 2, 3$ and 4; the agreement of f_α^{BW} worsens for larger α because sub-leading terms of C_α^{BW} (in addition to the leading one described by Eq. (1.51)) become more relevant as we increase α. The same thing occurs with the exact Renyi entropy [35]. Note that for $\alpha = 1$ the exact calculations predict $f_1 = 0$. The coefficient f_1^{BW} will be discussed below. These results strongly indicate that, in the asymptotic regime, $C_\alpha^{BW}(L)$ is not just qualitatively, but also quantitatively in agreement with the leading asymptotic behavior of the exact corrections.

We now consider the finite-system partitions with both OBC and PBC; see Fig. 1.15 (a2) and (a3). The correction $C_\alpha^{BW}(L)$ exhibits the expected oscillatory behavior with L. For OBC, this behavior occurs even for the $\alpha = 1$ case, see Fig. 1.20 (left) (a1). Furthermore, by fitting these results with Eq. (1.54), we observe that the values of p_α^{BW} are also in agreement with the exact results $p_\alpha = 1/\alpha$ and $p_\alpha = 2/\alpha$ for the OBC and PBC, respectively, see Fig. 1.20 (left) (a2) and (b2). These results indicate that the leading asymptotic term of C_α^{BW} is given by d_α (Eq. (1.51)).

Despite the agreement between C_α^{BW} and the exact results in the asymptotic limit, a comparison between $C_\alpha^{BW}(L)$ and the exact results still shows some tiny discrepancies, see Fig. 1.20. Although not visible in Fig. 1.19 (right) (a) these tiny discrepancies also exist for the infinite PBC case. The question then is what is the nature of these discrepancies. The results discussed so far indicate the following: while the leading term of $C_\alpha^{BW}(L)$ coincides with d_α (Eq.(1.51)), subleading corrections, that are most likely present in both the exact and the BW $C_\alpha(L)$, are different (at least, at the scale accessible to our numerical calculations).

In order to better analyze the point raised in the last paragraph, we discuss now the behavior of the von Neumann entropy for systems with PBC. In this case, the exact S_1 does not exhibit any oscillating term, and the leading term of C_1 is not given by d_α [35, 136]. It is interesting to note that S_1^{BW} also does not oscillate with L, as can be seen in Fig. 1.20 (right). Nevertheless, unlike the $\alpha > 1$ cases, the trends of the size scaling of the BW and the exact C_α are completely different. This fact explains the tiny discrepancy $dS_\alpha/S_\alpha < 10^{-3}$. In this case, already the leading term of $C_\alpha^{BW}(L)$ differs from the exact corrections.
We note that the scaling exponent that determines the asymptotic behavior of $dS_\alpha \sim 1/L^{\gamma_\alpha}$ does not depend on α, and is $\gamma_\alpha \approx 1.9$, see Fig. 1.20 (right) (a2) and (b2). The fact that γ_α is independent of α is in line with the previous statement that the correction d_α is present in both the BW and the exact S_α, i.e., this factor cancels out when we consider the difference dS_α. Finally, we observe that the discrepancy of the BW REs is almost independent of α, as expected from the discussion above.

We now discuss the results for $\Delta \neq 0$. In this case, the investigation of the asymptotic behavior of C_α^{BW} is hindered by the small system sizes that one can achieve with ED. In addition,

the tiny discrepancies between the BW and the exact results, $dS_\alpha/S_\alpha < 0.1\%$, are difficult to access with QMC due to the statistical errors in the MC estimates. Despite these technical issues, the results obtained with both ED and QMC show that the behavior of C_α^{BW} is in line with the exact results. The exact Rènyi entropy (and C_α) is obtained with ED for subsystem sizes $L \leq 12$ and DMRG for $L > 12$. In the DMRG calculation we obtain the entanglement spectrum of the original system by keeping 100 - 150 states and using the ground state as the target state in the proper symmetry sector.
In Fig. 1.21 (a) and (b), we show some examples of the scaling of C_α^{BW} obtained with QMC for $L \leq 30$, and two different values of Δ. For PBC, C_α^{BW} oscillates with L for $\alpha = 2$, but not for $\alpha = 1$, as it is expected for the exact C_α. By fitting C_2^{BW} with Eq. (1.54), we obtain the following values for the scaling exponent p_2^{BW} for two case values of the anisotropy Δ: $p_2^{BW}(\Delta = 0.5) = 0.78(3)$ and $p_2^{BW}(\Delta = 0.9) = 0.61(7)$. These results have a discrepancy of almost 4% with respect to the the exact results: $p_2 = 0.75$ ($\Delta = 0.5$) and $p_2 \approx 0.583$ ($\Delta = 0.9$), for the XXZ model with PBC, $p_2 = K$, where $K = \pi/\left(2\arccos(-\Delta)\right)$ is the Luttinger liquid parameter. This discrepancy seems to be unaffected by potential logarithmic corrections that are present at the isotropic point.

The results of C_α^{BW} obtained with ED for $L \leq 15$ are also in agreement with the exact ones, as can be seen in Fig. 1.21 (c) and (d). The discrepancy dS_α goes to zero as a power law, $dS_\alpha \sim 1/L^{\gamma_\alpha}$, see Fig. 1.21 (c2) and (d2). Furthermore, the scaling exponent γ_α is almost independent of α, as observed for the XX model with larger subsystem sizes. This feature can be explained if we assume that the correction d_α is present in both the BW and the exact S_α, i.e., this factor cancels out when we consider the difference dS_α.

Transverse field Ising and quantum three-states Potts models. In this section, we discuss the behavior of S_α^{BW} for models that are characterized by discrete global symmetries.
First, we consider the transverse field Ising model(TFIM), whose Hamiltonian and phase diagram has been reviewed in Sec. 1.1.5. It is worth to point out that for this model the EH of a half-partition in an infinite chain was computed exactly away from the critical point [16]. The result perfectly matches our lattice version of the BW theorem; however, it does not predict the prefactor β_{EH}. Here, instead, we focus on the quantum critical point, where the TFIM is characterized by a CFT with $c = 1/2$ and the exact sound velocity is equal to $v = 2$. As it occurs

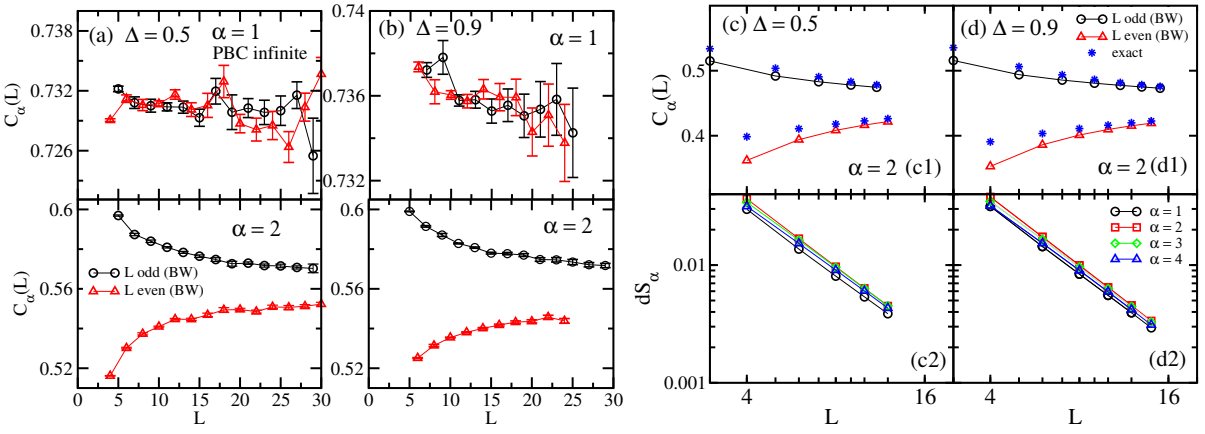

Figure 1.21: In panels (a) $\Delta = 0.5$ and (b) $\Delta = 0.9$ we present the correction to the scaling of S_α^{BW} obtained with QMC for the infinite PBC partition. In panels (c) $\Delta = 0.5$ and (d) $\Delta = 0.9$ we obtain the results with ED and DMRG (see text) for the finite PBC partition: (c1) and (d1) show the corrections to the scaling of S_2^{BW}, while in (c2) and (d2) we present the discrepancy between the BW and the exact REs for different values of α.

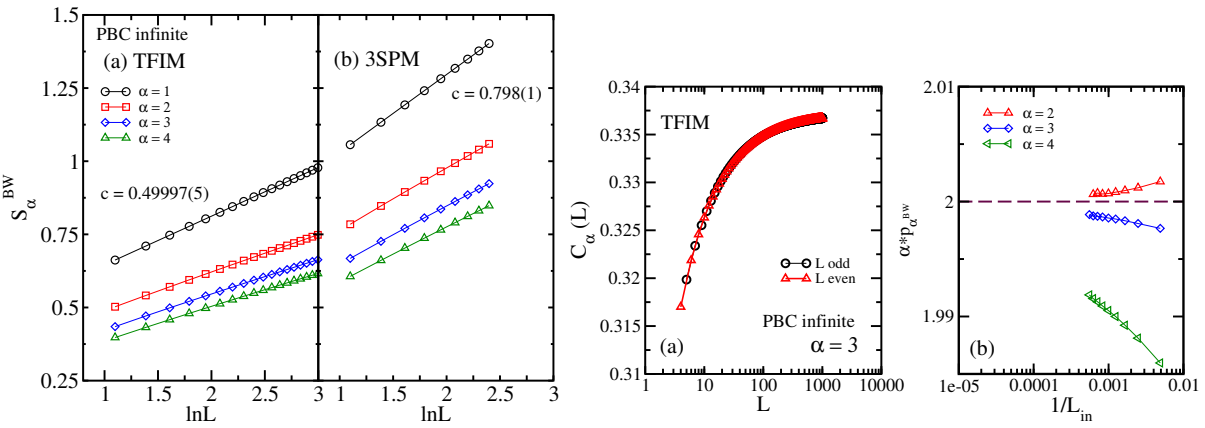

Figure 1.22: **Left.** BW Rényi entropy for the (a) transverse field Ising and the (b) three-state Potts model for different values of α. Results for both even and odd values of L are shown. In panel (a) we obtain S_α^{BW} by diagonalizing the corresponding free-fermion BW-EH of the TFIM, while in panel (b) we use ED (see text). The values of the central charge extracted from S_1^{BW} are presented. **Right.** C_α is presented in panel (a), while in panel (b) we show the results of the calculated p_α^{BW} using the fitting procedure described in the main text; the dashed line represents the exact value of αp_α.

for the XX model, the BW-EH of the TFIM can be mapped to a quadratic Hamiltonian with the aid of the Jordan-Wigner transformation. For this model we are able to consider systems up to size $L = 10^3$.

We further consider the three-state Potts Model (3SPM) (see Sec. 1.1.5). As in the TFIM case, we focus on the quantum critical point, $g = 1$. In this case the system is described by a CFT with the central charge $c = 4/5$ [76, 77], and the exact sound velocity is $v = 3\sqrt{3}/2$ [75]. We use ED to obtain the $S_\alpha^{BW}(L)$ for systems with sizes up to $L = 12$.

Before discussing the scaling properties of the deviations with respect to the exact result, we briefly illustrate the overall scaling of $S_\alpha^{BW}(L)$ as a function of L. The latter is depicted in Fig. 1.22, for both the TFIM and the 3SPM. No oscillations with L are present, as expected for these models [37]. Here we just show results for the infinite PBC case, however, we also confirmed similar results for the other EHs described in the Sec. 1.3.1. Furthermore, we calculated the central charge by fitting S_α^{BW} to the CFT formula, Eq. (1.48). The outcome is in perfect agreement with the exact results, as can be seen in Fig. 1.22 (a) and (b). In particular, for the 3SPM we obtain $c \approx 0.798$, from S_1^{BW}, which has a discrepancy of just 0.3% with respect to the exact result, $c = 4/5$. It is worth emphasizing that this result is obtained for subsystem sizes up to just $L \leq 12$, which signals the fact that S_1^{BW} is barely affected by corrections to the CFT formula, contrarily to what is observed for the Rényi entropy of the XXZ model.

We now discuss the behavior of the corrections to the CFT formula, $C_\alpha(L)$. We start by considering an infinite system, and fit $C_\alpha^{BW}(L)$ for L within the interval $[L_{in}, 10^3]$ for different values of α to Eq.(1.54), see Fig. 1.22 (right) (a). As we increase L_{in}, the parameter p_α^{BW} converges to the exact result $p_\alpha = 2/\alpha$ [35] (see Fig. 1.22 (right) (b)).

For the finite-system partitions, we explicitly compare C_α^{BW} with the exact results. In this case, we focus on the PBC case. As we see in Fig. 1.23 (a), for $\alpha = 3$, the discrepancy between the exact and the BW results is almost negligible (e.g., $dS_3/S_3 < 10^{-3}$ even for $L \approx 10$). The exact and the BW corrections have the same behavior as L increases, i.e., $C_\alpha^{BW}(L)$ increases and then saturates to a constant value, which also strongly indicates that the leading term of the exact and the BW $C_\alpha(L)$ are the same. Consequently one can conclude that the discrepancy dS_α is due to subleading terms present in both the BW and the exact $C_\alpha(L)$. Although not shown here, we have also observed similar behavior for all the $\alpha > 1$ cases that we considered.

For the case of the von Neumann entropy, the size scaling of C_α^{BW} has a different trend compared

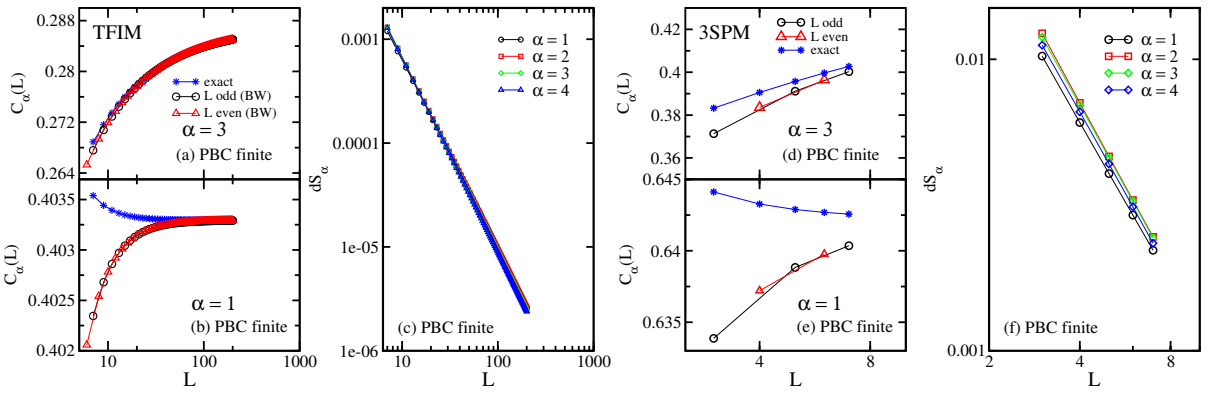

Figure 1.23: Results for the transverse field Ising model are presented in panels (a)-(c). Panels (a) and (b) show the correction to the scaling of the BW Rènyi entropy for the finite PBC partition with $\alpha = 3$ and $\alpha = 1$, respectively, while in panel (c) we consider the discrepancy, dS_α, as a function of the subsystem size, L. We obtain these results by diagonalizing the corresponding free-fermion BW-EH. In panels (d)-(f) are presented results for the three-states Potts model with the same set of parameters of panels (a)-(c), respectively, and using ED (see text).

to the exact results, see Fig. 1.23 (b). As discussed for the XXZ model, since the exact C_1 differs from d_α (Eq. (1.51)) [35, 136, 37], already the leading term of C_1^{BW} is different from the exact corrections.

Finally, we observe that dS_α goes to zero as a power law, $dS_\alpha \sim 1/L^{\gamma_\alpha}$, see Fig. 1.23 (c). The scaling exponent γ_α does not depend on α ($\gamma_\alpha \approx 1.8$), as can be seen in Fig. 1.23 (c). Similarly to the conclusions that we drew for the XXZ model, this result can be explained by the fact that the α-dependent correction d_α (see Eq. (1.51)) is present in both the BW and the exact S_α with comparable numerical coefficients.

For the 3SPM, due to size limitation, we were not able to compute the exponent p_α^{BW}. Nevertheless, in Fig. 1.23 (d)-(f), we show how the behavior of C_α^{BW} is qualitatively in agreement with exact results. In particular, we note that the scaling exponent γ_α associated to the power law, $dS_\alpha \sim 1/L^{\gamma_\alpha}$ (see Fig. 1.23 (f)) is almost independent of α.

To summarize our investigation of the accuracy of the BW REs, we observed that for all the models considered here the almost negligible discrepancies ($dS_\alpha/S_\alpha < 10^{-3}$ even for subsystems with $L \approx 10$) vanish as $L \to \infty$. For a finite partition, the corresponding value of dS_α can be understood as follows: both the logarithmically-divergent CFT term, Eq. (1.48), and the leading corrections to the CFT scaling (see Eq. (1.51)) are properly described by S_α^{BW} (with the exception of $\alpha = 1$ for PBC). Finally dS_α is related to subleading corrections, that are associated to both the BW and the exact results. The investigation of the nature of the subleading corrections to C_α^{BW} is beyond the scope of this work.

Bilinear-biquadratic model. All the models under investigation so far can be either mapped into free-fermion chain or solved by Bethe ansatz, and thus are considered integrable models. In fact, integrability is a key ingredient to carry out the analysis presented in the previous sections, because it gives the exact value of the sound velocity $v = 2\pi/\beta$, which allows the computation of S_α^{BW} (see Eqs. (1.44) and (1.45)). However, v can be computed numerically in non-integrable models, allowing to compute S_α^{BW} in these cases. We thus consider as an example of non-integrable model the bilinear-biquadratic model (BBM)

$$H = \sum_{n=1}^{L_T} \vec{S}_n \cdot \vec{S}_{n+1} + g(\vec{S}_n \cdot \vec{S}_{n+1})^2. \tag{1.56}$$

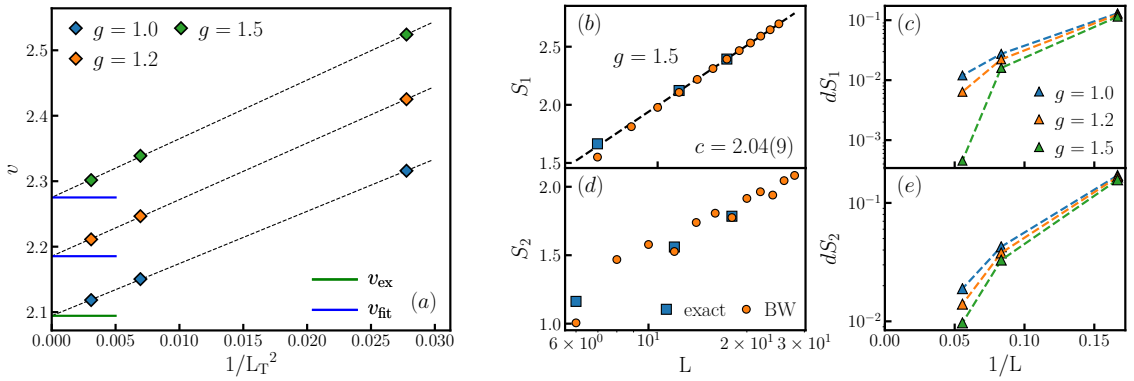

Figure 1.24: (a) Sound velocity as defined in Eq. (1.58) for $L_T = 6, 12, 18$. Dashed lines indicate the power-law fit with fixed power 2. Blue horizontal lines are the fitted asymptotic values of v, while the green line is the exact known value $v = 2\pi/3$ for the integrable point $g = 1$. The fitted value for these points deviates from the exact one with a relative error $< 10^{-6}$. Panels (b),(d) show the exact S_α for $\alpha = 1, 2$ (blue squares) and the BW S_α^{BW} (orange circles) for $g = 1.5$ (non-integrable point) obtained with ED. The dashed line is a fit of the last 5 points from the BW von Neumann entropy. The resulted central charge is in perfect agreement with the expected value, $c = 2$ (c),(e) Discrepancy between S_α^{BW} and the exact S_α, as defined in Eq. (1.55), for $g = 1, 1.2, 1.5$.

The phase diagram of this model hosts a gapped Haldane phase for $-1 < g < 1$. The two boundaries of this phase are gapless Bethe-integrable points whose underlying CFTs have central charges $c = 3/2$ for $g = -1$ and $c = 2$ for $g = 1$ [142, 143]. For $g < -1$ the system is gapped, while for $g > 1$, although the integrability is lost, the low-energy degrees of freedom are described by a CFT with $c = 2$. Here we consider the region $g > 1$, and investigate the applicability of the BW-EH ansatz in the absence of integrability. We use periodic boundary conditions in order to exploit translation symmetry in the computation of the exact S_α. The system is frustrated when L_T is not a multiple of 3. As we need even system sizes in order to compute half-system entanglement, we use ED to compute S_α for $L_T = 6, 12, 18$.

We employ the BW-EH for finite systems with PBC (Eq. (1.42)). S_α^{BW} is obtained for $L_T \leq 22$ using ED. The sound velocity v can be extracted from the finite size scaling of the ground state energy, assuming the knowledge of the central charge [144, 145]. However, here we follow another route. Based on the very precise relation between the spectrum of the BW-EH, $\{\epsilon_\alpha^{BW}\}$, and the eigenvalues of ρ_A, $\{\lambda_\alpha\}$, namely

$$\lambda_\alpha = \frac{e^{-2\pi\varepsilon_\alpha^{BW}/v}}{Z_{BW}}, \tag{1.57}$$

we can compute v from the first two eigenvalues of the BW-EH and ρ_A via the relation

$$v = \frac{2\pi(\varepsilon_1^{BW} - \varepsilon_0^{BW})}{\log(\lambda_0/\lambda_1)}. \tag{1.58}$$

We verify that Eq. (1.57) holds for $g \geq 1$. First, we compute v for $g = 1$, where the exact sound velocity $v = 2\pi/3$ is known from the Bethe ansatz solution. Despite we have only 3 points at disposal, the extrapolation of the inifinite-size value of v by fitting $|v(L_T) - 2\pi/3|$ with a power law A/L^γ ($\gamma = 2$) gives a value for v that is within 0.5 % level of the exact result. Given the apparent absence of sub-leading corrections, this procedure gives results which are more accurate than the values extracted from the finite size scaling of the ground state energy (see Fig. 1.24 (a)). In fact the latter is known to be affected by logarithmic corrections [146]. Assuming the

aforementioned power-law scaling, we then extract the value of v for $g > 1$ by considering a two-parameter fit on 3 points; see Fig. 1.24 (a).

Given the small system sizes that we can reach with ED, we do not discuss the accuracy of C_α^{BW} for the BBM, instead, we focus our analysis on the comparison between S_α^{BW} and the exact S_α. In Fig. 1.24, we consider S_α^{BW} for $g = 1, 1.2, 1.5$. As can be seen from Figs. 1.24 (c) and (e), the discrepancy, dS_α, decreases with system size and even for $L = 9$, we observe a discrepancy $dS_\alpha \approx 10^{-2}$. This result is observed not only at the integrable point, $g = 1$, but also away from it, i.e., $g = 1.2$ and 1.5. Furthermore, the central charge extracted from the size scaling of S_1^{BW} for $g = 1.5$ is in perfect agreement with the exact result, $c = 2$, see Fig. 1.24 (b). Note that there is not sign of frustration felt by exact ground state in the von Neumann entropy computed from the BW-EH. These results demonstrate that the applicability of the BW-EH ansatz is not restricted to integrable models.

1.3.3 Conclusions

We presented an extensive numerical investigation of the accuracy of the BW Rényi entropy for one-dimensional critical models. We observed that they converge to the exact results in the thermodynamic limit, and capture not only the CFT logarithmically-divergent term, but also some universal finite-size corrections to the CFT formula. We showed that the power-law decay of the leading term of C_α^{BW} is related to the scaling dimension of the energy density operator p_α (with the exception of $\alpha = 1$ for PBC).

In Ref. [139] it was recently shown that the exact lattice EH of free-fermion chains at half-filling (XX model) is equal to the conformal expression (Eq. (1.3) with the appropriate $\lambda(n)$) if one includes the hopping at finite distance in the continuum limit of the entanglement lattice Hamiltonian. This result shows that the tiny long-range terms present in the exact EH, but absent in the BW-EH, are irrelevant terms in the asymptotic limit, and explains why the BW REs are remarkably close to the exact results in the thermodynamic limit. Our observation that $dS_\alpha \to 0$ for the XXZ and 3SPM models indicates that possible long-range terms present in the exact EH of these critical interacting lattice models are also irrelevant in the thermodynamic limit.

On the other hand, the observation that S_α^{BW} properly describes universal lattice-finite-size effects associated to the scaling exponent $p_\alpha = \eta X_e/\alpha$, can be understood if one considers the conformal mapping used to obtain the EH of the partitions considered here [46]. Remarkably, we observe that even the coefficient of these corrections are almost equal to the exact ones. We thus conclude that the almost negligible discrepancy dS_α is related to subleading corrections affecting both the exact and the BW C_α. From a methodological point of view, this demonstrate that our approach may be used to check convergence of tensor network states in conformal phases, especially for large values of the central charge (since the complexity of the Wang-Landau method is not affected by the entanglement of the ground state wave function).

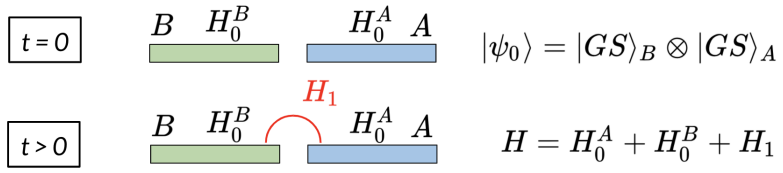

Figure 1.25: Schematic representation of the local quench protocol. The initial state is the product of the ground state of the two decoupled subsytems A and B. For simplicity we can assume $H_A = H_B = \sum_{i\in A/B} h_i$. At time $t = 0$ an interaction between A and B is switched on, and the systems is let evolving with the Hamiltonian $H = \sum_{i\in A\cup B} h_i$.

1.4 Outlook

In this chapter, we gave a comprehensive characterization of ground state entanglement Hamiltonians in a wide variety of lattice models, in one and two dimensions. Our results demonstrate the applicability of quantum field theory to reproduce, with high accuracy, zero-temperature equilibrium properties of many-body quantum systems in a strikingly simple fashion. Moreover, we showed that the implications of our findings can give guidance to overcome the computational complexity of many-body ground states in more than one dimension.

The predicting power of conformal field theory extends well beyond equilibrium physics. Conformal field theory can be applied to describe the dynamics of one-dimensional many-body systems after a quantum quench [147], and to provide an analytical expression for time-dependent entanglement Hamiltonians [46]. This fact might be key to climb over the so-called entanglement barrier: quantum dynamics generates an increasing amount of entanglement over the initial state, precluding the possibility of efficiently representing the state at all times. Having parametrical control over the entanglement Hamiltonian of the state at time t enables the use of Quantum Monte Carlo algorithms to compute time-dependent quantities for arbitrarily large times.

One example is provided by the entanglement Hamiltonian after a local quantum quench. The quench protocol is depicted in Fig. 1.25. We take an initial state which is the product of two identical ground states of an Hamiltonian $H_A = H_B$, where A and B are two equal-length partition of an open chain. We can think about this state as the ground state of an Hamiltonian $H = H_A + H_B$, in which A and B are decoupled, namely the Hamiltonian density h on the link between A and B is zero. When the Hamiltonian H is critical and A and B are semi-infinite lines, conformal field theory provides an expression for the entanglement Hamiltonian at time t [46]:

$$\tilde{H}_A(t) = 2\pi \int_A dx \frac{x|x-t|}{t}\, T(x,t) + \int_A dx \frac{x|x+t|}{t}\, \bar{T}(x,t), \tag{1.59}$$

where the T and $\bar{T}$ are the two chiral components of the stress-energy tensor in the CFT. They can be expressed as

$$T(x,t) = \frac{h(x,t)+p(x,t)}{2}, \qquad \bar{T}(x,t) = \frac{h(x,t)-p(x,t)}{2}, \tag{1.60}$$

where h and p are the Hamiltonian and momentum density, respectively.Since a local quench injects a non-extensive amount of energy in the system, the resulting dynamics is governed by the low energy states of the full systems. In this regime we can expect that CFT gives a reasonable description of the time-evolved state.
In order to put Eq. (1.59) on the lattice we need to find the lattice counterpart of the momentum density p. However, the momentum operator is highly non-local on the lattice, meaning that it cannot be expressed as the sum over all lattice sites of a local density. This issue can be

circumvented by observing that the stress-energy tensor is a 2×2 matrix that reads

$$T_{\mu\nu} = \begin{pmatrix} h & j_h \\ p & j_p \end{pmatrix}, \tag{1.61}$$

where j_h and j_p are the currents associated to the densities h and p. Assuming Lorentz invariance, which is only approximate (at low energy) on the lattice, the stress-energy tensor is symmetric: $j_h = p$. Moreover, energy and momentum conservation imply:

$$\partial_t h + \partial_x j_h = 0, \qquad \partial_t p + \partial_x j_p = 0, \tag{1.62}$$

The first equation can be put on the lattice by rewriting the temporal derivative using Schröedinger equation

$$\partial_t h_n = i\,[H, h_n] = i \sum_k [h_k, h_n] = i\,([h_{n-1}, h_n] + [h_{n+1}, h_n]) \tag{1.63}$$

and discretizing the spatial derivative to yield the following lattice expression for the momentum density

$$p_n = i\,[h_{n-1}, h_n] \tag{1.64}$$

Combining the last equation with Eq. (1.59), we can obtain a lattice version of the time-dependent entanglement Hamiltonian:

$$\tilde{H}_A(t) = \frac{\pi}{v} \sum_{n \in A} \frac{n|n - vt|}{vt} \left(h_n(t) + p_n(t)\right) + \frac{\pi}{v} \sum_{n \in A} \frac{n|n + vt|}{vt} \left(h_n(t) - p_n(t)\right), \tag{1.65}$$

where the model-dependent sound velocity v has been restored. Notice that the presence of the momentum density p_n implies that the $\tilde{H}_A(t)$ is complex, signaling the breaking of time-reversal invariance. From a numerical perspective Eq. (1.65) would require to compute the time evolution of $h_n(t)$ and $p_n(t)$, which is impractical for large systems. There are two ways to escape this problem. Either we shift the integration variable in Eq. (1.59) to express $\tilde{H}_A(t)$ in terms of T and $\bar{T}$ computed at $t = 0$ (making the integration domain changing with time), or we use the CFT time-evolution $T(x,t) = T(x - vt)$ and $\bar{T}(x,t) = \bar{T}(x + vt)$ (properly discretized). In both cases we get a discontinuous function of time, which becomes smoother as the system size increases. Understanding its predictive power and its regimes of applicability shall be object of future investigation.

Bibliography

[1] G. Giudici et al., "Entanglement Hamiltonians of lattice models via the Bisognano-Wichmann theorem", *Phys. Rev. B* 98 (2018), p. 134403.

[2] T. Mendes-Santos et al., "Measuring von Neumann entanglement entropies without wave functions", *New Journal of Physics* 22.1 (2020), p. 013044.

[3] T. Mendes-Santos et al., "Entanglement Hamiltonian of quantum critical chains and conformal field theories", *Phys. Rev. B* 100 (2019), p. 155122.

[4] L. Amico et al., "Entanglement in many-body systems", *Rev. Mod. Phys.* 80 (2008), pp. 517–576.

[5] P. Calabrese, J. Cardy, and B. Doyon, "Entanglement entropy in extended quantum systems", *J. Phys. A: Math. Theor.* 42.50 (2009), p. 500301.

[6] J. Eisert, M. Cramer, and M. B. Plenio, "Colloquium: Area laws for the entanglement entropy", *Rev. Mod. Phys.* 82 (2010), pp. 277–306.

[7] E. Fradkin, *Field Theories of Condensed Matter Systems*, Cambridge University Press, 2013.

[8] N. Laflorencie, "Quantum entanglement in condensed matter systems", *Phys. Rep.* 646 (2016), p. 1.

[9] S. R. White, "Density matrix formulation for quantum renormalization groups", *Phys. Rev. Lett.* 69.19 (1992), pp. 2863–2866.

[10] U. Schollwöck, "The density-matrix renormalization group", *Rev. Mod. Phys.* 77.1 (2005), pp. 259–315.

[11] U. Schollwöck, "The density-matrix renormalization group in the age of matrix product states", *Ann. Phys.* 326.1 (2011), pp. 96–192.

[12] E. Witten, "APS Medal for Exceptional Achievement in Research: Invited article on entanglement properties of quantum field theory", *Rev. Mod. Phys.* 90 (2018), p. 045003.

[13] M. Dalmonte, B. Vermersch, and P. Zoller, "Quantum Simulation and Spectroscopy of Entanglement Hamiltonians", *Nat. Phys.* (2018).

[14] H. Pichler et al., "Measurement Protocol for the Entanglement Spectrum of Cold Atoms", *Phys. Rev. X* 6.4 (2016), p. 041033.

[15] I. Peschel, M. Kaulke, and Ö. Legeza, "Density-matrix spectra for integrable models", *Ann. der Phys.* 8.2 (1999), pp. 153–164.

[16] I. Peschel and V. Eisler, "Reduced density matrices and entanglement entropy in free lattice models", *J. Phys. A: Math. Theor.* 42.50 (2009), p. 504003.

[17] H. Itoyama and H. B. Thacker, "Lattice Virasoro algebra and corner transfer matrices in the Baxter eight-vertex model", *Phys. Rev. Lett.* 58.14 (1987), p. 1395.

[18] V. Eisler and I. Peschel, "Analytical results for the entanglement Hamiltonian of a free-fermion chain", *J. Phys. A: Math. Theor.* 50.28 (2017), p. 284003.

[19] V. Eisler and I. Peschel, "Properties of the entanglement Hamiltonian for finite free-fermion chains", *Journal of Statistical Mechanics: Theory and Experiment* 2018.10 (2018), p. 104001.

[20] B. Nienhuis, M. Campostrini, and P. Calabrese, "Entanglement, combinatorics and finite-size effects in spin chains", *J. Stat. Mech.* 2009.02 (2009), P02063.

[21] J. J. Bisognano and E. H. Wichmann, "On the duality condition for a Hermitian scalar field", *J. Math. Phys.* 16.4 (1975), pp. 985–1007.

[22] J. J. Bisognano and E. H. Wichmann, "On the duality condition for quantum fields", *J. Math. Phys.* 17.3 (1976), pp. 303–321.

[23] J. Eisert, M. Cramer, and M. B. Plenio, "Colloquium : Area laws for the entanglement entropy", *Rev. Mod. Phys.* 82.1 (2010), pp. 277–306.

[24] C. Holzhey, F. Larsen, and F. Wilczek, "Geometric and renormalized entropy in conformal field theory", *Nuclear Physics B* 424.3 (1994), pp. 443–467.

[25] P. Calabrese and J. Cardy, "Entanglement entropy and quantum field theory", *Journal of Statistical Mechanics: Theory and Experiment* 2004.06 (2004), P06002.

[26] P. Calabrese and J. Cardy, "Entanglement entropy and conformal field theory", *J. Phys. A: Math. Theor.* 42.50 (2009), p. 504005.

[27] A. Kitaev and J. Preskill, "Topological Entanglement Entropy", *Phys. Rev. Lett.* 96 (2006), p. 110404.

[28] M. Levin and X.-G. Wen, "Detecting Topological Order in a Ground State Wave Function", *Phys. Rev. Lett.* 96, 110405 (2006), p. 110405.

[29] M. A. Metlitski and T. Grover, *Entanglement Entropy of Systems with Spontaneously Broken Continuous Symmetry*, 2011, arXiv: 1112.5166 [cond-mat.str-el].

[30] A. B. Kallin et al., "Anomalies in the entanglement properties of the square-lattice Heisenberg model", *Phys. Rev. B* 84 (2011), p. 165134.

[31] M. B. Hastings et al., "Measuring Renyi Entanglement Entropy in Quantum Monte Carlo Simulations", *Phys. Rev. Lett.* 104 (2010), p. 157201.

[32] S. Humeniuk and T. Roscilde, "Quantum Monte Carlo calculation of entanglement Rényi entropies for generic quantum systems", *Phys. Rev. B* 86.23 (2012).

[33] J. Helmes and S. Wessel, "Entanglement entropy scaling in the bilayer Heisenberg spin system", *Phys. Rev. B* 89 (2014), p. 245120.

[34] C. M. Herdman et al., "A path integral Monte Carlo method for Rényi entanglement entropies", *Phys. Rev. E* 90 (2014), p. 013308.

[35] P. Calabrese et al., "Parity Effects in the Scaling of Block Entanglement in Gapless Spin Chains", *Phys. Rev. Lett.* 104 (2010), p. 095701.

[36] M. Dalmonte, E. Ercolessi, and L. Taddia, "Estimating quasi-long-range order via Rényi entropies", *Phys. Rev. B* 84.8 (2011), p. 085110.

[37] J. C. Xavier and F. C. Alcaraz, "Finite-size corrections of the entanglement entropy of critical quantum chains", *Phys. Rev. B* 85 (2012), p. 024418.

[38] A. E. Feiguin", "Finite-temperature density matrix renormalization using an enlarged Hilbert space", *Physical Review B* 72.22 (2005).

[39] A. W. Sandvik and J. Kurkijärvi, "Quantum Monte Carlo simulation method for spin systems", *Phys. Rev. B* 43 (1991), pp. 5950–5961.

[40] R. Haag, *Local quantum physics: Fields, particles, algebras*, Springer Science, 2012.

[41] G. Wong et al., "Entanglement Temperature and Entanglement Entropy of Excited States", *JHEP* 12 (2013), p. 20.

[42] R. Arias et al., "Local temperatures and local terms in modular Hamiltonians", *Phys. Rev. D* 95 (2017), p. 065005.

[43] P. D. Hislop and R. Longo, "Modular structure of the local algebras associated with the free massless scalar field theory", *Commun. Math. Phys.* 84 (1982), pp. 71–85.

[44] R. Brunetti, D. Guido, and R. Longo, "Modular structure and duality in conformal quantum field theory", *Commun. Math. Phys.* 156.1 (1993), pp. 201–219.

[45] H. Casini, M. Huerta, and R. C. Myers, "Towards a derivation of holographic entanglement entropy", *Journal of High Energy Physics* 2011.5 (2011), p. 36.

[46] J. Cardy and E. Tonni, "Entanglement Hamiltonians in two-dimensional conformal field theory", *Journal of Statistical Mechanics: Theory and Experiment* 2016.12 (2016), p. 123103.

[47] H. Casini and M. Huerta, "Reduced density matrix and internal dynamics for multicomponent regions", *Class. Quant. Grav.* 26.18 (2009), p. 185005.

[48] G. Y. Cho, A. W. W. Ludwig, and S. Ryu, "Universal Entanglement Spectra of Gapped One-dimensional Field Theories", *Phys. Rev. B* 95 (2017), p. 115122.

[49] P. Calabrese, J. Cardy, and I. Peschel, "Corrections to scaling for block entanglement in massive spin chains", *J. Stat. Mech.* 2010.09 (2010), P09003.

[50] V. Alba, M. Haque, and A. M. Läuchli, "Boundary-Locality and Perturbative Structure of Entanglement Spectra in Gapped Systems", *Phys. Rev. Lett.* 108 (2012), p. 227201.

[51] D. J. Luitz, N. Laflorencie, and F. Alet, "Participation spectroscopy and entanglement Hamiltonian of quantum spin models", *J. Stat. Mech.* 2014.8 (2014), P08007.

[52] V. Alba, M. Haque, and A. M. Läuchli, "Entanglement spectrum of the Heisenberg XXZ chain near the ferromagnetic point", *J. Stat. Mech.* 2012.08 (2012), P08011.

[53] J. I. Cirac et al., "Entanglement spectrum and boundary theories with projected entangled-pair states", *Phys. Rev. B* 83.24 (2011), p. 245134.

[54] H. Li and F. D. M. Haldane, "Entanglement spectrum as a generalization of entanglement entropy: Identification of topological order in non-Abelian fractional quantum hall effect states", *Phys. Rev. Lett.* 101 (2008), p. 010504.

[55] N. Regnault, *Entanglement Spectroscopy and its Application to the Quantum Hall Effects*, 2015, arXiv: 1510.07670 [cond-mat.str-el].

[56] B. Swingle and T. Senthil, "Geometric proof of the equality between entanglement and edge spectra", *Phys. Rev. B* 86 (2012), p. 045117.

[57] A. Botero and B. Reznik, "Spatial structures and localization of vacuum entanglement in the linear harmonic chain", *Phys. Rev. A* 70.5 (2004), p. 052329.

[58] Y. Chen and G. Vidal, "Entanglement contour", *J. Stat. Mech.* 2014.10 (2014), P10011.

[59] I. Frérot and T. Roscilde, "Area law and its violation: A microscopic inspection into the structure of entanglement and fluctuations", *Phys. Rev. B* 92.11 (2015), p. 115129.

[60] A. Coser, C. De Nobili, and E. Tonni, "A contour for the entanglement entropies in harmonic lattices", *J. Phys. A: Math. Theor.* 50.31 (2017), p. 314001.

[61] E. Tonni, J. Rodríguez-Laguna, and G. Sierra, "Entanglement hamiltonian and entanglement contour in inhomogeneous 1D critical systems", *J. Stat. Mech.* 2018.4 (2018), p. 043105.

[62] P. Calabrese and A. Lefevre, "Entanglement spectrum in one-dimensional systems", *Phys. Rev. A* 78.3 (2008), p. 032329.

[63] F. Pollmann and J. E. Moore, "Entanglement spectra of critical and near-critical systems in one dimension", *New J. Phy.* 12.2 (2010), p. 025006.

[64] V. Alba, P. Calabrese, and E. Tonni, "Entanglement spectrum degeneracy and the Cardy formula in 1+1 dimensional conformal field theories", *J. Phys. A: Math. Theor.* 51.2 (2017), p. 024001.

[65] D. D. Blanco et al., "Relative entropy and holography", *JHEP* 2013.8 (2013), p. 60.

[66] N. Lashkari, "Relative Entropies in Conformal Field Theory", *Phys. Rev. Lett.* 113.5 (2014), p. 051602.

[67] V. Balasubramanian, J. J. Heckman, and A. Maloney, "Relative entropy and proximity of quantum field theories", *JHEP* 2015.5 (2015), p. 104.

[68] D. L. Jafferis et al., "Relative entropy equals bulk relative entropy", *JHEP* 2016.6 (2016), p. 4.

[69] P. Ruggiero and P. Calabrese, "Relative entanglement entropies in 1 + 1-dimensional conformal field theories", *JHEP* 2017.2 (2017), p. 39.

[70] A. Kosior, M. Lewenstein, and A. Celi, "Unruh effect for interacting particles with ultracold atoms", *SciPost Phys.* 5 (2018), p. 61.

[71] O. F. Syljuåsen and A. W. Sandvik, "Quantum Monte Carlo with directed loops", *Phys. Rev. E* 66 (2002), p. 046701.

[72] A. E. Feiguin and S. R. White, "Finite-temperature density matrix renormalization using an enlarged Hilbert space", *Phys. Rev. B* 72 (2005), 220401(R).

[73] J. Sólyom and P. Pfeuty, "Renormalization-group study of the Hamiltonian version of the Potts model", *Phys. Rev. B* 24 (1981), pp. 218–229.

[74] G. Mussardo, *Statistical Field Theory*, Oxford University Press, 2010.

[75] R. Kedem and B. M. McCoy, "Quasi-particles in the chiral Potts model", *Int. J. Mod. Phys. B* 8 (1994), p. 3601.

[76] V. S. Dotsenko, "Critical behaviour and associated conformal algebra of the Z3 Potts model", *Nucl. Phys. B* 235 (1984), pp. 54–74.

[77] P. Francesco, P. Mathieu, and D. Senechal, *Conformal field theory*, Springer, 1997.

[78] F. C. Alcaraz et al., "Surface exponents of the quantum XXZ, Ashkin-Teller and Potts models", *J. Phys. A: Math. Theor.* 20.18 (1987), pp. 6397–6409.

[79] N. M. B. V. E. Korepin and A. G. Izergin, *Quantum Inverse Scattering Method and Correlation Functions*, Cambridge University Press, 1993.

[80] N. Kitanine et al., "Large-distance asymptotic behaviour of multi-point correlation functions in massless quantum models", *J. Stat. Mech.* 2014.5 (2014), P05011.

[81] P. Kim et al., "Entanglement and corner Hamiltonian spectra of integrable open spin chains", *Phys. Rev. B* 94.19 (2016), p. 195110.

[82] G. B. Mbeng, V. Alba, and P. Calabrese, "Negativity spectrum in 1D gapped phases of matter", *Journal of Physics A: Mathematical and Theoretical* 50.19 (2017), p. 194001.

[83] H. Katsura, "Sine-square deformation of solvable spin chains and conformal field theories", *J. Phys. A: Math. Theor.* 45.11 (2012), p. 115003.

[84] F. Haldane, "Nonlinear field theory of large-spin Heisenberg antiferromagnets: semiclassically quantized solitons of the one-dimensional easy-axis Néel state", *Phys. Rev. Lett.* 50.15 (1983), p. 1153.

[85] W. Chen, K. Hida, and B. C. Sanctuary, "Ground State Phase Diagram of S=1 XXZ Chains with Uniaxial Single-Ion-Type Anisotropy", *Phys. Rev. B* 67 (2003), p. 104401.

[86] F. D. M. Haldane, "Spontaneous dimerization in the $S = \frac{1}{2}$ Heisenberg antiferromagnetic chain with competing interactions", *Phys. Rev. B* 25 (1982), p. 4925.

[87] K. Okamoto and K. Nomura, "Fluid-dimer critical point in $S = \frac{1}{2}$ antiferromagnetic Heisenberg chain with next nearest neighbor interactions", *Phys. Lett. A* 169 (1992), pp. 433–437.

[88] C. K. Majumdar and D. K. Ghosh, "On Next-Nearest-Neighbor Interaction in Linear Chain", *J. Math. Phys.* 10 (1969), p. 1388.

[89] S. R. White and I. Affleck, "Dimerization and incommensurate spiral spin correlations in the zigzag spin chain: Analogies to the Kondo lattice", *Phys. Rev. B* 54 (1996), p. 9862.

[90] A. W. Sandvik, "Finite-size scaling of the ground-state parameters of the two-dimensional Heisenberg model", *Phys. Rev. B* 56.18 (1997), p. 11678.

[91] A. W. Sandvik and C. J. Hamer, "Ground-state parameters, finite-size scaling, and low-temperature properties of the two-dimensional $S = \frac{1}{2}$ XY model", *Phys. Rev. B* 60 (1999), pp. 6588–6593.

[92] B. B. Beard et al., "Square-Lattice Heisenberg Antiferromagnet at Very Large Correlation Lengths", *Phys. Rev. Lett.* 80 (1998), pp. 1742–1745.

[93] C.-M. Chung et al., "Entanglement Spectroscopy using Quantum Monte Carlo", *Phys. Rev. B* 89 (2014), p. 195147.

[94] F. Parisen Toldin and F. F. Assaad, "Entanglement Hamiltonian of Interacting Fermionic Models", *Phys. Rev. Lett.* 121 (2018), p. 200602.

[95] W. Zhu, Z. Huang, and Y.-C. He, "Reconstructing entanglement Hamiltonian via entanglement eigenstates", *Phys. Rev. B* 99 (2019), p. 235109.

[96] J. Rodríguez-Laguna et al., "Synthetic Unruh effect in cold atoms", *Phys. Rev. A* 95.1 (2017), p. 013627.

[97] P. V. Buividovich and M. I. Polikarpov, "Numerical study of entanglement entropy in SU(2) lattice gauge theory", *Nucl. Phys. B* 802 (2008), p. 458.

[98] H. Casini, M. Huerta, and J. A. Rosabal, "Remarks on entanglement entropy for gauge fields", *Phys. Rev. D* 89 (2014), p. 085012.

[99] F. Wang and D. P. Landau, "Efficient, Multiple-Range Random Walk Algorithm to Calculate the Density of States", *Phys. Rev. Lett.* 86 (2001), pp. 2050–2053.

[100] M. A. Metlitski, C. A. Fuertes, and S. Sachdev, "Entanglement entropy in the $O(N)$ model", *Phys. Rev. B* 80 (2009), p. 115122.

[101] M. Troyer, S. Wessel, and F. Alet, "Flat Histogram Methods for Quantum Systems: Algorithms to Overcome Tunneling Problems and Calculate the Free Energy", *Phys. Rev. Lett.* 90 (2003), p. 120201.

[102] S. Wessel et al., "Optimized broad-histogram ensembles for the simulation of quantum systems", *Journal of Statistical Mechanics: Theory and Experiment* 2007.12 (2007), P12005.

[103] S. Inglis and R. G. Melko, "Wang-Landau method for calculating Rényi entropies in finite-temperature quantum Monte Carlo simulations", *Phys. Rev. E* 87 (2013), p. 013306.

[104] R. E. Belardinelli, S. Manzi, and V. D. Pereyra, "Analysis of the convergence of the $1/t$ and Wang-Landau algorithms in the calculation of multidimensional integrals", *Phys. Rev. E* 78 (2008), p. 067701.

[105] B. Bauer et al., "The ALPS project release 2.0: open source software for strongly correlated systems", *Journal of Statistical Mechanics: Theory and Experiment* 2011.05 (2011), P05001.

[106] *A working code that generates the necessary input files to run with ALPS Wang Landau (qwl) [105] can be found in https://github.com/tiagomendessantos/BW-entanglement-Hamiltonian* ().

[107] N. Laflorencie et al., "Boundary Effects in the Critical Scaling of Entanglement Entropy in 1D Systems", *Phys. Rev. Lett.* 96 (2006), p. 100603.

[108] H.-Q. Zhou et al., "Entanglement and boundary critical phenomena", *Phys. Rev. A* 74 (2006), p. 050305.

[109] M. Dalmonte, E. Ercolessi, and L. Taddia, "Estimating quasi-long-range order via Rényi entropies", *Phys. Rev. B* 84.8 (2011), p. 085110.

[110] D. J. Luitz et al., "Universal logarithmic corrections to entanglement entropies in two dimensions with spontaneously broken continuous symmetries", *Phys. Rev. B* 91 (2015), p. 155145.

[111] N. Laflorencie, D. J. Luitz, and F. Alet, "Spin-wave approach for entanglement entropies of the $J_1 - J_2$ Heisenberg antiferromagnet on the square lattice", *Phys. Rev. B* 92 (2015), p. 115126.

[112] A. Sen, H. Suwa, and A. W. Sandvik, "Velocity of excitations in ordered, disordered, and critical antiferromagnets", *Phys. Rev. B* 92 (2015), p. 195145.

[113] H. F. Song et al., "Entanglement entropy of the two-dimensional Heisenberg antiferromagnet", *Phys. Rev. B* 83 (2011), p. 224410.

[114] B. Kulchytskyy et al., "Detecting Goldstone modes with entanglement entropy", *Phys. Rev. B* 92 (2015), p. 115146.

[115] A. W. Sandvik and D. J. Scalapino, "Order-disorder transition in a two-layer quantum antiferromagnet", *Phys. Rev. Lett.* 72 (1994), pp. 2777–2780.

[116] L. Wang, K. S. D. Beach, and A. W. Sandvik, "High-precision finite-size scaling analysis of the quantum-critical point of $S = 1/2$ Heisenberg antiferromagnetic bilayers", *Phys. Rev. B* 73 (2006), p. 014431.

[117] S. Whitsitt, W. Witczak-Krempa, and S. Sachdev, "Entanglement entropy of large-N Wilson-Fisher conformal field theory", *Phys. Rev. B* 95 (2017), p. 045148.

[118] R. K. Kaul, R. G. Melko, and A. W. Sandvik, "Bridging lattice-scale physics and continuum field theory with quantum Monte Carlo simulations", *Annu. Rev. Con. Mat. Phys.* 4 (2013), p. 179.

[119] C. Moura Alves and D. Jaksch, "Multipartite Entanglement Detection in Bosons", *Phys. Rev. Lett.* 93 (2004), p. 110501.

[120] A. J. Daley et al., "Measuring Entanglement Growth in Quench Dynamics of Bosons in an Optical Lattice", *Phys. Rev. Lett.* 109 (2012), p. 020505.

[121] R. Islam et al., "Measuring entanglement entropy through the interference of quantum many-body twins", *Nature* 528 (2015), p. 77.

[122] T. Brydges et al., "Probing entanglement entropy via randomized measurements", *Science* 364 (2019), p. 260.

[123] A. Elben et al., "Rényi Entropies from Random Quenches in Atomic Hubbard and Spin Models", *Physical Review Letters* 120.5 (2018).

[124] B. Vermersch et al., "Unitary n -designs via random quenches in atomic Hubbard and spin models: Application to the measurement of Rényi entropies", *Physical Review A* 97.2 (2018).

[125] D. A. Abanin and E. Demler, "Measuring entanglement entropy of a generic many-body system with a quantum switch", *Phys. Rev. Lett.* 109 (2012), p. 020504.

[126] H. Pichler et al., "Measurement Protocol for the Entanglement Spectrum of Cold Atoms", *Phys. Rev. X* 6 (2016), p. 041033.

[127] I. Frerot, "A quantum statistical approach to quantum correlations in many-body systems", PhD thesis, Universite de Lyon, 2017.

[128] L. Amico et al., "Entanglement in many-body systems", *Rev. Mod. Phys.* 80.2 (2008), pp. 517–576.

[129] F. Holzhey C. Larsen and F. Wilczek, *Nucl. Phys. B* 424 (1994), pp. 443–467.

[130] G. Vidal et al., "Entanglement in Quantum Critical Phenomena", *Phys. Rev. Lett.* 90 (2003), p. 227902.

[131] J. Cardy and P. Calabrese, "Unusual corrections to scaling in entanglement entropy", *Journal of Statistical Mechanics: Theory and Experiment* 2010.04 (2010), P04023.

[132] J. C. Xavier and F. C. Alcaraz, "Rényi entropy and parity oscillations of anisotropic spin-s Heisenberg chains in a magnetic field", *Phys. Rev. B* 83 (2011), p. 214425.

[133] S. T. Flammia et al., "Topological Entanglement Rényi Entropy and Reduced Density Matrix Structure", *Phys. Rev. Lett.* 103 (2009), p. 261601.

[134] I. Peschel, "On the reduced density matrix for a chain of free electrons", *J. Stat. Mech.* 06 (2004), P06004.

[135] J. Calabrese P. Cardy and B. Doyon, *J. Phys. A: Math. Theor.* 42 (2009), p. 500301.

[136] P. Calabrese and F. H. L. Essler, "Universal corrections to scaling for block entanglement in spin-1/2XXchains", *Journal of Statistical Mechanics: Theory and Experiment* 2010.08 (2010), P08029.

[137] M. Dalmonte, E. Ercolessi, and L. Taddia, "Critical properties and Rényi entropies of the spin-$\frac{3}{2}$ XXZ chain", *Phys. Rev. B* 85 (2012), p. 165112.

[138] V. Eisler and I. Peschel, "Properties of the entanglement Hamiltonian for finite free-fermion chains", *Journal of Statistical Mechanics: Theory and Experiment* 2018.10 (2018), p. 104001.

[139] V. Eisler, E. Tonni, and I. Peschel, "On the continuum limit of the entanglement Hamiltonian", *Journal of Statistical Mechanics: Theory and Experiment* 2019.7 (2019), p. 073101.

[140] I. Peschel, M. Kaulke, and O. Legeza, "Density-matrix spectra for integrable models", English, *Annalen der Physik* 8.2 (1999), pp. 153–164.

[141] M. Dalmonte, B. Vermersch, and P. Zoller, "Quantum Simulation and Spectroscopy of Entanglement Hamiltonians", *Nat. Phys.* 14 (2018), p. 827.

[142] F. C. Alcaraz and M. J. Martins, "Conformal invariance and critical exponents of the Takhtajan-Babujian models", *Journal of Physics A: Mathematical and General* 21.23 (1988), pp. 4397–4413.

[143] C. Itoi and M.-H. Kato, "Extended massless phase and the Haldane phase in a spin-1 isotropic antiferromagnetic chain", *Phys. Rev. B* 55 (1997), pp. 8295–8303.

[144] H. W. J. Blöte, J. L. Cardy, and M. P. Nightingale, "Conformal invariance, the central charge, and universal finite-size amplitudes at criticality", *Phys. Rev. Lett.* 56 (1986), pp. 742–745.

[145] I. Affleck, "Universal term in the free energy at a critical point and the conformal anomaly", *Phys. Rev. Lett.* 56 (1986), pp. 746–748.

[146] A. W. Ludwig and J. L. Cardy, "Perturbative evaluation of the conformal anomaly at new critical points with applications to random systems", *Nuclear Physics B* 285 (1987), pp. 687–718.

[147] P. Calabrese and J. Cardy, "Quantum quenches in extended systems", *Journal of Statistical Mechanics: Theory and Experiment* 2007.06 (2007), P06008–P06008.

Chapter 2

Parent Hamiltonians for low-entanglement quantum states

This chapter is based on unpublished work and on the following publication:

[1] X. Turkeshi, T. Mendes-Santos, G. Giudici, M. Dalmonte
Entanglement-Guided Search for Parent Hamiltonians
Physical Review Letters 122, 150606 (2019)

Variational wave functions have played a pivotal role in boosting the understanding of strongly correlated systems [2, 3, 4, 5, 6, 7]. The success of ansatz wave functions has naturally motivated the search for the corresponding parent Hamiltonians, with considerable success in several contexts, including the study of topological matter [8, 9, 10], one-dimensional systems [11, 12], and tensor networks [13, 14]. Recent experimental progresses in quantum engineering of synthetic systems [15, 16, 17, 18, 19] have opened an additional perspective in the search for parent Hamiltonians: thanks to the high degree of interactions tunability, these experiments provide a clean route toward the realization of tailored quantum dynamics. This has stimulated a renewed theoretical interest as of late. In Refs. [20, 21, 22, 23, 24, 25, 26], a series of approaches has been proposed for determining, given an initial quantum state $|\Psi\rangle$, a Hamiltonian operator H which has $|\Psi\rangle$ has an eigenvector, very remarkably, even utilizing limited information such as low-order correlation functions [22, 23, 24, 26]. However, as discussed in depth in Ref. [23, 27], it remains unclear if a generic procedure exists to determine an (approximate) Hamiltonian operator that has $|\Psi\rangle$ as its ground state, mostly due to the fact that controlling the dimension of the target Hamiltonian space is not possible under generic assumptions. A crucial obstacle in devising a generic algorithm to achieve this goal is the non-uniqueness of the solution, even upon imposing translation invariance and locality requirements on the target parent Hamiltonian. In this chapter we will take two completely different, and complementary, approaches to tackle this problem.

In Sec. 2.1, we will assume a parametrization for the candidate ground state, guided by field theoretical constraints between the parent Hamiltonian itself and the entanglement structure of $|\Psi\rangle$. The basic idea behind our strategy is to connect the reduced density matrix ρ of the half-partition of $|\Psi\rangle$ to an ansatz given by the Bisognano-Wichmann theorem [28, 29, 30, 31] adapted to the lattice [32]. The method provides an immediate connection between the input vector $|\Psi\rangle$ and its translational invariant parent Hamiltonian H through ρ. The entire procedure can be carried out using different numerical methods that rely on evaluating expectation values at finite (entanglement) temperature, including finite-temperature density-matrix-renormalization-group

(TDMRG) [33, 34] and quantum Monte Carlo simulations [35], as we explicitly demonstrate. We successfully apply our method to reconstruct approximate parent Hamiltonians for a broad range of wave functions encompassing physical phenomena as diverse as quantum criticality with dynamical critical exponent $z = 1$, topological matter, and quantum antiferromagnets, to name a few.

In Sec. 2.2, we will investigate parent Hamiltonians of tensor network states. In this context, a robust theory exists which provides rigorous bounds on the locality of the parent Hamiltonian, together with sufficient conditions for the uniqueness of their ground state [36, 37, 38]. The bond dimension of the state yields an upper bound on the locality of the Hamiltonian. In one-dimension this implies that for a matrix product state with bond dimension D, defined on a Hilbert space with local dimension d, the range of the parent Hamiltonian is $k \sim \log D^2 / \log d$. In two-dimensions the situation is more complicated, since for a fixed number of sites, various patches can be chosen to construct the parent Hamiltonian, depending on the geometry of the lattice. As a matter of fact, even for tensor networks with small bond dimension ($D \leq 3$), a straightforward construction results in Hamiltonians that are not as local their one-dimensional counterparts. However, a given tensor network state possesses a whole family of parent Hamiltonians, and an optimization over this (non-linear) space of operators can be performed to obtain the most local parent Hamiltonian. After developing a simple method to achieve this goal, we will focus on the SU(2)-invariant resonating valence bond (RVB) state on the kagome lattice, which can be written as a tensor network with bond dimension $D = 3$ [14]. The physical relevance of this state stems from the symmetries it shares with real materials. Furthermore, it constitutes one of the simplest examples of topologically ordered state [14]. We will show that the freedom in the construction of the parent Hamiltonian can be exploited to reduce its range. We demonstrate that the optimization does not spoil the topological properties of the Hamiltonian, and that the RVB state is the exact ground state of the optimized Hamiltonian.

2.1 Entanglement guided search for parent Hamiltonians

The key element of our approach is to combine an ansatz for the reduced density matrix of the candidate ground state to a minimization procedure based on relative entropy [39]: this guarantees that the target space of potential parent Hamiltonians is convex (even if no statement can be made a priori on the convergence rate to the right solution), and its volume is system size independent.

In Sec. 2.1.1 we introduce the theoretical background required to motivate our ansatz, and we describe in great detail our approach. In Sec. 2.1.2 we illustrate the effectiveness of the procedure and discuss its scaling to the right solution by considering three examples, which encompass qualitatively different phenomena: conformal phases in the one-dimensional (1D) XXZ chain [4]; the Haldane chain as an epitome of a symmetry-protected topological phase [40]; and eventually, an example of strongly coupled quantum critical point in the two-dimensional (2D) bilayer Heisenberg antiferromagnet [41, 42, 43]. In Sec. 2.1.3 we discuss the stability of our method when the target Hamiltonian space is enlarged, and one the candidate ground state is an excited state of some operator in the target space. Finally, in Sec. 2.1.4 we draw our conclusions.

2.1.1 Parent Hamiltonian search algorithm

The parent Hamiltonian search we propose is guided by a set of field theory results, which go under the name of Bisognano-Wichmann (BW) theorem [28, 29, 30, 31], which we briefly review. While it is well known that for local Hamiltonians the ground state contains (potentially complete) information about the Hamiltonian spectrum, this theorem allows to quantitatively establish this correspondence at the field theoretic level.

Given a pure state $|\Psi\rangle$ and a bipartition $A \cup B$, one can re-express the reduced density matrix as:

$$\rho = \mathrm{Tr}_B |\Psi\rangle\langle\Psi| = \frac{e^{-H_A}}{Z_A}, \quad Z_A = \mathrm{Tr}_A e^{-H_A}. \tag{2.1}$$

The operator H_A is called entanglement (or modular) Hamiltonian [44, 31] and, its spectrum is known as entanglement spectrum [45]. The BW theorem states that if $|\Psi\rangle$ is the vacuum state of a relativistic quantum field theory defined by an Hamiltonian density $h(x)$, and the bipartition is over half-space (e.g. in $D+1$ dimensions $A = \{\vec{x} | x_1 > 0\}$), then:

$$H_A = \beta \int_{x_1>0} x_1 h(\vec{x}) d^D x \tag{2.2}$$

The parameter β is a prefactor related to the sound velocity of the theory; it is referred to as the inverse entanglement temperature. Recently, based both on exact analytical results and growing numerical evidence [46, 47, 48, 49, 50, 32, 51, 52, 53], it has been argued that these results are applicable to obtain very accurate (if not exact) approximations of entanglement Hamiltonians of lattice models, as long as their low-energy physics is effectively described by a relativistic quantum field theory. We stress that in lattice models, the field-theory limit is intended as the regime where the correlation length is much larger than the lattice spacing. While not generic, this common structure encompasses a plethora of phenomena in the field of strong correlations, including quantum critical points and phases with emergent relativistic description. As a case sample, in 1D, the theorem reads $H_A = \beta \sum_{n>0} n\, h_n$, which is the discretized version of the field theory result, where h_n are the local (i.e., defined on sites and on bonds) terms of the lattice Hamiltonian. The result is trivially extended to D>1.

Equipped with the direct relation between $|\Psi\rangle$ and the system Hamiltonian provided by the discretized version of Eq. (2.2) [32], we formulate now our search algorithm.

procedure RECONSTRUCTION($\Psi, \{O_{\alpha,r}\}$)
  Initialization: $\vec{w}^{(0)}$, error $= 10$, $\eta = 4$
  Compute: $\sum_r r\langle O_{\alpha,r}\rangle_\Psi$
  while error $<$ threshold **do**
    Compute: $\sum_r r\langle O_{\alpha,r}\rangle_{\vec{w}^{(n)}}$
    Compute: $\partial_\alpha S$
    Compute: $\vec{w}^{(n+1)} = \vec{w}^{(n)} - \eta\nabla S$
    if $||\vec{w}^{(n+1)} - \vec{w}^{(n)}||$ >error **then**
      $\eta = \eta/2$
      error $= ||\vec{w}^{(n+1)} - \vec{w}^{(n)}||$
  return $H_{\rm rec} = \sum_{\alpha,r} w_\alpha^{(N)} O_{\alpha,r}$

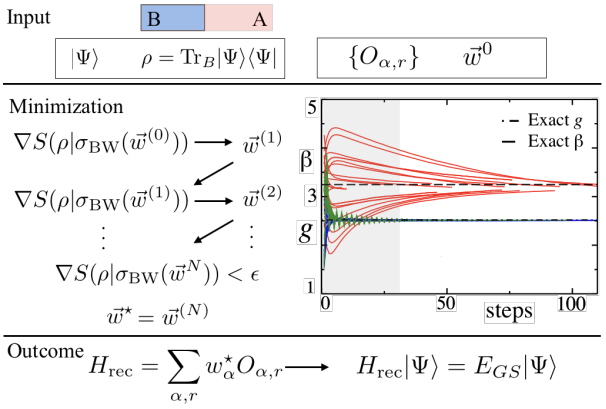

Figure 2.1: **Left.** Algorithm for the parent Hamiltonian search. **Right.** Schematics of the parent Hamiltonian search. The starting point is the wave-function of interest $|\Psi\rangle$ (with a half-partition reduced density matrix ρ), a set of local operators $\{O_{\alpha,r}\}$, and an initial guess for their coefficients w_α^0. The relative entropy S between ρ and an ansatz Bisognano-Wichmann reduced density matrix $\sigma(\{O_{\alpha,r}, w_\alpha^n\})$ is evaluated at each step of the minimization procedure. The procedure is then stopped once the desired accuracy (ϵ) is reached: the final outcome are the couplings w_α^* of the parent Hamiltonian, and the entanglement inverse temperature β. The inset shows a sample of our results for the bilayer Heisenberg model at the critical point (see text). Different lines correspond to minimization from different initial sets $\vec{w}_0$. Convergence within 0.1% of the correct value of g (interlayer coupling; blue and green) and β (red lines) is typically reached after 30 (grey area) and $\simeq$200 steps, respectively.

1) Input: Given a lattice input state $|\Psi\rangle$ and a local basis of hermitian operators $\{O_{\alpha,r}\}$ labeled by a lattice index r and an internal index α, our goal is to find the coefficients $\vec{w}^\star$ of the linear combination:

$$H(\vec{w}) = \sum_\alpha w_{\alpha,r} O_{\alpha,r}, \tag{2.3}$$

such that the input state is its ground state. We call this local operator the reconstructed Hamiltonian $H_{\rm rec} = H(\vec{w}^\star)$. Here, we focus on translationally invariant Hamiltonians, and thus set $w_{\alpha,r} = w_\alpha$.

2) Minimization: In order to construct $H_{\rm rec}$, we propose an optimization procedure based on minimizing the relative entropy [54, 55] utilizing as trial reduced density matrix the BW one. The relative entropy between two density matrices ρ and σ is defined as [39, 56]:

$$S(\rho|\sigma) = \mathrm{Tr}(\rho\log\rho) - \mathrm{Tr}(\rho\log\sigma). \tag{2.4}$$

For our purpose here, this function has two key features: it is non-negative, i.e. $S(\rho|\sigma) \geq 0$, with the equality holding if $\rho = \sigma$; and it is joint-convex. This latter property ensures the uniqueness of a global minimum for the function $S(\rho|\sigma)$ with fixed ρ.

In the context of our problem, the left argument ρ encodes the input data, that is, $\rho = \mathrm{Tr}_B|\Psi\rangle\langle\Psi|$. The right argument σ is the reduced density matrix of the GS of $H(\vec{w})$, which returns the parent Hamiltonian at the end of the procedure. We thus express σ by using the Bisognano-Wichmann density matrix in eq. (2.1):

$$\sigma_{\rm BW}(\vec{w}) = \frac{e^{-H_{\rm BW}(\vec{w})}}{Z_A(\vec{w})}; \quad Z_A(\vec{w}) = \mathrm{Tr}_A e^{-H_{\rm BW}(\vec{w})}, \tag{2.5}$$

with H_A of the form:

$$H_{\rm BW}(\vec{w}) = \sum_{\alpha}\sum_{r>0} w_\alpha\, r\, O_{\alpha,r}. \tag{2.6}$$

Minimization is pursued by adaptive gradient descent (GD). For practical purposes, we use the notation $\partial_\alpha = \partial/\partial w_\alpha$ and:

$$\langle O\rangle_{\rm dat} \equiv {\rm Tr}(O\rho), \quad \langle O\rangle_{{\rm BW},\vec{w}} \equiv {\rm Tr}(O\sigma_{\rm BW}(\vec{w})). \tag{2.7}$$

Now, given a configuration of parameters $\vec{w}^{(n)}$, we compute the gradient of the relative entropy:

$$\begin{aligned}\partial_\alpha S(\rho_{\rm dat}|\sigma_{\rm BW}(\vec{w})) &= \partial_\alpha \left(\langle H(\vec{w})\rangle_{\rm dat} - \log Z_A(\vec{w})\right)|_{\vec{w}^{(n)}} \\ &= \langle \tilde{h}_\alpha\rangle_{\rm dat} - \langle \tilde{h}_\alpha\rangle_{{\rm BW},\vec{w}^{(n)}}.\end{aligned} \tag{2.8}$$

To compute the relative entropy gradient at some value $\vec{w}^{(n)}$ we thus just need the averages of the correlation functions correspodent to the terms allowed in the EH, evaluated over the ansatz state and over the BW density matrix evaluated with $\vec{w}^{(n)}$ of the operators $O_{\alpha,r}$. Thus, rewriting the previous equation in a more explicit form, we need to compute:

$$\partial_\alpha S(\rho|\sigma_{\rm BW}(\vec{w})) = \sum_{r>0} r(\langle O_{\alpha,r}\rangle_{\rm dat} - \langle O_{\alpha,r}\rangle_{{\rm BW},\vec{w}^{(n)}}). \tag{2.9}$$

3) Outcome: Under the assumptions above, the parent Hamiltonian is given by the set of parameters that uniquely minimize the relative entropy; that is, the coefficients:

$$\vec{w}^\star = \arg\min_{\vec{w}} S(\rho|\sigma_{\rm BW}(\vec{w})). \tag{2.10}$$

in combination with Eq. (2.3), determine the parent Hamiltonian. Thus, if minimization is achieved and the relative entropy at the minimum is close to zero, we claim that the input state is the ground state of the reconstructed Hamiltonian:

$$H_{\rm rec} = \sum_\alpha w^\star_{\alpha,r} O_{\alpha,r}, \tag{2.11}$$

$$H_{\rm rec}\Psi = E_{GS}\Psi. \tag{2.12}$$

The minimization procedure of $S(\rho|\sigma)$ can be carried out in several ways: below, we utilize adaptive gradient descent methods. Given an initial configuration, we carry out the minimization of $S(\rho|\sigma)$ by evaluating the *error*:

$$\epsilon = ||\eta\nabla S(\rho|\sigma_{\rm BW}(\vec{w}))||, \tag{2.13}$$

where η is a control parameter, until convergence to the given accuracy in the coupling parameters of H_{BW} is reached. For the sake of convenience, we consider here a 10^{-3} error threshold, that already returns a very accurate parent Hamiltonian. This passage does not require access to the wave function, but is rather carried out evaluating the expectation value of local correlators at finite (entanglement) temperature: as such, it is immediately amenable to a series of methods, including Monte Carlo - as we show below[1]. Since the minimization space has a

[1]We note that this minimization can be in principle carried out using GS methods as well; however, this does not give access to the relative entropy, rendering a final check more challenging, as it requires the full knowledge

constant dimension with system size, and since it is convex, we expect a mild - if any - scaling with system size of the time to solution. In Fig. 2.1 we report the pseudocode (left) and the schematics of the algorithm (right), together with a sample of our results for the two-dimensional bilayer Heisenberg antiferromagnet.

Before proceeding, it is worth pointing out that the method is not immediately suited to simple wave functions, where correlations vary at the lattice spacing level (like a product state). This is due to the field theoretical input we employ, which might fail in these regimes. Another potential limitation is that it is not possible to capture parent Hamiltonians with quadratic spectra, such as ferromagnets. Failure is straightforward to diagnose - the relative entropy minimum will attain a large value, indicating the result is not correct.

2.1.2 Benchmark of the method

Below, we purposely benchmark our strategy focusing purposely on non-trivial wave functions which lack simple tensor network representations. As discussed above, this choice is motivated by the fact that tensor-network wave-function posses typically very small correlation length. Thus, they do not satisfy the assumption of our ansatz for the ground state reduce density matrix.

Parent Hamiltonian of conformal phases. We consider the ground states of the XXZ spin-1/2 chain, defined as:

$$H = \sum_{\langle i,j \rangle} \left(S_i^x S_j^x + S_i^y S_j^y + \Delta S_i^z S_j^z \right), \tag{2.14}$$

where $\langle \cdot \rangle$ is the restriction to nearest neighbor terms, and S_i^α are spin-1/2 operators at the site i. The model hosts a gapless phase for $-1 < \Delta \leq 1$, described at low-energies by a $c = 1$ CFT (Luttinger liquid); in addition, it displays a ferromagnetic (antiferromagnetic) phase for $\Delta \leq -1 (\Delta > 1)$. Both the gapless and the antiferromagnetic phase (in the vicinity of $\Delta = 1$) shall be captured by our approach.

To test our method, we choose as ansatz wavefunctions the ground state of Eq. (2.14) for various values of Δ, and as the basis of operators $\{O_{\alpha,r}\} = \{S_r^a S_{r+1}^b, S_r^a\}$ with $a, b = x, y, z$ and r the lattice-site label. This implies that, given a half-partition of the system $A \cup B$, we compute the reduced density matrix over A of the candidate ground state Ψ (in our examples the ground state of eq. (2.14)) and we fit this with a model entanglement Hamiltonian (EH) of the BW type:

$$H_{\mathrm{BW}} = \sum_{\alpha, r>0} w_\alpha r O_{\alpha,r} \tag{2.15}$$

$$= \sum_{a,b=x,y,z} \sum_{r>0} r \left(w_{ab} S_{a,r} S_{b,r+1} + w_a S_{a,r} \right). \tag{2.16}$$

As a first illustration, we show in Fig. 2.2 (right) the relative entropy landscape between the BW EH correspondent to the GS of the Heisenberg model, with free parameters Δ and β. The plot shows a unique minimum at the expected value $\Delta = 1$ and $\beta = 4$ [53]. We define the convergence parameters as $w_\alpha = \beta J_\alpha$, and consider open boundary conditions (as in the examples below).

We employed exact diagonalization (ED) for small system sizes (up to $L = 12$) when considering all the 12 coefficients $\{w_{ab}, w_a\}$ in our model. While in the case in which we utilized the $U(1)$-symmetric version of the algorithm ($w_{xx} = w_{yy} \neq w_{zz} \neq 0$ and the other couplings set to

of the wave-function.

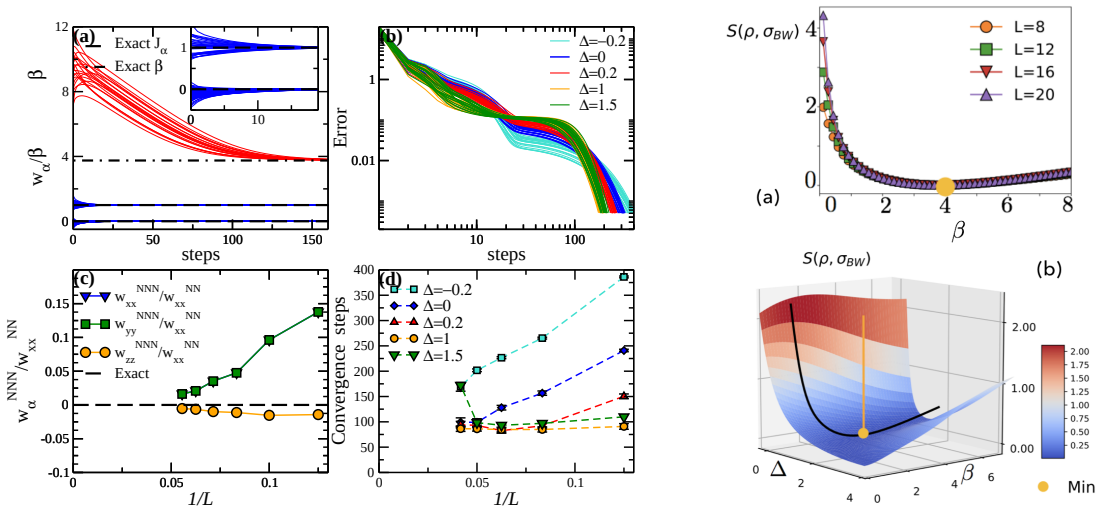

Figure 2.2: **Left.** Parent Hamiltonian search for the XXZ chain. (a) Ratios $J_\alpha = w_\alpha/\beta$ (blue lines) and β (red lines) as functions of the minimization steps. We compare with the exact coupling and entaglement temperature. Here, $L = 12$ and $\Delta = 1$. We consider the full basis of operators $\{w_\alpha\}$ (see text). (b) Error, Eq. (2.13), as function of the minimization steps; the value Δ label the different input state used, ground state of the respective XXZ Hamiltonian. (c) System size scaling of the ratios of the average converged w_α^{NNN} and $w_{xx} = w_{xx}^{\mathrm{NN}}$ at $\Delta = 0.5$ (see text). (d) Average convergence steps over initial realizations of the coupling as a function of system size. The convergence rate typically improves with system size. **Right.** Landscape of the relative entropy landscape between ρ (obtained from the ground state at $\Delta = 1$) and $\sigma_{BW}(\Delta, \beta)$ for $L = 12$: the minimum is at $(1, 4)$. Panel (a) shows a planar cut ($\Delta = 1$) for different system sizes.

zero) we were able to perform computations up to $L = 24$ with ED and finite temperature density matrix renormalization group (TDMRG). In the former case we can exploit magnetization conservation by computing the full eigensystem of σ_{BW} upon restriction to all symmetry sectors. In the latter case we can still exploit $U(1)$ symmetry by preparing the purified state (system + ancilla) in an eigenstate of the total magnetization (see [34] for details). The number of states kept during the imaginary-time-evolution, which provides the desired thermal state, was chosen to increase during the evolution, starting from 20 up to 100 states per block.
We considered uniform random instances of $\vec{w}^{(0)}$ over the interval $I = [2, 6]$ (in order to keep computational costs cheap, the neat results are unchanged by this choice) and averaged over a hundred of initial conditions; we kept track of these by fixing the seeds of the pseudo-random number generators implemented.

Fig. 2.2 (left) shows the outcomes of the algorithm using ED up to a total system size $L = 12$ (panel (a,b)), ED with symmetry restrictions up to $L = 18$ (panel (c)), and TDMRG up to $L = 24$ (panel (d)). In panel (a), we plot the w_α as a function of the steps for different initial guesses $\vec{w}_0$: the symmetries of the systems are rapidly identified (unwanted terms vanishing), and the couplings of the parent Hamiltonian converge to the correct ratios after few steps; the entanglement temperature converges slower. The relative entropy indicating vicinity to the exact solution (Fig. 2.2 (b)) displays few plateaus, and eventually converges (exponentially fast) to the correct solution. In Fig. 2.2(c), we plot the results when we include the next nearest neighbor terms (couplings) $S_r^a S_{r+2}^a$ (w_{aa}^{NNN}) with $a = x, y, z$ in the symmetry sector of the local basis; we considered the ansatz ground state with $\Delta = 0.5$. The coefficients of these additional terms are scaling to zero; this is expected because BW ansatz works better at larger correlation length (see Sec. 2.1.3 for a detailed discussion). We remark that scaling with system size is not trivial for critical systems, due to the structure of reduced density matrices [57, 58] (right). Finally, in

Fig. 2.2(d) we plot the number of convergence steps needed to reach $\epsilon = 10^{-3}$ threshold using only two free parameters (i.e. w_{zz} and $w_{xx} = w_{yy}$) for simplicity: remarkably, the procedure becomes simpler when increasing system size. The case $\Delta = 1.5$ shows an abrupt increase at $L = 24$: this is an artifact of the minimization and it is easily removed. These results are fully consistent with the relative entropy landscape depicted in Fig. 2.2 (right).

Parent Hamiltonian of a symmetry-protected topological phase. As a model with non-trivial topological behavior, we discuss here the Haldane chain [40, 4], described by the Hamiltonian Eq. (2.14) with spin-1 operators. For $0 < \Delta \lesssim 1.2$, the model supports a symmetry protected topological phase [40, 59]. We used ED with adaptive gradient descent to determine the parent Hamiltonian for different values of Δ. In this case, we have chosen a subset of the full basis of local hermitian operators up to two body terms $\{O_{\alpha,r}\} = \{S^a_r S^b_{r+1}, S^a_r\}$ (i.e., we do not include spin-1 local operators as $(S^\alpha_r)^2$). The results of the minimization procedure are illustrated in Fig. 2.3 (left): in full analogy with the s 1/2 case, the couplings quickly converge to the correct results, while β convergence is slower. In all instances we studied, the relative entropy converged faster to 0 in the gapped, topological regime (Fig. 2.3 (left) (b)).

Parent Hamiltonian of a two-dimensional quantum critical point. In our third example, we consider 2D antiferromagnets described by Eq. (2.14). In order to check the feasibility of the approach in 2D, we investigated convergence to the correct entanglement temperature in the Heisenberg model (without changing the Hamiltonian parameters). We put the system on a cylinder and we choose the partition depicted in Fig. 2.3 (right) (a).

To do so, first, we use the quantum Monte Carlo (QMC) method Stochastic Series expansion to obtain $\sum_r r\langle O_{\alpha,r}\rangle_{\Psi_0}$; where $\langle O_{\alpha,r}\rangle$ is obtained for temperatures low enough to guarantee that the system already converged to the ground state (e.g., $\beta = 4L$). Second, during the gradient descent minimization part, we consider the BW ansatz for the EH of the ground state half-bipartition

$$H_{\rm BW} = \beta \sum_{\vec{i}} i_x S_{(i_x,i_y)} S_{(i_x+\delta,i_y)} + \beta \sum_{\vec{i}} (i_x - 1/2)\, S_{(i_x,i_y)} S_{(i_x,i_y+\delta)}. \tag{2.17}$$

where $i_x > 0$, and β_c is the entanglement inverse temperature (see Fig. 2.3 (right) (b)). Convergence was achieved typically after a few tens steps. We plot in Fig. 2.4 (left) (a) the error ϵ at fixed β: this correctly features a minimum at the right value $\beta = 2\pi/v = 3.792$ [60], weakly dependent on system size, as expected [53]. The landscape is sharper at larger L, leading to a faster convergence of the algorithm.

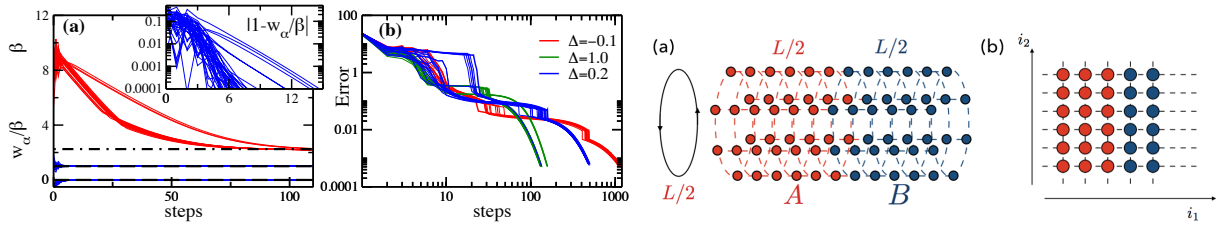

Figure 2.3: **Left.** Parent Hamiltonian search for the Haldane chain with $L = 8$. (a) $J_\alpha = w_\alpha/\beta$ and β as functions of the minimization steps; the initial state is at $\Delta = 1$. The inset shows a magnification up to 14 steps of $|1 - w_\alpha/\beta|$: convergence to the correct solution at 10^{-4} level is typically achieved after 6 steps. (b) Error as function of minimization steps for different values of Δ. **Right.** (a) Partition used for the $2D$ model: $L/2 \times L/2$. (b) Direction i_1 is perpendicular to the cut (and starts from the open boundary); i_2 is parallel to the cut and wraps around the cilinder.

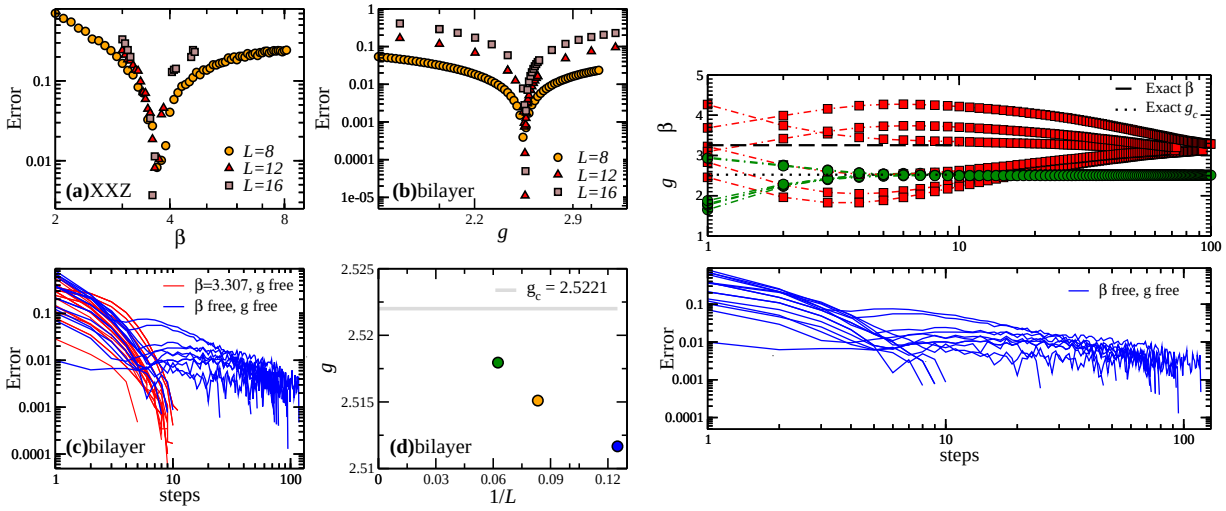

Figure 2.4: **Left.** (a-b) Error between the exact and the BW reduced density matrix, Eq. (2.13), as a function of temperature for the 2D Heisenberg model (a), and as a function of g for the bilayer Heisenberg model at $\beta = 3.3$ (b). (c)Error as a function of the minimization step for $L = 8$; the error decreases quickly, without any plateau as in the 1D case. (d) Converged inter-to-intra layer coupling versus linear system size. **Right.** (Top) Convergence of the parameters at $L = 8$ in the bilayer Heisenberg model. We see that the coupling constant converges faster that the entanglement temperature. (Bottom) Error trajectories as a function of steps.

Finally, we consider the bilayer Heisenberg model (HM)

$$H_{\text{bilayer}} = \sum_{l=1,2} \sum_{\langle \vec{i},\vec{j} \rangle} S_{\vec{i},l} S_{\vec{j},l} + g \sum_{\vec{i}} S_{\vec{i},1} S_{\vec{i},2}, \tag{2.18}$$

where $\vec{i}$ and $\vec{j}$ label the sites within the planes (square lattice), and l are the label of the planes. For $g = 0$, the ground state of the two uncoupled planes has antiferromagnetic (AFM) long-range order; while an AFM-Singlet quantum phase transition, whose low-energy physics is described by a non-linear sigma model, takes place at $g = g_c$ [42]. We then tested our approach to reconstruct the correct parent Hamiltonian for the bilayer Heisenberg model, characterized by the ratio of inter-to-intra layer coupling g [42, 43]. In particular, we focused on its critical point, which separates a disordered and an antiferromagnetic phase, and is located at $g_c = 2.52210(5)$ [43, 61]. At this point, the system dynamics is described by a σ-model [41, 43, 35]. Before applying our procedure, we performed a check on the relative entropy manifold as a function of the coupling g at fixed β (Fig. 2.4 (left) (b)): the minimum of the error signals the correct coupling.

We then adopt two different protocols: in the first one, we fixed the entanglement temperature to the expected one ($\beta_c = 3.307$), and let the coupling g free (red lines in Fig. 2.4 (left) (c)), while in the second, we let both g and β vary (blue lines). In both cases, the error ϵ quickly diminishes (slower in the second case due to more parameters to be optimized, see Fig. 2.4 (right) for the latter case). Most importantly, at the end of the minimization, the value of g is extremely close to the correct one, which seems to be correctly reproduced in the thermodynamic limit (Fig. 2.4 (left) (d)). Given the complexity of the system wave function, this serves as a strong benchmark for our strategy: reconstructing the parent Hamiltonian, in this case, takes only a few tens of steps, each one corresponding to a MC simulation of the BW entanglement Hamiltonian.

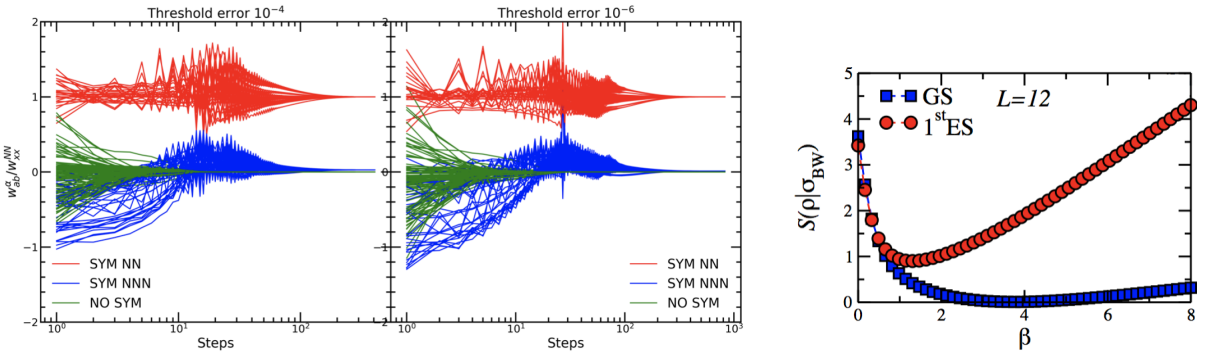

Figure 2.5: **Left.** Trajectories for various initial couplings when the target state is the ground state of the XXZ chain at $\Delta = 1.0$ and $L = 16$. Here *SYM NN* and *SYM NNN* refer to the nearest neighbor and next-nearest neighbor couplings associated to symmetry-preserving couplings, respectively; while *NO SYM* refers to the non-symmetric sectors. In both cases, one can clearly identify two regimes: first, all couplings which are not U(1) invariant are reduced to zero. Second, the NNN couplings vanish, typically after $\propto 10^2$ steps. **Right.** Relative entropy landscape for the XXZ chain at $\Delta = 1$ for the ground state and the first excited state. The minimum value of the relative entropy between the first excited state and the BW ansatz, as a function of the entanglement temperature β, is much larger than the ground state minimum.

2.1.3 Stability of the method

So far we analyzed test cases in which the parent Hamiltonian of the input state was known a priori to be extremely local (only nearest-neighbor interactions). This leads to a choice of operators O_α that dramatically reduces the number of parameters to be optimized. Here, we discuss in more details the performance of our method when longer range operator are included in the basis. For simplicity, we focus on the spin-1/2 XXZ chain, employing as a target state the ground state of the nearest-neighbor Hamiltonian, and we consider up to next nearest hopping terms:

$$H_{\mathrm{BW}} = \sum_{\alpha, r>0} w_\alpha r O_{\alpha,r} \sum_{a,b=x,y,z} \sum_{r>0} r\left(w_{ab}^{\mathrm{NN}} S_{a,r} S_{b,r+1} + w_{ab}^{\mathrm{NNN}} S_{a,r} S_{b,r+2} + w_a S_{a,r}\right). \tag{2.19}$$

We run simulations with ED up to $L = 16$ fixing the error threshold for the algorithm at 10^{-4} and 10^{-6}. The results in Fig. 2.5 (left) show that non-symmetric terms are again get rid of quickly, while it takes longer to converge for all the $U(1)$-symmetry preserving terms. The next-nearest neighbor coefficients w^{NNN} reach a very small, non-vanishing value of order 10^{-2}. As it is suggested from Fig. 2.2 (left) (c), this is a finite-size effect.

We now briefly discuss how the algorithm copes with excited states. Fig. 2.5 (right) shows the landscape of the relative entropy between the BW ansatz for the ground state of the isotropic XXZ chain and the first excited state, as a function of β. The first excited state attains minimum relative entropy for a value of β different from the ground state, and the height of the minimum is of order one. This does not imply that the algorithm would fail in finding a parent Hamiltonian for excited states, it simply implies that an operator basis containing only the (ground state-)parent Hamiltonian density would produce a negative answer from our procedure, apparent by the not-small value of the minimum relative entropy. This is in sharp contrast with the result produced by other methods, based on the minimization of the variance of the input state (e.g. Ref. [23]). They would simply fail, finding the same Hamiltonian they would find with the ground state as an input state. Although not part of this work, it would be interesting to study the efficiency of the algorithm when fed with low energy excited states, upon including more

parameters in the optimization.

2.1.4 Conclusions

We proposed a method to guide the search of parent Hamiltonians utilizing insights on the entanglement structure of ground state wave functions based on the Bisognano-Wichmann theorem adapted to the lattice. We benchmarked the feasibility of our strategy utilizing several input wave functions, finding convergence to the correct solution in a number of steps that typically decreases with system size. As our results show, the strategy is suited to identify parent Hamiltonians in both massive and critical scenarios: the latter is particularly challenging, as in these cases, simple analytical intuition on the structure of the parent Hamiltonian is oftentimes not available due to the absence of a finite length scale. It will be interesting to extend the method to gauge theories, which play a pivotal role in the understanding of spin liquids [62, 10], and whose Hilbert space structure requires a more refined approach [63, 64].

2.2 Tensor network parent Hamiltonians: locality optimization

Tensor network (TN) states have proven to be the most simple representatives of a wide variety of quantum phases of matter. Although in one dimension matrix product states (MPS) are known to be powerful ansatze to approximate ground states of local Hamiltonians, in two dimensions the situation is more controversial. In the last decades, numerous numerical approaches based on projected entangled pair states (PEPS) have been developed [65, 66, 67, 68, 69, 70], aimed at probing their capability of capturing the essential physical properties of two-dimensional many-body systems. However, their computational complexity [71] and the lack of rigorous bounds on the accuracy of finite-bond dimensional PEPS to reproduce ground states of local Hamiltonians did not allow them so far to outperform other existing numerical approaches.

In this work, we take a different perspective: we investigate the family of exact parent Hamiltonians associated with a given TN state. The theory of TN states offers a well-established framework for the study of their parent Hamiltonians. It provides a standard procedure to write down parent Hamiltonians in a straightforward manner, and it gives criteria to infer a priori about the degeneracy of their ground space. The parent Hamiltonian construction is carried out locally, thus making unnecessary a computationally expensive (or intractable) finite-size scaling. This fact remarkably allows to tackle two-dimensional problems with modest effort. While in one dimension MPSs with small bond dimension generally lead to extremely local parent Hamiltonians, in two dimensions PEPS parent Hamiltonians can be rather complex, yet they are not unique. We can thus exploit this freedom to search for the optimal Hamiltonian given certain locality constraints.

In Sec. 2.2.1 we describe in detail the procedure to construct a parent Hamiltonian for a TN states, together with the sufficient conditions for the state to be the unique (or finitely-degenerate) ground state. In Sec. 2.2.2 we introduce an algorithm to exploit the freedom in the standard construction, to find the most local operator in the family of the parent Hamiltonians associated with a given state. In Sec. 2.2.3 we benchmark the method on sample cases in which the most local parent Hamiltonian is well known, and we apply it to investigate the parent Hamiltonian of the SU(2) invariant RVB state on the kagome lattice. In Sec. 2.2.4 we draw our conclusions.

2.2.1 Injectivity and ground state degeneracy

Assuming to have a translation-invariant TN representation of a quantum state, with bond dimension D and physical dimension d, the construction of its parent Hamiltonian is illustrated in Fig. 2.6 (left). The first step consists in contracting a certain number of tensors to form a patch of sites on the physical lattice (see Fig. 2.6 (left) (a), in which the patch is a cross on a square lattice). The parent Hamiltonian construction is carried out locally on this patch of sites, to yield the Hamiltonian density on the patch. The parent Hamiltonian is obtained by covering periodically the whole lattice with the chosen patch. Contracting the tensors on the selected group of sites produces a linear map $\mathcal{P}$ which maps the virtual space $(\mathbb{C}^D)^{\otimes N_b}$ into the local physical Hilbert space $(\mathbb{C}^d)^{\otimes N_s}$, where N_b is the number of virtual bonds and N_s is the number of physical sites, which are nearest neighbor on the lattice (Fig. 2.6 (left) (b)). If N_s is large enough and the map $\mathcal{P}$ has a trivial kernel, $\mathrm{Ker}\mathcal{P} = \{0\}$, its image $\mathrm{Im}\mathcal{P}$ does not cover the entire local Hilbert space. In this case any operator which is non-trivial only on the orthogonal complement $(\mathrm{Im}\mathcal{P})^\perp$ automatically annihilates the state locally (Fig. 2.6 (left) (c)). If such an operator is strictly positive, the periodic TN turns out to be the unique zero-energy ground state of the parent Hamiltonian on a periodic cluster. This fact implies that the parent Hamiltonian is not unique: any hermitian strictly positive operator on $(\mathrm{Im}\mathcal{P})^\perp$ yields a good parent Hamiltonian for the TN state.

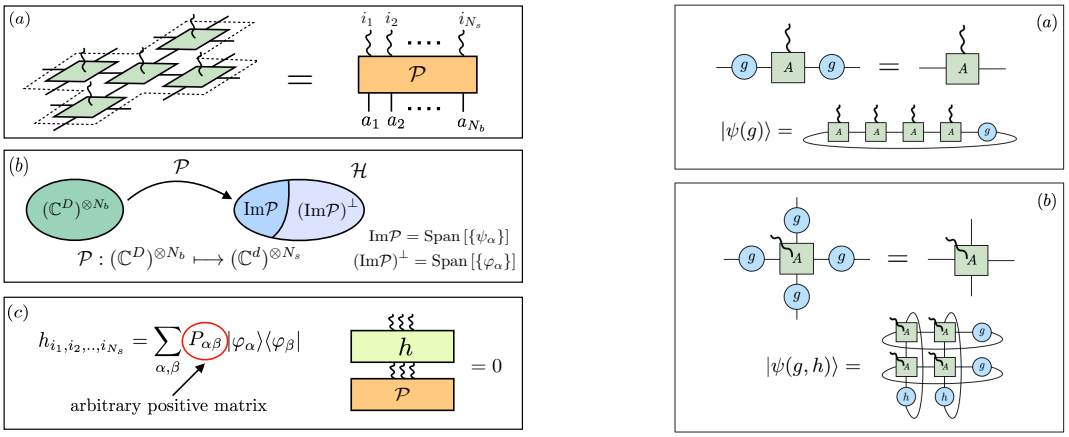

Figure 2.6: **Left.** Schematics of the parent Hamiltonian construction. (a) The elementary tensors are blocked on a large enough (see the text) number of sites N_s. (b) A map $\mathcal{P}$ from the virtual to the physical space is defined, and the orthogonal complement $(\mathrm{Im}\mathcal{P})^\perp \neq \{0\}$ is computed. (c) A parent Hamiltonian for the state is obtained by taking an arbitrary (hermitian) operator which is strictly positive on $(\mathrm{Im}\mathcal{P})^\perp$. If the TN is injective, it will be the unique ground state of the constructed parent Hamiltonian, and $N_s \geq N_b \log D$. **Right.** Pictorial representation of a $\mathbb{Z}_2$-injective TN. The operators g provide a virtual representation of the virtual $\mathbb{Z}_2$ symmetry group ($g^2 = 1$). The tensor is $\mathbb{Z}_2$-injective if it is injective its restriction to the $\mathbb{Z}_2$-invariant virtual subspace. In such cases the parent Hamiltonian will be two-fold generate on a ring (a) (with ground states $|\psi(1)\rangle$, $|\psi(g)\rangle$) and four-fold degenerate on a torus (b) (with ground states $|\psi(1,1)\rangle$, $|\psi(1,g)\rangle$, $|\psi(g,1)\rangle$, $|\psi(g,g)\rangle$).

If $\mathrm{Ker}\mathcal{P} = \{0\}$ for a large enough patch of sites the TN state is said to be injective. This condition is sufficient to guarantee the non-degeneracy of the ground state manifold of the parent Hamiltonian, meaning that the state will be its unique ground state. Notice that the locality of the parent Hamiltonian is ensured by the fact that the parent Hamiltonian density cannot have a support larger than N_s. We refer to Refs. [37, 38] for rigorous proofs of the statements made above.

Translation-invariant TNs generically satisfy the injectivity condition [37], however, if the tensor is left invariant by the application of some operators on the virtual legs, the map $\mathcal{P}$ can have a non-trivial kernel on any, arbitrarily large, patch of physical sites. We focus here on the case in which the virtual operators form a representation of the $\mathbb{Z}_2$ symmetry group $\{1, g\}$, with $g^2 = 1$, but the discussion can be extended to more general groups [38]. The state is called $\mathbb{Z}_2$-injective if (there is a patch of sites on which) the map $\mathcal{P}$ is injective when restricted to the $\mathbb{Z}_2$-invariant subspace of the virtual space. When $\mathbb{Z}_2$-injectivity is met, the ground space of the parent Hamiltonian will be two-fold degenerate on a ring (1D) and four-fold degenerate on a torus (2D) [38]. The degenerate ground states are obtained from the periodic TN by virtual insertions of the symmetry operators (see Fig. 2.6 (right)).
The simplest example of $\mathbb{Z}_2$-injective MPS is the GHZ state: $|\psi\rangle = \left(|\uparrow\rangle^{\otimes L} + |\downarrow\rangle^{\otimes L}\right)/\sqrt{2}$, where L is the length of the chain. A translation invariant MPS representation is provided by the following matrices:

$$A^\uparrow = \begin{pmatrix} 1 & 0 \\ 0 & 0 \end{pmatrix} \qquad A^\downarrow = \begin{pmatrix} 0 & 0 \\ 0 & 1 \end{pmatrix}. \tag{2.20}$$

The $\mathbb{Z}_2$ virtual symmetry generator is given by $g = \mathrm{diag}(1, -1)$, and the two states in Fig. 2.6 (right) (a) (i.e. $|\psi_\pm\rangle = \left(|\uparrow\rangle^{\otimes L} \pm |\downarrow\rangle^{\otimes L}\right)/\sqrt{2}$) are degenerate ground states of the Hamiltonian $H = -\sum_{i=0}^{L} Z_i Z_{i+1}$, where Z is the Pauli matrix σ^z.
Another one-dimensional example is the translation-invariant Majumdar-Ghosh (MG) state [72]:

$|\psi\rangle \propto |\psi_1\rangle + |\psi_2\rangle$, where $|\psi_1\rangle = (|\uparrow\downarrow\rangle - |\downarrow\uparrow\rangle)^{\otimes L/2}$ and $|\psi_2\rangle$ the one-site translation of $|\psi_1\rangle$. An MPS representation is

$$A^{\uparrow} = \begin{pmatrix} 0 & 1 & 0 \\ 0 & 0 & 0 \\ -1 & 0 & 0 \end{pmatrix} \qquad A^{\downarrow} = \begin{pmatrix} 0 & 0 & 1 \\ 1 & 0 & 0 \\ 0 & 0 & 0 \end{pmatrix}. \tag{2.21}$$

The $\mathbb{Z}_2$ generator is $g = \mathrm{diag}(1, -1, -1)$, and the two states obtained after inserting either the identity or g on one virtual link are the two degenerate ground states of the Hamiltonian $H = \sum_{i=0}^{L} \left(\vec{S}_i \cdot \vec{S}_{i+1} + \frac{1}{2}\vec{S}_i \cdot \vec{S}_{i+2}\right)$, where $\vec{S} = (S^x, S^y, S^z)$ are the spin-1/2 representation matrices of SU(2). Note that the ground state degeneracy in these two examples originates from the spontaneous symmetry breaking of (global) spin flip symmetry for the GHZ state, and one-site translation symmetry for the MG state. Note also that the parent Hamiltonian provided for the MPSs above are not positive definite, since a constant additive term has been omitted. The corresponding positive definite Hamiltonian would come from blocking the MPS tensors on $N_s = 2$ and $N_s = 3$ sites for GHZ and MG states, respectively, and taking the projector on $(\mathrm{Im}\mathcal{P})^{\perp}$ as Hamiltonian density. We will consider two-dimensional examples in what follows.

We conclude this section by mentioning that it is possible to prove that parent Hamiltonians of injective TNs in one dimension are gapped. This fact does not hold in two dimensions, where PEPS parent Hamiltonians can be gapless, and their ground state can produce power-law correlations for local observables [37].

2.2.2 Locality optimization algorithm

In the previous section, we stressed that the parent Hamiltonian of a TN state is not unique. Different choices for the positive operator on $(\mathrm{Im}\mathcal{P})^{\perp}$ produce different Hamiltonian densities. These densities can be as local as the patch of N_s sites used to construct them, or they can be more local, meaning that they don't have to include interactions that span the whole patch. This is particularly relevant when the group of sites is very large, as it often happens when constructing PEPS parent Hamiltonians on two-dimensional lattices. Below, we devise an algorithm that attempts an optimization to make the Hamiltonian density as local as possible on the chosen patch.

The starting point in what follows is to expand the target Hamiltonian on a basis of (local) operators O_a

$$H = \sum_a c_a O_a, \qquad O_a = (O_a)^{\dagger}. \tag{2.22}$$

It is crucial to keep the dimension of the basis as small as possible. This can be done by assuming that the parent Hamiltonian shares all the symmetries with the TN state.
The key idea of the algorithm is to ensure that the target Hamiltonian vanishes on $\mathrm{Im}\mathcal{P}$ and it is strictly positive on its orthogonal complement. One possible way to achieve this is to write

$$H(\mathrm{Im}\mathcal{P}) = 0 \qquad \Leftrightarrow \qquad H = \sum_{\alpha,\beta} P_{\alpha\beta} |\varphi_\alpha\rangle\langle\varphi_\beta|. \tag{2.23}$$

Since we want this operator to be a superposition of the local operators in the basis, as in Eq. (2.22), we require that

$$F\left(c_a, P_{\alpha\beta}\right) = \left|\left| \sum_a c_a O_a - \sum_{\alpha,\beta} P_{\alpha\beta} |\varphi_\alpha\rangle\langle\varphi_\beta| \right|\right|^2 = X_A \, \mathcal{M}_{AB} \, X_B = 0, \tag{2.24}$$

where the vector $X_A = (-c_a, P_{\alpha\beta})$ contains both the information on the coefficients c_a of the parent Hamiltonian written in a local operator basis, and on the positive matrix $P_{\alpha,\beta}$ representing the parent Hamiltonian as a strictly positive operator on $(\mathrm{Im}\mathcal{P})^{\perp}$.
Due to orthonormality of the basis $\langle\varphi_\alpha|\varphi_\beta\rangle = \delta_{\alpha\beta}$, the matrix $\mathcal{M}$ is extremely sparse and it reads

$$\mathcal{M}_{AB} = \left(\begin{array}{c|c} M_{ab} & R_{a,\alpha\beta} \\ \hline R_{\gamma\delta,b} & \delta_{\alpha\gamma}\delta_{\beta\delta} \end{array}\right), \qquad M_{ab} = \mathrm{Tr}(O_a O_b), \qquad R_{a,\alpha\beta} = \langle\varphi_\alpha|O_a|\varphi_\beta\rangle. \tag{2.25}$$

So far we have obtained an eigenvalue problem whose solution are Hamiltonians that annihilate the PEPS's image. An equivalent (and much simpler) eigenvalue problem would result by only imposing that the $H = \sum_a c_a O_a$ annhilates $\mathrm{Im}\mathcal{P}$. However, this would not enforce the positivity of the final results, which is fundamental to ensure that the TN state is the ground state. Hence, instead of solving directly Eq. (2.24) to get the null space of Eq. (2.25), we minimize the quadratic form in Eq (2.24) on the non-linear space of positive definite matrices $P_{\alpha\beta}$. Namely the target Hamiltonian will be given by the coefficients c_a such that

$$(c_a, P_{\alpha\beta}) = \mathrm{ArgMin}\, F\left(c_a, P_{\alpha\beta}\right), \qquad P \geq \mathbb{1}, \tag{2.26}$$

where the eigenvalues of P will be assumed larger than one without loss of generality.
A possible route to solve the optimization problem of above is to apply a gradient descent algorithm to the cost function F, and project onto the desired space at each step. The initial point is chosen to have a vanishing local Hamiltonian, i.e. $c_a = 0$ for all a, and the identity as the initial $P_{\alpha\beta}$. Since the cost function is a quadratic form, the gradient can be efficiently computed by simple matrix multiplication. The algorithm is thus as follows:

1. $X_{in} = (0, \mathbb{1})$
2. $X' = X - \eta\, \nabla F(X) = X - 2\eta\, \mathcal{M} \cdot X, \quad \eta < 1$
3. $X'' = \mathrm{Proj}(X')$
4. Repeat from 2. until convergence.

The projection in 3. has to enforce the condition $P \geq \mathbb{1}$. This can be achieved by taking the $P_{\alpha\beta}$ components of the vector X, and setting to one all the diagonal elements of the triangular part of its Schur decomposition which dropped below one at step 2., namely:

$$\mathrm{Proj}(X) = \begin{pmatrix} c \\ \mathrm{Proj}(P) \end{pmatrix} = \begin{pmatrix} c \\ Z^\dagger\, \mathrm{Proj}(T)\, Z \end{pmatrix} = \begin{pmatrix} c \\ Z^\dagger\, \widetilde{T}\, Z \end{pmatrix} \tag{2.27}$$

where the triangular matrix $\widetilde{T}$ is the same as T, but all the diagonal entries that were smaller than one in T are set to one in $\widetilde{T}$.

Symmetries. The dimension of the parameter space of the optimization algorithm is $D_O + (D_{\mathrm{Im}^\perp})^2$, where D_O is the dimension of the operator basis. The number of parameters can be reduced if the target Hamiltonian is invariant under some symmetry. In this case the matrix $P_{\alpha\beta}$ breaks into blocks labelled by the eigenvalues of the symmetry generator:

$$P = \bigoplus_\lambda P^\lambda \tag{2.28}$$

Upon proper choice of the basis of local operators, the same is true for all the O_a. The dimension of the parameter space is thus reduced to $D_O + \sum_\lambda (D_\lambda)^2$, where D_λ is the dimension of the intersection of $(\mathrm{Im}\mathcal{P})^\perp$ with each eigenspace of the symmetry generator. The cost function in Eq. (2.24) becomes

$$F\left(c_a, P^\lambda_{\alpha\beta}\right) = \sum_\lambda \left|\left| \sum_a c_a O^\lambda_a - \sum_{\alpha,\beta} P^\lambda_{\alpha\beta} |\varphi^\lambda_\alpha\rangle\langle\varphi^\lambda_\beta| \right|\right|^2 = \\ = c_a \mathrm{Tr}(O_a O_b)\, c_b - 2c_a \sum_\lambda \langle\varphi^\lambda_\alpha|O^\lambda_a|\varphi^\lambda_\beta\rangle P^\lambda_{\alpha\beta} + \sum_\lambda (P^\lambda_{\alpha\beta})^2 = X_A\, \mathcal{M}_{AB}\, X_B = 0, \tag{2.29}$$

where O^λ is the restriction of O to the symmetry sector labeled by λ, and the fact that O_a is block diagonal for all a has been used. The vector $X_A = \left(-c_a, P^{\lambda_1}_{\alpha\beta}, P^{\lambda_2}_{\alpha\beta}, \dots\right)$ and the matrix $\mathcal{M}$ reads

$$\mathcal{M}_{AB} = \begin{pmatrix} M & R_{\lambda_1} & 0 & 0 \\ R^\dagger_{\lambda_1} & \mathbb{1}_{\lambda_1} & R_{\lambda_2} & 0 \\ 0 & R^\dagger_{\lambda_2} & \mathbb{1}_{\lambda_2} & \ddots \\ 0 & 0 & \ddots & \ddots \end{pmatrix}, \qquad M_{ab} = \mathrm{Tr}(O_a O_b), \qquad R_{a,\alpha\beta} = \langle\varphi_\alpha|O_a|\varphi_\beta\rangle. \tag{2.30}$$

An example which we will utilize in the following is SU(2) symmetry. In that case we take $\lambda = s, S^z$, where s is the quantum number of the total square angular momentum $S^2 = (S^x)^2 + (S^y)^2 + (S^z)^2$ (with eigenvalue $s(s+1)$) and S^z is the total z-component on the chosen patch of physical sites: $S^z = \sum_i S^z_i$. Note that, thanks to rotational invariance, the $P_{\alpha,\beta}$ blocks are independent from the eigenvalue S^z, and the cost function in Eq. (2.29) becomes

$$F\left(c_a, P^\lambda_{\alpha\beta}\right) = c_a \mathrm{Tr}(O_a O_b)\, c_b - 2c_a \sum_s (2s+1) \langle\varphi^{s,0}_\alpha|O^{s,0}_a|\varphi^{s,0}_\beta\rangle P^s_{\alpha\beta} + \sum_s (2s+1)(P^s_{\alpha\beta})^2, \tag{2.31}$$

where the factor $(2s+1)$ takes into account the multiplicity of the eigenvalue S^z for a given s, and the generators $|\varphi^{s,S^z}_\alpha\rangle$ need to be computed only in the $S^z = 0$ sector. This further reduces the number of variational parameters down to $D_O + \sum_s (D_s)^2$, where D_s is the dimension of the simultaneous eigenspace of S^2 and S^z, which does not depend on the eigenvalue of S^z.
To monitor the status of the convergence during the minimization we directly compute the cost function at each step. To speed up the convergence we employ an adaptive step size $\eta_n = \langle\delta X_n, \delta X_n\rangle / \langle\delta X_n, \delta G_n\rangle$, where $\delta X_n = X_n - X_{n-1}$ and $\delta G_n = G_n - G_{n-1}$ are the point and gradient displacements at the n-th step of the optimization [73].

2.2.3 Applications

We now benchmark our method on one- and two-dimensional TN states whose most local parent Hamiltonian is known, although it is not trivially obtained as projector onto $(\mathrm{Im}\mathcal{P})^\perp$. We then apply it to the SU(2) RVB state on the kagome lattice, whose minimal patch of sites is a star of $N_s = 12$ sites.

The AKLT state on a chain. The AKLT state is the unique ground state of the Hamiltonian

$$H = \sum_{i=1}^{L} \vec{S}_i \cdot \vec{S}_{i+1} + \frac{1}{3}(\vec{S}_i \cdot \vec{S}_{i+1})^2, \tag{2.32}$$

where $\vec{S} = (S^x, S^y, S^z)$ are the spin-1 representation matrices of SU(2). This model was first proposed in Ref. [74] as an example of spin system with SU(2) symmetry, and with a gapped ground state which does not break any discrete[2] symmetry. In particular, the AKLT model was introduced as an instance of system satisfying the Haldane conjecture [76], and it was then understood that it realizes what is now known as symmetry-protected topological order [77, 78, 79]. The MPS representation of the AKLT state is depicted in Fig. 2.7 (left) (a).

This MPS is injective, and a parent Hamiltonian can be constructed upon blocking at least 2 sites ($N_s = 2$). In this case the physical Hilbert space is the product of two spin-1 representation: $1 \otimes 1 = 0 \oplus 1 \oplus 2$, $\mathrm{Im}\mathcal{P} = 0 \oplus 1$, and $(\mathrm{Im}\mathcal{P})^\perp = 2$. Here the integers $s = 0, 1, 2$ denote the spin-s representation of SU(2). Taking as Hamiltonian density the projector onto $(\mathrm{Im}\mathcal{P})^\perp$ results in the parent Hamiltonian in Eq. (2.32) (modulo an additive constant to ensure positivity). However, if $N_s > 2$ is taken, longer range terms appear in the projector parent Hamiltonian. Hence, we test the algorithm to find the matrix $P_{\alpha\beta}$ (see Sec. 2.2.2) necessary to reproduce the two-sites Hamiltonian in Eq. (2.32). We include only Heisenberg interactions on nearest-neighbor sites in the operator basis. For instance, with $N_s = 3$ the operator basis is $\{\mathrm{Id}, \vec{S}_1 \cdot \vec{S}_2, (\vec{S}_1 \cdot \vec{S}_2)^2, \vec{S}_2 \cdot \vec{S}_3, (\vec{S}_2 \cdot \vec{S}_3)^2\}$. Fig. 2.7 (right) shows the results of the minimization procedure: the (projected) gradient descent with adaptive step converges in ~ 200 and ~ 1500 steps for $N_s = 3$ and $N_s = 4$, respectively. The final result for the matrix $P_{\alpha,\beta}$ is not a projector, and (although not shown) the Hamiltonian density obtained is equal to Eq. (2.32) within numerical precision. Notice that in one dimension this fact is very simple to understand. We know that the most local Hamiltonian density is a projector onto the $N_s = 2$ local Hilbert space. However, since densities on two overlapping $N_s = 2$ patches are not orthogonal, their sum is not a projector.

The toric code on the square lattice. The toric code Hamiltonian reads [80]

$$H = -\sum_v \prod_{i \in v} Z_i - \sum_p \prod_{i \in p} X_i, \tag{2.33}$$

where v and p stand for vertices and plaquettes on a tilted square lattice (see Fig. 2.8 (left) (a)). This Hamiltonian has a four-fold degenerate ground space on a torus and provides the simplest example of topological order: despite the ground state degeneracy, no spontaneous symmetry breaking occurs. One of the four ground states can be written as

$$\prod_p \left(1 + \sum_{i \in p} X_i\right) |0\rangle = \sum_\ell \prod_{i \in \ell} X_i |0\rangle, \tag{2.34}$$

where $|0\rangle$ is the product state with all the sites in the eigenstate of Z with eigenvalue -1, and the r.h.s. is a sum over all the loop configurations ℓ made of adjacent plaquettes. This state admits a translation invariant PEPS representation depicted in Fig. 2.8 (left) (b) [81].

The PEPS is $\mathbb{Z}_2$-injective, where the $\mathbb{Z}_2$ virtual symmetry operator is $g = Z$. The four de-

[2]Spontaneous breaking of continuous symmetry is prohibited, in one-dimension, by the Mermin-Wagner theorem [75]. Nevertheless, SU(2) invariant spin chains can break discrete symmetries (see for instance the MG state introduced in Sec. 2.2.2.

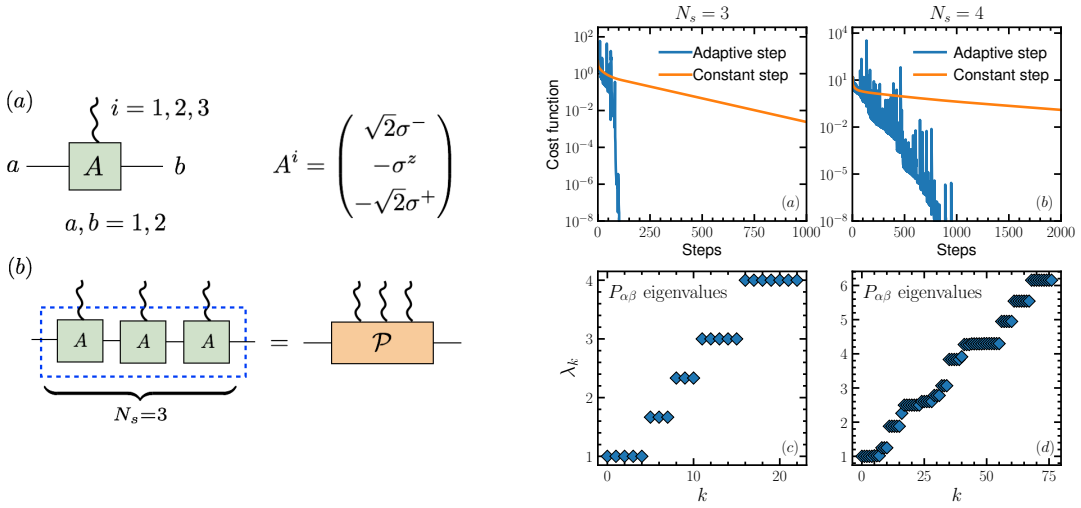

Figure 2.7: **Left.** (a) TN representation of the AKLT state. (b) 3-sites blocking of the MPS tensors to yield the map $\mathcal{P}$, starting point of the parent Hamiltonian construction. In this case the number of blocked sites N_s is larger than the minimum N_s required to build the most local parent Hamiltonian, Eq. (2.32). **Right.** (a),(b) Cost function F Eq. (2.24) during the minimization. The adaptive step-gradient descent procedure converges much faster (~ 200 and 1500 steps to reach $F \sim 10^{-12}$ for $N_s = 3$ and $N_s = 4$, respectively) than the constant step one ($\eta = 0.5$). (c),(d) Eigenvalues of the matrix $P_{\alpha\beta}$ at convergence ($F < 10^{-12}$). The result shows that the maximally local Hamiltonian when $N_s > 2$ is not a projector onto $(\mathrm{Im}\mathcal{P})^{\perp}$.

generate ground states of the Hamiltonian Eq. (2.33) are obtained from the PEPS by virtual insertions of this operator as illustrated in Fig. 2.6 (right) (b).
In order to construct the parent Hamiltonian from the PEPS representation of the state in Eq. (2.34), we need to block two tensors to get a local Hilbert space with $N_s = 8$ sites, as shown in Fig. 2.8 (left) (c). The dimension of $(\mathrm{Im}\mathcal{P})^{\perp}$ is 224 and the projector on this subspace is a Hamiltonian density that contains operators with support on all the 8 sites. Fig. 2.8 (right) (a) shows the component[3] of the density H_{Id} on an orthonormal operator basis made of all the possible products of Pauli matrices on the 8 sites. We apply the algorithm of Sec. 2.2.2 starting from an operator basis with 4-sites operators on crosses and plaquettes, each one made out of a single Pauli matrix : $X^{\otimes 4}, Y^{\otimes 4}, Z^{\otimes 4}$. Therefore, the basis contains 10 operators (including the identity), and the total number of variational parameters is $10 + 224^2 \sim 5 \cdot 10^4$. Since the PEPS posses a $\mathbb{Z}_2$ global physical symmetry, we can apply the symmetric version of the algorithm to reduce the number of parameters down to $10 + 2 \cdot (112)^2 \sim 2.5 \cdot 10^4$. The cost function during the minimization is plotted in Fig. 2.8 (right) (b). Both versions of the algorithm converge to the minimum in ~ 200 steps. However, it is computationally much cheaper for the symmetric version to perform a single step. Although in this case exploiting symmetries is not indispensable, it will be crucial in the next example, where a single optimization would be prohibitive without their use. Also in this case the algorithm succeeds in finding the expected parent Hamiltonian, i.e. Eq. (2.33). In Fig. 2.8 (right) (c),(d) we show the coefficients of the Hamiltonian density, on the 8 sites, at convergence, and its eigenvalues. The latter demonstrate that the most local density is not a projector on the 8-sites local Hilbert space.

The SU(2) RVB state on the kagome lattice. Resonating valence bond states are defined as equal-weight superpositions of all nearest-neighbor dimer coverings of a given two-dimensional

[3]The scalar product in the operator space is: $\langle O_1 | O_2 \rangle = \mathrm{Tr}(O_1^{\dagger} O_2)$.

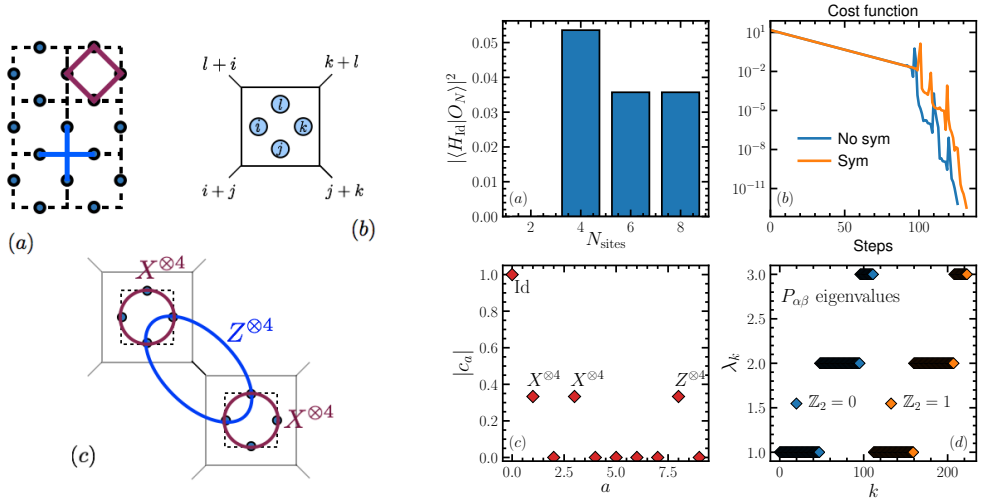

Figure 2.8: **Left.** (a) Tilted lattice for the toric code Hamiltonian. Plaquette terms are product of Xs on the blue line, cross terms are product of Zs on the purple line. (b) PEPS representation of the toric code state. Each tensor maps the virtual space to a physical space of 4 sites a on a tilted square lattice. (c) Most local parent Hamiltonian for the toric code. The cross and the plaquette terms appear, respectively, once and twice in the minimal patch to obtain the parent Hamiltonian ($N_s = 8$). **Right.** (a) Square overlaps of the (projector) parent Hamiltonian of the toric state, when an 8-sites patch is considered for the construction. The Hamiltonian contains 4, 6 and 8-sites operators. Overlaps are normalized to have total sum equal to one ($|\langle H_{\text{Id}}|\text{Id}\rangle|^2$ is not shown). (b) Cost function during the minimization, using the adaptive step. Symmetric and non-symmetric versions of the algorithm achieve convergence in the same number of steps, but the symmetric version reduces significantly the computation cost. (c) Operators coefficients at convergence. When only cross and plaquette terms (made of X,Y or Z) are included in the basis, the algorithm produces the expected result within numerical accuracy. (d) Eigenvalues of the matrix $P_{\alpha,\beta}$ at convergence, divided in the two physical $\mathbb{Z}_2$ symmetry sectors. The most local Hamiltonian is not a projector on $(\text{Im}\mathcal{P})^{\perp}$.

lattice. In quantum dimer models, on frustrated lattices, they have been known for decades to be simple representatives of topologically ordered phases [82]. When orthogonal dimer coverings are replaced by SU(2) singlets coverings, the RVB state becomes a good candidate for describing the physics of frustrated magnets. On the kagome lattice, it was shown to be in the same $\mathbb{Z}_2$ spin liquid phase of the dimer RVB [14], and demonstrated to be even more stable against perturbation [83]. Despite simple ansatze for the ground state wave functions of physically relevant models, as simple as the nearest-neighbor Heisenberg model, have been devised starting from the SU(2) singlets RVB state [84], its exact parent Hamiltonian is known to be quite complicated. It was first proven that the Hamiltonian density can be written on two overlapping stars [14], and then on a single star of the kagome lattice [85].
We attempt here to reduce the degree of locality of the Hamiltonian density by applying the method described in Sec. 2.2.2 to a star-shaped patch made of $N_s = 12$ sites.

The TN representation of the SU(2) RVB state was introduced in Ref. [14], and it is illustrated in Fig. 2.9 (left) (a). Notice that SU(2) singlets come with an orientation: downward (upward) triangles are oriented clockwise (anti-clockwise)[4]. Fig. 2.9 (left) (b) shows the patch of 12 sites that we consider in what follows: the virtual space consists of 6 bonds with dimension $D = 3$. The PEPS is $\mathbb{Z}_2$-injective, with $\mathbb{Z}_2$ virtual symmetry operator $g = \text{diag}(1, -1, -1)$. Since the dimension of $(\text{Im}\mathcal{P})^{\perp}$ is 3731, the number of variational parameters would be $> 10^7$. By exploiting SU(2) symmetry as explained in Sec. 2.1.2, together with the spatial symmetries of the star-

[4] A non-equivalent state is obtained by taking upward and downward triangles oriented in the same way.

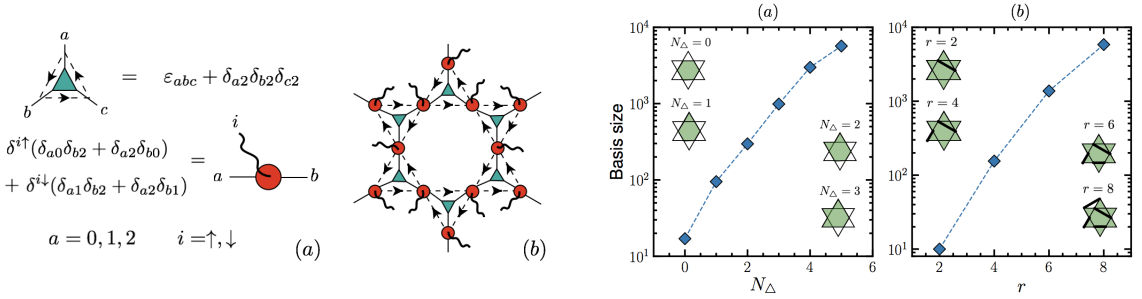

Figure 2.9: **Left.** (a) TN representation for the RVB state made of SU(2) singlets. The turquoise triangle is a tensor with only virtual indices, the virtual state 2 indicate the absence of a singlet in both adjacent links. The red circle is a projector that places the end of a singlet onto a site whenever the pair of virtual states $0, 2$ ($\uparrow$) or $0, 1$ ($\downarrow$) is met. (b) 12-sites patch of tensors taken for the parent Hamiltonian construction. **Right.** Operator basis dimension for the two cases considered here. The basis contains all the SU(2) invariant operators on the hexagon plus $N_\triangle$ adjacent triangles attached (a), or on the whole star and with support on at most r sites (b). In both cases operator are symmetrized w.r.t. the six-fold rotations and reflection (w.r.t. to a vertical axis trhough the center) of the star.

shaped patch (we used the six-fold rotation around the center and the reflection w.r.t. the vertical axis), we are able to break the $P_{\alpha\beta}$ variational matrix in blocks, for a total of 20931 parameters. We can exploit the same symmetries to select the operators to be included in the basis. SU(2) symmetry implies that the latter are written as $O_a = T_a^{k_1 k_2 .. k_r} S_{i_1}^{k_1} S_{i_2}^{k_2} .. S_{i_r}^{k_r}$, where the index $k = x, y, z$ runs on the adjoint representation of SU(2), the index $i = 1, 2, ..12$ runs on the 12 sites of the star patch, and the tensor T_a is SU(2) invariant, i.e. $T_a^{k_1 k_2 .. k_r} U_{j_1}^{k_1} U_{j_2}^{k_2} .. U_{j_r}^{k_r} = T_a^{j_1 j_2 .. j_r}$ for all SU(2) matrices U in the $s = 1$ (adjoint) representation. Operators with odd rank (r) are not necessary, since they have purely imaginary entries, while the RVB state is real. All the even rank tensors can be written in terms of product of the Kronecker delta δ_{ij} and an even number of completely anti-symmetric tensors ε_{ikl}. However, since a product of two ε can be expressed in terms of Kronecker delta[5], only the latter are needed to write down all the SU(2) invariant tensors with even rank. This means that all even-rank SU(2) invariant operators can be written as products of Heisenberg interactions. These are the operators that we include in the basis, upon taking their (star-)rotation and reflection invariant combinations. We observe that all products of $r/2$ Heisenberg interactions form an overcomplete set of operators for $r \geq 8$ [86]. This is not an issue for the algorithm, as long as a strictly positive parent Hamiltonian can be written as a linear combination of the available operators.

We run the algorithm with two different basis choices. In the first case, we take operators with support on the central hexagon of the star plus $N_\triangle$ adjacent triangles attached to it (with operator up to rank $r = 8$), in the second case we take operator with arbitrary range on the start with at most rank r. We then enlarge the basis by varying independently $N_\triangle$ and r. In Fig. 2.9 (right) we plot the dimension of the basis (the maximum size we considered is < 6000).
Depending on the basis size the algorithm may take several thousands of steps to converge, and it does not always find an exact parent Hamiltonian. This is signaled by the fact that at convergence[6] the cost function is not vanishing within numerical precision. The final result is plotted in Fig. 2.10 (left). A good parent Hamiltonian density is found when $N_\triangle = 4$ (~ 3000 operators in the basis) or $r = 8$ (~ 6000 operators in the basis).
In order to check the validity of the Hamiltonian found by the algorithm, we performed exact diagonalization on small tori, employing periodic clusters depicted in Fig. 2.11, including up to

[5] $\varepsilon_{ijk}\varepsilon_{lmn} = \delta_{il}(\delta_{jm}\delta_{kn} - \delta_{jn}\delta_{km}) - \delta_{im}(\delta_{jl}\delta_{kn} - \delta_{jn}\delta_{kl}) + \delta_{in}(\delta_{jl}\delta_{km} - \delta_{jm}\delta_{kl})$

[6] We monitor the status of convergence by computing the norm displacement vector at consecutive steps $\epsilon = ||X_n - X_{n-1}||$. We stop the algorithm when $\epsilon < 10^{-10}$.

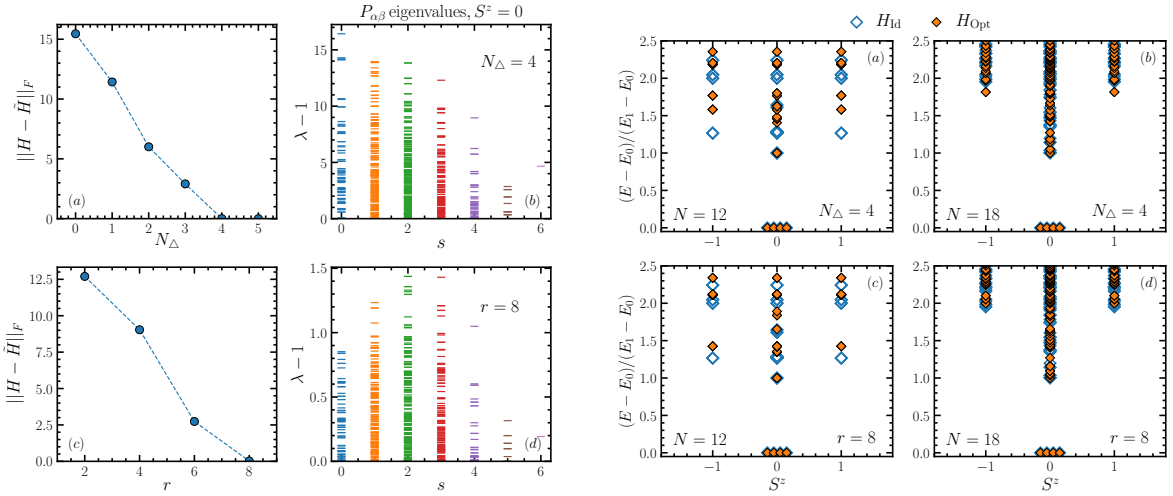

Figure 2.10: **Left.** (a),(c) Minimum for the cost function Eq. (2.29) at convergence. When $N_\triangle < 4$ or $r < 8$ the algorithm does not find a minimum at zero norm, indicating the failure in writing a parent Hamiltonian on the chosen basis. (b),(d) Eigenvalues of matrix $P_{\alpha,\beta}$ in the $S^z = 0$ sector, for each S^2 sector, for $N_\triangle = 4$ and $r = 8$. In both cases the algorithm succeed in finding an exact parent Hamiltonian, and the latter is not a projector. **Right.** Comparison between the low energy spectra of the RVB parent Hamitlonian obtained as a projector on $(\mathrm{Im}\mathcal{P})^\perp$ (blue empty diamonds) and the optimized Hamiltonian (orange filled diamonds) obtained on a basis of operators with up to 4 triangles around the hexagon (a),(b), and up to rank 8 (c),(d). Periodic clusters with $N = 12$ (a),(c) and $N = 18$ (b),(d) are considered (see Fig. 2.11 (left)).

8 unit cells of the kagome lattice ($N = 24$ sites). In Fig. 2.10 (right) we plot the comparison between the spectrum of the projector parent Hamiltonian and the optimized one on clusters of 12 and 18 sites. The expected topological four-fold degeneracy of the ground space is accurate within 10^{-9}. Note however that the two spectra are not identical already at very low energy. We verified that the overlap of the RVB state with the ground-space of the optimized Hamiltonian is equal to 1 within numerical accuracy, for clusters up to $N = 24$ sites. In Fig. 2.11 (right) (a) we show the expectation value of the optimized parent Hamiltonian ($N_\triangle = 4$) on the RVB state on a torus. The energy of the RVB state is almost vanishing, but it is not compatible with zero (within numerical accuracy). We attribute this issue to small numerical imprecisions in the minimization procedure, which is carried out on a fairly large parameter space. Finally, the lowest gap of the optimized Hamiltonian is plotted in Fig. 2.11 (right) (b), as a function of the linear size of the cluster (L_y). The result mildly scales with L_y, and clearly shows a gap of order one between the four degenerate ground states and the rest of the spectrum.

To sum up: the locality optimization algorithm is able to find a parent Hamiltonian density which is more local than the whole star-shaped patch we started from, and it includes products of up to 4 Heisenberg interactions. The parent Hamiltonian does not only have the RVB state as a ground state, but it also shares the four-fold topological degeneracy expected from an exact parent Hamiltonian for this state. In principle, it should be possible to gain physical intuition on the operators that are essential to obtain a good parent Hamiltonian for the RVB state. However, we found it hard in practice, due to the large number of operators in the basis (~ 3000 at least). Although certain operators contribute more than others to the final result (e.g. the number of operators O_a such that $|c_a/c_0| > 0.5$, where c_0 is the largest coefficient of the identity operator, are only 10), all the operators appear to be necessary to give high overlap with the RVB state, and to reproduce the correct ground state degeneracy.

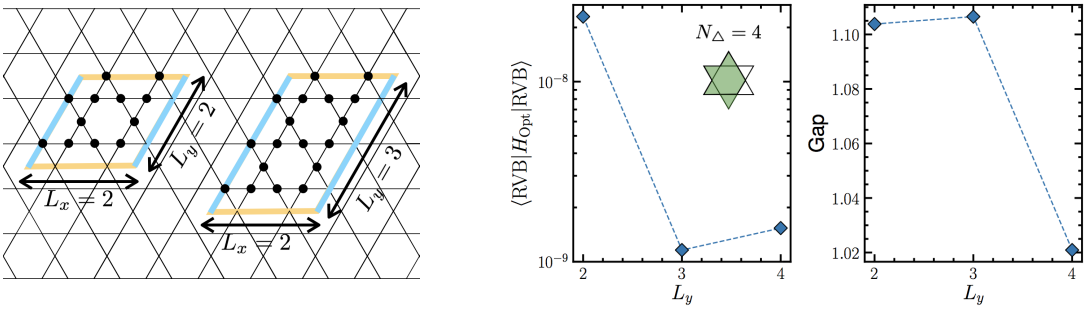

Figure 2.11: **Left.** Periodic cluster used to check the goodness of the parent Hamiltonian obtained from the minimization. The clusters covers $L_x L_y$ unit cells, for a total number of sites $N = 3L_x L_y$. We are able to compute the low energy states for clusters including up to $N = 24$ sites ($L_x = 2$,$L_y = 4$). **Right.** RVB state expectation value on (a) and lowest gap of (b) the optimized parent Hamiltonian, for increasing system size.

2.2.4 Conclusions

We exploited the freedom in the construction of parent Hamiltonians for TN states to optimize their locality. We formulated an algorithm that locally searches for a parent Hamiltonian by taking as inputs a patch of lattice sites and a basis of local operators. We benchmarked the algorithm on simple one- and two-dimensional examples, and we applied it to tackle the tougher problem of finding a local parent Hamiltonian for the RVB state made of SU(2) singlets, on the kagome lattice. We found that the previously-believed-to-be minimal degree of locality of the parent Hamiltonian density (a star on the kagome lattice) can be reduced to 10 sites (one hexagon plus four adjacent triangles) and that only operators supported on up to 8 sites (product of four Heisenberg interactions) have to be included. In face of the partial success of this optimization, the RVB state parent Hamiltonian appears to be extremely fine-tuned, in that a very large number of operators with small coefficients are necessary to reproduce the expected features. Likely, a more efficient parametrization of the operator basis might significantly reduce its dimension and clarify the nature of each interaction term that is necessary to include.

We remark that the conditions at the basis of our algorithm are sufficient but not necessary. In fact, the construction outlined in Sec. 2.2.1 inevitably yields a frustration-free parent Hamiltonian for the input TN state. We cannot exclude that other approaches might lead to more local exact (or approximate) parent Hamiltonians for the RVB state, however they would hinder the local nature of our method, which is key to deal with the problem in more than one dimension.

2.3 Outlook

In this chapter, we approached the problem of finding a parent Hamiltonian starting from an a priori-given wavefunction from two different perspectives. In Sec. 2.1, we based the parent Hamiltonian search on a QFT representation of the target state RDM, developing an algorithm suitable for states with large ξ/a, where ξ and a are the correlation length and lattice spacing respectively. In Sec. 2.2, we dealt with parent Hamiltonians of tensor network states with small bond dimension, employing an optimization method to find the most local exact parent Hamiltonian for the input state.

These two classes of states –large correlation length and exact tensor network– do not intersect in one dimension. In fact, while 1D critical states generally exhibit a bipartite entanglement spectrum with fat tails, that leads to an entanglement entropy diverging with sytems size, MPSs have an ES distribution with no tails and a bipartite entanglement entropy that stays finite in the thermodynamic limit. Furthermore, QFT arguments provide a direct relation between the entanglement entropy and the correlation length: $S \sim \log \xi$ [87]. This relation is not satisfied by MPSs, that can display correlations that do not decay with the distance, despite having a finite entanglement entropy [88]. In two dimensions, power-law correlations can arise from low-bond dimensional PEPS [81], however the parent Hamiltonians of these states seem to generate a non Lorentz invariant dynamics [89], signaling a non-linear dispersion relation of the gapless low energy excitations of PEPS parent Hamiltonians. In fact, a general understanding of these excitations and of their possible continuum description with QFT tools is still an open problem. Analyzing how well the method of Sec. 2.1 copes with PEPS is a promising route to achieve this goal.

The work discussed in Sec. 2.1 consisted in benchmarking the method on sample cases in which the parent Hamiltonian was known a priori. The most natural extension is to apply the search algorithm to problems where the parent Hamiltonian is completely unknown. In Ref. [90] the algorithm has been tested on Jastrow-Gutzwiller wavefunctions in one dimension. The next step would be to tackle two-dimensional problems where relativistic invariance is expected at low energy, by taking appropriate input states. In fact, as we demonstrated, the method is amenable to quantum Monte Carlo techniques, that make it scalable in any dimension, as long as the search is limited to sing-problem free Hamiltonians.

The algorithm presented in Sec. 2.2, other than optimizing on the family of parent Hamiltonians associated to a tensor network state, gives access to an explicit representation of the Hamiltonian density in terms of physical operators, e.g. Heisenberg interactions for SU(2) invariant Hamiltonians. To further simplify the result it might be possible to devise appropriate truncation schemes for the optimized parent Hamiltonian, in the same spirit of Ref. [91]. After the truncation, the parent Hamiltonian would stop being exact for the input state, which, however, could maintain a large overlap with the true ground state. Arguably, this fact would imply that the truncated parent Hamiltonian yield the same low energy physical properties of the target state.

Bibliography

[1] X. Turkeshi et al., "Entanglement-Guided Search for Parent Hamiltonians", *Phys. Rev. Lett.* 122.15 (2019), p. 150606.

[2] X.-G. Wen, *Quantum Field Theory of Many-Body Systems*, Oxford University Press, 2004.

[3] M. Greiter, *Mapping of Parent Hamiltonians: From Abelian and non-Abelian Quantum Hall States to Exact Models of Critical Spin Chains*, Springer Heidelberg, 2011.

[4] E. Fradkin, *Field Theories of Condensed Matter Systems*, Cambridge University Press, 2013.

[5] R. B. Laughlin, "Anomalous Quantum Hall Effect: An Incompressible Quantum Fluid with Fractionally Charged Excitations", *Phys. Rev. Lett.* 50.18 (1983), pp. 1395–1398.

[6] N. Read and E. Rezayi, "Beyond paired quantum Hall states: Parafermions and incompressible states in the first excited Landau level", *Phys. Rev. B* 59.12 (1999), pp. 8084–8092.

[7] G. Moore and N. Read, "Nonabelions in the fractional quantum hall effect", *Nuclear Physics B* 360.2-3 (1991), pp. 362–396.

[8] F. D. M. Haldane, "Fractional Quantization of the Hall Effect: A Hierarchy of Incompressible Quantum Fluid States", *Phys. Rev. Lett.* 51.7 (1983), pp. 605–608.

[9] E. Kapit and E. Mueller, "Exact Parent Hamiltonian for the Quantum Hall States in a Optical Lattice", *Phys. Rev. Lett.* 105 (2010), p. 215303.

[10] T. Grover, Y. Zhang, and A. Vishwanath, "Entanglement entropy as a portal to the physics of quantum spin liquids", *New. J. Phys.* 15.2 (2013), p. 025002.

[11] F. D. M. Haldane et al., "Yangian symmetry of integrable quantum chains with long-range interactions and a new description of states in conformal field theory", *Phys. Rev. Lett.* 69.14 (1992), pp. 2021–2025.

[12] I. Affleck et al., "Rigorous results on valence-bond ground states in antiferromagnets", *Phys. Rev. Lett.* 59.7 (1987), pp. 799–802.

[13] U. Schollwöck, "The density-matrix renormalization group in the age of matrix product states", *Ann. Phys.* 326.1 (2011), pp. 96–192.

[14] N. Schuch, I. Cirac, and D. Pérez-García, "PEPS as ground states: Degeneracy and topology", *Ann. Phys.* 325.10 (2010), pp. 2153–2192.

[15] I. Bloch, J. Dalibard, and S. Nascimbène, "Quantum simulations with ultracold quantum gases", *Nat. Phys.* 8.4 (2012), pp. 267–276.

[16] R. Blatt and C. Roos, "Quantum simulations with trapped ions", *Nat. Phys.* 8.4 (2012), pp. 277–284.

[17] I. Buluta, S. Ashhab, and F. Nori, "Natural and artificial atoms for quantum computation", *Rep. Prog. Phys.* 74.10 (2011), p. 104401.

[18] I. M. Georgescu, S. Ashhab, and F. Nori, "Quantum simulation", *Rev. Mod. Phys.* 86.March (2014), pp. 153–185.

[19] J. I. Cirac and P. Zoller, "Goals and opportunities in quantum simulation", *Nat. Phys.* 8.4 (2012), pp. 264–266.

[20] B. Swingle and I. H. Kim, "Reconstructing Quantum States from Local Data", *Phys. Rev. Lett.* 113.26 (2014), p. 260501.

[21] J. R. Garrison and T. Grover, "Does a Single Eigenstate Encode the Full Hamiltonian?", *Phys. Rev. X* 8.2 (2018), p. 021026.

[22] X.-L. Qi and D. Ranard, "Determining a local Hamiltonian from a single eigenstate", *Quantum* 3 (2019), p. 159.

[23] E. Chertkov and B. K. Clark, "Computational Inverse Method for Constructing Spaces of Quantum Models from Wave Functions", *Phy. Rev. X* 8.3 (2018), p. 031029.

[24] E. Bairey, I. Arad, and N. H. Lindner, "Learning a Local Hamiltonian from Local Measurements", *Phys. Rev. Lett.* 122 (2019), p. 020504.

[25] M. Dupont and N. Laflorencie, "Many-body localization as a large family of localized ground states", *Phys. Rev. B* 99 (2019), p. 020202.

[26] M. Dupont, N. Macé, and N. Laflorencie, "From eigenstate to Hamiltonian: Prospects for ergodicity and localization", *Phys. Rev. B* 100 (2019), p. 134201.

[27] A. Vishwanath, "From local observables in a single eigenstate to parent Hamiltonians", *Journal Club for Condensed Matter Physics, Jan. 2018, https://www.condmatjclub.org/uploads/2018/01/JCCM_January_2018_02.pdf* ().

[28] J. J. Bisognano and E. H. Wichmann, "On the duality condition for a Hermitian scalar field", *J. Math. Phys.* 16.4 (1975), pp. 985–1007.

[29] J. J. Bisognano and E. H. Wichmann, "On the duality condition for quantum fields", *J. Math. Phys.* 17.3 (1976), pp. 303–321.

[30] R. Haag, *Local quantum physics: Fields, particles, algebras*, Springer Science, 2012.

[31] E. Witten, "APS Medal for Exceptional Achievement in Research: Invited article on entanglement properties of quantum field theory", *Rev. Mod. Phys.* 90 (2018), p. 045003.

[32] M. Dalmonte, B. Vermersch, and P. Zoller, "Quantum Simulation and Spectroscopy of Entanglement Hamiltonians", *Nat. Phys.* (2018).

[33] S. R. White, "Density matrix formulation for quantum renormalization groups", *Phys. Rev. Lett.* 69.19 (1992), pp. 2863–2866.

[34] A. E. Feiguin and S. R. White, "Finite-temperature density matrix renormalization using an enlarged Hilbert space", *Phys. Rev. B* 72 (2005), 220401(R).

[35] R. K. Kaul, R. G. Melko, and A. W. Sandvik, "Bridging Lattice-Scale Physics and Continuum Field Theory with Quantum Monte Carlo Simulations", *Ann. Rev. Cond. Matt. Phys.* 4.1 (2013), pp. 179–215.

[36] M. Fannes, B. Nachtergaele, and R. F. Werner, "Finitely correlated states on quantum spin chains", *Communications in Mathematical Physics* 144.3 (1992), pp. 443–490.

[37] D. Perez-Garcia et al., "Peps as Unique Ground States of Local Hamiltonians", *Quantum Info. Comput.* 8.6 (2008), pp. 650–663.

[38] N. Schuch, I. Cirac, and D. Pérez-García, "PEPS as ground states: Degeneracy and topology", *Ann. Phys.* 325.10 (2010), pp. 2153–2192.

[39] V. Vedral, "The role of relative entropy in quantum information theory", *Rev. Mod. Phys.* 74.1 (2002), p. 197.

[40] F. Haldane, "Nonlinear field theory of large-spin Heisenberg antiferromagnets: semiclassically quantized solitons of the one-dimensional easy-axis Néel state", *Phys. Rev. Lett.* 50.15 (1983), p. 1153.

[41] A. V. Chubukov, S. Sachdev, and J. Ye, "Theory of two-dimensional quantum Heisenberg antiferromagnets with a nearly critical ground state", *Phys. Rev. B* 49.17 (1994), p. 11919.

[42] A. W. Sandvik and D. J. Scalapino, "Order-disorder transition in a two-layer quantum antiferromagnet", *Phys. Rev. Lett.* 72 (1994), pp. 2777–2780.

[43] L. Wang, K. S. D. Beach, and A. W. Sandvik, *Phys. Rev. B* 73.1 (2006), p. 014431.

[44] N. Laflorencie, "Quantum entanglement in condensed matter systems", *Phys. Rep.* 646 (2016), p. 1.

[45] N. Regnault, *Entanglement Spectroscopy and its Application to the Quantum Hall Effects*, 2015, arXiv: 1510.07670 [cond-mat.str-el].

[46] H. Itoyama and H. B. Thacker, "Lattice Virasoro algebra and corner transfer matrices in the Baxter eight-vertex model", *Phys. Rev. Lett.* 58.14 (1987), p. 1395.

[47] I. Peschel and V. Eisler, "Reduced density matrices and entanglement entropy in free lattice models", *J. Phys. A: Math. Theor.* 42.50 (2009), p. 504003.

[48] P. Kim et al., "Entanglement and corner Hamiltonian spectra of integrable open spin chains", *Phys. Rev. B* 94.19 (2016), p. 195110.

[49] W. Zhu, Z. Huang, and Y.-C. He, "Reconstructing entanglement Hamiltonian via entanglement eigenstates", *Phys. Rev. B* 99 (2019), p. 235109.

[50] F. Parisen Toldin and F. F. Assaad, "Entanglement Hamiltonian of Interacting Fermionic Models", *Phys. Rev. Lett.* 121 (2018), p. 200602.

[51] V. Eisler and I. Peschel, "Properties of the entanglement Hamiltonian for finite free-fermion chains", *Journal of Statistical Mechanics: Theory and Experiment* 2018.10 (2018), p. 104001.

[52] A. Kosior, M. Lewenstein, and A. Celi, "Unruh effect for interacting particles with ultracold atoms", *SciPost Phys.* 5 (2018), p. 61.

[53] G. Giudici et al., "Entanglement Hamiltonians of lattice models via the Bisognano-Wichmann theorem", *Phys. Rev. B* 98 (2018), p. 134403.

[54] M. H. Amin et al., "Quantum Boltzmann Machine", *Phys. Rev. X* 8 (2018), p. 021050.

[55] H. J. Kappen, "Learning quantum models from quantum or classical data" (2018), eprint: arXiv:1803.11278.

[56] D. D. Blanco et al., "Relative entropy and holography", *JHEP* 2013.8 (2013), p. 60.

[57] G. Wong et al., "Entanglement temperature and entanglement entropy of excited states", *JHEP* 2013.12 (2013), p. 20.

[58] N. Lashkari, "Relative Entropies in Conformal Field Theory", *Phys. Rev. Lett.* 113.5 (2014), p. 051602.

[59] W. Chen, K. Hida, and B. C. Sanctuary, "Ground State Phase Diagram of S=1 XXZ Chains with Uniaxial Single-Ion-Type Anisotropy", *Phys. Rev. B* 67 (2003), p. 104401.

[60] B. B. Beard et al., "Square-Lattice Heisenberg Antiferromagnet at Very Large Correlation Lengths", *Phys. Rev. Lett.* 80 (1998), pp. 1742–1745.

[61] A. Sen, H. Suwa, and A. W. Sandvik, "Velocity of excitations in ordered, disordered, and critical antiferromagnets", *Phys. Rev. B* 92 (2015), p. 195145.

[62] F. Becca et al., *Variational Wave Functions for Frustrated Magnetic Models*, Springer Series in Solid-State Sciences edited by C. Lacroix, P. Mendels, and F. Mila, 2011.

[63] P. V. Buividovich and M. I. Polikarpov, "Numerical study of entanglement entropy in SU(2) lattice gauge theory", *Nucl. Phys. B* 802 (2008), p. 458.

[64] H. Casini, M. Huerta, and J. A. Rosabal, "Remarks on entanglement entropy for gauge fields", *Phys. Rev. D* 89 (2014), p. 085012.

[65] F. Verstraete and J. I. Cirac, *Renormalization algorithms for Quantum-Many Body Systems in two and higher dimensions*, 2004, arXiv: cond-mat/0407066 [cond-mat.str-el].

[66] J. Jordan et al., "Classical Simulation of Infinite-Size Quantum Lattice Systems in Two Spatial Dimensions", *Phys. Rev. Lett.* 101 (2008), p. 250602.

[67] H. C. Jiang, Z. Y. Weng, and T. Xiang, "Accurate Determination of Tensor Network State of Quantum Lattice Models in Two Dimensions", *Phys. Rev. Lett.* 101 (2008), p. 090603.

[68] H. N. Phien et al., "Infinite projected entangled pair states algorithm improved: Fast full update and gauge fixing", *Phys. Rev. B* 92 (2015), p. 035142.

[69] P. Corboz, "Variational optimization with infinite projected entangled-pair states", *Phys. Rev. B* 94 (2016), p. 035133.

[70] M. P. Zaletel and F. Pollmann, "Isometric Tensor Network States in Two Dimensions", *Phys. Rev. Lett.* 124 (2020), p. 037201.

[71] N. Schuch et al., "Computational Complexity of Projected Entangled Pair States", *Phys. Rev. Lett.* 98 (2007), p. 140506.

[72] C. K. Majumdar and D. K. Ghosh, "On Next-Nearest-Neighbor Interaction in Linear Chain. I", *Journal of Mathematical Physics* 10.8 (1969), pp. 1388–1398.

[73] B. Zhou, L. Gao, and Y.-H. Dai, "Gradient Methods with Adaptive Step-Sizes", *Computational Optimization and Applications* 35.1 (2006), pp. 69–86.

[74] I. Affleck et al., "Valence bond ground states in isotropic quantum antiferromagnets", *Communications in Mathematical Physics* 115.3 (1988), pp. 477–528.

[75] N. D. Mermin and H. Wagner, "Absence of Ferromagnetism or Antiferromagnetism in One- or Two-Dimensional Isotropic Heisenberg Models", *Phys. Rev. Lett.* 17 (1966), pp. 1133–1136.

[76] F. Haldane, "Continuum dynamics of the 1-D Heisenberg antiferromagnet: Identification with the O(3) nonlinear sigma model", *Physics Letters A* 93.9 (1983), pp. 464–468.

[77] F. Pollmann et al., "Entanglement spectrum of a topological phase in one dimension", *Phys. Rev. B* 81 (2010), p. 064439.

[78] N. Schuch, D. Pérez-García, and I. Cirac, "Classifying quantum phases using matrix product states and projected entangled pair states", *Phys. Rev. B* 84 (2011), p. 165139.

[79] X. Chen, Z.-C. Gu, and X.-G. Wen, "Classification of gapped symmetric phases in one-dimensional spin systems", *Phys. Rev. B* 83 (2011), p. 035107.

[80] A. Kitaev, "Fault-tolerant quantum computation by anyons", *Annals of Physics* 303.1 (2003), pp. 2–30.

[81] F. Verstraete et al., "Criticality, the Area Law, and the Computational Power of Projected Entangled Pair States", *Phys. Rev. Lett.* 96 (2006), p. 220601.

[82] R. Moessner and K. S. Raman, "Quantum Dimer Models", *Introduction to Frustrated Magnetism: Materials, Experiments, Theory*, ed. by C. Lacroix, P. Mendels, and F. Mila, Berlin, Heidelberg: Springer Berlin Heidelberg, 2011, pp. 437–479.

[83] M. Iqbal, H. Casademunt, and N. Schuch, "Topological spin liquids: Robustness under perturbations", *Phys. Rev. B* 101 (2020), p. 115101.

[84] M. Iqbal, D. Poilblanc, and N. Schuch, "Gapped $\mathbb{Z}_2$ spin liquid in the breathing kagome Heisenberg antiferromagnet", *Phys. Rev. B* 101 (2020), p. 155141.

[85] Z. Zhou, J. Wildeboer, and A. Seidel, "Ground-state uniqueness of the twelve-site RVB spin-liquid parent Hamiltonian on the kagome lattice", *Phys. Rev. B* 89 (2014), p. 035123.

[86] E. A. Kearsley and J. T. Fong, "Linearly independent sets of isotropic Cartesian tensors of ranks up to eight", *Journal of Research of the National Bureau of Standards, Section B: Mathematical Sciences* (1975), p. 49.

[87] P. Calabrese and J. Cardy, "Entanglement entropy and quantum field theory", *Journal of Statistical Mechanics: Theory and Experiment* 2004.06 (2004), P06002.

[88] M. M. Wolf et al., "Quantum Phase Transitions in Matrix Product Systems", *Phys. Rev. Lett.* 97 (2006), p. 110403.

[89] Y. Hotta, "Tensor-network algorithm for nonequilibrium relaxation in the thermodynamic limit", *Phys. Rev. E* 93 (2016), p. 062136.

[90] X. Turkeshi and M. Dalmonte, "Parent Hamiltonian Reconstruction of Jastrow-Gutzwiller Wavefunctions", *SciPost Phys.* 8 (2020), p. 42.

[91] A. E. B. Nielsen, G. Sierra, and J. I. Cirac, "Local models of fractional quantum Hall states in lattices and physical implementation", *Nature Communications* 4.1 (2013), p. 2864.

Chapter 3

Constrained models: from ground state to non-equilibrium properties

This chapter is based on the following publications:

[1] G. Giudici, A. Angelone, G. Magnifico, Z. Zeng, G. Giudice, T. Mendes-Santos, M. Dalmonte
Diagnosing Potts criticality and two-stage melting in one-dimensional hard-core boson models
Physical Review B 99, 094434 (2019)

[2] F. M. Surace, P. P. Mazza, G. Giudici, A. Lerose, A. Gambassi, M. Dalmonte
Lattice gauge theories and string dynamics in Rydberg atom quantum simulators
Physical Review X 10, 021041 (2020)

[3] G. Giudici, F. M. Surace, J. E. Ebot, A. Scardicchio, M. Dalmonte
Breakdown of ergodicity in disordered U(1) lattice gauge theories
Physical Review Research 2, 032034(R) (2020)

Recent years have witnessed growing theoretical interest in constrained many-body quantum systems, driven by the success in the realization of experimental platforms in which the coherent quantum dynamics of such systems can be reliably simulated [4]. A constraint on the Hilbert space is enforced in quantum simulators as a large energy penalty, induced by the engineered interactions, on some class of not-allowed states. For instance, in the experiment of Ref. [4] the effective dipole-dipole interactions between excited states in Rydberg atom arrays [5] forbids two nearby atoms to be simultaneously excited. The resulting model will be the main focus of this chapter. First introduced in Ref. [6] by Fendley, Sengupta, and Sachdev (FSS), the model describes an array of one-dimensional strongly interacting hard-core bosons in the presence of occupation constraints on nearest-neighbor (NN), and with additional interactions on next-to-nearest-neighbor (NNN), sites. Initially discussed due to its connections with integrable models, its successful implementation in Rydberg atom arrays led to further theoretical investigation of its peculiar equilibrium [7, 8, 9, 10, 11] and out-of-equilibrium properties [12, 13, 14, 15, 16].

The experimental setup is schematically illustrated in Fig. 3.1. It consists of a one-dimensional array of L optical traps, each of them hosting a single atom. The atoms are trapped in their electronic ground state (black circle), denoted by $|\downarrow\rangle_j$, where j numbers the trap. These ground states are quasi-resonantly coupled to a single Rydberg state, i.e., a highly excited electronic level, denoted by $|\uparrow\rangle_j$. The dynamics of this chain of qubits $\{|\uparrow\rangle, |\downarrow\rangle_j\}_{j=1,\dots,L}$ is governed by

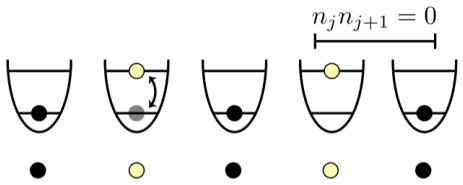

Figure 3.1: Schematics of a Rydberg atom chain. Each potential well of the optical lattice hosts a single atom, which can be either in the ground (black) or excited Rydberg (yellow) state. The two levels are coupled by a laser field. The Rydberg blockade prevents the simultaneous excitations of neighboring atoms.

the following Ising-type Hamiltonian [17, 18]:

$$H_{\text{Ryd}} = \sum_{j=1}^{L} (\Omega\, \sigma_j^x + \delta\, \sigma_j^z) + \sum_{j<\ell=1}^{L} V_{j,\ell}\, n_j n_\ell, \tag{3.1}$$

where σ_j^α are Pauli matrices at site j, the operator $n_j = (\sigma_j^z + 1)/2$ signals the presence of a Rydberg excitation at site j, 2Ω and 2δ are the Rabi frequency and the detuning of the laser excitation scheme, respectively, and $V_{j,\ell}$ describes the interactions between atoms in their Rydberg states at sites (j, ℓ). This interaction is strong at short distances and decays as $1/|j-\ell|^6$ at large distances. By introducing the Rydberg blockade parameter R_b defined from

$$V(R_b) = \Omega, \tag{3.2}$$

the interaction can be tuned to produce the so-called Rybderg blockade. When $R_b = 1$ the simultaneous occupancy of the excited Rydberg state for nearby atoms is prohibited. This gives an effective constraint $n_j n_{j+1} = 0$. Increasing R_b from 1 to 2 is equivalent to introduce a NNN interaction between the spins, where NNN occupancy is prohibited when $R_b = 2$. The dynamics described by H_{Ryd} has already been realized in several experiments utilizing either optical lattices or optical tweezers [19, 20, 4]. This particular scenario has been investigated in Ref. [4] for the first time.

In the various regimes described above, the resulting effective Hamiltonian reads

$$H_{\text{Eff}}(d) = \sum_{j=1}^{L} \left(\Omega\, \sigma_j^x + 2\delta\, n_j\right) + V_d \sum_{j=1}^{L} n_j n_{j+d}, \tag{3.3}$$

with H_{Eff} acting on the constrained Hilbert space without double occupancies on nearest-neighbor sites when $R_b \in [1, 2]$, on next-to-nearest neighbor sites when $R_b \in [2, 3]$, and so on. Note that when R_b ranges in $[d-1, d]$, with d an integer, the parameter V_d takes value in $[0, \infty]$. In what follows we will concentrate on the Hamiltonian Eq. (3.3) when $R_b \in [1, 2]$, and we will allow the parameter V_2 to take all real values. We will refer to this model as the FSS model [6].

The FSS model displays a variety of phases and phase transitions at zero temperature. In particular, there are two ordered phases with $\mathbb{Z}_2$ and $\mathbb{Z}_3$ order [6] and a disordered phase in which long-range correlations can be incommensurate with the lattice spacing [9]. The phase diagram hosts two integrable lines, and continuous phase transitions belonging to various conformal invariant universality classes, such as the Ising, tricritical Ising and 3-states Potts [21]. Moreover, it exhibits gapless phases described by Luttinger liquid theory [22], as well as second order phase

transitions which do not fit in the conformal field theory framework [23, 24, 25]. Although significant theoretical and numerical effort has been devoted to comprehensively understand these diverse universal phenomena [6, 8, 9], their character in specific regions of the phase diagram is still debated.

In Sec. 3.1 we aim at clarifying the nature of the $\mathbb{Z}_3$-order-to-disorder transition in the limiting case of infinite NNN repulsion, which we refer to as the *doubly blockaded regime*, in analogy with the more common NN blockade. We show that the melting of the ordered phase, in this regime, takes place via an intermediate gapless phase. This critical phase is enclosed between two continuous phase transitions. From the disordered side, the transition is of the BKT type, while from the ordered side the universality class is not captured by conformal field theory (CFT).

We compute many of the critical exponents of these transitions with different methods. As we discuss below, our findings are only able to provide a rough estimate for the size of the incommensurate (IC) phase, due to the presence of anomalously large finite-size effects. In parallel, we test some of the methods employed on the exactly located 3-states Potts critical point; this helps us to emphasize differences and similarities between the two melting phase transitions. We also give a full characterization of the Potts critical point by computing its critical exponents, and by matching the low-lying energy spectrum on the lattice with the universal predictions provided by conformal field theory. This characterization provides a quantitative and unambiguous testbed to verify Potts quantum criticality in experiments based on spectroscopic probes.

We employ various methods to tackle the problem numerically, focusing on periodic geometries in order to avoid boundary effects, which are particularly detrimental for constrained models in the vicinity of ordered phases. We exploit at best the small quantum dimension of the Hilbert space to compute the ground state and the lowest excited states exactly up to 54 sites. We perform studies of up to 120 sites via quantum Monte Carlo (QMC), using an imaginary-time path integral method sharing many similarities with the worm algorithm [26], adapted to simulate Hamiltonians with off-diagonal terms such as those of the FSS model and with updates designed to automatically respect its occupation constraints. We use the density matrix renormalization group (DMRG) algorithm [27] to compute the ground state of periodic chains up to 108 sites. In this case, we implement the constraint by giving a large penalty to the states which are not allowed in the Hilbert space. We also present results for the experimentally realized open chain scenario by simulating open chains up to 718 sites with a 1-site DMRG algorithm formulated in the matrix product state (MPS) language, which allows us to realize the constraint exactly by representing efficiently the global projector on the constrained Hilbert space as a matrix product operator (MPO).

Besides the very rich ground state physics, constrained quantum systems have recently attracted considerable attention due to their peculiar dynamical properties. As first observed in the Rydberg atom experiment realized in Ref. [4], the Hamiltonian Eq. (3.1) generates an anomalously slow dynamics starting from specific initial states. The initial state chosen in the experiment was a simple product state in which the hard-bosons occupy every other site. Although this state has very high expectation value on the Rydberg Hamiltonian (w.r.t. to the ground state energy), the time-evolution of local observables did not show signature of thermalization within the experimentally accessible time-scales. This fact is at odds with the general expectation provided by the eigenstate thermalization hypotesis (ETH) [28, 29, 30]: the dynamics of initial states with finite energy density should rapidly thermalize to the microcanonical ensemble at energy $E = \langle\psi_0|H|\psi_0\rangle$. This is ensured by assuming the following form for the matrix elements of local observables between nearby energy eigenstates $|E_\alpha\rangle$

$$\langle E_\alpha|O|E_\beta\rangle = \bar{O}(E)\,\delta_{\alpha\beta} + e^{-S(E)}\,f(E,\omega)R_{\alpha\beta}. \tag{3.4}$$

Here $\bar{O}(E)$ and $e^{S(E)}$ are the expectation value of the observable O and the density of states at energy $E = (E_\alpha + E_\beta)/2$, which are both expected to be smooth function of E for large systems. $f(E, \omega)$ is an unknown function of E and of the energy difference $\omega = E_\alpha - E_\beta$ and $R_{\alpha\beta}$ is a random variable with zero mean and unit variance. Subsequent theoretical work [13] demonstrated that the essential ingredients inducing an ETH violation in the Rydberg Hamiltonian are already present in the simplified, hard-constrained Hamiltonian Eq. (3.3). In particular, the source of this violation was identified in a small ($\sim L$) subset of atypical eigenstates dubbed quantum many-body scars.

In Sec. 3.2, starting from a different perspective, we show that the dynamics of Rydberg excitations in these chains is exactly mapped onto a spin-1/2 quantum link model (QLM), a $U(1)$ lattice gauge theory (LGT) where the gauge fields span a finite-dimensional Hilbert space, equivalent to a lattice Schwinger model in the presence of a topological term [31]. Gauge theories are key for our understanding of fundamental interactions. An intense theoretical activity aimed at quantum simulating LGTs via atomic quantum systems [32, 33, 34] has already led to the first door-opener experimental realization in a system of four trapped ions [35]. However, there is presently no experimental evidence that atomic systems can be used to simulate LGTs at large scales. In this respect, our work serves as a remarkably straight route towards this goal, providing an immediate interpretation of the experiment of Ref. [4] as the first large-scale quantum simulation of a LGT at the edge of classical computational methods [36].

The key element of our mapping is that gauge invariance has a natural counterpart in the Rydberg blockade mechanism, which constrains the Hilbert space in the same way as Gauss law does in gauge theories. From a theoretical viewpoint, the mapping offers a hitherto unexplored perspective on the anomalously slow relaxation observed in experiments: the long-lived oscillations in the population of excited Rydberg atoms correspond to a string inversion, a phenomenon which is directly tied to string breaking [37, 38, 39] prototypical of gauge theories including dynamical matter. The mapping indicates that this phenomenon has a natural interpretation in the LGT framework, and suggests the occurrence of slow dynamics in other $U(1)$ gauge theories, such as higher-spin QLMs [40], Higgs theories [41, 42], and the Schwinger model [43, 44]. These theories have been widely discussed in the context of Schwinger pair production taking place at high-intensity laser facilities, thus providing a highly unexpected, direct link between apparently unrelated experimental platforms [45, 39, 46, 47, 48].

We discuss the generality of this type of quantum evolution by extending our analysis to other relevant instances of "slow dynamics", characterized by the absence of relaxation on all time scales corresponding to any microscopic coupling present in the system. As initial states, we focus on those consisting of particle-antiparticle pairs, corresponding to regular configurations of the Rydberg-atom arrays with localized defects, which are accessible within the setup of Ref. [4]. We show that these defects propagate ballistically with long-lived coherent interference patterns. This behavior is found to be governed by special bands of highly excited eigenstates characterized by a regularity in the energy-momentum dispersion relation. These findings open up a novel perspective which complements and extends towards gauge theories recent approaches to slow relaxation in Rydberg-blockaded atomic chains [13, 12, 49, 14, 16, 15].

So far the discussion was focused on the slow dynamics emerging from a specific initial state, in a lattice gauge theory. The final section of this chapter is devoted to study the role of gauge symmetry in disordered systems that exhibit ergodicity violations in a strong sense, i.e. that do not depend on the choice of the initial state. In the quantum realm the notion of ergodicity is strictly tied to the eigenstate thermalization hypothesis Eq. (3.4). The latter provides a sensible justification for the use of microcanonical ensembles in place of their Hamiltonian dynamics to compute long term averages of observables. An established mechanism to circumvent thermalization is provided by Anderson localization [50]. The latter describes how non-interacting systems can feature a dynamical phase in which diffusion (and hence transport) and ergodicity

are suppressed without any need to fine-tune the Hamiltonian to an integrable one. Remarkably, this mechanism has been shown to survive the introduction of interactions at the perturbative level [51, 52], a phenomenon dubbed many-body localization (MBL) [53, 54, 55, 56]. However, owing to the fundamentally more complex nature of many-body theories, establishing the breakdown of ergodicity and characterizing the ergodic/non-ergodic transition in generic, interacting microscopic models has proven challenging. At the practical level, this is due to the fact that quantum chaos (which underlies ETH) is ultimately linked to the full spectral content of a theory [57], where the applicability of analytical techniques is less established with respect to low-energy studies [58, 59, 51, 52, 60, 61, 62, 63, 64, 65].

An archetypal example in this field has been the one-dimensional (1D) Heisenberg model with random fields [66], where, in the absence of SU(2) symmetry [67, 68, 69, 70], first signatures of the breakdown of ergodicity were established at finite volume. Despite a follow-up impressive numerical effort [71, 72, 73, 74, 75, 76], the precise location of the localization transition in this and similar microscopic models is still actively debated. A systematic drift of the would-be critical disorder strength was noticed already as early as in Ref. [66]. The finite-size scaling theory close to the phase transition is also still far from being satisfactory, with the numerically extracted critical exponents [73, 74, 77] at odds with strong disorder renormalization group predictions [78, 79], and not compatible with the Harris criterion [80, 81]. A recent analysis based on a different finite-size scaling ansatz was proposed where the transition point drifts *linearly* with system sizes [82], which however seems to apply, at small sizes, also to models where localization is demonstrated on solid grounds [83, 84]. On top of this, a recent analysis discussed how large a system size one should analyze to go beyond the transient behavior in numerical or experimental studies [85]. The challenge is thus to identify generic mechanisms where, oppositely to the case of spin chains, interactions and disorder can cooperate (rather than compete) in establishing ergodicity breaking, potentially leading to completely novel scenarios in terms of finite-size scaling relavant to exact simulations and experiments [86, 87].

In Sec. 3.3, we show how lattice gauge theories (LGTs) [88, 89] provide a framework within which the transition between ergodic and non-ergodic behavior can be studied using conventional, well controlled numerical methods. The key element of this observation is the *cooperative* effect of disorder and Coulomb law, which leads to a localization phenomenon that - as we show below - is parametrically different from what observed in other models. In concrete, we illustrate this mechanism in the context of the 1D lattice Schwinger model - quantum electrodynamics in 1D. By analyzing spectral correlations in the presence of a random charge background, we demonstrate how $U(1)$ lattice gauge theories display key signatures of ergodicity breaking, allowing to draw a sharp boundary for the ergodic regime for sufficiently strong gauge couplings, at the system sizes accessible via exact diagonalization.

3.1 Quantum phase transitions in a Rydberg atom chain

In this section we consider the hard-constrained Hamiltonian in the family of operators in Eq. (3.3) with $d = 2$. We interpret the many-qubit systems arising from the Rydberg atom setup as a chain of hard-core bosons where each site can either empty or occupied. We study the ground state and the low energy spectrum in the vicinity of two different melting transition. The first transition is a single point, located on an integrable line, which is known to be well described by the 3-states Potts model universality class. The second occurs in the regime $V_2 \to \infty$, and understanding its nature is the main purpose of this work. The reason for the choice of this regime is threefold: it is the farthest regime from the Potts critical point, it may allow for a comparatively larger incommensurate phase (if any) thanks to the fact that the role of perturbations moving away from the exactly solvable line is typically larger; it is of easy experimental access; it is amenable to exact simulations up to comparatively larger sizes with respect to the rest of the phase diagram.

The structure of this section is the following. In Sec. 3.1.1, we present the Hamiltonian of the model, reviewing in detail previous theoretical results. In Sec. 3.1.2, we discuss the methods we employ, and investigate the vicinity of the Potts transition point, in particular, performing an analysis based on level spectroscopy. In Sec. 3.1.3, we study in detail the doubly blockaded regime. In Sec. 3.1.4, we draw our conclusions and discuss some future perspectives.

3.1.1 Model Hamiltonian and review of previous results

The Hamiltonian of the FSS model is given by

$$H = \sum_{i=1}^{L}(d_i + d_i^\dagger) + U\sum_{i=1}^{L} n_i + V\sum_{i=1}^{L} n_i n_{i+2} \tag{3.5}$$

where $d_i^\dagger$ (d_i) is the creation (destruction) operator for a hard-core boson on site i and $n_i = d_i^\dagger d_i$. In terms of the experimentally realizable Hamiltonian in Eq. 3.1 the $U = 2\delta/\Omega$ and V can be tuned by varying the parameter R_b defined in Eq. (3.2). The Hilbert space we consider is subjected to the constraint $n_i n_{i+1} = 0$; namely, two particles cannot occupy NN sites. When this restriction is imposed, the number of states $\dim\mathcal{H}_L$ in the Hilbert space for a chain of length L satisfies, in the case of open boundary conditions (OBC), the recursive equation

$$\dim\mathcal{H}_L = \dim\mathcal{H}_{L-1} + \dim\mathcal{H}_{L-2} \tag{3.6}$$

whose solution is the Fibonacci sequence, which behaves asymptotically for large L as $\dim\mathcal{H}_L \sim \phi^L$, where $\phi = 1.6180...$ is the golden ratio. The dimension of $\mathcal{H}$ becomes even smaller in the limit $V \to \infty$, which is equivalent to saying that there have to be at least two empty lattice sites between two particles, i.e., $n_i n_{i+1} = 0$ and $n_i n_{i+2} = 0$. It is easy to see that in this case $\dim\mathcal{H}_L$ satisfies the equation

$$\dim\mathcal{H}_L = \dim\mathcal{H}_{L-1} + \dim\mathcal{H}_{L-3} \tag{3.7}$$

which asymptotically means $\dim\mathcal{H}_L \sim \zeta^L$, with $\zeta = 1.4655...$ Notice that when V ranges in $[0, +\infty)$ the experimental parameter R_b ranges between 1 and 2.

The model was first proposed as the quantum version of the 2-dimensional classical hard-square model [6], which is known to host two integrable lines [90]. One of the two lines crosses the period-three-to-disorder line exactly at the Potts critical point, whose location is thus known analytically. The classical-to-quantum mapping results in a constrained quantum Hilbert space

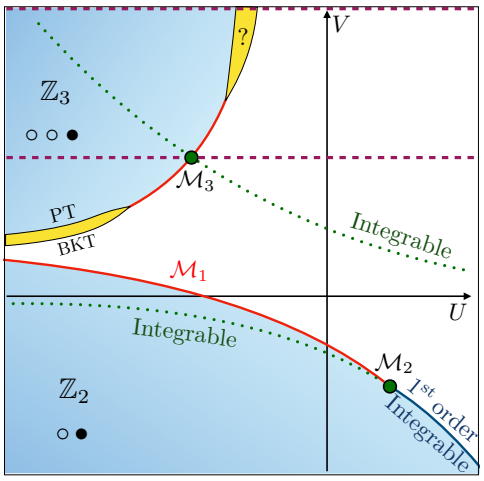

Figure 3.2: Phase diagram of the model Hamiltonian Eq. (3.5). Ordered phases are colored in light blue. Red (blue) lines indicate second (first) order phase transitions. On the green dotted lines the model is integrable. The integrable line in the lower half plane is on top of the transition line when the transition is of the first order. The two lines separate at the tricritical point $\mathcal{M}_2$, where the transition becomes continuous. After this point, the second-order phase transition belongs to the Ising universality class. The integrable line in the upper half plane crosses the second-order transition line exactly at the $\mathcal{M}_3$ critical point, belonging to the Potts model universality class. Below this point, on the transition line, a gapless phase (lower yellow region, not in scale) opens, enclosed within a Pokrovsky-Talapov (PT) and Berezinskii-Kosterlitz-Thouless (BKT) transition. Above this point, the opening of a gapless phase (upper yellow region, not in scale) is under debate. Purple dashed lines are studied in this work.

which is not in product form. As already noted in Ref. [9] and further discussed below, the peculiar way order is realized in the system causes extremely strong finite-size effects, especially when OBC are applied. This poses challenges for tensor-network based techniques, which usually rely on these boundary conditions, since the computational effort must be increased in order to access larger system sizes. Oppositely, the milder scaling of the Hilbert space dimension allows us to exactly diagonalize the system up to lengths which roughly double the usual lengths accessible in spin chains. Since periodic boundary conditions (PBC) eliminate boundary effects, in addition to providing momentum symmetry for a direct diagonalization of the quantum Hamiltonian, they will be employed throughout this work, with the exception of the tensor network simulations presented in Sec. 3.1.3.

The phase diagram of the model is depicted in Fig. 3.2. The two integrable lines are parametrized by

$$V(U+V)=1. \tag{3.8}$$

One of the two lines is defined on the upper half plane (U,V), and crosses the order-disorder transition line exactly at the Potts critical point mentioned above, for $V=V_c=[(\sqrt{5}+1)/2]^{5/2}$; it is thus described at low energies by the third conformal field theory in the minimal series, $\mathcal{M}_3$ [21]. The gapped ordered phase extends to a region in the quadrant $V>0$, $U<0$, where the order-disorder transition is not always a sharp transition. In particular, it was shown in Ref. [6] that in the limit case $U\to-\infty$ and $V=-U/3$ the separation line is in fact a thin gapless phase (yellow region in Fig. 3.2) characterized by the Luttinger liquid (LL) universality class. The transition from the ordered phase to the gapless phase belongs to the Pokrovsky-Talapov (JNPT) universality class [23, 24], and has dynamical critical exponent $z=2$. Conformal invariance is then restored in the continuum description and the transition from the gapless phase to the disordered phase is of the Berezinskii-Kosterlitz-Thouless type [22]. Moreover, a recent detailed analysis [9] exhibited strong numerical evidence that the very same picture persists on the order-

disorder transition line, up to a Lifshitz point located below the integrable line, beyond which the transition is sharp and of the chiral Huse-Fisher type [25]. However, the precise location of the Lifshitz point could not be estimated. The authors also confirmed the position and nature of the Potts critical point by computing the correlation length critical exponent ν coming from both phases.

What happens above the integrable line is more controversial. A DMRG-OBC study [9] is in favor of a chiral transition up to another Lifshitz point after which a LL phase opens again, with a PT transition on the ordered side and a BKT transition on the disordered side. The width of the intervening LL phase was estimated at the order of 0.001. It was also noted that, above the Potts point, boundary effects are sizable at system sizes on the order of several hundred sites, as testified by an anomalous scaling of the von Neumann entropy. Instead, an exact diagonalization (ED) study [8], using PBC, indicated that there is no Lifshitz point, and the transition remains chiral up to $V = \infty$, with a dynamical critical exponent $1 < z \lesssim 1.33$.

In what follows we will focus on two lines at constant V (purple dashed lines in Fig. 3.2). The phase diagram on the first line is very well understood and we will use it as a benchmark to test field theory predictions in this exotic quantum chain. The second line is located at $V = \infty$ and, as discussed above, its phase structure is still under debate.

3.1.2 Potts critical point

In this section, we study the finite-size properties of the Potts critical point. This is important not only to test some of the methods we are going to employ in the following sections, but also to understand which universal properties can be experimentally measured with the available setups of $\simeq$50 spins. Moreover, it is of theoretical interest, as there are very few lattice realizations of Potts criticality that can be studied in such a systematic fashion [91, 92, 93].

The CFT behind the Potts model universality class is one of the modular invariant realizations of the third model in the minimal series: $\mathcal{M}_3$ [94]. Its central charge is 4/5 and the most relevant primary fields, namely the energy density and the order parameter, carry anomalous dimensions $\eta_\varepsilon = 4/5$ and $\eta_\sigma = 4/15$. These two numbers imply that the correlation length and order parameter critical exponents are $\nu = (2 - \eta_\varepsilon)^{-1} = 5/6$ and $\beta = \nu\eta_\sigma/2 = 1/9$.

The position of the Potts critical point in the phase diagram of the quantum Hamiltonian in Eq. (3.5) is known exactly by integrability arguments [6] and its location has been checked numerically both via gap scaling analysis [8] as well as from vanishing inverse correlation length [9]. Its critical exponents have been computed on the lattice, and a clear signature of the underlying CFT has been observed [6, 8, 9]. However, the low-energy spectrum of the lattice Hamiltonian has never been matched with the CFT one and a full characterization of the phase transition has never been given. Furthermore, contrary to the lattice Potts model, the $\mathbb{Z}_3$ symmetry is not an exact global symmetry of the FSS model. It is thus non-trivial to identify the whole operator content from the energy eigenvalues on the lattice.

Before performing level spectroscopy, we test some of the methods we will employ in the next section to witness second-order phase transitions without any assumption on the spacetime symmetry of the underlying field theory, namely non-analyticity in the quantum concurrence [95, 96] (which is a measure of single spin entanglement) as well as in the fidelity susceptibility [97, 98]. The latter also allows us to extract the critical exponent ν of the ordered phase [99, 100, 101]. We then compute the central charge of the CFT from the logarithmic scaling of the entanglement entropy [102] and we show that the CFT regime is reached with system sizes accessible to present experiments. We proceed by matching momentum symmetry sectors on the lattice with $\mathbb{Z}_3$ sectors in the CFT. We match several low-lying eigenvalues with the corresponding primary fields and we discuss the finite-size scaling corrections with respect to CFT predictions. Finally, we extract the anomalous dimension η_σ of the order parameter by comparing its lattice two-point function

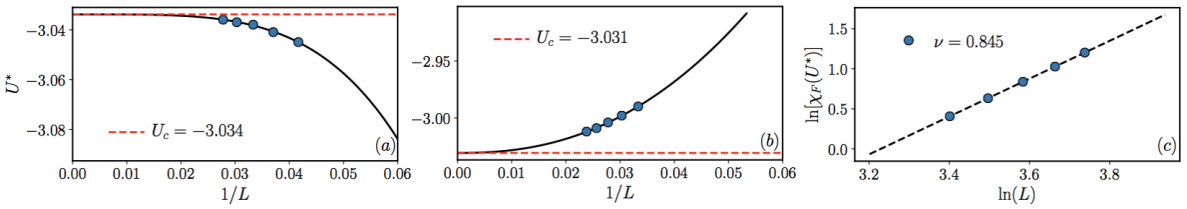

Figure 3.3: (a) Power-law fit of the peak position $U^*(L)$ of the first derivative of the concurrence Eq. (3.9), for L from 24 to 36 sites. The scaling exponent extracted from this range of system sizes is $\gamma = 4.0 \pm 0.1$, but it is not stable including smaller sizes. The critical position we get from the fit is $U_c = -3.03 \pm 0.04$. (b) Power-law fit of the peak position $U^*(L)$ in the fidelity susceptibility Eq. (3.10), for L from 30 to 42 sites. The result is stable when smaller system sizes are included. Taking into account small variations with respect to the range of lengths employed in the fit, the scaling exponent and the critical point position we get are $\gamma = 2.4 \pm 0.1$ and $U_c = -3.03 \pm 0.01$. (c) Scaling of the maximum of χ_F according to Eq. (3.11) for L from 30 to 42 sites. The correlation length critical exponent slightly increases when smaller system sizes are included in the fit. By taking into account variations with respect to the range of lengths fitted we get $\nu = 0.84 \pm 0.01$, in good agreement with the exact value $\nu = 5/6 = 0.8333...$

with the one of a CFT on a ring [21].

Critical point location. As we will see below, in order to locate the critical point, it is useful to utilize a procedure which is not biased by any assumption on the nature of the phase transition, such as conformal invariance and a consequent scaling of the gap with a dynamical critical exponent $z = 1$. Here we use two methods based on the nonanalytic behavior displayed by generic functions in the presence of continuous phase transitions. The concurrence is a measure of entanglement for spin systems [96, 103], and is defined as

$$C = \max(0, \lambda_1 - \lambda_2 - \lambda_3 - \lambda_4) \tag{3.9}$$

where the λ_i are the square roots of the eigenvalues in decreasing order of the matrix $\sqrt{\rho_{i,j}}(\sigma^y \otimes \sigma^y)\rho^*_{i,j}(\sigma^y \otimes \sigma^y)\sqrt{\rho_{i,j}}$, where $\rho_{i,j}$ is the reduced density matrix of two sites located at positions i and j (here we show results for $j = i + 2$) [1]. The function $C(U)$ is expected to have an infinite derivative at a gapless critical point in the thermodynamic limit [95, 96]. At finite size, the derivative $\partial_U C$ has a peak which sharpens with increasing system size at a value $U^*(L)$ which converges to the critical point when $L \to \infty$.

In Fig. 3.3(a), we plot the value of the position of the peak of $\partial_U C$, $U^*(L)$, at the Potts critical point as a function of $1/L$. The position of the critical point at $L \to \infty$, U_c, is obtained by fitting $U^*(L)$ with the power-law function, $U^*(L) = U_c + A/L^\gamma$. The best-fitting exponent for system sizes from 24 to 36 sites is $\gamma = 4.0 \pm 0.1$ and the extracted position of the critical point is $U_c = -3.03 \pm 0.04$, in good agreement with the exact value $U_c = -3.0299\ldots$. Note however, that the result is not stable when smaller system sizes are included in the fit. We attribute this instability to the limited number of sizes we can reliably simulate in the scaling regime, due to the challenging nature of the calculation of concurrence.

Another quantity that is used to locate and characterize the critical point is the fidelity susceptibility

$$\chi_F = \frac{-2 \ln |\langle \psi_0(U) | \psi_0(U + \delta U) \rangle|}{\delta U^2} \tag{3.10}$$

where $|\psi_0(U)\rangle$ is the ground-state wave function for a fixed value of U. As the derivative of the

[1] Since the Hilbert space is not a product of single-site Hilbert spaces, in order to compute the reduced density matrix we simply plunge back the ground state of the system into the full Hilbert $(\mathbb{C}^2)^{\otimes L}$.

concurrence, χ_F exhibits a peak at the position $U^*(L)$, when plotted as a function of U. The size scaling of $U^*(L)$ provides an alternative approach to establish the position of the critical point, U_c; see Fig. 3.3(b). In contrast to the concurrence, the numerical calculation of the fidelity is less expensive and allows us to reach system sizes up to $L = 42$. This yields a best-fitting result which is stable against the range of system sizes included in the fit for $L \geq 24$. The best-fitting parameters we get considering lengths from 27 up to 42 sites gives $U_c = -3.03(1)$, where the error takes into account variations against the system sizes included in the fit. Furthermore, a scaling theory for the height of the peak of χ_F does exist [100, 101] and allows us to obtain the correlation length critical exponent via

$$\chi_F(U^*) \sim L^{2/\nu}. \tag{3.11}$$

Note that this power-law scaling is independent of the value of the dynamical critical exponent z. In this way we get a value of ν in perfect agreement with the expected value for the Potts model universality class; see Fig. 3.3(c).

Finally, we wish to mention a very peculiar fact which allows us to locate the critical point with arbitrary precision and arbitrary small system sizes: exactly at the critical point, the on-site boson density has vanishing finite-size corrections. The position of U_c can thus be obtained by measuring the boson density for different system sizes and tuning the couplings until size independence is observed. We believe that this fact is due to the integrable structure beyond the critical spin chain. In Fig. 3.4 (left), we report the finite-size scaling of the density at the critical point and for two values of U very close to it, together with the curve crossing of densities computed for different system sizes as a function of U for $V = V_c$, which allows a precise determination of the position of the critical U.

Entanglement entropy. Continuous, relativistic phase transitions in a 1D system display a logarithmic divergence of the entanglement entropy. Once conformal invariance is ensured, an inexpensive way to identify the universality class is by computing the coefficient of the logarithmic growth of the entanglement as a function of the subsystem size. This coefficient is known to be proportional to the central charge of the CFT [102], and for the case of half partition in PBC reads

$$S = \frac{c}{3} \ln L + A. \tag{3.12}$$

In Fig. 3.4 (right) (a), we plot the entanglement entropy for the critical values (U_c, V_c) analytically known. This result shows how moderate sizes are already yielding a very precise value for the central charge. In Fig. 3.4 (right) (b), the effective central charge, defined as [104]

$$c = 3 \, \frac{S(2L) - S(L)}{\ln 2}, \tag{3.13}$$

is plotted for fixed $V = V_c$, and varying U across the transition. The central charge exhibits a bell-shape dependence on U, observed in other cases as well [105], with a peak which is approaching the expected position marked with a green dashed line. Note that different bells touch only at the critical point, which is the only value of U at which the effective central charge is not decreasing with increasing system size. This is in agreement with Zamolodchikov's theorem [106] in the presence of a single critical point.

CFT level spectroscopy. Computing the entanglement entropy is a convenient way of extracting universal information from a quantum spin chain, since it does not involve non-universal parameters like the sound velocity. However, the central charge alone does not uniquely identify

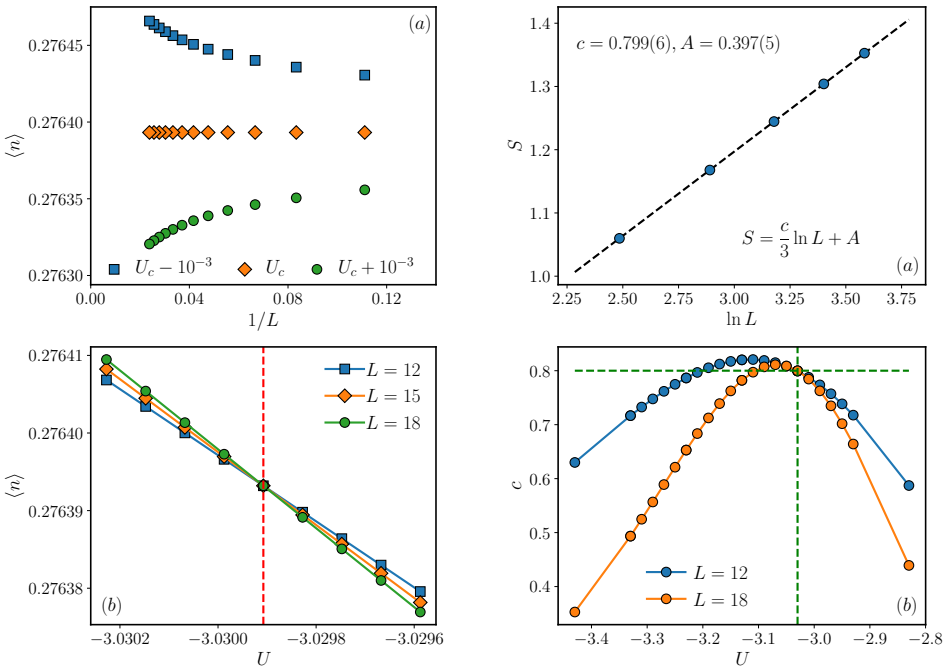

Figure 3.4: **Left.** (a) Finite-size scaling of the boson density at the transition point and close to it. Exactly at the transition point, the density does not scale. (b) Boson density as a function of U for $V = V_c$ and different chain lengths. The lines sharply cross at the transition point (dashed red line) for any system size, since finite-size corrections vanish exactly at the critical point. **Right.** (a) Finite-size scaling of the entanglement entropy of a half partition, for L from 12 to 36 sites. The slope is the one expected from CFT already for system sizes $L \leq 24$, indicating negligible finite-size corrections to the CFT predictions Eq. (3.12). (b) Effective central charge as defined in Eq. (3.13). The peak is sharpening as the system size is increased and the peak position is moving towards the expected value $U_c = -3.0299...$. Curves for different lengths cross almost exactly at this value of U, indicating the presence of a single critical point in which the effective central charge is nondecreasing.

the CFT. The full operator content for a CFT on a ring of length L can be determined from the energy levels, which are spaced according to the formula [21]

$$E_n - E_{GS} = \frac{2\pi v}{L}(\Delta + m + \overline{\Delta} + \ell) \qquad m, \ell \in \mathbb{N} \tag{3.14}$$

where n is a label for the nth excited state, $(\Delta, \overline{\Delta})$ are the weights of the two chiral representations of the Virasoro algebra in the CFT, and v is the non-universal sound velocity, which depends on the microscopic realization of the CFT. The ground-state energy itself is affected by universal finite-size corrections proportional to the central charge,

$$E_{GS} = \varepsilon_0 L - \frac{\pi v c}{6L}, \tag{3.15}$$

where ε_0 is the ground-state energy density in the thermodynamic limit. Below, we analyze the spectrum obtained by exact diagonalization of the lattice Hamiltonian, for systems with $L \leq 42$, in each momentum sector [2]. After extracting the central charge from the entropy scaling, Eq. (3.15) allows us to compute the sound velocity. The result we obtain by fitting

[2]Note that, in the $k = 0$ sector, we did not split the spectra according to their reflection symmetry, since the latter seems not to correspond to charge conjugation symmetry of the two charged sectors

the ground-state energy for L up to 42 is $v = 2.49(7)$. Another possibility is to fit directly the dispersion relation of the low-energy states, which should be linear and proportional to v. A sample of the low-lying spectrum is shown in Fig. 3.5 (left) (a) for a system of $L = 39$. To obtain the velocity, we perform a linear fit of the smallest available momentum at each system size. The value of v obtained in this way is different for right and left moving particles, and in both cases deviates from the velocity extracted from the ground state energy by a few percent (see Fig. 3.5 (left) (b)). This is caused by large finite-size corrections affecting these eigenvalues. This chiral symmetry breaking at finite size might be caused by the chiral perturbation driving the system on the second-order transition line. Interestingly, by taking the average of the corresponding right and left energy levels, the dominant terms of these corrections cancel out, and full agreement with the value extracted from the ground-state energy scaling is recovered.

Once the sound velocity is known, Eq. (3.14) can be used to extract all the conformal dimensions from the gaps in the low-energy spectrum of the lattice Hamiltonian. The operators in the CFT are labeled by a $\mathbb{Z}_3$ quantum number [3] $Q = 0, \pm 1$ [92, 93]. Since the model does not have an exact $\mathbb{Z}_3$ symmetry, we have to find an alternative way of labeling the low-lying states.

The $Q = \pm 1$ sectors have to be degenerate and this degeneracy is exact at finite size in the spectrum of the lattice Hamiltonian Eq. (3.5) with PBC. This fact is ensured by the presence of the non-commuting momentum and reflection symmetries, which implies that eigenstates of H with momenta K and $-K$ have the same energy. In the $\mathbb{Z}_3$-ordered phase and close to it the states with momentum $K = \pm 2\pi/3$ happen to be the lowest-energy excitations above the ground state and the Brillouin zone appears to be split in three, as shown in Fig. 3.5 (left) (a). It is thus clear how to identify the $\mathbb{Z}_3$ symmetry sectors: the neutral sector and the two charged sectors consist of the energy levels close to $K = 0$ and $K = \pm 2\pi/3$, respectively. This labeling naturally connects to the symmetry-breaking structure of the ground-state manifold within the ordered phase.

The operator content of the two non-degenerate symmetry sectors in the CFT with PBC is the following [92] :

$$Q = 0: \quad (0,0), \left(\frac{2}{5}, \frac{2}{5}\right), \left(\frac{7}{5}, \frac{2}{5}\right), \left(\frac{2}{5}, \frac{7}{5}\right), \left(\frac{7}{5}, \frac{7}{5}\right), (0,3), (3,0), (3,3). \tag{3.16}$$

$$Q = \pm 1: \quad \left(\frac{1}{15}, \frac{1}{15}\right), \left(\frac{2}{3}, \frac{2}{3}\right). \tag{3.17}$$

The eigenvalues of the lattice Hamiltonian are then spaced according to Eq. (3.14) and they correspond to the CFT operators above, with all their descendants $(\Delta, \overline{\Delta})_{(k,\ell)}$. However, not all the descendants are allowed and their degeneracy can be computed starting from the Rocha-Caridi formula [93]. The momentum of these states in the CFT is instead given by

$$\tilde{P} = \frac{2\pi}{L} P = \frac{2\pi}{L}(\Delta + m - \overline{\Delta} - \ell) \qquad m, \ell \in \mathbb{N}. \tag{3.18}$$

Note that the CFT momentum is not the lattice momentum for this Hamiltonian. The CFT momentum on the lattice is measured starting from the ground states of each $\mathbb{Z}_3$ sector, which we label by $P = 0$ (see Fig. 3.5 (left) (a)).

We now proceed with the matching of the low-energy gaps on the lattice with the CFT

[3] The full symmetry group of the Potts model is the permutation group $S_3 = \mathbb{Z}_3 \times \mathbb{Z}_2$. However, the $\mathbb{Z}_2$ symmetry generator leaves invariant only $\mathbb{Z}_3$ neutral states, namely the ones labeled by $Q = 0$. Thus the $Q = 0$ sector splits into two subsectors labeled by a $\mathbb{Z}_2$ quantum number. Since this will not be necessary to identify gaps with operator, it will not be used in the text.

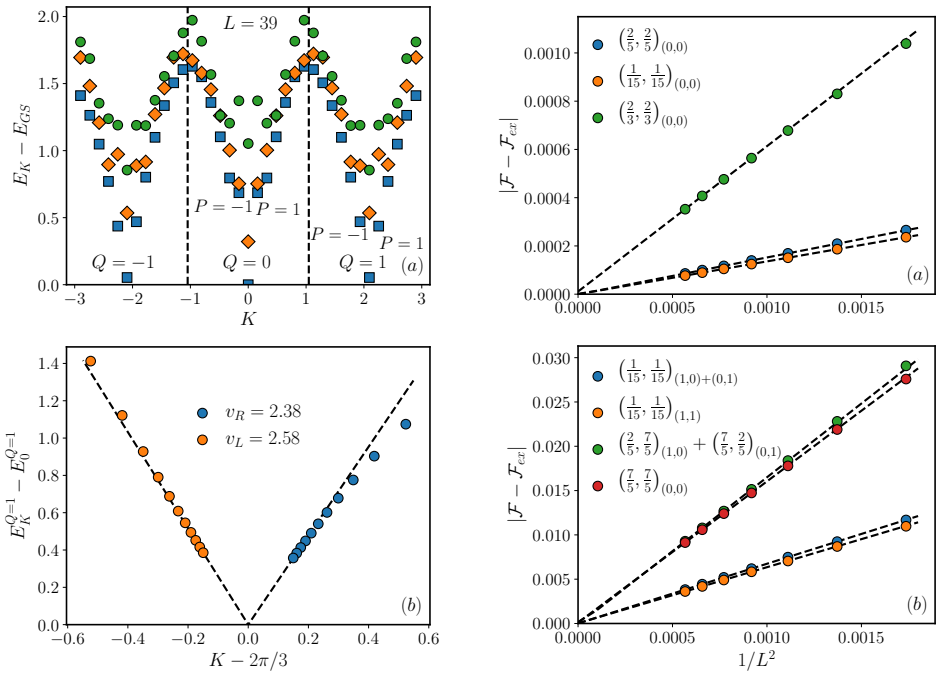

Figure 3.5: **Left.** (a) Lowest-lying eigenvalues of lattice momentum sectors for a chain of length $L = 39$. Eigenvalues close to $K = 0$ and $K = \pm 2\pi/3$ correspond to the $\mathbb{Z}_3$ sectors $Q = 0$ and $Q = \pm 1$ in the CFT. Conformal towers are already distinguishable and primary operators corresponding to each energy level can be easily guessed by comparing the lowest gaps with Eq. (3.18) together with Eqs. (3.16) and (3.17). (b) Linear fitting of the lowest eigenvalue close to the ground state of the $Q = 1$ sector for different system sizes from $L = 12$ to $L = 42$. The zero reference energy is taken as the ground-state energy of the sector for the given system size. Chiral symmetry is broken on the lattice, most likely because of an irrelevant perturbation which scales away in the thermodynamic limit. **Right.** Finite-size scaling of the universal function $\mathcal{F}$ in Eq. (3.19) with respect to the CFT expected value. (a) First and second gaps in the $Q = 1$ sector (orange and green) and first gap in the $Q = 0$ sector (blue). Finite-size corrections scale as L^{-2} with a coefficient of magnitude 10^{-4} for the first two gaps. (b) Third gap in $Q = 1$ sector (orange), first gap in the $Q = 1$ sector with momentum $P = \pm 1$ (blue), average of the second of fifth gap (green) and third gap (red) in the $Q = 0$ sector. The finite-size corrections are always quadratic in the inverse length of the chain upon appropriate average between CFT states not invariant under $(\Delta, k) \leftrightarrow (\overline{\Delta}, \ell)$.

prediction Eq. (3.14). Following Ref. [93], we define the universal function

$$\mathcal{F}(Q, P) = \frac{L}{2\pi v}\left(E_P^Q - E_{GS}\right) \underset{L\to\infty}{\sim} \Delta + k + \overline{\Delta} + \ell, \tag{3.19}$$

where Q and P are the CFT $\mathbb{Z}_3$ quantum number and momentum.

The results of the field correspondence are presented in Fig. 3.5 (right). Upon taking proper combinations of degenerate gaps, the finite-size corrections are of order L^{-2} for all the gaps, with a prefactor smaller than 10^{-3} for the lowest ones. We extrapolate the value of $\mathcal{F}$ by a two-parameter fit for system sizes up to $L = 42$. The agreement of the extrapolation with the CFT expected values is perfect once the sound velocity is tuned to $v = 2.49225$. In this respect, this method is the best way to estimate the sound velocity with the available system sizes.

The finite-size corrections to the universal function in Eq. (3.19) have been studied for this universality class in the 3-states Potts chain [92]. It was observed that their power-law exponent was 2 for most of the nondegenerate gaps and a number between 0.5 and 1 for other degenerate gaps. Here we argue that the latter corrections appear only in CFT states $(\Delta, \overline{\Delta})_{(k,\ell)}$ for which

$(\Delta, k) \neq (\bar{\Delta}, \ell)$. Upon taking the average of the eigenvalues in which Δ, k and $\overline{\Delta}, \ell$ are exchanged these dominant corrections vanish. Formally

$$\mathcal{F}(\Delta, \overline{\Delta}, k, \ell) = \Delta + \overline{\Delta} + k + \ell + \frac{A_{k,\ell}^{(\Delta,\overline{\Delta})}}{L^{\gamma}} + \frac{B_{k,\ell}^{(\Delta,\overline{\Delta})}}{L^2} + \dots$$
$$A_{k,\ell}^{(\Delta,\overline{\Delta})} = -A_{\ell,k}^{(\overline{\Delta},\Delta)} \tag{3.20}$$

To support this statement we give two examples where this is manifest. We take the lowest-lying pair of states in the $Q = 1$ sector of H with momentum $P = \pm 1$, i.e., $(1/15, 1/15)_{(1,0)}$ and $(1/15, 1/15)_{(0,1)}$. We then take the pair of states in the $Q = 0$ sector with momentum $P = 0$, i.e., $(2/5, 7/5)_{(1,0)}$ and $(7/5, 2/5)_{(1,0)}$. On the spin chain these two states correspond to the second and fifth excited state in the $K = 0$ sector. Their finite-size scaling is plotted in Fig. 3.5 (right) (b), where these two gaps are denoted by blue and green circles, respectively. The same agreement is observed with many other levels not reported here. We are able to match irrelevant CFT operators with large conformal weights as $(0, 3)$, $(3, 0)$, and $(3, 3)$ and the rule for which the dominant finite-size corrections cancel still applies.

Density and order parameter two-point functions. It is, in general, a difficult task to associate matrices on the lattice to primary fields in the CFT. The operator for which this procedure is trivial is the order parameter, namely the most relevant operator in the CFT which is not invariant under a symmetry transformation, i.e., the primary field $(1/15, 1/15)$. Its anomalous dimension is thus $\eta_\sigma = 4/15$ and its two-point function is expected to behave as a power law with this exponent. $\mathbb{Z}_3$ order is realized on the lattice through a period-3 boson-density wave; thus the (complex) order parameter takes the form [6]

$$O_i = n_i + e^{i2\pi/3} n_{i+1} + e^{-i2\pi/3} n_{i+2}. \tag{3.21}$$

Exploiting translational invariance, we can write its two-point function in terms of the density two-point function as

$$\langle O_r^\dagger O_0 \rangle = 3\langle n_0 n_r \rangle + e^{i2\pi/3}\big(2\langle n_0 n_{r+1}\rangle + \langle n_0 n_{r-2}\rangle\big) + \quad + e^{-i2\pi/3}\big(2\langle n_0 n_{r-1}\rangle + \langle n_0 n_{r+2}\rangle\big). \tag{3.22}$$

Although this quantity is expected to be purely real, a small imaginary part is obtained when determining $\langle O_r^\dagger O_0 \rangle$ from numerical data, which we neglect. In order to take into account finite-size effects, we compare our results to the two-point function of the order parameter for a CFT on a ring of length L. For a primary field with conformal weights $\Delta = \overline{\Delta} = \eta/4$, it reads [21]

$$\langle O(x) O(y) \rangle = \frac{A}{\left[L \sin\left(\frac{\pi(x-y)}{L}\right)\right]^{\eta}} = \frac{A}{L^{\eta}} G\left(\frac{x-y}{L}\right). \tag{3.23}$$

We obtain an estimate of η by fitting the lattice two-point function with the expression above and free parameters A and η. In Fig. 3.6(b) we plot the lattice expectation value for different system sizes, rescaled by multiplication by L^η (where the value resulting from the fit mentioned above is taken for the latter), obtaining perfect data collapse on the universal scaling function $G(x)$ in Eq. 3.23. In Fig. 3.6(a) we plot the connected density-density expectation value, which also fits perfectly the CFT expression, with the same scaling dimension as the order parameter.

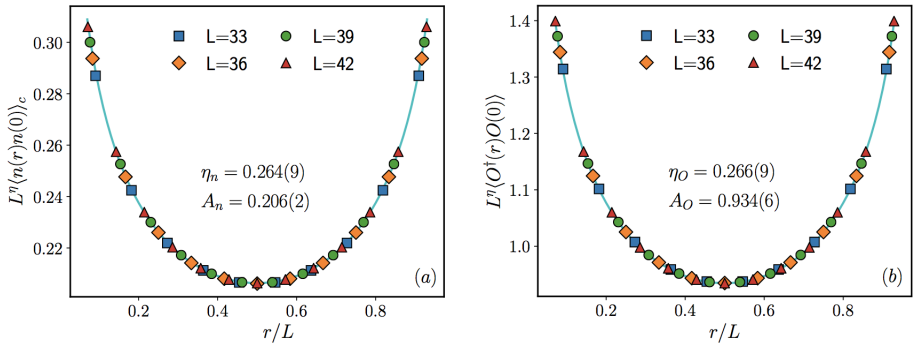

Figure 3.6: (a) Two-point function of the lattice order parameter Eq. 3.22 for different lengths L multiplied by L^η, with η fitted with the CFT expression Eq. 3.23. Estimate and error of the amplitude A and the exponent η are obtained upon taking the average of the results for different system sizes. (b) Same scaling as in (a) for the order parameter, which has the same scaling dimension as the density.

3.1.3 Doubly-blockaded regime

In this section, we study the phase diagram of the model Hamiltonian in Eq. (3.5) in the limit $V \to +\infty$. When $U \to -\infty$ the system is $\mathbb{Z}_3$-ordered and the order parameter in Eq. (3.21) is non vanishing. For finite and large negative U, the finite-size spectrum of the Hamiltonian behaves as in the usual $\mathbb{Z}_3$ spontaneously symmetry broken scenario: the ground state is nondegenerate and the first two low-lying excited states are exponentially close to it with a gap $\Delta \propto \exp(-L/\xi)$, where ξ is the correlation length. In the limit $U \to +\infty$ the ground state is the nondegenerate state with no bosons and $\mathbb{Z}_3$ symmetry is not broken. A transition between these two regimes is expected in the middle.

In what follows, we provide evidence that there are two continuous phase transitions located at $U_{c1} \lesssim -1.96$ and $U_{c2} \simeq -1.915$. At the first transition, the ground state of the system switches from a period-3 ordered state to a quasi-long-range-ordered, critical phase with incommensurate density-density correlations, known as the *floating phase*. At the second transition point, the system passes from the gapless critical phase to a disordered phase. For the first transition we compute, with different methods, the location of the critical point, the correlation length critical exponent ν, the dynamical critical exponent z, and the order parameter critical exponent β. We then show that the second transition is consistent with the BKT scaling ansatz, according to which the correlation length vanishes exponentially and the gap finite-size scaling at the transition point is affected by logarithmic corrections [107].

We finally show that for values of U inside the floating phase $U_{c1} \leq U \leq U_{c2}$ the scaling of the entanglement entropy is in agreement with the Luttinger liquid universality class, where the central charge c equals 1.

Quantum concurrence and fidelity susceptibility. By means of the same methods tested in Sec. 3.1.2, we now proceed to investigate the transition points by studying the behavior of the quantum concurrence and the fidelity susceptibility. These observables are not known to be generically sensitive to BKT transitions [108]; for this reason, we expect them to only diagnose the presence of the first of the two transitions mentioned above. We carry out exact diagonalization calculations up to $L = 54$ sites for ground-state properties, and consider sizes $L = 3n, n \in \mathbb{N}$ to avoid incommensurability effects.

The derivative of the concurrence exhibits the same behavior discussed in Sec. 3.1.2, namely a peak which is sharpening and moving towards the critical point, U_c, with increasing system size. In order to extrapolate the position of the maximum $U^*(L)$ for $L \to \infty$ we fit it with a power law

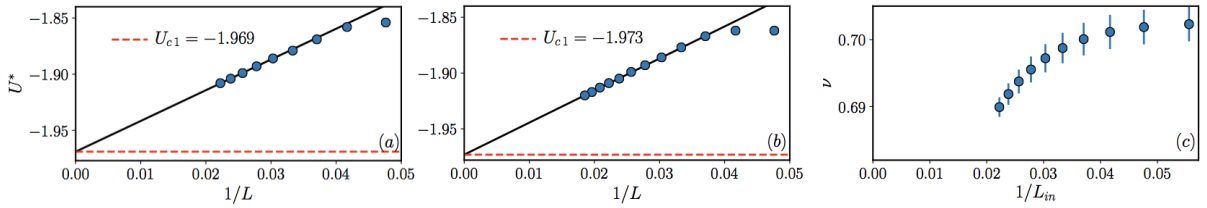

Figure 3.7: (a) Linear fit of the peak position $U^*(L)$ of the first derivative of the quantum concurrence Eq. (3.9) vs $1/L$, for L from 33 to 45 sites. The result of the fit is stable against the system sizes included in the fit and the critical position we obtain $U_{c1} = -1.969 \pm 0.005$, where the error takes into account variations with respect to the system sizes included in the fit. (b) Linear extrapolation of the peak position $U^*(L)$ vs $1/L$ in the fidelity susceptibility Eq. (3.10), for L from 39 to 54 sites. The result is stable when smaller system sizes are included and the critical point position we get is $U_{c1} = -1.973 \pm 0.005$. Error considerations are the same as in panel (a). (c) Correlation length critical exponent obtained from the scaling of the maximum of χ_F according to Eq. (3.11) for $L = L_{in}, L_{in} + 3, ..., 54$ as a function of L_{in}. The critical exponent decreases when smaller system sizes are excluded from the fit and saturation is not reached with the maximum lengths we can access. We note that a strong sensitivity of critical exponents with respect to system sizes was already observed in Ref. [9].

with scaling exponent $\gamma = 1$. In this way, we obtain a value $U_{c1} = -1.969 \pm 0.005$, which is stable against the range of system sizes included in the fit. By performing the same analysis for the peak of the fidelity susceptibility, Eq. 3.10, we get instead a critical value $U_{c1} = -1.973 \pm 0.005$. The results are plotted in Fig. 3.7(a)-(b). Both of these results illustrate the fact that finite-size effects in this regime are comparatively larger than close to the Potts critical point. In particular, employing sizes on the order of $L \simeq 30$ would lead to wrong estimates in both cases: the scaling regime for what concerns entanglement and wave-function properties seems to be only reached above $L = 33$.

Exploiting the known finite-size critical scaling of the peak of χ_F described by Eq. 3.11, we obtain a critical exponent $\nu = 0.70 \pm 0.05$. We stress that the latter estimate is very sensitive to the system sizes employed in the analysis. In particular, the larger the system sizes included in the fit, the smaller the ν obtained (see Fig. 3.7(c)). In Ref. [8], the value $\nu \simeq 5/7$ was extracted from data collapse of the gaps, assuming the value $z \simeq 4/3$ for the dynamical critical exponent. This evidence was used to conclude that the transition does not belong to the PT universality class, for which $\nu = 1/2$ and $z = 2$. Although the variation of the exponent with the system sizes considered seems very slow, we cannot exclude, based on our data, that it eventually reaches the value expected for a phase transition of the PT type, as found in Ref. [9] for the critical regime below the Potts point.

Critical point location through data collapse. We now exploit the finite-size scaling theory which applies in the proximity of a second-order phase transition [109] to extract the values of U_{c1}, z, and ν from the lowest spectral gap Δ. With this aim, we adopt an approach very similar to the one taken in Refs. [110, 111].

First we compute a universal scaling function F from ED data for Δ for different system sizes. This scaling function will depend on some unknown critical exponent γ and on the dimensionless ratio L/ξ, L being the system size and ξ the correlation length: $F = F(\gamma, L/\xi)$. We then assume a functional form for ξ in terms of the critical point position U_c and, if finite, of its critical exponent ν: $\xi = \xi(U, U_c, \nu)$. We use this functional form to express the scaling function F in terms of the variable $x = \ln(L/\xi) = x(L, U, U_c, \gamma, \nu)$. Finally, we combine data for F for different system sizes and we look for the values of U_c, ν, γ which produce the best data collapse. This is achieved by fitting $f(x) = F(e^x)$ with an arbitrary high-degree polynomial and minimizing

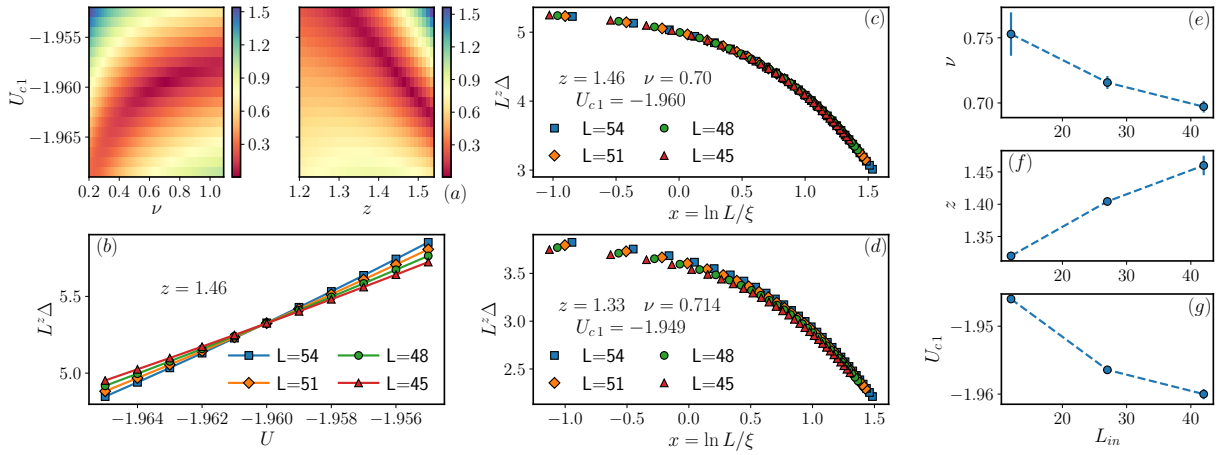

Figure 3.8: (a) Density plot of the square root of the sum of the squared residuals in the (ν, U_{c1}) and (z, U_{c1}) planes for the best-fitting values of z and ν, respectively. (b) Crossing of the gaps, upon multiplication by L^z for the best fitting z. The crossing indicates the position of the critical point. (c) Data collapse of ED numerical data, with $U \in [U_{c1} - 0.03, U_{c1}]$ with the parameters U_{c1}, z, ν which minimize the polynomial fit of the universal scaling function in Eq. (3.24). (d) Same as in (c), but with parameters U_{c1}, z, ν taken from Ref. [8]. (e)-(g) Critical exponents and critical point location obtained by applying the procedure described in Sec. 3.1.3 for sets of 5 system sizes $L = L_{in}, ..., L_{in} + 12$ with increasing L_{in}. The average is obtained by varying the size of the interval $[U_{c1} - \delta U, U_{c1}]$ with $0.01 \leq \delta U \leq 0.03$, the degree of the polynomial being fixed to 10. The errorbar is the standard deviation of the obtained results.

the sum of the squared residuals. By considering a full functional collapse instead of extracting the thermodynamic limit gap from single parameter data, this method copes relatively well with finite-size effects, even in the most critical BKT scenario. Indeed, in the latter case it allows us to locate transition points with a precision similar to (if not better than) approaches based on matching conformal dimensions [110, 111], which are based on assuming a specific functional dependence between lattice and field theory operators.

Since at a quantum phase transition all low-lying eigenvalues of the Hamiltonian are expected to be separated from the ground state by a power-law decaying gap $\Delta \sim 1/L^z$, where z is the dynamical critical exponent, we can obtain a scaling function by multiplying the lowest gap by L^z:

$$F\left(\frac{L}{\xi}\right) = L^z \Delta \,. \tag{3.24}$$

Assuming that the phase transition has a finite ν exponent, we have

$$\xi \sim (U_{c1} - U)^{-\nu} \,. \tag{3.25}$$

We can then find the best-fitting values of ν,z, and U_{c1} via the procedure described above. It is fundamental to check the stability of the result with respect to the degree of the polynomial, the size of the interval from which the value of $U < U_{c1}$ is taken, and most importantly, the system sizes which are included in the fit. We find that, in our case, the result is very stable with respect to the first two, but we get stability with respect to the system sizes we have at our disposal only if we include the largest ones (up to $L_{\max} = 54$). In particular, by including sizes of increasing magnitude we observe a decrease in our estimates for U_{c1} and ν, and an increase in the one of z. In Fig. 3.8(c) we show the result obtained by including all systems sizes $45 \leq L \leq 54$. The data collapse shows deviations of order 10^{-2}, and is considerably more accurate than the one performed with the values reported [8] with $L_{\max} = 36$ (see Fig. 3.8(d)).

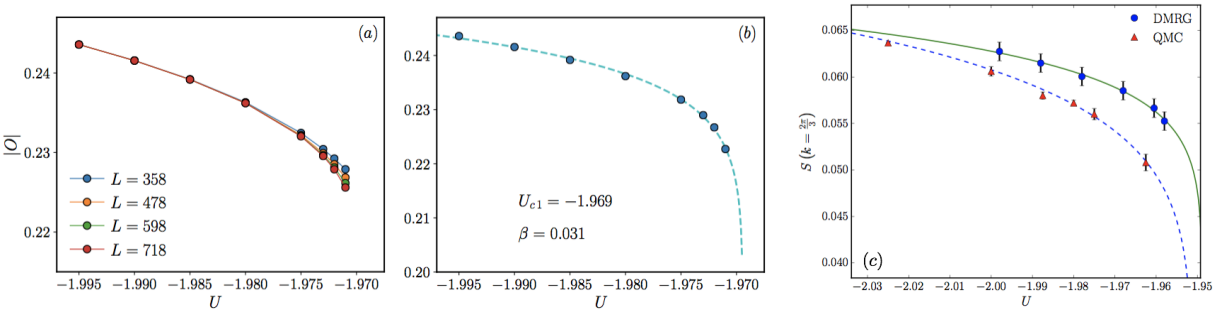

Figure 3.9: (a) Order parameter computed by averaging the one-point function $O_j = e^{i2\pi j/3} n_j$ on $L/2$ sites in the bulk. $\mathbb{Z}_3$ symmetry is spontaneously broken by the choice of the number of sites on the open chain, i.e., a multiple of 3 plus 1 site. The obtained order parameter does not scale with the system size for $U < -1.975$. (b) Infinite-size limit value of the order parameter, extrapolated in $1/L$ and power-law fit of the resulting curve. The obtained critical exponent and critical point position are $\beta = 0.031 \pm 0.005$ and $U_{c1} = -1.969 \pm 0.002$. (c) $S(2\pi/3)$ as a function of the parameter U. Symbols represent QMC (triangles) and DMRG (circles) for the ground state of model Eq. (3.5), extrapolated in the thermodynamic limit (see text). The dashed and solid line are a power-law fitting function (see text) used to interpolate QMC and DMRG results, respectively.

However, as shown in Figs. 3.8(e)-(f), the z and ν exponents are still varying with the system size. Although the trend exhibited by this data does not allow any extrapolation, we clearly see that the true scaling regime has not yet been reached. This leaves open the possibility that z and ν will eventually approach the values expected from a JNPT transition, namely 2 and 1/2, respectively [24]. The best estimates we can give from our data of critical exponents and critical point position are: $z = 1.48 \pm 0.1$, $\nu = 0.7 \pm 0.1$, $U_{c1} = -1.960 \pm 0.005$.

Since the methods employed over the next subsection will rely on assumptions, we find it useful to summarize the analysis performed so far. All diagnostics are compatible with the presence of a second order phase transition. The location and nature of the transition are extremely sensitive to the system sizes investigated. Regarding the location of the transition point, sizes up to $L \simeq 30$ are not sufficient to determine it, while the estimates using all three methods are rather stable after $L \simeq 45$. Entanglement-based methods return $U_{c1} = -1.973 \pm 0.005$ and $U_{c1} = -1.969 \pm 0.005$, respectively. The method based on gap collapse returns $U_{c1} = -1.960$; for this last method, it is challenging to include a rigorous error bar. However, it is worth noting that the best data collapse obtained up to $L = 36$ returns $U_{c1} = -1.949$, in agreement with Ref. [8]; this clearly signals that the critical point is drifting to considerably smaller values of U as size increases (see Fig. 3.8(g)), in agreement with the entanglement-based diagnostics.

A similar conclusion holds for the critical exponents: as clearly observed in the fidelity susceptibility scaling, even at sizes of order $L = 54$, the critical exponent has not yet reached its thermodynamic value. The data collapse of the finite-size gaps fully confirms this picture. This motivates the study in the next subsection, where we will employ different – but assumption-dependent – methods to determine some of the properties of this second-order transition. From the analysis performed here, we can anticipate that, even if larger system sizes are studied, depending on the observable, a systematic underestimation of the modulus of the critical point location $|U_{c1}|$ is expected. As we will see, this is particularly critical for the methods discussed in the next section.

Order parameter. In this section, we investigate the disappearance of the $\mathbb{Z}_3$ order across the second-order phase transition. We do so by utilizing three methods: a QMC and DMRG study with PBC, and a 1-site DMRG study with OBC. Our focus in the following will be on

correlation functions and the order parameter of the $\mathbb{Z}_3$ order. As such, we will be assuming that there is an exact mapping between the lattice operators describing the latter, and its field theory counterpart. While this condition is typically satisfyingly fulfilled for most lattice models displaying quantum critical behavior, we opted for a more conservative approach in the context of the FSS model in the doubly blockaded regime. The reason is that the constraint acts at the lattice spacing level irrespectively of how close one is to the critical point. This suggests that defining field operators that do not change at the lattice spacing level are nontrivial, making the connection between lattice and continuum not immediate. While this feature has no consequence on spectral and wave-function properties, it is highly likely that it affects the finite-size behavior of correlation functions.

We perform quantum Monte Carlo (QMC) simulations using a modified version of the worm algorithm [26], adapted to simulate Hamiltonians with off-diagonal terms such as those of the FSS model and with updates designed to automatically respect its occupation constraints. The method allows us to directly measure quantities such as energy, particle density, and the static structure factor:

$$S(k) \equiv \frac{1}{L^2} \sum_{i,j=1}^{L} e^{-ikr_{ij}} \langle n_i n_j \rangle \,, \tag{3.26}$$

where k is one of the allowed lattice momenta, and r_{ij} is the distance between sites i and j. In the $\mathbb{Z}_3$–ordered phase the structure factor will feature a peak at a wave vector $k = 2\pi/3$, corresponding to the periodicity of the $\mathbb{Z}_3$-periodic charge density waves. The value of the peak is equal to the squared $\mathbb{Z}_3$ order parameter in Eq. (3.21), and therefore follows a power-law behavior [112] $S(2\pi/3) \sim |U - U_c|^{2\beta}$ when approaching the critical point U_c from the ordered phase.

We obtained an estimation of the position of the critical point, as well as the critical exponent β, by interpolating the QMC results with the expected power-law behavior. We studied system sizes up to $L = 120$ sites and temperatures down to $T = 1/128$ (where the magnitude of the off-diagonal part of the Hamiltonian is taken as a unit of energy). Extrapolation in the inverse temperature has been employed to determine ground-state results where direct convergence in T (i.e., results identical within their uncertainty for one or more pairs of temperatures $(T, T/2)$) was not observed. Below $U = -1.96$, no further extrapolation in the system size was necessary, since direct convergence in size was always observed. Above this value, however, our extrapolated values were not fully converged in size and inverse temperature (also due to considerably slower MC dynamics). We therefore restricted our investigation to the $U < -1.96$ region. Figure 3.9 (c) shows the QMC data (triangles) as well as the power-law interpolation (purple line). The resulting values are $U_{c1} = -1.951(5)$, $\beta = 0.059(7)$ [4].

An independent estimate of the critical point and critical exponent β has been obtained by computing $S(2\pi/3)$ via DMRG (circles in Fig. 3.9 (c)) and performing the same extrapolation as above (solid green line in Fig. 3.9 (c)). We approximated the exact Hilbert space in the DMRG by giving a large penalty to not-allowed states. This is achieved by adding to the Hamiltonian a term $\lambda \sum_i n_i n_{i+1} + n_i n_{i+2}$, with $\lambda = 10^3$. Unfortunately, performing a rigorous extrapolation in $\lambda \to \infty$ is extremely difficult: the main reason is that, for increasingly larger values of λ, the diagonalization at each DMRG step becomes extremely sensitive to numerical errors due to the large difference in the matrix elements of the Hamiltonian matrix. However, for a fixed value of λ, we expect a difference on the order of $1/\lambda$ when comparing local observables, such as energies, with ED data. The absence of any other unforeseen source of systematic error due to the finite value of λ can be confirmed by direct verification. Indeed, with our choice of $\lambda = 10^3$, if we calculate the energy gap between the ground state and the first excited level for

[4] These confidence intervals only indicate the error in the fit; the same applies to the DMRG estimate of the same quantities.

$L = 54$ and $U = -1.950$, the discrepancy between DMRG and ED is of the (expected) order of $\epsilon_\Delta \approx 10^{-3}$. This check is very important because it allows us to understand that the limit $\lambda \to \infty$ is approached perturbatively. Despite this violation of the constraint which directly affects local observables, we obtain a good agreement with ED when we study other quantities such as entanglement entropy and central charge. For instance, using the same values of L and U, we obtain a difference in the central charge on the order of $\epsilon_c \approx 10^{-4}$ with respect to ED results. In our DMRG implementation, we take an elementary cell made of 3 sites in order to have a local representation of the $\mathbb{Z}_3$ order. This also allows us to discard 4 of the 8 states in the blocked DMRG-site. Simulations were performed by keeping the truncation error below 10^{-7} using up to 1000 DMRG states and ensuring that the energy variance of the ground state is of the same order of the truncation error.

We observe that DMRG results (after an extrapolation in $1/L$ of the squared $\mathbb{Z}_3$ order parameter for $84 \leq L \leq 120$) yields a larger value for $S(2\pi/3)$ than QMC, possibly due to the approximations required to impose the occupation constraint. The results of the extrapolation are $U_{c1} = -1.948 \pm 0.007$ and $\beta = 0.036 \pm 0.005$.

As a final test bed for the results above, we compute directly the order parameter in Eq. (3.21) by variationally optimizing the ground state with MPS methods on an open chain in which the constraint is implemented exactly. The method we use exploits the exact relation between MPOs and finite-state automata [113], and is described in detail in the Appendix. We are able to variationally optimize the MPS for chains of up to 718 sites. The computational resources required to accurately approximate the ground state are relatively small: a bond dimension of $200-300$ is sufficient to keep the variance of the Hamiltonian below 10^{-9}. We explicitly break $\mathbb{Z}_3$ symmetry by choosing system sizes which are multiples of 3 plus 1 site. This makes energetically favored states in which there are two bosons at the edges, thus breaking the symmetry without adding any term in the Hamiltonian. Extrapolation to the thermodynamic limit is then performed vs $1/L$. The result is plotted in Fig. 3.9. We compute the order parameter by averaging the one-point function on $L/2$ sites in the bulk. The fit of the averaged order parameter as a function of U returns a critical exponent $\beta = 0.031 \pm 0.005$ and a critical point location $U_{c1} = -1.969 \pm 0.002$. The error attributed takes into account variations of the fitting parameters obtained by considering different sets of values of U and computing the order parameter by performing the average over a different number of sites in the bulk of the chain.

Summarizing, the direct study of the order parameter provides similar information to that of the quantities analyzed in the previous subsection: upon increasing system sizes, the position of the second-order transition systematically drifts toward larger values of $|U_{c1}|$. It is informative to note that this shift is compatible with a "finite-size" location of the transition point based on the wave-function variation captured by the fidelity susceptibility: as can be seen from Fig. 3.7(b), a finite-size estimate at around $L \simeq 120/800$ would return a critical coupling of order $U_{c1} \simeq -1.95/1.97$, respectively. The incompatibility with the extrapolated values of the structure factor between DMRG and QMC indicates that approaching an exactly blockaded regime in experiments is challenging (see, e.g., the relatively large deviations in estimating β), even if, in terms of transition point location, the difference is of order 0.003.

BKT transition and the floating phase. The presence of a systematic drift towards smaller values of U_{c1} as a function of the system size may signal the presence of an intermediate phase between the ordered and disordered ones. A first check on this hypothesis can be obtained via investigation of the entanglement entropy. To this end, we perform DMRG simulations up to $L = 108$ sites. In Fig. (3.10) we plot the entanglement entropy for fixed $U = -1.95$ as a function of the cord distance on the ring $\kappa(\ell) = L/\pi \sin(\ell\pi/L)$, ℓ being the length of the subsystem on the lattice, for different system sizes. By directly fitting the scaling of the entropy for this value of U, which belongs to the region between U_{c1} and U_{c2} according to all our estimates, we are able

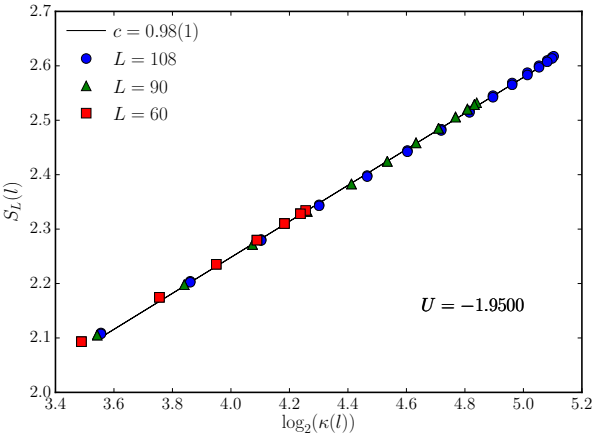

Figure 3.10: Entanglement entropy for fixed U inside the floating phase as a function of the logarithm of the cord length in the CFT ring. The fit produces a central charge in a perfect agreement with the Luttinger liquid CFT.

to obtain a central charge in a good agreement with a $c = 1$ CFT. This is a strong indication of the presence of a critical phase for $U > U_{c1}$, compatible with the Luttinger liquid universality class. We note that for nonrelativistic critical points or phases, the entanglement entropy is not bound by a logarithmic growth, and even if so, the coefficient could be arbitrary. This implies that, assuming there is no fine-tuning, a $c = 1$ point or phase is present here.

As discussed above, all entanglement-related quantities signal a single second-order phase transition. This implies that the transition between the IC and disordered phase shall belong to the BKT universality class, in agreement with field theoretical insights [9, 6].

By carrying out the same analysis of Sec. 3.1.3 on the lowest gap in the energy spectrum, we can estimate the location of the BKT transition, which is expected to occur for $U \geq -1.95$. The scaling ansatz differs from the one in the previous section for two reasons: the dynamical critical exponent is $z = 1$, and the exponential divergence of the correlation length is

$$\xi \sim \exp\left(\frac{b}{\sqrt{U - U_{c2}}}\right), \tag{3.27}$$

where b is a nonuniversal constant, independent of U. Moreover, logarithmic corrections are known to intervene at the end of RG lines of fixed points. In the case of a BKT point the functional form of these corrections is known to be [107] $\Delta \sim L^{-1}[1 + 1/(2\ln L + C)]^{-1}$, for some model-dependent constant C. On the basis of this field theory result we take as the scaling function for the gap [110, 111]

$$\Delta^* = L\left(1 + \frac{1}{2\ln L + C}\right)\Delta = F\left(\frac{L}{\xi}\right). \tag{3.28}$$

This scaling ansatz, in combination with the procedure previously discussed, has been tested in various spin chains where the location of the BKT transition point was analytically known [111]. In these cases, the method was found to slightly underestimate the width of the gapless region; in our case here, one thus expects that this method will overestimate the value of $|U_{c2}|$. In terms of accuracy, the estimate obtained with this method is compatible with state-of-the-art diagnostics based on targeting operator dimensions via correlation functions.

In our case, we observe the same shifting of the critical point towards negative U as we take

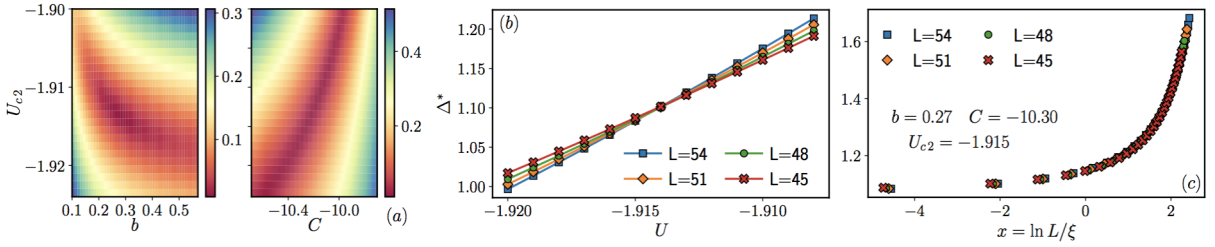

Figure 3.11: (a) Density plot of the square root of the sum of the squared residuals in the (b, U_{c1}) and (C, U_{c1}) planes for the best-fitting values of C and b, respectively. (b) Crossing of the logarithmically corrected gaps, upon multiplication by L^z (where $z = 1$) and taking the best-fit value for C. The crossing indicates the position of the critical point. (c) Data collapse of ED numerical data, with $U \in [U_{c2}, U_{c2} + 0.03]$ with the parameters U_{c2}, b, C which correspond to the best polynomial fit of the universal scaling function in Eq. (3.28).

increasingly large system sizes. A sample result of the largest system sizes we have investigated is plotted in Fig. 3.11; the quality of the data collapse is excellent, as testified by the small value of the sum of the discarded weights. By taking into account variations of the optimal parameters with respect to the set of system sizes and amplitude of the intervals considered, we get $b = 0.27 \pm 0.05$, $C = 10.0 \pm 0.5$, $U_{c2} = -1.915 \pm 0.008$ as the best estimate of the scaling function and transition point location.

3.1.4 Conclusions

In this work, we have investigated the physics of the hard-core boson constrained model of Eq. (3.5) in the region of the phase diagram surrounding the $\mathbb{Z}_3$-ordered phase. In the first part of the study, we considered the vicinity of the Potts critical point. Since the position of the latter is analytically known, we have used this regime to benchmark entanglement-based techniques to detect quantum criticality in constrained models. In particular, we have shown how concurrence and fidelity susceptibility are able to accurately determine the exact location of the critical point with accuracy of order 0.1% in units of the coupling U. At the critical point, we have carried out an extensive investigation of the low-lying energy spectrum, matching such spectrum with the one expected from the $\mathcal{M}_3$ minimal model. Our data suggest that it is possible, within experimentally achievable system sizes, to unambiguously diagnose Potts quantum criticality by just measuring spectral properties. We have also observed systematic suppression of finite-size corrections in local observables, a feature which we believe is due to integrability at the critical point.

In the second part of the work, we have investigated the melting of the ordered phase in the so called doubly blockaded regime, that is, in the presence of infinite next-to-nearest-neighbor repulsion. We have observed the presence of a gapless regime, i.e., an incommensurate phase, already found in the same model below the Potts transition point. Our results show how this phase is surrounded by a second-order phase transition from one side, and a Berezinskii-Kosterlitz-Thouless transition on the other. The position of the latter has been determined using an advanced gap scaling technique at $U_{c2} = -1.915 \pm 0.008$.

Regarding the second-order phase transition, we have found that reaching a scaling regime for entanglement (concurrence and fidelity susceptibility) properties requires sizes $L > 30$. Reaching this regime is also required to determine the location of the transition point utilizing spectral properties. Due to the difficulty in performing calculations for these sizes, entanglement and spectral methods only allow us to provide a lower bound to the position of this critical point, $U_{c1} \lesssim -1.96$. Similarly, we can only provide bounds for the critical exponents; in particular, we find a systematic drift of the value of ν toward smaller values, and of z toward higher values.

These findings are not compatible with previous results [8] based on sizes up to $L = 36$, while they are compatible with a potential emergence of Pokrovsky-Talapov critical behavior observed below the Potts point [9] and with a series of different non-relativistic critical scenarios proposed in related field theories [10]. Following the analogy between the FSS and the chiral clock model suggested in Ref. [8], our findings indicate that, in the FSS model, the critical line separating the ordered and disordered regimes ultimately reaches the regime corresponding to large chiral angles in the clock model, where an incommensurate phase intervenes between the two phases [114].

We have complemented our analysis with numerical simulations monitoring the behavior of solid order across the transition, using both quantum Monte Carlo and tensor network methods. These methods predict a position of the phase transition that strongly depends on the considered boundary conditions. In all cases, the position of U_{c2} is quite distinct from U_{c1} with respect to the numerical uncertainty of our results.

Our results suggest that the strong-coupling regime is relatively convenient to observe phases with incommensurate order, as the size of the floating phase is considerably larger than at smaller couplings. Moreover, spectral properties should be favored as probes over correlation functions, which seem to be more sensitive to finite-size effects. In addition, the presence of a relatively extended transient scaling regime in terms of system sizes partly supports the observation made in Ref. [7] regarding Kibble-Zurek scaling: while the combined effects of a second-order and nearby BKT transition have not been discussed in detail to the best of our knowledge, it is likely that the presence of the latter affects rather dramatically the dynamics over parameter space, due to exponentially vanishing gaps. We leave the investigation of such a scenario (which has been shown to be experimentally achievable [115]) to a future study. Finally, it would be interesting to systematically consider the effect of additional interaction terms that are present in experiments: despite their modest magnitude (as they decay very similarly to van der Waals interactions), those terms may sensibly affect the size of the incommensurate phase.

3.2 Lattice gauge theories and string dynamics in Rydberg atom quantum simulators

We present here an exact mapping of the Hamiltonian in Eq. (3.3) with $d = 2$ and $V_2 = 0$ into a $U(1)$ LGT with truncated gauge field. The mapping provides a system in which the matter degrees of freedom is integrated out via Gauss law. As we will show, the detuning frequency is responsible for giving a mass to the matter particles. This result, other than demonstrating that the Rydberg experimental setup of Ref. [4] constitutes a (potentially large-scale) quantum simulator of a LGT, will be used to interpret the slow dynamics generated by the Rydberg Hamiltonian, outlined in the introduction to this chapter, in terms of known phenomena in LGT.

After describing the mapping in Sec. 3.2.1, we give a gauge-theory interpretation of the dynamics of this system in Sec. 3.2.2. More specifically, we explain the density oscillations observed in the Rydberg chain as a time evolution alternating between the two vacua of the LGT. We discuss the effect of the truncation on the gauge field by comparing the same dynamics in a discretized version of quantum electrodynamics, namely the Schwinger model [43]. In Sec. 3.2.3 we analyze the propagation of defects onto the vacuum state, highlighting the connection of these defect-states to the atypical eigenstates investigated in Ref. [13]. Finally, in Sec. 3.2.4 we give our conclusion and outlook.

3.2.1 Rydberg blockade as a gauge symmetry constraint

We establish here the exact mapping between the FSS Hamiltonian in Eq. (3.3) governing the dynamics of the Rydberg atom quantum simulator in Ref. [4] and a $U(1)$ LGT. The latter describes the interaction between fermionic particles, denoted by Φ_j and residing on the lattice site j, mediated by a $U(1)$ gauge field, i.e., the electric field $E_{j,j+1}$, defined on lattice bonds, as depicted in Fig. 3.12. We use here Kogut-Susskind (staggered) fermions [44], with the conventions that holes on odd sites represent antiquarks $\bar{q}$, while particles on even sites represent quarks q. Their dynamics is described by:

$$H = -w \sum_{j=1}^{L-1} (\Phi_j^\dagger U_{j,j+1} \Phi_{j+1} + \text{h.c.}) + m \sum_{j=1}^{L} (-1)^j \Phi_j^\dagger \Phi_j + J \sum_{j=1}^{L-1} E_{j,j+1}^2, \tag{3.29}$$

where the first term provides the minimal coupling between gauge and matter fields through the parallel transporter $U_{j,j+1}$ with $[E_{j,j+1}, U_{j,j+1}] = U_{j,j+1}$, the second term is the fermion mass, and the last one is the electric field energy. The generators of the $U(1)$ gauge symmetry are defined as

$$G_j = E_{j,j+1} - E_{j-1,j} - \Phi_j^\dagger \Phi_j + \frac{1 - (-1)^j}{2}, \tag{3.30}$$

and satisfy $[H, G_j] = 0$, so that gauge invariant states $|\Psi\rangle$ satisfy Gauss law $G_j|\Psi\rangle = 0$ for all values of j. Restricting the dynamics to their subspace is by far the most challenging task for quantum simulators. Different formulations of $U(1)$ LGTs are obtained for different representations of gauge degrees of freedom $E_{j,j+1}$. While in the standard Wilsonian formulation — i.e., the lattice Schwinger model — they span infinite-dimensional Hilbert spaces, here we first focus on the $U(1)$ QLM formulation [40, 116], where they are represented by spin variables, i.e., $E_{j,j+1} = S^z_{j,j+1}$ and $U_{j,j+1} = S^+_{j,j+1}$, so that $[E_{j,j+1}, S^+_{j,j+1}] = S^+_{j,j+1}$. As noted in Ref. [117], this formulation is particularly suited for quantum simulation purposes.

In the following, we consider the QLM with spin $S = 1/2$, in which all the possible configurations of the electric field have the same electrostatic energy, rendering the value of J incon-

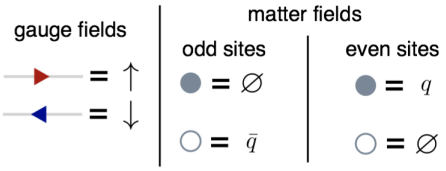

Figure 3.12: Degrees of freedom of a $U(1)$ LGT in the spin-1/2 quantum link model (QLM) formulation. Gauge fields are represented by spin variables residing on links. Matter fields are represented by Kogut-Susskind fermions: an occupied site corresponds to the vacuum on odd sites, and to a quark q on even sites. An empty site, instead, to the vacuum on even sites and to an anti-quark $\bar{q}$ on odd sites.

sequential; in Sec. 3.2.2 we show that this model is equivalent to the lattice Schwinger model in the presence of a θ-angle with $\theta = \pi$ [5]. The Hilbert space structure following Gauss law is particularly simple in this case [117]: as depicted in Fig. 3.13, for each block along the chain consisting of two electric fields neighbouring a matter field at site j, there are only three possible states, depending on the parity of j. In fact, in a general (1+1)-dimensional $U(1)$ LGT, the configuration of the electric field along the chain determines the configuration of the charges via the Gauss law. Accordingly, H in Eq. (3.29) can be recast into a form in which the matter fields Φ_j are integrated out.

We now provide a transformation which maps exactly the latter form into the FSS Hamiltonian (3.3). The correspondence between the two Hilbert spaces is realized by identifying, alternately on odd and even lattice sites, the computational basis configurations of the atomic qubits allowed by the Rydberg blockade with the classical configurations of the electric field allowed by the Gauss law (see Fig. 3.13). In terms of the two Hamiltonians Eqs. (3.3) and (3.29), this unitary transformation consists in identifying the operators $\sigma_j^z \leftrightarrow (-1)^j 2 S_{j-1,j}^z$, $\sigma_j^x \leftrightarrow (\Phi_{j-1}^\dagger S_{j-1,j}^+ \Phi_j + \text{h.c.})$, $\sigma_j^y \leftrightarrow -i(-1)^j (\Phi_{j-1}^\dagger S_{j-1,j}^+ \Phi_j - \text{h.c.})$ and the parameters $\Omega = -w$, $\delta = -m$. This mapping can be applied both for open and periodic boundary conditions and it overcomes the most challenging task in quantum simulating gauge theories, by restricting the dynamics directly within the gauge-invariant Hilbert space.

Compared to the opposite strategy of integrating out the gauge fields, our procedure based on integrating out matter degrees of freedom has major experimental implications. With the first approach one would obtain linearly raising potentials which do not appear easily in the synthetic quantum systems, and lead to very large energy scales (of the order of the system size). Since the overall timescale of most experiments is limited by noise, having couplings with relative ratios of order L is a severe limitation for analogue experiments, and partially affects also digital efforts. The only states that would violate Gauss law are nearest-neighbor occupied sites which are strongly suppressed by the Rydberg blockade. Additional terms in the Hamiltonian, such as next-nearest neighbour interactions of Rydberg excitations, are mapped to gauge invariant terms (e.g., next-nearest neighbour interactions between electric fields). From a theoretical viewpoint, the line of thought of our scheme is similar to the one used in hybrid Monte Carlo schemes, where one first integrates out the matter fields, and then deals with a purely bosonic action.

Beyond providing a direct link between Gauss law and the Rydberg blockade mechanism, the most important feature of the mapping is that it provides an immediate connections between Rydberg experiments and particle physics phenomena, as we describe below.

[5] The similarity between the phenomenology of the two models was pointed out in Ref. [117]. Here, we are instead interested in establishing an exact relation.

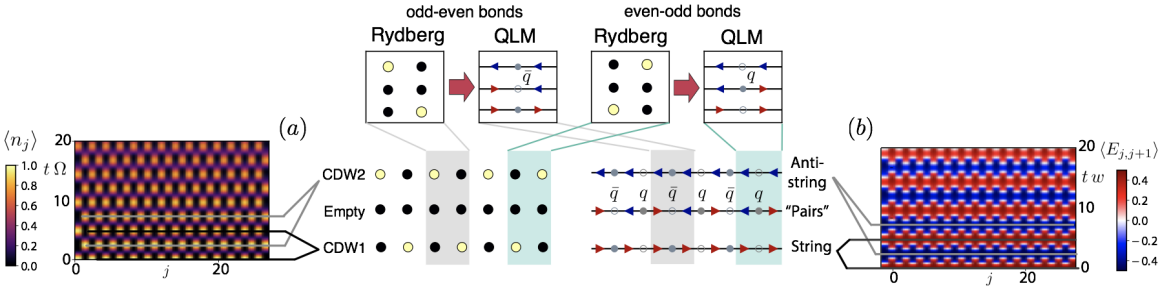

Figure 3.13: Mapping between Rydberg-blockaded states and configurations of the electric field constrained by the Gauss law in the QLM. Due to the staggered electric charge, the allowed configurations of the electric field depend on the link, as illustrated. The two so-called charge-density wave configurations "CDW1" and "CDW2" of the Rydberg-atom arrays are mapped onto the "string" and "anti-string" states, respectively, characterized by uniform rightward or leftward electric fluxes. The empty configuration with all Rydberg atoms in their ground state is mapped to a state filled by adjacent particle-antiparticle pairs. (a) Time evolution of the Rydberg array governed by the effective Hamiltonian $H_{\rm FSS}$ in Eq. (3.3), starting from the CDW1 state. The plot shows the space and time resolved population $\langle n_j \rangle$ of the excited Rydberg atoms. (b) Evolution of the expectation value of the electric field operator $E_{j,j+1}$ in the QLM. This dynamics maps exactly onto the ones shown in panel (d) via the mapping illustrated in panel (c). The thin lines highlight the oscillation between CDW1, CDW2 (left,bottom of panel (c)) or string and anti-string (right) states. In these simulations, $L = 24$ and $\delta = m = 0$.

3.2.2 Gauge-theory interpretation of the real-time dynamics

The exact description of Rydberg-blockaded chains in terms of a $U(1)$ LGT allows us to shed a new light on the slow dynamics reported in Ref. [4], by interpreting them in terms of well-studied phenomena in high-energy physics, related to the production of particle-antiparticle pairs after a quench akin to the Schwinger mechanism.

In the experiment, the system was initialized in a charge density wave state (CDW1 in Fig. 3.13), and subsequently, the Hamiltonian was quenched, inducing slowly-decaying oscillations between CDW1 and CDW2. As shown in Fig. 3.13, CDW1 and CDW2 are mapped onto the two states of the $S = 1/2$-QLM with uniform electric field $S^z_{j,j+1} = \pm 1/2$. The experimental results in Ref. [4] may thus be interpreted as the evolution starting from one of the two degenerate bare particle vacua $|0_\pm\rangle$ (i.e, the vacua in the absence of quantum fluctuations, $w = 0$) of the gauge theory. In Fig. 3.13 (a) and in the first column of Fig. 3.14, we illustrate this dynamics as it would be observed in the excitation density $\langle n_j \rangle$ along the Rydberg-atom quantum simulators ("Rydberg") and compare it with that of the electric field $\langle E_{j,j+1} \rangle$ within its gauge-theory description ("Quantum link model") in Fig. 3.13 (b) and in the second column of Fig. 3.14, respectively, utilizing exact diagonalization[6].

The qualitative features of this evolution are strongly affected by quantum fluctuations, whose impact is quantified by the ratio between the coupling constant w and the particles mass m. For small values of m/w (first two lines in Fig. 3.14), production of particle-antiparticle pairs occurs at a finite rate. We remark that this effect is reminiscent of the Schwinger mechanism [37], which however concerns pair creation from the true (and not the bare) vacuum. These particles get accelerated by the electric field and progressively screen it, until coherent pair annihilation takes place and eventually brings the system to a state with opposite electric flux. This process, referred to as *string inversion*, occurs several times in a coherent fashion; similarly to what is observed in string breaking scenarios (e.g., in other LGTs [47, 118]), this causes a dramatic slowdown of thermalization and of quantum information propagation. As a further evidence, we

[6]Exact diagonalization is performed on the gauge invariant subspace: for large L, its dimension grows as ϕ^L, where ϕ is the golden ratio, thus allowing to access rather large system sizes.

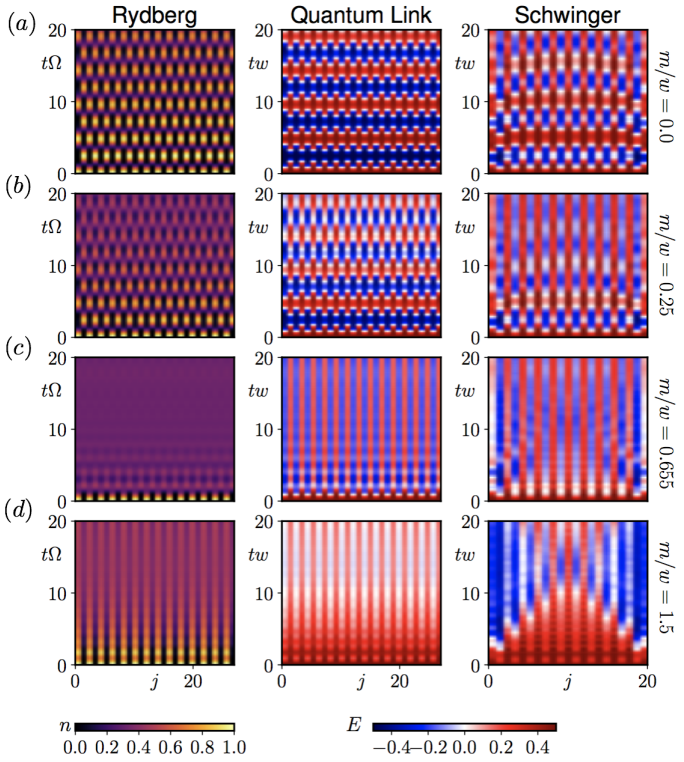

Figure 3.14: Slow dynamics in Rydberg atoms, $U(1)$ quantum link model (QLM), and the lattice Schwinger model. Coherent quantum evolution of (first column) the local Rydberg excitation density profile $n_j(t) = \langle n_j(t) \rangle$ in the FSS model, starting from a charge-density wave, of the local electric field profile (second column) $E_{j,j+1}(t) = \langle S^z_{j,j+1}(t) \rangle$ in the QLM, and (third column) $\langle L_{j,j+1}(t) - \theta/(2\pi) \rangle$ in the lattice Schwinger model (see Eq. (3.29)) with $J/w = 1.5$ and $\theta = \pi$. The four rows correspond to increasing values of the detuning δ (Rydberg) or, equivalently, of the particles mass $m = -\delta$ (QLM and Schwinger model). Figures 3.13 (a) and 3.13 (b) correspond to the first two plots in panel (a) here. Data in the first and second columns are connected by a unitary transformation, while a remarkable similarity is manifest between the second and third column despite the larger Hilbert space of the gauge degrees of freedom in the Schwinger model. The persistent string inversions observed within the symmetric phase with $m < m_c = 0.655|w|$ (first two lines) are suppressed as the quantum critical point is approached. The dynamics in the third column features edge effects due to the imposed open boundary conditions.

compute both the total electric flux and the vacuum persistence amplitude (or Loschmidt echo), defined as $G_+(t) = |\langle 0_+|e^{-iHt}|0_+|\rangle|^2$, whose large value $\simeq 1$ was already noted in Ref. [119]. The anomalous long-lived oscillations of these quantities experimentally detected with Rydberg atom arrays in Ref. [4] show a clear analogy with several previous numerical studies of the real-time dynamics of higher-spin QLMs [47] as well as of the Schwinger model [45, 120, 46] and Higgs theories [42]. In addition, as noted in Ref. [117], the dynamics discussed here describes the coherent oscillations of the parity-symmetric order parameter (in our case, $\langle E_{j,j+1} \rangle$) as a function of time, reminiscent of the decay of a chiral condensate in QCD [48]. We thus provide here a bridge among all these observations.

However, if fermionic particles are sufficiently heavy, with m/w exceeding a critical threshold, pair production is a virtual process and string inversion cannot be triggered, as shown in the third and fourth line of Fig. 3.14. We find that this behavior is related to the quantum phase transition occurring in the FSS model at $\delta_c = -0.655|\Omega|$ [6]. This transition corresponds to the spontaneous breaking of the chiral symmetry in the LGT (3.30) at $m_c = 0.655|w|$ [121]. The four rows in Fig. 3.14 show the temporal evolution of the same initial uniform flux configuration (CDW or

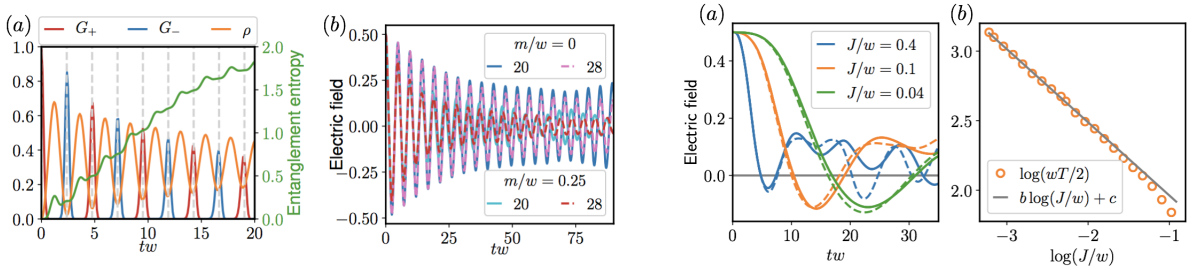

Figure 3.15: **Left.** Characterization of slow dynamics in the FSS model. (a) Hilbert space characterization of the persistent string inversions ($m = 0$, $L = 28$): alternating strong revivals of the overlaps $G_\pm(t) = |\langle 0_\pm|e^{-iHt}|0_+||\rangle^2$ with the two bare vacuum states $|0_\pm\rangle$, corresponding to the two charge-density wave configurations of Rydberg-atom arrays. Both the total density $\rho = \langle \rho_j \rangle$ of particle-antiparticle pairs, with $\rho_j = (-1)^j \Phi_j^\dagger \Phi_j + [1 - (-1)^j]/2$ and the half-chain entanglement entropy (see the supplementary information) have regularly-spaced maxima between the peaks. (b) Persistent oscillations of electric field for two values of the mass and of the system size. **Right.** Oscillation of the electric field in the Schwinger model with $\theta = \pi$. (a) Time evolution of the average electric field. The initial state is the bare vacuum with $E_{j,j+1} = 1/2$ and the chain has periodic boundary conditions. The solid and dashed lines correspond to $L = 14$ and $L = 12$ respectively. Exact simulations are performed via truncation of the local Hilbert space to dimension 16, i.e. $|E_{j,j+1}| < 15/2$, and the constrained Hamiltonian for the electric field is obtained by eliminating matter degrees of freedom. (b) Period of the oscillations as a function of J and w. Data points correspond to values of the half-period obtained for $L = 14$. The solid line is the function $b\log(J/w) + c$, where $b = -0.526$ and $c = 4.2$ are obtained through a fit in the region $J/w < 0.1$.

"string" in Fig. 3.13) upon increasing values of the mass $m/w = 0, 0.25, 0.655, 1.5$ corresponding to the dynamics ((a), (b)) at $m < m_c$, ((c)) at the quantum critical point $m = m_c$, and ((d)) at $m > m_c$.

Fig. 3.15 (left) further illustrates the appearance of string inversions for $m < m_c$ and the corresponding slow dynamics. Panel (a) shows the long-lived revivals of the many-body wavefunction in terms of the evolution of the probability $G_\pm(t)$ of finding the system at time t in the initial bare vacuum state $|0_+\rangle$ or in the opposite one $|0_-\rangle$, corresponding to G_+ or G_-, respectively, as well as in terms of the time-dependent density ρ of particle-antiparticle pairs. Although not shown here, the entanglement entropy of half system also displays an oscillatory behavior. Panel (b) shows the scaling of the collective oscillations of the electric field with respect to the system size L, as well as their persistence with a small but non-vanishing fermion mass $m < m_c$.

Slow dynamics in the Schwinger model. The above phenomenology is not restricted to QLMs, but is expected to be a generic feature of LGTs including dynamical matter. We show this in the context of a Wilsonian LGT, i.e., the lattice version of the Schwinger model in Eq. (3.29). As discussed below, the model dynamics is, at the lattice level, remarkably different from the PXP model (no constraints when written in spin language, different Hilbert space scaling, different interactions, etc.). The key aspect is, instead, the common field-theoretical framework.

In this case, $U_{j,j+1} = e^{i\vartheta_{j,j+1}}$ are $U(1)$ parallel transporters with vector potential $\vartheta_{j,j+1}$, the corresponding electric field operator is $E_{j,j+1} = L_{j,j+1} - \theta/(2\pi)$, where $L_{j,j+1}$ have integer spectrum and $\theta/(2\pi)$ represents a uniform classical background field parameterized by the θ-angle. Canonical commutation relations for the gauge degrees of freedom read $[\vartheta_{j,j+1}, L_{p,p+1}] = i\delta_{jp}$. In our numerical simulations, we utilize the spin formulation of the model obtained upon integration of the gauge fields under open boundary conditions [122, 123].

We consider the case of a θ-angle with $\theta = \pi$, such that the electric field $E_{j,j+1}$ has half-integer spectrum. Then, in the limit $J/w \to \infty$ the term $JE_{j,j+1}^2$ in the Hamiltonian suppresses all the values of the electric field that are different from $\pm 1/2$. This implies that the electric field can

be represented by a spin-1/2 S^z operator and that the lattice Schwinger model is equivalent to the spin-1/2 QLM discussed above. We find evidence that the corresponding behaviour persists qualitatively down to $J \simeq w$, when the electrostatic energy competes with the matter-field interaction, as shown in the third column of Fig. 3.14. Despite the strong quantum fluctuations allowed in principle by the exploration of a locally infinite-dimensional Hilbert space, a qualitative similarity with the case of the locally finite-dimensional Hilbert space of the QLM is manifest in the second column of Fig. 3.14, related to the observed dynamics in Ref. [4]. At a more quantitative level, we see that the periods of the oscillations in the lattice Schwinger model and in the QLM (for the same couplings) are in good agreement.

Even more drastically, we observe persistent oscillations also down to $J \ll w$ (see Fig. 3.15 (right)), a regime in which the period becomes longer upon decreasing J. As we will discuss below, the reasons for such oscillations persisting at the very opposite regime with respect to the constrained one is related to the field theoretical origin of such behavior, which can be even captured at a quantitative level via simple analytical approximations.

We remark that the lattice Schwinger model with unbounded levels of the gauge fields is substantially different from the QLM: not only the Hilbert space is much larger, but also the effective spin-1/2 model describing it features long-range Coulomb interactions. Therefore, the generality of the occurrence of oscillations which do not decay on time scales immediately related to the microscopic couplings points to a rather robust underlying mechanism. In fact, we suggest here that this behavior may arise from a universal field-theoretical description of the non-equilibrium dynamics of states possessing a well-defined continuum limit.

Concerning the $U(1)$ LGTs discussed in this work, the reference continuum field-theory description is provided by the Schwinger model, representing quantum electrodynamics in one spatial dimension [43]. In the massless limit $m = 0$, this model can be exactly mapped by bosonization to a free scalar bosonic field theory [37]. For a non-zero mass, the model is described in terms of the canonically conjugate fields Π and ϕ by the Hamiltonian

$$H_{\mathrm{B}} = \int \mathrm{d}x \left[\frac{1}{2}\Pi^2 + \frac{1}{2}(\partial_x \phi)^2 + \frac{1}{2}\frac{e^2}{\pi}\phi^2 - cm\omega_0 \cos(2\sqrt{\pi}\phi - \theta) \right]. \tag{3.31}$$

Within this bosonized description, the field $\phi(x,t)$ represents the electric field, and for $m = 0$ all of its Fourier modes $\tilde{\phi}(k)$ correspond to decoupled harmonic oscillators. In this case, the evolution starting from a false vacuum with a uniform string of non-vanishing electric field $\langle \phi(x, t = 0) \rangle = \text{const} \neq 0$ represents an excitation of the single uniform mode with $k = 0$, and hence the electric field will show uniform periodic string inversions around zero, with a frequency $\omega_0 = e/\sqrt{\pi}$, where e is the charge of the fermion. A non-vanishing value of m leads to the additional anharmonic term in Eq. (3.31). The resulting total potential shows a transition from a shape with a single minimum for $m < m_c$ to two symmetric minima for $m > m_c$, analogous to the spontaneous breaking of chiral symmetry on the lattice. This weak local non-linearity introduced by a small m couples the various Fourier modes and hence induces a weak integrability breaking. In this case, the uniform string inversions of the electric field evolving from a false vacuum configuration with $\langle \tilde{\phi}(k = 0) \rangle \neq 0$ are expected to be superseded by slow thermalization processes at long times (see, e.g., Ref. [124]). In the context of cold gases, a reminiscent slow relaxation has been observed in interfering bosonic Luttinger liquids, whose Hamiltonian dynamics has some similarities to the one discussed here [125].

We suggest that a remnant of this slow dynamics induced by the underlying integrable field theory may persist in lattice versions of this gauge theory as long as initial states with a well-defined continuum limit are considered. With the latter, we mean states whose field configuration is smooth at the level of the lattice spacing: for our case here, the two Neel states represent the smoother ones, as they correspond to the bare vacuum of the fermionic fields, and no electric field

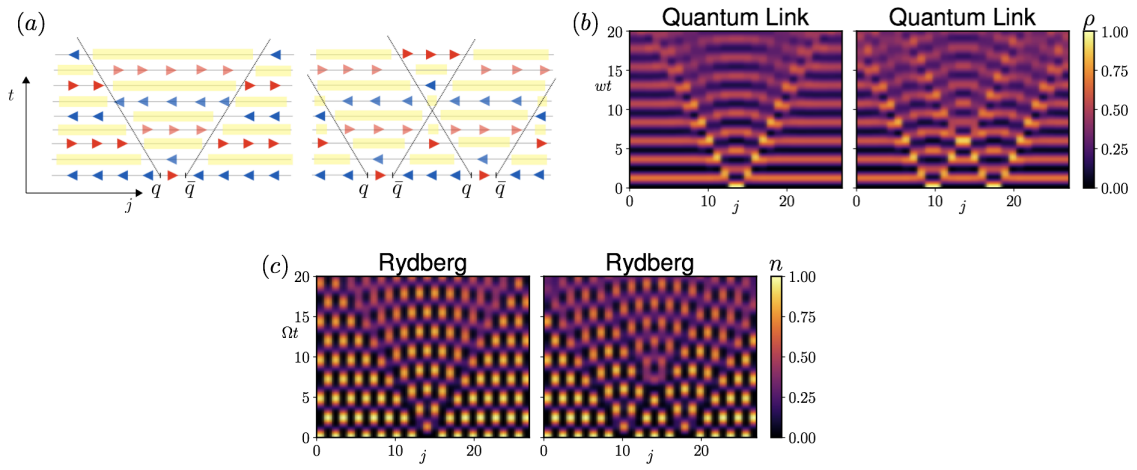

Figure 3.16: Slow dynamics of particle-antiparticle pairs. (a) Cartoon states representing the propagation of particle-antiparticle pairs q-$\bar{q}$. The notation is the same as in Fig. 3.13, while the yellow stripes denote regions of space with largest particle density and therefore $\langle E_{j,j+1} \rangle \simeq 0$. (b) Evolution of the particle density in the QLM starting from a bare vacuum or "string" state, see Fig. 3.12, with initial particle-antiparticle pairs. (c) Same as in panel (b), but in the Rydberg excitation density representation. Left column: the oscillations observed in the light-cone shaped region originating from the particles is expected to be out of phase with respect to those of the bare vacuum. Right column: In the presence of two q-$\bar{q}$ pairs, an additional change of periodicity is expected in correspondence of elastic scattering. In these simulations, $m = \delta = 0$.

excitations. At a qualitative level, the effect of integrability-breaking induced by lattice effects is expected to be much weaker in the small Hilbert space sector involving uniform excitations with $k = 0$ only, where the long-lived string inversion dynamics takes place. The number of states in this sector grows linearly with the lattice size L and their energy spans an extensive range, in agreement with the characteristics of "many-body quantum scars", see Ref. [13] and Sec. 3.2.3 below.

At a quantitative level, we test our prediction on the lattice Schwinger model with $\theta = \pi$, whose continuum limit is obtained by scaling the parameters with the lattice spacing a in such a way that $J = e^2 a/2$, $w = 1/(2a)$, and $a \to 0$ [126]. In order to address this regime, we perform a scaling analysis as a function of J/ω. According to the field theory, in this limit the period of the oscillations scales as $T \propto 1/\sqrt{Jw}$: as shown in Fig. 3.15 (right), this scaling is indeed satisfied for $J \ll w$, where we obtain a fitting dependence of $T \propto (J\omega)^{-0.526}$ within a few percent from the expected exponent.

3.2.3 Propagation of particle-antiparticle pairs

States of the QLM corresponding to particle-antiparticle pairs in the bare vacuum can be constructed in Rydberg-atom quantum simulators by preparing two or more defects in a charge-density wave configuration, each corresponding to pairs of adjacent non-excited Rydberg atoms.

As an illustration, we discuss how the time-evolution of one or two particle-antiparticle pairs for $m < m_c$ features the emergence of slow dynamics. In Fig. 3.16, we show the time evolution of both the particle density in the QLM and the corresponding density of excitations in the Rydberg chain, fixing for simplicity $m = 0$. The pairs in the initial state break and ballistic spreading of quark and antiquark takes place. The string inversion dynamics induced by this propagation shows coherent interference patterns with long-lived oscillations. Due to retardation effects induced by the constrained dynamics, these oscillations are shifted by half a period with respect to the vacuum oscillation, as captured by second-order perturbation theory.

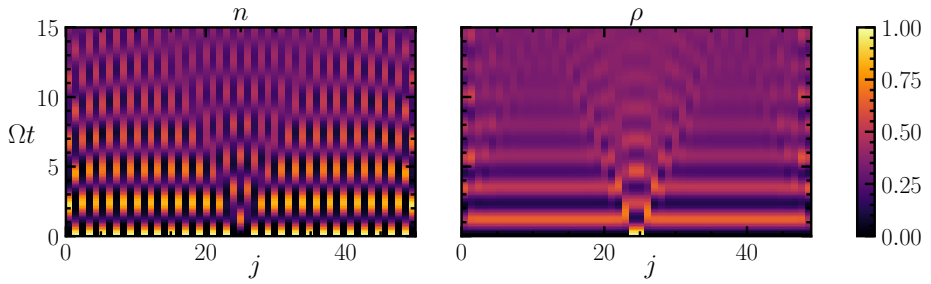

Figure 3.17: Propagation of a particle-antiparticle pair q-$\bar{q}$ with realistic Rydberg interactions. Left panel: density of Rydberg excitations. Right panel: density of particles/antiparticles (ρ in the QLM language). Results are obtained for a chain of $L = 51$ sites governed by the realistic Hamiltonian (3.1) with $V_{ij} = V_1 r_{ij}^{-6}$ and no constraints in the Hilbert space. Parameters: $\delta = 0$, $V_1/\Omega = 25.6$ ($R_b \simeq 1.5$). We checked explicitly that the violation of Rydberg blockade is always small, $\langle n_j n_{j+1} \rangle < 10^{-2}$.

This unusual dynamics turns out to be robust under experimentally realistic conditions. In Fig. 3.17 we consider the evolution of a particle-antiparticle pair, the simulated dynamics of which is not constrained to the subspace satisfying $n_j n_{j+1} = 0$ and includes the effect of the long-range Rydberg interactions between atoms. The evolution is performed via tensor network techniques based on the time-dependent variational principle [127], in the unconstrained Hilbert space with the Hamiltonian in Eq. (3.1), with $\delta = 0$ and $V_{j,k} = V_1 |j - k|^{-6}$. The value of $V_1/\Omega = 25.6$ is the same as considered in Ref. [4], corresponding to a Rydberg blockade radius $R_b \simeq 1.5$. The dynamics displayed in Fig. 3.17 is similar to the constrained one in Fig. 3.16 (b),(c) at short times, after which the effects of having realistic interactions gradually kick in.

Spectral properties and bands of non-thermal states. We now characterize the anomalous ballistic spreading of particle-antiparticle pairs discussed above in terms of the emergence of corresponding anomalous spectral properties of the FSS model, which generalize those recently observed [13] in the special case $m = 0$, involving families of special energy eigenstates referred to as "many-body quantum scars". The latter are constituted by towers of regularly-spaced states in the many-body spectrum with alternating momentum $k = 0$ and $k = \pi$, characterized by non-thermal expectation values of local observables as well as by anomalously large overlaps with the charge-density wave initial states. The long-lived coherent oscillating behavior has been attributed in Ref. [13] to the existence of these "scarred" eigenstates.

Fig. 3.18 (a) shows that the modulus of the overlap between the energy eigenstate $|\psi\rangle$ with energy E and the above described inhomogeneous states $|\phi_{q\bar{q}}\rangle$ with momentum k clearly identifies a number of special bands of highly-excited energy eigenstates characterized each by an emerging functional relationship $E(k)$. As shown in Fig. 3.18 (d) some of the states in these bands strongly deviate from the thermal value $\langle n_j \rangle_{th} \simeq 0.276$. This fact has already been observed in the previously studied quantum-scarred eigenstates, which coincide with the extremal points of these bands at momenta $k = 0$ and $k = \pi$. A closer inspection of these energy-momentum relations, presented in Fig. 3.18 (b), shows that they are close to cosine-shaped bands, suggesting the emergence of single-particle excitations in the middle of the many-body energy spectrum.

We further characterize this spectral structure by constructing a quasi-particle variational ansatz $|\chi_k\rangle$ on top of the exact matrix-product-state zero-energy eigenstate of the Hamiltonian

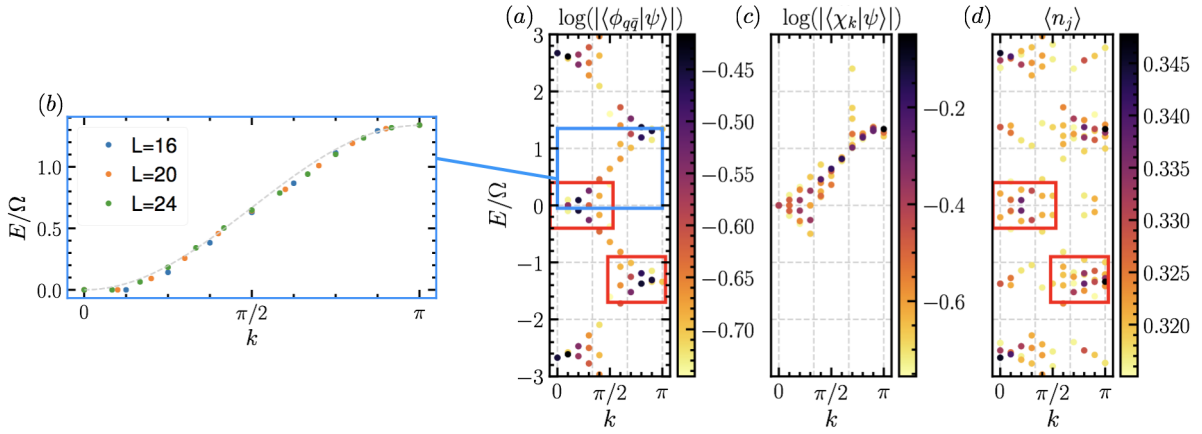

Figure 3.18: Emergent quasi-particle description of highly-excited states. (a) Largest overlaps of the initial state $|\phi_{q\bar{q}}\rangle$ with a localized defect in a charge-density wave configuration of the Rydberg-atom chain with the energy eigenstates $|\psi\rangle$ of the FSS Hamiltonian ($\delta = 0, L = 20$) in Eq. (3.3), as a function of their corresponding momentum and energy. Within the gauge-theory description, the initial state corresponds to having a localized particle-antiparticle pair q-$\bar{q}$. (b) The eigenstates with the largest overlaps display a regular functional dependence of energy on momentum that is remarkably close to a simple cosine band. (c) The largest overlaps of the optimal matrix-product state quasi-particle ansatz $|\chi_k\rangle$ built on an exact eigenstate with zero energy (see the main text) accurately reproduce the corresponding emergent quasi-particle band of panel (a). (d) Anomalous (non-thermal) expectation values of a local observable in energy eigenstates. The red boxes highlight the correspondence between the most relevant eigenstates building up $|\phi_{q\bar{q}}\rangle$ (panel (a)) and the most non-thermal eigenstates (panel (d)). The emergent spectral structure illustrated in this picture underlies the clean ballistic spreading of particle-antiparticle pairs displayed in Fig. 3.16.

in Eq. (3.3) with $\delta = 0$, recently put forward in Ref. [49]. We employ the following wavefunction

$$|\chi_k\rangle = \sum_{j=1}^{L} e^{-ikj} O_{j-1,j,j+1} |\Phi_{k=0}\rangle, \tag{3.32}$$

where $|\Phi_{k=0}\rangle$ is the exact eigenstate found in Ref. [49] with momentum $k = 0$ and energy 0, and $O_{j-1,j,j+1}$ is a three-site operator depending on a number of variational parameters. Due to the constraints, the space where this operator acts is reduced from dimension 2^3 to 5. The inversion symmetry with respect to site j reduces the number of free variational parameters in $O_{j-1,j,j+1}$ to 11. We choose a basis of operators $\{M^{\alpha}_{j-1,j,j+1}\}_{\alpha=1}^{11}$ for parameterizing $O_{j-1,j,j+1}$ and define

$$|\phi^{\alpha}_k\rangle = \sum_{j=1}^{L} e^{-ikj} M^{\alpha}_{j-1,j,j+1} |\Phi_{k=0}\rangle. \tag{3.33}$$

For each k, we minimize the energy variance in the space spanned by the states $|\phi^{\alpha}_k\rangle$. To this aim, we compute the three matrices $N^k_{\alpha\beta} = \langle\phi^{\alpha}_k|\phi^{\beta}_k\rangle$, $P^k_{\alpha\beta} = \langle\phi^{\alpha}_k|H|\phi^{\beta}_k\rangle$, $Q^k_{\alpha\beta} = \langle\phi^{\alpha}_k|H^2|\phi^{\beta}_k\rangle$. Since the number of linearly independent states in the set $\{|\phi^{\alpha}_k\rangle\}$ varies with k, we diagonalize the matrix of the norms N_k and we compute the (rectangular) matrix U^k whose columns are the eigenvectors of N^k having non-zero eigenvalues. We then find the vector $\boldsymbol{c_k} = \left(c^1_k, \ldots, c^m_k\right)$ that minimizes

$$\sigma^2_H = \frac{\boldsymbol{c_k}^{\dagger} U^{k\dagger} Q^k U^k \boldsymbol{c_k}}{\boldsymbol{c_k}^{\dagger} U^{k\dagger} N^k U^k \boldsymbol{c_k}} - \left(\frac{\boldsymbol{c_k}^{\dagger} U^{k\dagger} P^k U^k \boldsymbol{c_k}}{\boldsymbol{c_k}^{\dagger} U^{k\dagger} N^k U^k \boldsymbol{c_k}} \right)^2 . \tag{3.34}$$

By introducing the matrix U^k we restrict the minimization to states with non-zero norms, thus further reducing the number of variational parameters to $m(k) \leq 11$. The optimal wavefunction is then obtained as

$$|\chi_k\rangle = \sum_{\alpha=1}^{11} \sum_{\beta=1}^{m} U^k_{\alpha\beta} c^\beta_k |\phi^\beta_k\rangle. \tag{3.35}$$

As shown in Fig. 3.18 (c), the optimal quasi-particle ansatz has the largest overlap with the states on the energy-momentum bands of special eigenstates closest to zero energy, thus reinforcing the above emergent quasi-particle picture.

Tuning the topological θ-angle in Rydberg experiments. So far, our discussion has focused exclusively on the relation between Rydberg experiments and the Schwinger model with topological angle $\theta = \pi$. A natural question to ask is whether, within the present setting, it is possible to realize genuinely confining theories, i.e., generic values of the topological angle $\theta \neq \pi$.

This is possible within the strong coupling limit upon introducing a linear term in the electric field. With reference to the lattice Schwinger model introduced in Sec. 3.2.2 and notations therein, we see that the two lowest degenerate energy states of the local electric field for $\theta = \pi$ (i.e. $L_{j,j+1} = 0, +1$) are split when θ deviates from π, with an energy gap $\Delta = J|\theta/\pi - 1|$. In order to keep the structure of the Hilbert space compatible with the FSS model, one requires this Δ to be much smaller than the gaps with the other states, which are of the order of J. This implies that, within the QLM formulation, we can only access very small deviations from $\theta = \pi$: this is not a limiting factor, and we will show how this simple setting already allows to witness the effects of confinement in the dynamics. The confining nature of the potential can be intuitively understood as follows: starting form the bare vacuum (the "string" state in Fig. 3.13), creating and separating a particle-antiparticle pair at a distance ℓ entails the creation, between the two, of a string of length ℓ with opposite electric field. The corresponding energy cost is proportional to $\ell\Delta$, signalling the confining nature of the potential. Accordingly, the lattice Schwinger model with strong $J \gg \Omega, m, \Delta$ and with a topological angle $\theta = \pi(1 \pm \Delta/J)$ is efficiently approximated by the QLM with an additional term linear in the electric field and proportional to Δ.

In turn, within the exact mapping outlined in Sec. 3.2.1 and illustrated in Fig. 3.13, this $\theta-$angle term corresponds to an additional staggered field in the FSS model, leading to the Hamiltonian:

$$H_{\rm Ryd} = \sum_{j=1}^{L} (\Omega\, \sigma^x_j + \delta\, \sigma^z_j) + \sum_{j=1}^{L} (-1)^j \frac{\Delta}{2} \sigma^z_j. \tag{3.36}$$

The new term can be experimentally realized, e.g., by utilizing a position dependent AC Stark shift or, alternatively, a space-dependent detuning on the transition between ground and Rydberg states (it was realized, for example, in a recent work reported in Ref. [128]).

In Fig. 3.19 (left), we show the effect of the $\theta-$angle on the evolution of the total electric field in the QLM starting from a uniform string state. Also in this case, the dynamics observed can be understood using the bosonized field theory in Eq. (3.31). As explained in Sec. 3.2.2, the integrability breaking term which appears for $m > 0$ has the effect of damping the oscillations. Moreover, from the same equation we can predict that the impact of a variation of the θ-term on the dynamics is enhanced when we increase the mass, as data clearly show. This enhancement of the θ-dependence becomes more evident when we cross the transition point: while in the symmetric phase with $m < m_c$, the explicit symmetry breaking caused by the electric field energy imbalance leads to damping of the string inversions, in the broken-symmetry (chiral) phase with $m > m_c$ the effect of confinement is dramatic, causing the persistence of the initial electric string, with small long-lived oscillations. Focusing on the latter phase, in Fig. 3.19 (right) we show the dynamical evolution of a finite electric string generated by a particle-antiparticle pair (left

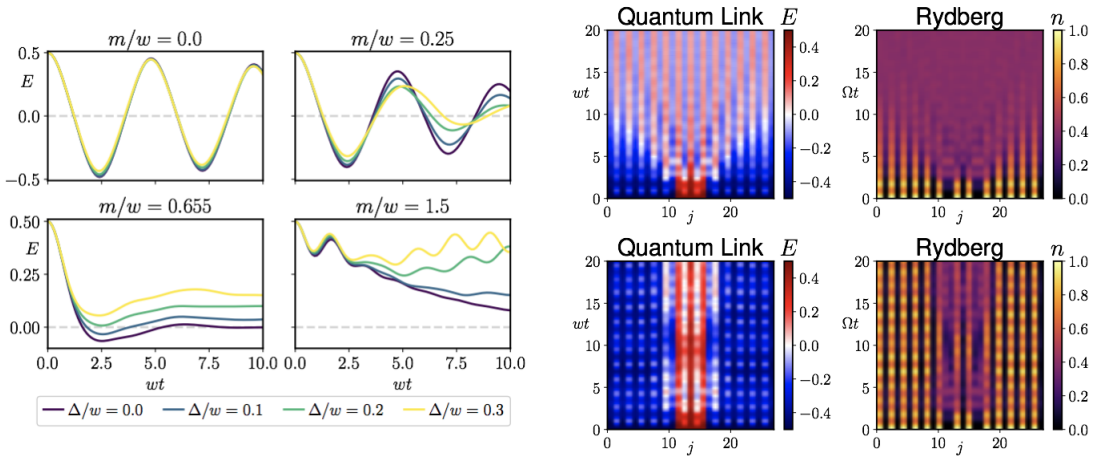

Figure 3.19: **Left.** Effect of the $\theta-$angle on the dynamics of the electric field from uniform string states of the QLM. Data are shown for a chain of $L = 28$ sites, for increasing values of the particle mass m/w and of the parameter Δ, quantifying the deviation of the $\theta-$angle from π (see the main text). Dynamics for $\Delta = 0$ corresponds to the second column of Fig. 3.14. **Right.** $\theta-$angle and string-breaking dynamics. Evolution of a bare particle-antiparticle pair state is displayed in terms of space- and time-dependent electric field in the QLM (left panels) and of the density of excited atoms in the Rydberg array (right panels), with $m = -\delta = 1.5\Omega$ and $L = 28$. Simulations in the top row have $\Delta = 0$, corresponding to the deconfined field theory with $\theta = \pi$. Effects of confinement emerge in the second row, where a non-vanishing $\Delta = 0.3\Omega$ stabilizes the electric string.

panels), at the deconfined point $\theta = \pi$ (top) and in the confined phase with $\theta \neq \pi$ (bottom). The right panels show the same evolution as it would appear in terms of measurements of Rydberg atom excitations. While for $\Delta = 0$ nothing prevents the initially localized bare particles to propagate along the chain (top panels), the presence of a linear confining potential proportional to Δ between them stabilizes the electric string, leading to effective Bloch oscillations of the edges and to a surprisingly long lifetime [129] (bottom panels). This effect signals that confinement can dramatically affect the non-equilibrium dynamics, potentially slowing it down as observed in both gauge theories [130] and statistical mechanics models [131, 129, 132]. In this regime, the model shows the same qualitative signatures of confinement as the quantum Ising chain in transverse and longitudinal field: the long-lived coherent oscillations, the suppression of the light-cone spreading [131] and the presence of anomalous eigenstates [132].

3.2.4 Conclusions

We proved that the large-scale quantum simulation of lattice gauge theories has already been achieved in state-of-the-art experiments with Rydberg atoms, as it can be realized by establishing a mapping between a $U(1)$ gauge theory and Rydberg atom arrays. At the theoretical level, we showed that this novel interpretation provides additional insights into the exotic dynamics observed in experiments, linking it to archetypal phenomena in particle physics. Our field-theoretic description immediately implies the generality and applicability to a wide variety of model Hamiltonians within experimental reach, and among them we extensively discuss the example of the lattice Schwinger model in the Wilson formulation. We expect that future studies can further deepen the connection between the statistical mechanics description of such behaviour and its gauge-theoretic interpretation, for instance, elucidating the effects of non-thermal states [13, 12, 49, 14] and emergent integrability [16, 15], and the role of confinement in slowing down the dynamics [131, 130, 129, 132, 133]. At the experimental level, our findings immediately motivate

further experiments along this direction, that can probe different aspects of gauge theories, such as the decay of unstable particle-antiparticle states after a quench, and might be combined with other quantum information protocols [134]. We show how by tuning the θ-angle – a possibility that is already available with current technologies – the different dynamical regimes expected from the field theory can be accessed. A particularly interesting perspective in this direction is the possibility of dynamically probing confinement via quantum quenches starting from a string embedded in the (bare) vacuum, a prototypical gedanken experiment in particle physics [45].

The quantum-simulation strategy we propose is based on the elimination of the matter degrees of freedom by exploiting Gauss law: This method does not rely on the specific formulation of the model and is in principle applicable to other lattice gauge theories (for a recent work along these lines see for example Ref. [135]). An intriguing future extension is represented by theories with non-Abelian gauge symmetries, an example of which can be found in Ref. [136], where links with finite-dimensional Hilbert spaces are utilized. The integration of matter degrees of freedom is equally well suited for higher dimensions, and Rydberg atoms are a promising platform for pursuing this direction [137, 138], with the additional advantage that the major complication in realizing non-Abelian theories (i.e., engineering complicated and fine-tuned Gauss laws) is replaced by considerably simpler dynamical constraints. After the present analysis, the experiments performed in Ref. [4] represent a step-stone toward the ambitious realization of non-Abelian gauge theories in three spatial dimension, which remains an outstanding quest [36, 34].

3.3 Breakdown of ergodicity in disordered $U(1)$ lattice gauge theories

In this section we investigate a prototypical one-dimensional gauge theory, i.e. the Schwinger model [43] on a lattice, in the presence of a disordered background. We provide numerical evidence that 1D gauge theories may be an ideal candidate to display a smoother behavior in terms of finite volume effects, enabling the detection of a clear, system-size independent, deviation from ergodic behavior. Before entering into the details of our treatment, we find useful to illustrate a qualitative reasoning why this is the case. Contrary to typical inter-spin interactions, gauge-field mediated interactions typically slow down the system dynamics [139, 140, 141], and thus do not necessarily compete with disorder. In the typical Basko-Aleiner-Altshuler (BAA) scenario [51], interactions open up channels for delocalization by allowing a series of local rearrangements to create a resonance between two quantum states. This leads to a competition between disorder (increasing energy differences and denominators in perturbation theory) and interactions (increasing matrix elements and therefore the numerator). In the presence of one-dimensional Coulomb law, interactions cannot be introduced perturbatively and therefore a BAA-like analysis does not work. This is because a local rearrangement of the degrees of freedom (spins or particle occupation numbers) leads to a large (even extensive) change in energy, therefore suppressing the amplitude of having a resonant process. This behavior is reflected in finite-volume properties observed in previous numerical studies [142, 141, 143], that focused on quench dynamics and local observables.

The structure of the section is the following. In Sec. 3.3.1 we introduce the clean Schwinger model and its disordered version, motivating our choice for the source of disorder. In Sec. 3.3.2 we present the numerical results obtained from the analysis of diagnostics aimed at probing spectral correlations, namely the level statistics of nearby gaps and the spectral form factor. In Sec. 3.3.3 we interpret the results and we strengthen our interpretation by comparing them to what we obtain in other lattice gauge theories in a different regime.

3.3.1 The Schwinger model with disordered background charge

We focus here on the 1D version of quantum electrodynamics, namely the Schwinger model [144], in its Kogut-Susskind lattice regularized version [145]. The two components of a Dirac spinor (electron and positron) sit on even and odd sites. The corresponding Hamiltonian on an open chain of N sites reads:

$$H = -iw \sum_{n=1}^{N-1} \left(\psi_n^\dagger e^{i\varphi_{n,n+1}} \psi_{n+1} - h.c.\right) + J \sum_{n=0}^{N} (L_{n,n+1} + \theta/2\pi)^2 + m \sum_{n=1}^{N} (-1)^n \psi_n^\dagger \psi_n. \quad (3.37)$$

The matter degrees of freedom are N spinless fermions ψ_n living on the sites and the gauge degrees of freedom are $N+1$ unbounded bosons $L_{n,n+1}$ living the on the links. L and φ stand for electric field and vector potential, and they are conjugate variables: $[L, \varphi] = -i$; θ is a the lattice version of a topological angle, that we use below to tune between confined ($\theta \neq \pi$) and deconfined ($\theta = \pi$) regimes [146]. The first term represents the coupling between matter and gauge fields, the second is the electrostatic energy, and the third term gives a mass to the fermions. The Hamiltonian commutes with the generator of gauge transformations:

$$G_n = L_{n+1,n} - L_{n,n-1} - \psi_n^\dagger \psi_n + \frac{1}{2}[1 - (-1)^n]. \quad (3.38)$$

The local symmetry generated by G_n breaks the Hilbert space in superselection sectors. States

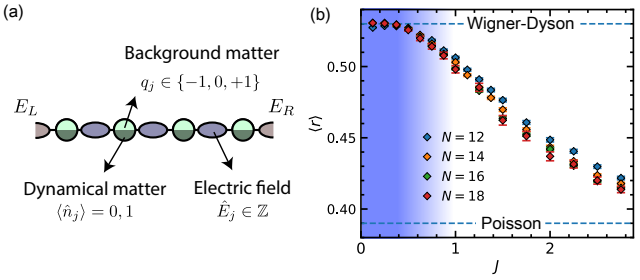

Figure 3.20: (a) Schematics of U(1) lattice gauge theories. The $U(1)$ gauge field lives on link between the sites of the chain. Dynamical matter (dark green) is a fermionic variable living on the sites, while static charges (light green) are random integers which take values $0, \pm 1$. (b) Average level spacing (see Eq. (3.43)) as a function of the gauge coupling J for different N (see text). The shaded region represents the estimated ergodic phase.

$|\Psi\rangle_{q_1,q_2,\ldots q_N}$ in each of those sectors are labeled by the distribution of background static charges $(q_1, q_2, \ldots q_N)$, defined as:

$$G_n |\Psi\rangle_{q_1,q_2,\ldots q_N} = q_n |\Psi\rangle_{q_1,q_2,\ldots q_N} \tag{3.39}$$

which is a discretized version of Gauss law. We set $m = 0$ and $w = 1$ in what follows. The mass term is not essential for the phenomenon we describe.

Disorder-free many-body localization dynamics in this system has been reported in Ref. [141]. There, the idea was to use superselection sectors in a clean system as an effective source of correlated disorder econded in the initial state. Other signatures of MBL in the presence of disordered on-site potentials were reported in Ref. [143]. Here, instead, we study the system properties to the presence of random, static background charges, that we randomly choose in the set $q_j = \{0, \pm 1\}$ with equal probability.

A computationally convenient representation is obtained via explicit integration of the gauge fields. This is a consequence of the well-known fact that Gauss law can be integrated exactly in one dimension. The mapping consists in a Jordan-Wigner transformation to cast the theory in spin language, and a gauge transformation on the spins to eliminate the vector potential ϕ from the resulting Hamiltonian. This procedure is reviewed in great detail in Ref. [147], and yields a spin-1/2 Hamiltonian. We define σ^α as the standard Pauli matrices. The resulting Hamiltonian is

$$H_0 = H_{\text{Hop}} + J H_{\text{Int}} + J H_{\text{Dis}}, \tag{3.40}$$

where H_{Hop} is just the hopping term $H_{\text{Hop}} = -\sum_{n=1}^{N-1} \left(\sigma_n^+ \sigma_{n+1}^- + \text{h.c.}\right)$, while the second and third terms read

$$H_{\text{Int}} = \frac{1}{2} \sum_{n=1}^{N-2} \sum_{\ell=n+1}^{N-1} (N - \ell) \sigma_n^z \sigma_\ell^z, \tag{3.41}$$

$$H_{\text{Dis}} = \frac{1}{2} \sum_{n=1}^{N-1} \left(\sum_{\ell=1}^{n} \sigma_\ell^z \right) \left[2 \sum_{j=1}^{n} q_j + \frac{(-1)^n - 1}{2} + \frac{\theta}{\pi} \right], \tag{3.42}$$

and describe the Coulomb interaction between dynamical charges (both terms), and the interaction between dynamical and static ones (the last term). Note that the parameter J measures at the same time disorder and interaction strength. The intimate relation between these two quantities is a natural consequence of the existence of Coulomb law: in any local theory in 1D, local background charges will inevitably generate a sink (or source) of the electric field, and thus their effect on the system is tied to the gauge coupling.

Below, we consider only static charge distributions such that $\sum_n q_n = 0$ and $q_n = 0, \pm 1$. We

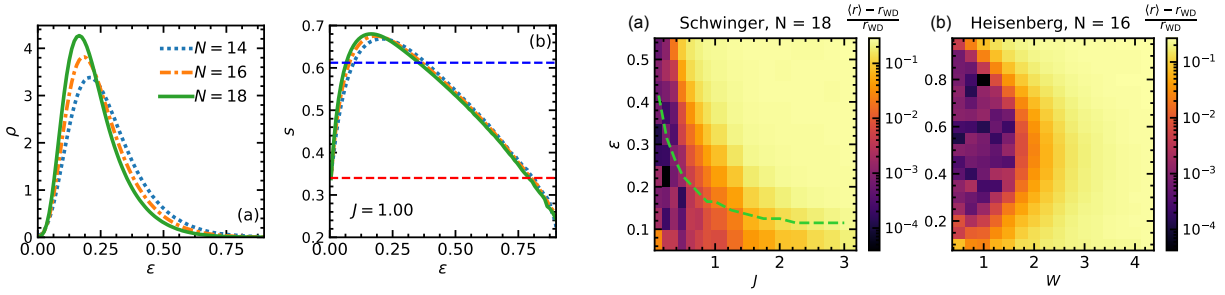

Figure 3.21: **Left.** Spectral density (a) and entropy per site (b) of the Hamiltonian Eq. (3.40) for different N and $J = 1$ as a function of the rescaled energy $\varepsilon = (E - E_{\min})/(E_{\max} - E_{\min})$. The blue dashed lines cut the spectrum keeping only the eigenvalues E s.t. $s(E)/s_{\max} > A$. We employed $A = 0.5$ for the computation of the level statistics r (blue) and $A = 0.9$ for the computation of the spectral form factor (red). **Right.** Energy-resolved r as a function of the rescaled energy ε, and gauge coupling J in the lattice gauge theory (a) and disorder strength W in the Heisenberg model (b). The green dashed line indicates the position of the maximum of the spectral density.

set the left boundary electric field $L_{0,1} = 0$ and restrict to charge neutrality, $\sum_n \psi_n^\dagger \psi_n = 0$. In order to avoid spurious effects close to $J = 0$ due to the system becoming non-interacting, we add a next-to-nearest-neighbor interaction of the form $H_\epsilon = \epsilon \sum_{n=1}^{N-2} \sigma_n^z \sigma_{n+2}^z$ and set $\epsilon = 0.5$.

3.3.2 Ergodicity breakdown from spectral diagnostics

To capture the breakdown of ergodicity, we focus on spectral properties. In this section, we study the Hamiltonian in Eq. (3.40) by full diagonalization in the Hilbert space sector with zero total spin along the z axis. In the gauge theory picture, this means zero dynamical total charge. We will compute the level statistics as extracted from the ratio of nearby gaps (see Eq. (3.43)) and the spectral form factor (see Eq. (3.44)). While the former represents a very popular witness in the MBL community, the latter has gained attention only recently in this context. As we will discuss in what follows, it encodes information on spectral correlations which goes beyond nearby eigenvalues, thus allowing a more in-depth characterization of the spectral bulk properties.

Average level spacing ratio. We define the ratio between nearby gaps as

$$r_\alpha = \frac{\mathrm{Min}\{\Delta E_\alpha, \Delta E_{\alpha+1}\}}{\mathrm{Max}\{\Delta E_\alpha, \Delta E_{\alpha+1}\}}. \tag{3.43}$$

Here α labels the eigenvalues of H for a given disorder realization. We average r over a spectral window centered on the most-likely eigenvalue, and over 1000 and 100 disorder realizations for $N < 18$ and $N = 18$ respectively.

As illustrated in Fig. 3.21 (left) (a), the Coulomb interaction makes the eigenvalue distribution ρ strongly asymmetric, due to the super-linear scaling of the largest eigenvalues in the spectrum. We thus cut the tails of the spectral density ρ by monitoring the thermodynamic entropy per site: $s = \log \rho / L$. This quantity has a well defined thermodynamic limit (see Fig. 3.21 (left) (b)) and can be used to select the most relevant part of the spectrum ensuring a smooth scaling with the system size. To compute the level statistics r we keep only the eigenvalues E for which $s(E)/s_{\max} > 0.9$ (blue dashed line in Fig. 3.21 (left) (b)). This corresponds to a fraction of eigenstates larger than 0.4, at $N = 14$, and it increases with N. For gauge theories, this procedure overestimates $\langle r \rangle$ at finite size: the reason is that, differently from spin chains, states at lower energy densities are typically less affected by Coulomb law, and thus less localized, at

small system sizes. This is illustrated in Fig. 3.21 (right) (a), where the energy resolved r-value is plotted as a function of gauge coupling and energy density [7]. Considering the full spectrum does not lead to quantitative changes in the transition region.

The resulting scaling of r versus J is plotted in Fig. 3.20 (b). The results illustrate how compatibility with a Wigner-Dyson distribution of the energy levels breaks down at around $J \simeq 0.5$; contrary to the Heisenberg model case (where the critical disorder strength increases by 50% when comparing $N = 12$ and $N = 18$), there is no appreciable finite-volume drift. We note that this behavior is fully compatible with the energy-resolved pattern of r plotted in Fig. 3.21 (right) (a): indeed, only states very close to the ground state are not localized, and as such, the global value of r is dominated by the vast majority of states that is localized (note that the vertical axis in Fig. 3.21 (right) (a) is limited to $\varepsilon \in [0.05, 0.55]$ for the sake of clarity). The ergodic region (shaded) is followed by a regime where $\langle r \rangle$ takes intermediate values: while it is not possible to reliably distinguish between emergent integrability (denoted by Poisson statistics) and an intermediate value of r, there is a clear finite-size trend toward the former for $J > 1$. Within statistical errors, we do not observe a clear crossing: longer chains routinely have smaller r values with respect to shorter chains. Finally, let us note that our diagnostics may actually underestimate the extent of the non-ergodic regime, as there exist random-matrix models where ergodicity is broken even in regimes where r is compatible with GOE [149].

Spectral form factor. As a further evidence of breakdown of ergodicity, we analyze spectral correlations which go beyond nearby eigenvalues via the spectral form factor (SFF), defined as

$$K(\tau) = \frac{1}{\mathcal{Z}} \left| \sum_{\alpha} g(\tilde{E}_\alpha) e^{i2\pi\tau\tilde{E}_\alpha} \right|^2 , \tag{3.44}$$

where $\tilde{E}_\alpha$ are the unfolded eigenvalues. In order to smooth the effects due to boundaries of the spectrum, we apply a gaussian filter $g(x) = e^{-\frac{(x-\mu)^2}{2(\eta\sigma)^2}}$, with μ and σ the average and variance of the disorder realization of the unfolded spectrum. η quantifies the strength of the filter, and we take $\eta = 0.3$ in what follows. $\mathcal{Z} = \sum_\alpha |g(\tilde{E}_\alpha)|^2$ is a normalization s.t. $K(\tau) \simeq 1$ for large τ. Before applying the filter, we cut the edges of the spectrum according to $s(E)/s_{\max} > 0.5$, which means we take a fraction of eigenvalues larger than 0.9. Upon unfolding, the Heisenberg time $t_{\rm H}$, corresponding to the timescale beyond which the discrete nature of the spectrum manifest itself and thus non-universal features kick in, is set to unity. The SFF in Eq. (3.44) is computed for each disorder realization for $\tau \in [0, 1]$ and an average over disorder is performed for each value of τ.

The analysis of $K(\tau)$ allows to probe if the system is ergodic [150, 82, 83]. This can be done by comparing the averaged SFF with the SFF expected from an ensemble of orthogonal random matrices with gaussian entries (GOE), $K_{\rm GOE} = 2\tau - \tau \log(1 + 2\tau)$. We call $\tau_{\rm GOE}$ the time, in Heisenberg units, at which departures of the SFF from $K_{\rm GOE}$ occur. We extract this quantity from the data as the first value of τ for which $|\log K(\tau)/K_{\rm GOE}| < 0.05$. We can then restore physical units $t_{\rm GOE} = \tau_{\rm GOE}\, t_H$, by computing the Heisenberg time t_H as the inverse averaged bulk gap. If the system is ergodic one expects $t_{\rm GOE}/t_{\rm H} \to 0$ in the thermodynamic limit (specifically, the Thouless time shall increase algebraically with N).

In Fig. 3.22 (left) (a) and (b), we plot the spectral form factor in the Schwinger model and Heisenberg model in their ergodic regions. The results in Fig. 3.22 (left) (c) correspond to a regime of gauge couplings whose r value departs from GOE: such departure is indeed confirmed by the fact that $t_{\rm GOE}/t_{\rm H}$ is not decreasing with system size, and oppositely, the SFF seems to

[7] Similar behavior occurs in the Bose-Hubbard model [148]

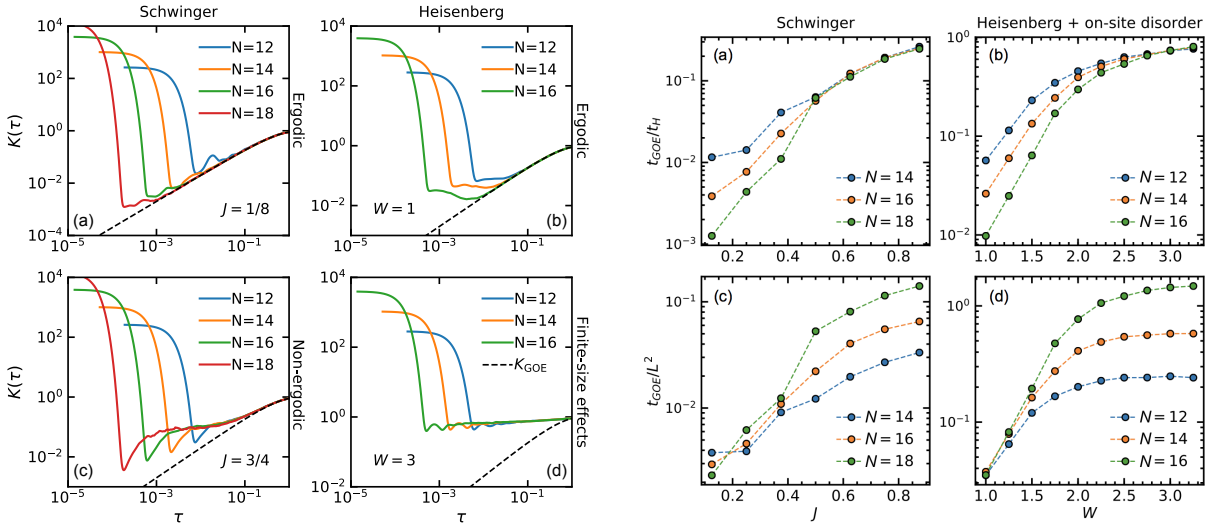

Figure 3.22: **Left.** Comparison between the SFF of the Hamiltonian Eq. (3.40) (a),(c) and of the Heisenberg model with on-site disorder (b),(d). In the deep ergodic region (a),(b) the SFF approaches the GOE prediction at times (in Heisenberg units) which decrease exponentially with the size of the system. For $J = 3/4$ in the LGT (c) the bulk of the spectrum is non-ergodic and the SFF deviates from the GOE prediction at intermediate times. For $W = 3$ in the Heisenberg chain (d) the level statistics is still flowing to WD, however the small effective localization length prevents accessing ergodic properties of the thermodynamic limit. **Right.** Comparison of $t_{\rm GOE}$ obtained from the spectral form factor vs disorder strength in the Schwinger model and in the Heisenberg model. Panels (a)-(b) show the ratio GOE time over Heisenberg time, which is directly extracted from the spectral form factor computed from the unfolded spectrum. Panels (c)-(d) show that at small disorder the Thouless time scales as N^2.

collapse on a finite linear region, which implies $\ln t_{\rm GOE} \sim N$; this timescale directly indicates that the system is not ergodic, and it is suggestive of an emergent localization even at this value of the coupling. We note that, in this parameter regime, we do not observe saturation of the Thouless time, which is instead evident in spin models (see Fig. 3.22 (left) (d) and Ref. [82]).

Finally, we comment on the consequences of our numerical observations on transport properties. The relation between $t_{\rm GOE}$ and transport has been clarified in Ref. [83] for non-interacting systems: $t_{\rm GOE}$ scales with the system size as the time t_{Th} a particle takes to spread through the entire system. Moreover, this scaling was used to precisely locate the Anderson localization transition on a D-dimensional cubic lattice: the critical disorder strength was determined by requiring $t_{\rm GOE} \sim t_H \sim L^D$, i.e. the time to reach scales as the Heisenberg time. In many-body quantum systems, instead, the equivalence of t_{Th} and $t_{\rm GOE}$ is more controversial, even in the deep ergodic region. The large-scale study of transport of Ref. [75] in the Heisenberg model with on-site disorder, based on the analysis of the spin current in the stationary state reached by the system when it is coupled to a bath at the boundaries, indicates that a transition from diffusive ($t_{Th} \sim L^2$) to sub-diffusive regime ($t_{Th} \sim L^\alpha$ with $\alpha < 2$) occurs at $W \simeq 0.5$. However the scaling of $t_{\rm GOE}$ in the same model, reported in Ref. [82] and depicted in Fig. 3.22 (right) (d), would suggest diffusive transport for disorder $W > 1$.

With this caveat in mind, we plot in Fig. 3.22 (right) the scaling of the $t_{\rm GOE}$ in the Schwinger model Eq. (3.40). The top panels (a) and (b) show the GOE time in Heisenberg units, as obtained from the spectral form factor computed from the unfolded spectrum. The bottom panels (c) and (d) show the GOE time in physical units rescaled by L^2. The data indicate a very similar scaling in the two models in the deep ergodic region. Transport properties in this regime are thus expected to be qualitatively similar in the both models.
We observe a striking difference between the two models by comparing panels (a) and (b) in

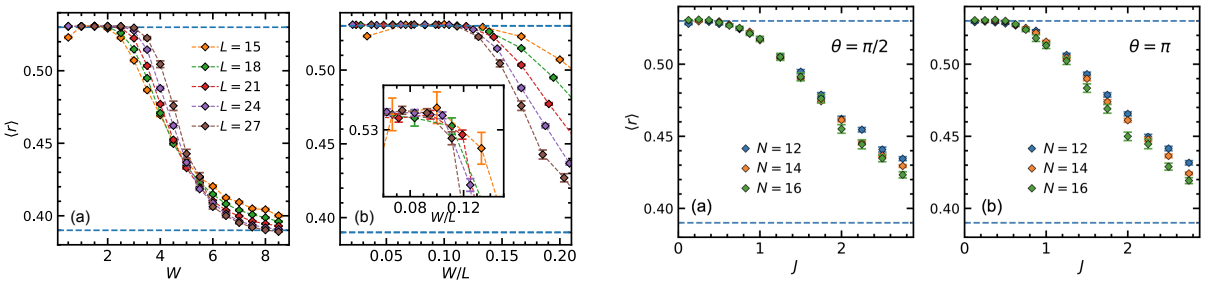

Figure 3.23: **Left.** Average level spacing ratio for the constrained spin model H_{QLM}, corresponding to the Schwinger model with truncated gauge fields. The finite-size scaling of $\langle r \rangle$ exhibits the same phenomenology as in the Heisenberg chain: $\langle r \rangle$ vs W (a) shows a crossing point drifting on the right for increasing N, $\langle r \rangle$ vs W/N (b) gives a good data collapse for $W/N < 0.1$. **Right.** Average level spacing ratio for the Schwinger model with non-zero topological angle $\theta = \pi/2$ (a) and $\theta = \pi$ (b). A non-zero θ does not change the outcome w.r.t. $\theta = 0$ (see Fig. 3.20 (b)), not even in the deconfined regime $\theta = \pi$.

Fig. 3.22 (right) for larger values of the disorder: while in the Schwinger model deviations from the GOE spectral form factor appear at a fraction of the Heisenberg time which is well below unity and independent from the system length, in the Heisenberg model these deviations occur at a time which is very close to the Heisenberg time. As argued in Ref. [82], the double scaling of t_{GOE} with system size and disorder strength (Fig. 3.22 (right) (b)) seems to suggest that a clear breakout from ergodic regime cannot be deduced from these data. This is in sharp contrast to the results we obtained in our model.
The fact that the ratio $t_{\mathrm{GOE}}/t_{\mathrm{H}}$ is size independent suggests that the suppression of transport is related to a size-independent scale, a very different scenario with respect to what is observed in Heisenberg models, characterized instead by anomalous transport properties [151, 152, 153, 154]: while it is not possible to immediately connect this mechanism to confinement, we naturally expect this emergent scale to be connected with the string tension, as the latter is size-independent and is the only parameter needed to characterize Coulomb interactions at large scales.

3.3.3 Discussion and conclusions

We conjecture that the origin of ergodicity breaking in lattice gauge theories stems from the fact that Coulomb law - which is acting at all energy scales - further constrains the system dynamics, and thus acts as an amplifier of any background disorder. In fact, for increasing system sizes, a larger fraction of the states of the spectrum will feature regions with a large accumulation of charge: as a consequence, the electrostatic energy (which is locally unbounded) becomes dominant and the effect of Coulomb interactions is enhanced. The presence of an unbounded energy density, which contrasts with the usual behaviour of spin models, does not affect low-energy states, but has important consequences on the rest of the spectrum: for instance, it systematically reduces the number of available resonances when size is increased. In order to substantiate this statement, we studied (1) the Schwinger model in its deconfining regime, $\theta = \pi$, and (2) a quantum link version of the model with truncated gauge fields, where Coulomb law is washed out by the truncation.

In Fig. 3.23 (left). we show r versus J for $\theta = \pi/2$ and $\theta = \pi$, the latter being the deconfining regime in the clean Schwinger model. Within error bars, we do not observe any difference between confining and deconfining regimes: in both cases, ergodicity breaks down in the same coupling window. We note that the fact that (de)confinement is not crucial here is not unexpected, as the latter is a phenomenon that only dictates the dynamics in the vicinity of the vacuum state.

As anticipated, we now consider a quantum link model in the presence of a background

disorder [155], with Hamiltonian

$$H_{QLM} = -w \sum_{j=1}^{L-1} (\psi_j^\dagger U_{j,j+1} \psi_{j+1} + \text{h.c.}) + J \sum_{j=1}^{L-1} E_{j,j+1}^2 + m \sum_{j=1}^{L} (-1)^j \psi_j^\dagger \psi_j, \tag{3.45}$$

where the first term is the matter-gauge coupling, the second is the electrostatic energy, and the third is the mass term. The gauge field operators are here represented by spin matrices $E_{j,j+1} = S^z_{j,j+1}$ and $U_{j,j+1} = S^+_{j,j+1}$, such that the commutation relation $[E_{j,j+1}, U_{j,j+1}] = U_{j,j+1}$ is satisfied. The Hamiltonian commutes with the local generators defined as

$$G_j = E_{j,j+1} - E_{j-1,j} - \psi_j^\dagger \psi_j + \frac{1-(-1)^j}{2}. \tag{3.46}$$

This model resembles the lattice Schwinger model in Eq. (3.40), but its Hilbert space is smaller: on each site the gauge field is truncated to a maximal value given by the dimension of the spin representation. Since the electrostatic term suppresses the large values of $E^2_{j,j+1}$, the truncation has minor effects on the ground state properties. The properties of the full spectrum, on the other hand, are expected to change drastically. The model in Eq. 3.45 in the gauge invariant sector (i.e. the one with no static charges, where $G_j = 0$ for every j) can be mapped to a constrained spin 1/2 model (the PXP model), as discussed in Sec. 3.2.1.

The Hamiltonian Eq. (3.45) is mapped to $H_{QLM} = \sum_i (-2m\ n_i - w\sigma_i^x)$, with $n = (1-\sigma^z)/2$, and it is restricted to the Hilbert space with $n_i n_{i+1} = 0$. In order to have a model where larger system sizes are accessible, we further constrain the Hilbert space to the sector with $n_i n_{i+2} = 0$: this constraint emerges when we include a strong next-to-nearest-neighbour interactions between electric fields in Eq. (3.45). The disorder is introduced by making the coefficient $W = -2m$ site-dependent. We obtain the Hamiltonian

$$H_{QLM} = \sum_i (W_i n_i - \sigma_i^x) \qquad n_i n_{i+1} = 0,\ n_i n_{i+2} = 0 \tag{3.47}$$

where we have fixed $w = 1$, and the W_i are drawn from a uniform distribution in the interval $[-W, W]$. In Fig. 3.23 (right), we show r versus the disorder strength W. We attempted a collapse scaling following [73], and assuming finite transition point W_c and correlation length critical exponent ν. The best fitting W_c and ν seem to increase linearly with size. The scaling of r follows rather closely the functional form proposed in Ref. [82]. These two observations indicate that, even in this model, the available system sizes are not sufficient to determine whether ergodicity is broken in the thermodynamic limit [85]. Overall, the findings on these two models support our conjecture above.

We have provided numerical evidence for the breakdown of ergodicity in disorderd $U(1)$ lattice gauge theories. Our results do not immediately indicate if localization kicks in right after such a breakdown, or if an intermediate non-ergodic, delocalized regime occurs. Further studies based on localization-specific diagnostics and transport properties may elucidate this aspect. The dynamical consequences of our results are immediately testable on quantum simulation platforms, where many-body dynamics of $U(1)$ lattice gauge theories has been recently realized [156, 4, 157], and, based on the nature of the interactions, might be extended to Yang-Mills theories.

3.4 Outlook

This chapter dealt with diverse equilibrium and non-equilibrium properties of the Rydberg atom quantum simulator governed by the Hamiltonian Eq. (3.1). Although we entirely focused on the one-dimensional case, experimental setups for simulating various higher-dimensional geometries are already available [19]. For this reason, an extension of the work discussed here to two dimensional systems is of uttermost importance.

In Sec. 3.1, we showed that the ground state phase diagram of the effective Rydberg Hamiltonian Eq. (3.3) accommodates narrow phases lying at the boundary of the broad ordered phases. Our work demonstrated that only an extremely careful analysis of finite size scaling can unambiguously resolve these tiny regions in parameter space. The ground state properties of the two-dimensional generalization of the experimentally realizable Hamiltonian Eq. (3.1) on a square lattice have been studied in Ref. [158] via tensor network methods. The resulting phase diagram as a function of detuning frequency δ and blockade radius R_b is depicted on the left in Fig. 3.24. The two-dimensional geometry enables a variety of ordered phases that seem to be directly connected by first or second order phase transitions. This fact is in sharp contrast with the one-dimensional scenario, where ordered phases are surrounded by narrow disordered regions, possibly resulting into gapless floating phases [159].
A deeper understanding of the interplay between different orders and of the phase transitions intervening between them can be achieved by studying the two-dimensional analogue of the exactly constrained model in Eq. (3.3). As R_b is increased, the effective Hamiltonian is acting on a Hilbert space with a constraint involving an increasing number of neighboring sites. For instance, when $R_b \in [1, \sqrt{2}]$ states with two occupied nearest-neighbor sites are discarded and the density-density interaction occurs between spins on the diagonal of the square lattice, yielding the Hamiltonian

$$H = \sum_{i,j} \sigma^x_{i,j} + U \sum_{i,j} n_{i,j} + V \sum_{i,j} (n_{i,j} n_{i+1,j-1} + n_{i,j} n_{i+1,j+1}), \qquad n_{i,j} n_{i,j+1} = n_{i,j} n_{i+1,j} = 0, \tag{3.48}$$

where the indices i and j label rows and columns of the square lattice. When V is varied from 0 to $+\infty$ the blockade radius R_b ranges from 1 to $\sqrt{2}$. This exact constraint is more severe than in one dimension, leading to a milder scaling of the Hilbert space dimension with the number of sites and allowing for an exact diagonalization analysis up to modest system sizes. The schematic phase diagram depicted on the right in Fig. 3.24 is deduced from the exact ground state of the constraint Hamiltonian on a 6×8 lattice with periodic boundary conditions, by analyzing various quantities, such as the fidelity susceptibility and the density-density structure factor. Two ordered phases –already identified in Ref. [158]– appear. In the checkerboard phase one of the two sublattices is fully occupied, the other being empty. In the striated phase the two sublattices exhibit antiferromagnetic order. In fact, from the exact diagonalization study it is easy to understand that these two phases are both characterized by an almost exact decoupling (at the ground state level) of the two sublattices of the square lattice. To understand the phase transition between these two ordered phases (green line in Fig. 3.24) it is thus enough to study the Hamiltonian in Eq. (3.48) restricted to one of the two sublattices. The restricted Hamiltonian gives a quantum Ising model with longitudinal and transverse field, which is ferromagnetic and antiferromagnetic when $V < 0$ or $V > 0$ respectively. The transition line between checkerboard and striated phases turns out to be exactly mapped on the continuous phase transition line between the paramagnetic and antiferromagnetic phases of the sublattice antiferromagnetic Ising model [160]. The coupling of the two sublattices occurs in correspondence of the grey line in Fig. 3.24 (right) and drives the two order-disorder transitions. The nature of checkerboard-to-disorder transition is most likely changing along the line. By analogy with the 1D case, we expect

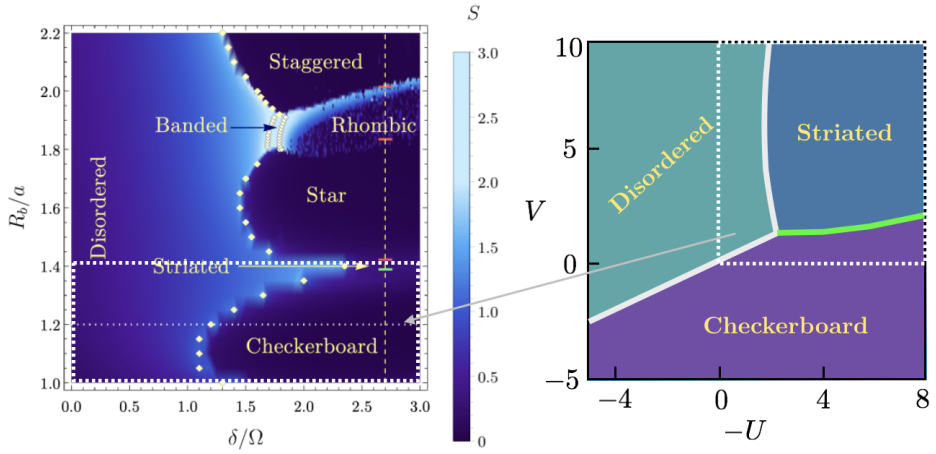

Figure 3.24: Comparison between the phase diagram of the experimentally realizable Rydberg Hamiltonian on a square lattice drawn in Ref. [158] by analyzing the ground state entanglement entropy computed with DMRG on a cylinder and the phase diagram of the effective constrained Hamiltonian Eq. (3.48) extracted from exact diagonalization study of a 6×8 square lattice with PBC. Chemical potential and laser frequencies are related by $U = -\delta/\Omega$, while increasing the blockade radius R_b from 1 to $\sqrt{2}$ is equivalent to vary V between 0 and $+\infty$. The dashed white lines enclose the corresponding regions in the two phase diagrams. The green line in both plots indicate a second order phase transition between the two ordered phases. The grey line on the plot on the right divides the phase diagram into two regions: in the disordered region the two sublattices are strongly coupled, while they are almost exactly decoupled, at the ground state level, in the two ordered regions.

a first order phase transition for large positive U and an Ising second order phase transition for small U, separated by a tricritical point. The character of the striated-to-disorder transition is, instead, completely unknown, and it is reasonable to expect interesting physics emerging there. We leave a more careful characterization of these critical phenomena for future work.

In Sec. 3.2, we proved that the Rydberg atom quantum simulator of the Hamiltonian in Eq. (3.1) reproduces the dynamics of a one-dimensional U(1) lattice gauge theory, and thus represents the largest scale LGT quantum simulator realized so far. The mapping we employed to achieve this result is based on the integration of the matter fields in a spin-1/2 quantum link model. Gauss law yields a local constraint on the gauge fields which is equivalent to the Rydberg blockade with radius one. The same strategy can be pursued in two dimensions: starting from a LGT with truncated gauge field, the matter degrees of freedom can be integrated out, resulting in a spin model for the gauge degrees of freedom. However, the two-dimensional Gauss law produces an highly non-local constraint on the spins, which does not map to the Rydberg blockade. This fact prevents to directly employ this approach for simulating synthetic gauge fields and it is still an open problem to translate this strategy into concrete implementation schemes. We leave this task for future investigation.

Finally, in Sec. 3.3, we studied the effect of a disordered background charge distribution on the lattice Schwinger model and we explored how the confining one-dimensional Coulomb interaction can lead to ergodicity breakdowns. The analysis performed there was entirely restricted to spectral properties. As such, its outcome is not informative on the properties of the eigenvectors. Extending the study to probes involving the eigenvectors, such as the inverse participation ratio or the entanglement entropy, is the next step to understand the relationship between the non-ergodic region and the typical scenario of many-body localization.

Bibliography

[1] G. Giudici et al., "Diagnosing Potts criticality and two-stage melting in one-dimensional hard-core boson models", *Phys. Rev. B* 99 (2019), p. 094434.

[2] F. M. Surace, G. Giudici, and M. Dalmonte, *Weak-ergodicity-breaking via lattice supersymmetry*, 2020, arXiv: 2003.11073 [cond-mat.stat-mech].

[3] G. Giudici et al., "Breakdown of ergodicity in disordered $U(1)$ lattice gauge theories", *Phys. Rev. Research* 2 (2020), p. 032034.

[4] H. Bernien et al., "Probing many-body dynamics on a 51-atom quantum simulator", *Nature* 551.7682 (2017), p. 579.

[5] M. D. Lukin et al., "Dipole Blockade and Quantum Information Processing in Mesoscopic Atomic Ensembles", *Phys. Rev. Lett.* 87 (2001), p. 037901.

[6] P. Fendley, K. Sengupta, and S. Sachdev, "Competing density-wave orders in a one-dimensional hard-boson model", *Phys. Rev. B* 69 (2004), p. 075106.

[7] R. Ghosh, A. Sen, and K. Sengupta, "Ramp and periodic dynamics across non-Ising critical points", *Phys. Rev. B* 97 (2018), p. 014309.

[8] R. Samajdar et al., "Numerical study of the chiral $\mathbb{Z}_3$ quantum phase transition in one spatial dimension", *Phys. Rev. A* 98 (2018), p. 023614.

[9] N. Chepiga and F. Mila, "Floating Phase versus Chiral Transition in a 1D Hard-Boson Model", *Phys. Rev. Lett.* 122 (2019), p. 017205.

[10] S. Whitsitt, R. Samajdar, and S. Sachdev, "Quantum field theory for the chiral clock transition in one spatial dimension", *Phys. Rev. B* 98 (2018), p. 205118.

[11] N. Chepiga and F. Mila, "DMRG investigation of constrained models: from quantum dimer and quantum loop ladders to hard-boson and Fibonacci anyon chains", *SciPost Phys.* 6 (2019), p. 33.

[12] C. J. Turner et al., "Quantum scarred eigenstates in a Rydberg atom chain: Entanglement, breakdown of thermalization, and stability to perturbations", *Phys. Rev. B* 98 (2018), p. 155134.

[13] C. Turner et al., "Weak ergodicity breaking from quantum many-body scars", *Nature Physics* 14 (2018), p. 745.

[14] W. W. Ho et al., "Periodic orbits, entanglement and quantum many-body scars in constrained models: matrix product state approach", *Phys. Rev. Lett.* 122 (2019), p. 040603.

[15] V. Khemani, C. R. Laumann, and A. Chandran, "Signatures of integrability in the dynamics of Rydberg-blockaded chains", *Phys. Rev. B* 99 (2019), p. 161101.

[16] S. Choi et al., "Emergent SU (2) dynamics and perfect quantum many-body scars", *Phys. Rev. Lett.* 122 (2019), p. 220603.

[17] I. Bloch, J. Dalibard, and S. Nascimbène, "Quantum simulations with ultracold quantum gases", *Nat. Phys.* 8.4 (2012), pp. 267–276.

[18] I. Lesanovsky and H. Katsura, "Interacting Fibonacci anyons in a Rydberg gas", *Phys. Rev. A* 86 (2012), p. 041601.

[19] D. Barredo et al., "Synthetic three-dimensional atomic structures assembled atom by atom", *Nature* 561 (2018), p. 79.

[20] J. Zeiher et al., "Coherent many-body spin dynamics in a long-range interacting Ising chain", *Phys. Rev. X* 7 (2017), p. 041063.

[21] P. Di Francesco, P. Mathieu, and D. Senechal, *Conformal Field Theory*, Graduate Texts in Contemporary Physics, New York: Springer-Verlag, 1997.

[22] A. O. Gogolin, A. A. Nersesyan, and A. M. Tsvelik, *Bosonization and strongly correlated systems*, Cambridge University Press, Cambridge, 1998.

[23] G. I. Japaridze and A. A. Nersesyan, "Magnetic-field phase transition in a one-dimensional system of electrons with attraction", *JETP Lett.* 27 (1978), p. 334.

[24] V. L. Pokrovsky and A. L. Talapov, "Ground State, Spectrum, and Phase Diagram of Two-Dimensional Incommensurate Crystals", *Phys. Rev. Lett.* 42 (1979), pp. 65–67.

[25] D. A. Huse and M. E. Fisher, "Commensurate melting, domain walls, and dislocations", *Phys. Rev. B* 29 (1984), pp. 239–270.

[26] N. V. Prokof'ev, B. V. Svistunov, and I. S. Tupitsyn, "Exact, complete, and universal continuous-time worldline Monte Carlo approach to the statistics of discrete quantum systems", *Journal of Experimental and Theoretical Physics* 87.2 (1998), pp. 310–321.

[27] S. R. White, "Density matrix formulation for quantum renormalization groups", *Phys. Rev. Lett.* 69.19 (1992), pp. 2863–2866.

[28] J. M. Deutsch, "Quantum statistical mechanics in a closed system", *Phys. Rev. A* 43 (1991), pp. 2046–2049.

[29] M. Srednicki, "Chaos and quantum thermalization", *Phys. Rev. E* 50 (1994), pp. 888–901.

[30] M. Rigol, V. Dunjko, and M. Olshanii, "Thermalization and its mechanism for generic isolated quantum systems", *Nature* 452.7189 (2008), pp. 854–858.

[31] S. Coleman, "More about the massive Schwinger model", *Ann. Phys.* 101.1 (1976), p. 239.

[32] E. Zohar, I. Cirac, and B. Reznik, "Quantum Simulations of Lattice Gauge Theories using Ultracold Atoms in Optical Lattices", *Rep. Prog. Phys.* 79 (2016), p. 014401.

[33] M. Dalmonte and S. Montangero, "Lattice gauge theories simulations in the quantum information era", *Contemp. Phys.* 57 (2016), p. 388.

[34] J. Preskill, "Simulating quantum field theory with a quantum computer", *arXiv.1811.10085* (2018).

[35] E. A. Martinez et al., "Real-time dynamics of lattice gauge theories with a few-qubit quantum computer", *Nature* 534 (2016), p. 516.

[36] U. J. Wiese, "Ultracold quantum gases and lattice systems: quantum simulation of lattice gauge theories", *Ann. Phys.* 525.10-11 (2013), p. 777.

[37] E. A. Calzetta and B. L. Hu, *Nonequilibrium Quantum Field Theory*, Cambridge Univ. Press, Cambridge, 2008.

[38] G. S. Bali et al., "Observation of string breaking in QCD", *Phys. Rev. D* 71 (2005), p. 114513.

[39] F. Hebenstreit, J. Berges, and D. Gelfand, "Real-Time Dynamics of String Breaking", *Phys. Rev. Lett.* 111 (2013), p. 201601.

[40] S. Chandrasekharan and U. .-.-J. Wiese, "Quantum link models : A discrete approach to gauge theories", *Nucl. Phys. B* 492 (1997), p. 455.

[41] Y. Kuno et al., "Real-time dynamics and proposal for feasible experiments of lattice gauge–Higgs model simulated by cold atoms", *New Journal of Physics* 17.6 (2015), p. 063005.

[42] Y. Kuno et al., "Quantum simulation of $(1 + 1)$-dimensional U(1) gauge-Higgs model on a lattice by cold Bose gases", *Phys. Rev. D* 95 (2017), p. 094507.

[43] J. Schwinger, "Gauge Invariance and Mass. II", *Phys. Rev.* 128 (1962), p. 2425.

[44] J. Kogut and L. Susskind, "Hamiltonian formulation of Wilson's lattice gauge theories", *Phys. Rev. D* 11 (1975), p. 395.

[45] F. Hebenstreit, J. Berges, and D. Gelfand, "Simulating fermion production in 1+1 dimensional QED", *Phys. Rev. D* 87 (2013), p. 105006.

[46] B. Buyens et al., "Confinement and String Breaking for QED_2 in the Hamiltonian Picture", *Phys. Rev. X* 6 (2016), p. 041040.

[47] T. Pichler et al., "Real-time Dynamics in U(1) Lattice Gauge Theories with Tensor Networks", *Phys. Rev. X* 6 (2016), p. 011023.

[48] K. Rajagopal and F. Wilczek, "Emergence of coherent long wavelength oscillations after a quench: Application to QCD", *Nucl. Phys. B* 404.3 (1993), pp. 577–589.

[49] C.-J. Lin and O. I. Motrunich, "Exact strong-ETH violating eigenstates in the Rydberg-blockaded atom chain", *Phys. Rev. Lett.* 122 (2019), p. 173401.

[50] P. W. Anderson, "Absence of diffusion in certain random lattices", *Phys. Rev.* 109 (1958), p. 1492.

[51] D. M. Basko, I. L. Aleiner, and B. L. Altshuler, "Metal–insulator transition in a weakly interacting many-electron system with localized single-particle states", *Ann. Phys.* 321 (2006), p. 1126.

[52] I. Gornyi, A. Mirlin, and D. Polyakov, "Interacting electrons in disordered wires: Anderson localization and low-T transport", *Phys. Rev. Lett.* 95 (2005), p. 206603.

[53] E. Altman and R. Vosk, "Universal Dynamics and Renormalization in Many-Body-Localized Systems", *Annual Review of Condensed Matter Physics* 6.1 (2015), pp. 383–409.

[54] R. Nandkishore and D. A. Huse, "Many-Body Localization and Thermalization in Quantum Statistical Mechanics", *Annual Review of Condensed Matter Physics* 6.1 (2015), pp. 15–38.

[55] J. Z. Imbrie, V. Ros, and A. Scardicchio, "Local integrals of motion in many-body localized systems", *Annalen der Physik* 529 (2017).

[56] D. A. Abanin et al., "Colloquium: Many-body localization, thermalization, and entanglement", *Reviews of Modern Physics* 91.2 (2019), p. 021001.

[57] F. Haake, "Quantum signatures of chaos", *Quantum Coherence in Mesoscopic Systems*, Springer, 1991, pp. 583–595.

[58] L. Fleishman and P. W. Anderson, "Interactions and the Anderson transition", *Phys. Rev. B* 21 (1980), pp. 2366–2377.

[59] B. L. Altshuler et al., "Quasiparticle lifetime in a finite system: A nonperturbative approach", *Phys. Rev. Lett.* 78 (1997), p. 2803.

[60] J. Z. Imbrie, "On Many-Body Localization for Quantum Spin Chains", *Journal of Statistical Physics* 163.5 (2016), pp. 998–1048.

[61] V. Ros, M. Müller, and A. Scardicchio, "Integrals of motion in the many-body localized phase", *Nucl. Phys. B* 891 (2015), pp. 420–465.

[62] W. De Roeck and F. Huveneers, "Asymptotic quantum many-body localization from thermal disorder", *Communications in Mathematical Physics* 332.3 (2014), pp. 1017–1082.

[63] W. De Roeck and F. Huveneers, "Scenario for delocalization in translation-invariant systems", *Phys. Rev. B* 90 (2014), p. 165137.

[64] W. De Roeck et al., "Absence of many-body mobility edges", *Physical Review B* 93.1 (2016), p. 014203.

[65] A. Chandran et al., "Many-body localization beyond eigenstates in all dimensions", *Phys. Rev. B* 94 (2016), p. 144203.

[66] A. Pal and D. Huse, "Many-body localization phase transition", *Phys. Rev. B* 82 (2010), p. 174411.

[67] P. Prelovšek, O. S. Barišić, and M. Žnidarič, "Absence of full many-body localization in the disordered Hubbard chain", *Physical Review B* 94.24 (2016), p. 241104.

[68] A. C. Potter and R. Vasseur, "Symmetry constraints on many-body localization", *Physical Review B* 94.22 (2016), p. 224206.

[69] I. V. Protopopov, W. W. Ho, and D. A. Abanin, "Effect of SU (2) symmetry on many-body localization and thermalization", *Physical Review B* 96.4 (2017), p. 041122.

[70] I. V. Protopopov et al., "Non-Abelian Symmetries and Disorder: A Broad Nonergodic Regime and Anomalous Thermalization", *Phys. Rev. X* 10 (2020), p. 011025.

[71] A. De Luca and A. Scardicchio, "Ergodicity breaking in a model showing many-body localization", *Europhys. Lett.* 101 (2013), p. 37003.

[72] J. Goold et al., "Total correlations of the diagonal ensemble herald the many-body localization transition", *Phys. Rev. B* 92 (2015), p. 180202.

[73] D. J. Luitz, N. Laflorencie, and F. Alet, "Many-body localization edge in the random-field Heisenberg chain", *Phys. Rev. B* 91 (2015), p. 081103.

[74] F. Pietracaprina et al., "Entanglement critical length at the many-body localization transition", *arXiv preprint arXiv:1610.09316* (2016).

[75] M. Žnidarič, A. Scardicchio, and V. K. Varma, "Diffusive and Subdiffusive Spin Transport in the Ergodic Phase of a Many-Body Localizable System", *Phys. Rev. Lett.* 117 (2016), p. 040601.

[76] F. Alet and N. Laflorencie, "Many-body localization: an introduction and selected topics", *Comptes Rendus Physique* 19.6 (2018), pp. 498–525.

[77] N. Macé, F. Alet, and N. Laflorencie, "Multifractal scalings across the many-body localization transition", *Physical review letters* 123.18 (2019), p. 180601.

[78] R. Vosk, D. A. Huse, and E. Altman, "Theory of the Many-Body Localization Transition in One-Dimensional Systems", *Phys. Rev. X* 5 (2015), p. 031032.

[79] P. T. Dumitrescu et al., "Kosterlitz-Thouless scaling at many-body localization phase transitions", *Physical Review B* 99.9 (2019), p. 094205.

[80] A. Chandran, C. Laumann, and V. Oganesyan, "Finite size scaling bounds on many-body localized phase transitions", *arXiv: 1509.04285 [cond-mat.dis-nn]* (2015).

[81] A. B. Harris, "Effect of random defects on the critical behaviour of Ising models", *Journal of Physics C: Solid State Physics* 7.9 (1974), pp. 1671–1692.

[82] J. Šuntajs et al., "Quantum chaos challenges many-body localization" (2019), arXiv: 1905.06345 [cond-mat.str-el].

[83] P. Sierant, D. Delande, and J. Zakrzewski, "Thouless Time Analysis of Anderson and Many-Body Localization Transitions", *Phys. Rev. Lett.* 124 (2020), p. 186601.

[84] D. A. Abanin et al., "Distinguishing localization from chaos: challenges in finite-size systems" (2019), arXiv: 1911.04501 [cond-mat.str-el].

[85] R. K. Panda et al., "Can we study the many-body localisation transition?", *EPL (Europhysics Letters)* 128.6 (2020), p. 67003.

[86] M. Schreiber et al., "Observation of many-body localization of interacting fermions in a quasi-random optical lattice", *Science* 349.6250 (2015), pp. 842–845.

[87] J. Smith et al., "Many-body localization in a quantum simulator with programmable random disorder", *Nat. Phys.* 12 (2016), pp. 907–911.

[88] K. G. Wilson, "Confinement of quarks", *Phys. Rev. D* 10.8 (1974), p. 2445.

[89] I. Montvay and G. Muenster, *Quantum Fields on a lattice*, Cambridge Univ. Press, Cambridge, 1994.

[90] R. Baxter, *Exactly Solved Models in Statistical Mechanics*, Dover books on physics, Dover Publications, 2007.

[91] J. Sólyom and P. Pfeuty, "Renormalization-group study of the Hamiltonian version of the Potts model", *Phys. Rev. B* 24 (1981), pp. 218–229.

[92] G. von Gehlen, V. Rittenberg, and T. Vescan, "Conformal invariance and correction to finite-size scaling: applications to the three-state Potts model", *Journal of Physics A: Mathematical and General* 20.9 (1987), p. 2577.

[93] G. von Gehlen and V. Rittenberg, "Operator content of the three-state Potts quantum chain", *Journal of Physics A: Mathematical and General* 19.10 (1986), p. L625.

[94] V. Dotsenko, "Critical behaviour and associated conformal algebra of the Z3 Potts model", *Nuclear Physics B* 235.1 (1984), pp. 54–74.

[95] A. Osterloh et al., "Scaling of entanglement close to a quantum phase transition", *Nature* 416.6881 (2002), pp. 608–610.

[96] L. Amico et al., "Entanglement in many-body systems", *Rev. Mod. Phys.* 80 (2008), pp. 517–576.

[97] S.-J. Gu, "Fidelity apporach to quantum phase transitions", *International Journal of Modern Physics B* 24.23 (2010), pp. 4371–4458.

[98] P. Zanardi and N. Paunković, "Ground state overlap and quantum phase transitions", *Phys. Rev. E* 74 (2006), p. 031123.

[99] W.-L. You, Y.-W. Li, and S.-J. Gu, "Fidelity, dynamic structure factor, and susceptibility in critical phenomena", *Phys. Rev. E* 76 (2007), p. 022101.

[100] D. Schwandt, F. Alet, and S. Capponi, "Quantum Monte Carlo Simulations of Fidelity at Magnetic Quantum Phase Transitions", *Phys. Rev. Lett.* 103 (2009), p. 170501.

[101] A. F. Albuquerque et al., "Quantum critical scaling of fidelity susceptibility", *Phys. Rev. B* 81 (2010), p. 064418.

[102] P. Calabrese and J. Cardy, "Entanglement entropy and conformal field theory", *J. Phys. A: Math. Theor.* 42.50 (2009), p. 504005.

[103] M. B. Plenio and S. Virmani, "An introduction to entanglement measures", *Quant.Inf.Comput.* 7 (2007), pp. 1–51.

[104] A. Läuchli and C. Kollath, "Spreading of correlations and entanglement after a quench in the one-dimensional Bose-Hubbard model", *J. Stat.* Mech. (2008), P05018.

[105] M. Dalmonte et al., "Cluster Luttinger liquids and emergent supersymmetric conformal critical points in the one-dimensional soft-shoulder Hubbard model", *Phys. Rev. B* 92 (2015), p. 045106.

[106] A. B. Zamolodchikov, "Irreversibility of the Flux of the Renormalization Group in a 2D Field Theory", *JETP Lett.* 43 (1986), [Pisma Zh. Eksp. Teor. Fiz.43,565(1986)], pp. 730–732.

[107] F. Woynarovich and H. .-.-P. Eckle, "Finite-size corrections for the low lying states of a half-filled Hubbard chain", *Journal of Physics A: Mathematical and General* 20.7 (1987), p. L443.

[108] G. Sun, A. K. Kolezhuk, and T. Vekua, "Fidelity at Berezinskii-Kosterlitz-Thouless quantum phase transitions", *Phys. Rev. B* 91 (2015), p. 014418.

[109] M. P. A. Fisher et al., "Boson localization and the superfluid-insulator transition", *Phys. Rev. B* 40 (1989), pp. 546–570.

[110] T. Mishra, J. Carrasquilla, and M. Rigol, "Phase diagram of the half-filled one-dimensional t-V-$V^{'}$ model", *Phys. Rev. B* 84 (2011), p. 115135.

[111] M. Dalmonte et al., "Gap scaling at Berezinskii-Kosterlitz-Thouless quantum critical points in one-dimensional Hubbard and Heisenberg models", *Phys. Rev. B* 91 (2015), p. 165136.

[112] L. Wang, K. S. D. Beach, and A. W. Sandvik, "High-precision finite-size scaling analysis of the quantum-critical point of $S = 12$ Heisenberg antiferromagnetic bilayers", *Phys. Rev. B* 73 (2006), p. 014431.

[113] G. M. Crosswhite and D. Bacon, "Finite automata for caching in matrix product algorithms", *Phys. Rev. A* 78 (2008), p. 012356.

[114] Y. Zhuang et al., "Phase diagram of the Z_3 Parafermionic Chain with Chiral Interactions", *Phys. Rev. B* 92 (2015), p. 035154.

[115] A. Keesling et al., "Quantum Kibble–Zurek mechanism and critical dynamics on a programmable Rydberg simulator", *Nature* 568.7751 (2019), pp. 207–211.

[116] D. Horn, *Phys. Lett. B* 100 (1981), p. 149.

[117] D. Banerjee et al., "Atomic Quantum Simulation of Dynamical Gauge Fields Coupled to Fermionic Matter: From String Breaking to Evolution after a Quench", *Phys. Rev. Lett.* 109 (2012), p. 175302.

[118] T. Chanda et al., *Confinement and Lack of Thermalization after Quenches in the Bosonic Schwinger Model*, 2020.

[119] Y.-P. Huang, D. Banerjee, and M. Heyl, "Dynamical quantum phase transitions in $U(1)$ quantum link models", *arXiv preprint arXiv:1808.07874* (2018).

[120] V. Kasper et al., "Schwinger pair production with ultracold atoms", *Phys. Lett. B.* 760 (2016), p. 742.

[121] E. Rico et al., "Tensor networks for Lattice Gauge Theories and Atomic Quantum Simulation", *Phys. Rev. Lett.* 112 (2014), p. 201601.

[122] C. J. Hamer et al., *Nucl. Phys. B* 208 (1982), p. 413.

[123] M. Bañuls et al., "The mass spectrum of the Schwinger model with matrix product states", *J. High Energy Phys.* 2013 (2013), p. 158.

[124] F. Fucito et al., "Approach to equilibrium in a chain of nonlinear oscillators", *Journal de Physique* 43.5 (1982), pp. 707–713.

[125] T. Langen, T. Gasenzer, and J. Schmiedmayer, "Prethermalization and universal dynamics in near-integrable quantum systems", *Journal of Statistical Mechanics: Theory and Experiment* 2016.6 (2016), p. 064009.

[126] T. Banks, L. Susskind, and J. Kogut, "Strong-coupling calculations of lattice gauge theories: (1 + 1)-dimensional exercises", *Phys. Rev. D* 13 (1976), p. 1043.

[127] J. Haegeman et al., "Unifying time evolution and optimization with matrix product states", *Phys. Rev. B* 94 (2016), p. 165116.

[128] A. Omran et al., "Generation and manipulation of Schrödinger cat states in Rydberg atom arrays", *Science* 365.6453 (2019), pp. 570–574.

[129] P. P. Mazza et al., "Suppression of transport in nondisordered quantum spin chains due to confined excitations", *Phys. Rev. B* 99 (2019), p. 180302.

[130] M. Brenes et al., "Many-body localization dynamics from gauge invariance", *Phys. Rev. Lett.* 120 (2018), p. 030601.

[131] M. Kormos et al., "Real time confinement following a quantum quench to a non-integrable model", *Nature Physics* 13 (2017), pp. 246–249.

[132] A. J. A. James, R. M. Konik, and N. J. Robinson, "Nonthermal states arising from confinement in one and two dimensions", *Phys. Rev. Lett.* 122 (2019), p. 130603.

[133] J. Park, Y. Kuno, and I. Ichinose, "Glassy Dynamics from Quark Confinement: Atomic Quantum Simulation of Gauge-Higgs Model on Lattice", *arXiv:1903.07297* (2019).

[134] C. Kokail et al., "Self-Verifying Variational Quantum Simulation of the Lattice Schwinger Model", *Nature* 569 (2019), p. 355.

[135] S. Notarnicola, M. Collura, and S. Montangero, "Real time dynamics quantum simulation of (1+ 1)-D lattice QED with Rydberg atoms", *arXiv preprint arXiv:1907.12579* (2019).

[136] E. Zohar and J. I. Cirac, "Removing Staggered Fermionic Matter in U(N)U(N) and SU(N)SU(N) Lattice Gauge Theories", *arXiv:1905.00652* (2019).

[137] A. W. Glaetzle et al., "Quantum Spin Ice and dimer models with Rydberg atoms", *Phys. Rev. X* 4 (2014), p. 041037.

[138] A. Celi et al., "Emerging 2D Gauge theories in Rydberg configurable arrays", *arXiv preprint arXiv:1907.03311* (2019).

[139] S. Kühn et al., "Non-Abelian string breaking phenomena with matrix product states", *Journal of High Energy Physics* 2015.7 (2015).

[140] T. Pichler et al., "Real-Time Dynamics in U(1) Lattice Gauge Theories with Tensor Networks", *Physical Review X* 6.1 (2016).

[141] M. Brenes et al., "Many-Body Localization Dynamics from Gauge Invariance", *Phys. Rev. Lett.* 120 (2018), p. 030601.

[142] R. M. Nandkishore and S. L. Sondhi, "Many-Body Localization with Long-Range Interactions", *Physical Review X* 7.4 (2017).

[143] A. A. Akhtar, R. M. Nandkishore, and S. L. Sondhi, "Symmetry breaking and localization in a random Schwinger model with commensuration", *Phys. Rev. B* 98 (2018), p. 115109.

[144] J. Schwinger, "The Theory of Quantized Fields. I", *Phys. Rev.* 82 (1951), pp. 914–927.

[145] J. Kogut and L. Susskind, "Hamiltonian formulation of Wilson's lattice gauge theories", *Phys. Rev. D* 11 (1975), pp. 395–408.

[146] S. Coleman, "More about the massive Schwinger model", *Annals of Physics* 101.1 (1976), pp. 239–267.

[147] C. Hamer, Z. Weihong, and J. Oitmaa, "Series expansions for the massive Schwinger model in Hamiltonian lattice theory", *Phys. Rev. D* 56.1 (1997), pp. 55–67.

[148] P. Sierant and J. Zakrzewski, "Many-body localization of bosons in optical lattices", *New Journal of Physics* 20.4 (2018), p. 043032.

[149] V. E. Kravtsov et al., "A random matrix model with localization and ergodic transitions", *New Journal of Physics* 17.12 (2015), p. 122002.

[150] M. Serbyn, Z. Papić, and D. A. Abanin, "Thouless energy and multifractality across the many-body localization transition", *Physical Review B* 96.10 (2017).

[151] K. Agarwal et al., "Anomalous Diffusion and Griffiths Effects Near the Many-Body Localization Transition", *Phys. Rev. Lett.* 114 (2015), p. 160401.

[152] D. J. Luitz and Y. Bar Lev, "Anomalous Thermalization in Ergodic Systems", *Phys. Rev. Lett.* 117 (2016), p. 170404.

[153] D. J. Luitz and Y. B. Lev, "The ergodic side of the many-body localization transition", *Annalen der Physik* 529.7 (2017), p. 1600350.

[154] D. J. Luitz, I. M. Khaymovich, and Y. B. Lev, "Multifractality and its role in anomalous transport in the disordered XXZ spin-chain", *SciPost Phys. Core* 2 (2020), p. 6.

[155] D. Banerjee et al., "Atomic quantum simulation of dynamical gauge fields coupled to fermionic matter: from string breaking to evolution after a quench", *Physical review letters* 109.17 (2012), p. 175302.

[156] E. A. Martinez et al., "Real-time dynamics of lattice gauge theories with a few-qubit quantum computer", *Nature* 534.7608 (2016), pp. 516–519.

[157] F. M. Surace et al., "Lattice Gauge Theories and String Dynamics in Rydberg Atom Quantum Simulators", *Phys. Rev. X* 10 (2020), p. 021041.

[158] R. Samajdar et al., "Complex Density Wave Orders and Quantum Phase Transitions in a Model of Square-Lattice Rydberg Atom Arrays", *Phys. Rev. Lett.* 124 (2020), p. 103601.

[159] M. Rader and A. M. Läuchli, *Floating Phases in One-Dimensional Rydberg Ising Chains*, 2019, arXiv: 1908.02068 [cond-mat.quant-gas].

[160] M. A. Neto and J. R. de Sousa, "Transverse Ising antiferromagnetic in a longitudinal magnetic field: study of the ground state", *Physics Letters A* 330.5 (2004), pp. 322–325.